INVESTIGATING THE EFFECTS OF Pd_n CLUSTER SIZE AND THE ALUMINA SUPPORT THICKNESS ON THE ELECTRONIC STRUCTURE, GEOMETRY, AND CATALYTIC ACTIVITY, PROBED VIA THE CO OXIDATION REACTION

by

Matthew David Kane

A dissertation submitted to the faculty of
The University of Utah
in partial fulfillment of the requirements for the degree of

Doctor of Philosophy

Department of Chemistry

The University of Utah

December 2014

The University of Utah Graduate School

STATEMENT OF DISSERTATION APPROVAL

The dissertation of **Matthew David Kane**

has been approved by the following supervisory committee members:

Scott L. Anderson	, Chair	**04/30/2014** Date Approved
Peter B. Armentrout	, Member	**04/30/2014** Date Approved
Michael D. Morse	, Member	**04/30/2014** Date Approved
Ilya Zharov	, Member	**04/30/2014** Date Approved
Clayton C. Williams	, Member	**04/30/2014** Date Approved

and by **Cynthia J. Burrows** , Chair of

the Department of **Chemistry**

and by David B. Kieda, Dean of The Graduate School.

ABSTRACT

The research presented in this dissertation probes the effects of the metal oxide support thickness as well as Pd_n cluster size on the catalytic efficiency as monitored by the CO oxidation reaction. Before any experiments could be conducted, a reliable Al evaporation source needed to be built and characterized to make a consistent and reliable alumina support for the Pd_n clusters. Despite an initial goal of determining how the Pd_n cluster size effects the reactivity, it turned out that the effects of the alumina film thickness, substrate dopants in the alumina, and identity of the base refractory metal substrate play a huge role in determining the catalytic reactivity. Before any size-selected experiments could be done, a detailed set of experiments probing the film was necessary to prevent convolution of Pd_n cluster size effects with the effects of a varying metal oxide support.

In addition to the catalytic activity determined via temperature programed reaction (TPR), both the electronic and geometric structures of the film and Pd_n clusters were studied through a combination of photoelectron spectroscopy (PES) and ion scattering spectroscopy, respectively. It will be shown through these methods, that for the conditions used here, the catalytic activity is governed by the ability of the Pd_n to bind and activate oxygen into a reactive species.

An introduction into the importance of catalysis and, more specifically, size selected model catalysis is described in Chapter 1. The instrument and description of the

custom made aluminum evaporation source and C type thermocouple are presented in Chapter 2. Chapter 3 focuses on all of the work for both alumina thickness and Pd_n cluster size effects supported on alumina films grown on Ta(110). Chapters 4 and 5 discuss the differing effects of the alumina film thickness and Pd_n cluster size for alumina films grown on a Re(0001) single crystal, respectively.

TABLE OF CONTENTS

ABSTRACT iii

ACKNOWLEDGEMENTS vii

Chapter

1 INTRODUCTION 1

1.1 Background 2
1.2 The importance of cluster size research 4
1.3 References 5

2 EXPERIMENTAL SETUP 9

2.1 The instrument 10
2.2 Metal evaporation source 12
2.3 Monitoring high and low temperatures in UHV 15
2.4 References 21

3 ALUMINA SUPPORT AND Pd_n CLUSTER SIZE EFFECTS ON ACTIVITY OF Pd_n FOR CATALYTIC OXIDATION OF CO 22

3.1 Introduction 23
3.2 Experimental methodology 25
3.3 Results and discussion 30
3.4 Conclusions 55
3.5 References 57

4 EFFECTS OF ALUMINA FILM THICKNESS ON CO OXIDATION ACTIVITY OVER Pd_{20}/ALUMINA/Re(0001): CORRELATED EFFECTS OF ALUMINA ELECTRONIC PROPERTIES AND Pd_{20} GEOMETRY ON ACTIVITY 62

4.1 Introduction 63

4.2 Experimental 67
4.3 Results 74
4.4 Discussion 98
4.5 Conclusions 118
4.6 References 118

5 MASS-SELECTED SUPPORTED CLUSTER CATALYSTS: SIZE EFFECTS ON CO OXIDATION ACTIVITY, ELECTRONIC STRUCTURE, AND THERMAL STABILITY OF Pd_n/ALUMINA ($n \leq 30$) MODEL CATALYSTS 130

5.1 Introduction 131
5.2 Experimental 135
5.3 Results and discussion 146
5.4 Conclusions 174
5.5 References 175

6 CONCLUSION 186

6.1 Conclusions 187

Appendices

A. SUPPORTING INFORMATION INCLUDED FOR CHAPTER 4 189

B. SUPPORTING INFORMATION INCLUDED FOR CHAPTER 5 209

ACKNOWLEDGEMENTS

I would first like to thank my advisor, mentor, and friend, Professor Scott L. Anderson, for graciously accepting me into his research group and offering me a summer research experience the year prior to my entry into graduate school. The past few years working with him has enabled me to grow both as a scientist and as a free thinker. I cannot imagine learning or enjoying my time more by working in any other group. I have learned to really appreciate science and think about the data presented to arrive at my own conclusion, before blindly accepting an interpretation as fact. Though often nerve racking when asked to do quick math to determine the gain of a multiplier or estimate the amount of adsorbates hitting a surface during sample cool down, I am proud to say I get less flustered and can quickly determine the calculation needed, not that my mental math ever got any faster.

As much as I enjoyed learning about surfaces and catalysts, my time in Utah would pale in comparison if even a single person from our research group had not decided to join. I will always remember my time spent the first year bonding with Brandon McMahon while taking classes and getting stuck trying to understand the integrals needed for the homework in Quantum 1, only to find out in class that the answer was zero. Though it seems so recent and distant at the same time, I will cherish the mentorship and friendship of Bill Kaden, to whom I attribute most of my technical lab skills, and desire to be very competitive in all sporting events. I would be lost in my

political understanding of the world were it not for the, sometimes unwanted, interjections about the policies of Ron Paul, courtesy of Jason Boyle, who also made me really rethink the priorities of what to focus on when writing papers and giving talks. The office would not be nearly as interesting without the constant pranking and jokes with Dave Bell, whose desk needs to be filled with packing peanuts if he ever gets a desk with drawers. The incoming group of graduate students, Tim Gorey, Yang Dai, Collin Howder, and Eric Baxter, become close friends and were crucial in helping me balance the stresses of the last year with all the fun and excitement of sharing my acquired lab skills. It was not until I had to mentor them that I realized how far I had come in my own understanding of operating in a lab. I am also very appreciative of the German exchange students, Sebastian Proch and Alex Weber, who befriended me and opened my eyes to another culture. Of all my group members, I need to thank F. Sloan Roberts most of all. The entirety of my Ph.D. was completed working side by side with Sloan, including everything from working on a lathe, to figuring out how to use an oscilloscope, or spending hours on end in the lab collecting data. Without our constant back and forth discussing of data and life, I am sure my tenure at Utah would have been much less fulfilling and taken twice as long.

I would also like to thank the other members of my committee: Professor Peter B. Armentrout, Professor Michael D. Morse, Professor Ilya Zharov, and Professor Clayton C. Williams, for providing feedback and lively discussions about my research. It is also important to give a big thank you to Ron Jones and Dale Heisler in the electronics shop. Without the two of you I would not have any idea how to perform even the simplest of tasks such as hooking up a power supply or complicated tasks such as probing through

the internals of an electronics box or electrical schematics. One of the best classes, machine shop, was taught by Dennis Romney; he taught me think about how to design a part, by how it would have to be made. I really appreciate all of the quick turnaround time on repairs and advice on how to approach a mechanical problem or machining technique. These are skills that I certainly will take with me into my personal life as well as in future instrumentation designs.

Finally, I want to thank all of the love and support of my friends and family. You have all helped me stay motivated and encouraged during this wonderful adventure. In particular, Lindsay McGough helped me tremendously by providing me motivation and encouragement to continue studying or working hard during the long sleepless nights. Dad, I want to especially thank you for teaching me to not be lazy, have a good work ethic, and not to simply rely on things being good enough, but to push as hard as I can. Mom, every time I have to make a graph, figure, poster, or power point, I think back to you helping me make posters back in middle school. Everything needed to be mounted just right and perfectly aligned back then, just like it does now. I really love that aspect and striving for perfection. Even if it means I spend way more time than I should to make something up to my standards, when no one else would notice the changes from the last few hours of nitpicking.

CHAPTER 1

INTRODUCTION

1.1 Background

Countless chemical reactions take place every day aided by catalysts. Without biological catalysts, commonly known as enzymes, a basic reaction needed for creating RNA and DNA, the decarboxylation of orotic acid, would take longer than the entire existence of mankind. The reaction proceeds so slowly that the half-life is estimated to be 78 million years, roughly 10^6 times longer than a typical human life. However, in the presence of a specific catalyst known as Orotidine 5'-phosphate decarboxylase, the half-life of this reaction is reduced by a factor of 10^{17}.[1] The catalysts in our body are, thankfully, already crafted and help provide the foundation for life, but catalysts also play a large role in many other fields including energy production, chemical synthesis, materials production, pollution reduction, and many more fields. Catalysts are estimated to account, either directly or indirectly, for 35% of the world's GDP.[2] With that much influence over the economic tides of the world, it is no surprise that there is a heavy focus on researching how to improve or create more efficient and cost effective catalysts.[3-11]

There are two main approaches to studying catalysts: application driven and fundamental driven. Application driven research refers to experiments conducted in efforts to make catalysts to enhance a reaction that can be scaled and used in an industrial setting. Fundamental driven research focuses on understanding the details of why and how the catalyst functions, to give insight to what can be used as a catalyst, and how to improve existing or create new catalysts. Typical application based catalysts are poorly characterized high surface area catalysts generally prepared via wet chemistry methods. While these catalysts are typically low cost, or else they would not be economically feasible, they are far from ideal for understanding how a reaction proceeds or where/how

reactant molecules interact with the catalyst. This is because commercial catalysts suffer from a range of sizes, compositions, binding arrangements to substrates (if it is a supported catalyst), contaminants, etc. In contrast, fundamental research generally focuses on well-defined catalysts that are too expensive to scale to industrial size production. Despite high costs, model catalysts allow studies to be undertaken with little to no contamination, small size distributions, specific binding arrangements on a support surface, and even control of the gases to which the catalyst is exposed, if experiments are conducted in ultra high vacuum (UHV). Due to the relative simplicity of these samples, in terms of variables within a given sample, these catalysts are often referred to as model-catalysts. By controlling all the variables around a model-catalyst, it is possible to change single variables in order to determine their effect on the overall catalytic activity and specificity.[12-15] In an ideal scenario, fundamental research would lead to a determination of which elements need to be combined, in specific ratios, on a tailored support to generate a stable, efficient catalyst based on the knowledge of how various reactants interact with the catalyst.

Model-catalyst systems can be studied by a wide array of techniques including some that concentrate on the surfaces of the catalyst system. Since reactions are typically thought to occur on the surface of a catalyst[4, 15, 16], it makes sense that the properties of the surface be extremely well characterized. Recent advances in techniques such as scanning tunneling microscopy (STM) and transmission electron microscopy (TEM) have allowed for imaging of catalysts with resolution better than 0.1 nm.[17] These imaging techniques allow for direct determination of catalyst geometry and binding orientations relative to a support. It has been previously shown that the geometry of a

catalyst can be modified via interactions with different support surfaces and that the catalyst geometry can have a large impact on the reactivity.[18, 19] Other key surface sensitive techniques such as photoelectron spectroscopy allow for the determination of the electronic structures of the catalyst. Both the geometric and electronic structures should play a large role in the interaction of reactants, and ultimately the reactivity and specificity of a catalyst.

One major concern regarding model-catalyst studies conducted in UHV, is what is known as the pressure gap. That is to say that reactivity and overall characterization methods in an ideal model-catalyst may not reflect/experience the same chemical mechanisms as a real world catalyst, due to elevated pressures and temperatures.[20-22] Fortunately, research done by Goodman et al. has shown that despite decreased pressures, both noble metal and supported model-catalysts exhibit CO oxidation that proceeds via the Langmuir-Hinshelwood mechanism.[21, 23, 24]

1.2 The importance of cluster size research

Early attempts to increase catalyst efficiency, focused on decreasing the catalyst particle size to increase the amount of surface area. However, studies have shown that catalyst particles smaller than a threshold size (< 1 nm) can exhibit properties that do not scale with the bulk properties.[25-28] A dramatic example of the effect of exceptionally small catalyst particles can be seen with Au as a catalyst for the CO oxidation reaction. Bulk Au is known to be fairly inert for CO oxidation, but Au clusters on the nanometer or smaller size range have proved to be active.[26, 29, 30] In fact, it was shown that gold clusters, even in the 3 nm size range are inactive for CO oxidation, but sub-nanometer

gold is the active catalyst.[31]. Other work has also shown that the addition or subtraction of one or two atoms can have a monumental effect on the reactivity of a catalyst. This was demonstrated where Au_7 was found to be a factor of 10 more catalytically active than Au_5.[26]

With the new knowledge that the catalyst particle size can play a significant role in catalytic activity, while maintaining a constant surface area, the obvious question becomes: how does the size affect the reactivity? A flurry of research has probed this question to identify that at these small catalyst sizes, the change of one or two atoms can drastically change both the electronic structure and geometric structure of the cluster.[5, 32-41] In addition to cluster size effects, a recent thrust of research has emerged concerning the identity and composition of the support film, and its role in the catalytic process. Unsurprisingly, the support can have several effects, including changing the supported cluster geometry and electronic structure, as well as providing a potential reservoir for the reactants to diffuse to the active catalytic site via surface mediated adsorption.[15, 42-47]

The work within this dissertation will highlight some of the effects of the film thickness of a thin, epitaxially grown alumina film and Pd_n ($n \leq 30$) cluster size on the reactivity for the CO oxidation reaction. It will be shown that by controlling these two variables, the reactivity can be tuned while altering the electron density for the supported Pd clusters.

1.3 References

1. A. Radzicka and R. Wolfenden, *Science*, 1995, **267**, 90-93.

2. Z. Ma and F. Zaera, *Heterogeneous Catalysis by Metals*, 2006.

3. H. L. Abbott, A. Aumer, Y. Lei, C. Asokan, R. J. Meyer, M. Sterrer, S. Shaikhutdinov and H.-J. Freund, *J. Phys. Chem. C.*, 2010, Article ASAP.

4. F. Gao and D. W. Goodman, *Annual Review of Physical Chemistry*, 2012, **63**, 265-286.

5. B. Yoon, U. Landman, V. Habibpour, C. Harding, S. Kunz, U. Heiz, M. Moseler and M. Walter, *J. Phys. Chem. C*, 2012, **116**, 9594-9607.

6. R. Campbell, J. Rodriguez and D. Goodman, *Physical Review B*, 1992, **46**, 7077-7087.

7. C. T. Campbell, *Surf. Sci. Rep.*, 1997, **27**, 1-112.

8. M. D. Kane, F. S. Roberts and S. L. Anderson, *Faraday Discussions*, 2013, **162**, 323.

9. W.-P. Zhou, S. Axnanda, M. G. White, R. R. Adzic and J. Hrbek, *J. Phys. Chem. C*, 2011, **115**, 16467-16473.

10. L. M. Molina, S. Lee, K. Sell, G. Barcaro, A. Fortunelli, B. Lee, S. Seifert, R. E. Winans, J. W. Elam, M. J. Pellin, I. Barke, V. von Oeynhausen, Y. Lei, R. J. Meyer, J. A. Alonso, A. Fraile Rodriguez, A. Kleibert, S. Giorgio, C. R. Henry, K.-H. Meiwes-Broer and S. Vajda, *Catalysis Today*, 2011, **160**, 116-130.

11. G. Pacchioni, *Physical Chemistry Chemical Physics: PCCP*, 2013, **15**, 1737-1757.

12. G. K. Wertheim, S. B. DiCenzo and D. N. E. Buchanan, *Phys. Rev. B*, 1986, **33**, 5384-5390.

13. U. Heiz, F. Vanolli, A. Sanchez and W.-D. Schneider, *J. Am. Chem. Soc.*, 1998, **120**, 9668-9671.

14. S. Shaikhutdinov, M. Heemeier, M. Bäumer, T. Lear, D. Lennon, R. J. Oldman, S. D. Jackson and H.-J. Freund, *Journal of Catalysis*, 2001, **200**, 330-339.

15. M. E. Vaida, T. M. Bernhardt, C. Barth, F. Esch, U. Heiz and U. Landman, *Physica Status Solidi B: Basic Solid State Physics*, 2010, **247**, 1001-1015.

16. K. An and G. A. Somorjai, *ChemCatChem*, 2012, **4**, 1512-1524.

17. P. E. Batson, N. Dellby and O. L. Krivanek, *Nature (London, United Kingdom)*, 2002, **418**, 617-620.

18. N. Lopez, J. K. Nørskov, T. V. W. Janssens, A. Carlsson, A. Puig-Molina, B. S. Clausen and J.-D. Grunwaldt, *Journal of Catalysis*, 2004, **225**, 86-94.

19. L. Giordano and G. Pacchioni, *Accounts of Chemical Research*, 2011, **44**, 1244-1252.

20. R. V. Rijn, M. D. Ackermann, O. Balmes, T. Dufrane, A. Geluk, H. Gonzalez, H. Isern, E. D. Kuyper, L. Petit, V. A. Sole, D. Wermeille, R. Felici and J. W. M. Frenken, *Review of Scientific Instruments*, 2010 **81**, 8.

21. S. M. Mclure and D. W. Goodman, *Chemical Physics Letters*, 2009, **469**, 13.

22. P. Rzeszotarski and Z. Kaszkur, *Physical Chemistry Chemical Physics*, 2009, **11**, 6.

23. M. S. Chen, Y. Cai, Z. Yan, K. K. Gath, S. Axnanda and D. W. Goodman, *Surface Science*, 2007, **601**, 5326-5331.

24. S. M. McClure, M. Lundwall, F. Yang and Z. G. Zhou, D. W., *Journal of Physical Chemistry C*, 2009, **113**, 9688-9698.

25. U. Heiz, A. Sanchez, S. Abbet and W. D. Schneider, *Journal of the American Chemical Society*, 1999, **121**, 3214-3217.

26. S. Lee, C. Fan, T. Wu and S. L. Anderson, *J. Am. Chem. Soc.*, 2004, **126**, 5682-5683.

27. M. Haruta, *Catalysis Today*, 1997, **36**, 153-166.

28. Q. Fu, H. Saltsburg and M. Flytzani-Stephanopoulos, *Science*, 2003, **301**, 935-938.

29. U. Heiz, S. Abbet, H. Hakkinen and U. Landman, *Materials Research Society Symposium Proceedings*, 2001, **648**, P9 1/1-P9 1/10.

30. K. Fukushima, G. H. Takaoka, J. Matsuo and I. Yamada, *Japanese Journal of Applied Physics, Part 1: Regular Papers, Brief Communications & Review Papers*, 1997, **36**, 813-818.

31. A. A. Herzing, C. J. Kiely, A. F. Carley, P. Landon and G. J. Hutchings, *Science*, 2008, **321**, 1331-1335.

32. Y. Watanabe, X. Wu, H. Hirata and N. Isomura, *Catalysis Science & Technology*, 2011, **1**, 1490-1495.

33. S. Proch, M. Wirth, H. S. White and S. L. Anderson, *J. Am. Chem. Soc.*, 2013, **135**, 3073−3086.

34. S. Peters, S. Peredkov, M. Neeb, W. Eberhardt and M. Al-Hada, *Surf. Sci.*, 2013, **608**, 129-134.

35. W. E. Kaden, W. A. Kunkel, F. S. Roberts, M. Kane and S. L. Anderson, *J. Chem. Phys.*, 2012, **136**, 204705.

36. V. Habibpour, Z. W. Wang, R. E. Palmer and U. Heiz, *Journal of Applied Sciences*, 2011, **11**, 1164-1170.

37. H. Haekkinen, B. Yoon, U. Landman, X. Li, H.-J. Zhai and L.-S. Wang, *J. Phys. Chem.*, 2003, **107**, 6168-6175.

38. W. E. Kaden, W. A. Kunkel, M. D. Kane, F. S. Roberts and S. L. Anderson, *J. Am. Chem. Soc.*, 2010, **132**, 13097–13099.

39. W. E. Kaden, T. Wu, W. A. Kunkel and S. L. Anderson, *Science*, 2009, **326**, 826-829.

40. M. S. Chen and D. W. Goodman, *Science*, 2004, **306**, 252-255.

41. M. Chen, Y. Cai, Z. Yan and D. W. Goodman, *J. Am. Chem. Soc.*, 2006, **128**, 6341-6346.

42. L. Kieken and M. Boudart, *Studies in Surface Science and Catalysis*, 1993, **75**, 1313-1324.

43. M. Bowker, P. Stone, R. Bennett and N. Perkins, *Surf. Sci.*, 2002, **497**, 155-165.

44. U. Heiz and E. L. Bullock, *Journal of Materials Chemistry*, 2004, **14**, 564-577.

45. M. A. Roettgen, S. Abbet, K. Judai, J.-M. Antonietti, A. S. Woerz, M. Arenz, C. R. Henry and U. Heiz, *J. Am. Chem. Soc.*, 2007, **129**, 9635-9639.

46. H. J. Freund and G. Pacchioni, *Chemical Society reviews*, 2008, **37**, 2224-2242.

47. I. Irfan, in *Physics and Astronomy*, University of Rochester, Rochester, New York, 2012, p. 232.

CHAPTER 2

EXPERIMENTAL SETUP

2.1 The instrument

The instrument used in this dissertation is described in detail in the experimental section of Chapter 5.[1] Briefly, the instrument, as pictured in Figure 2.1, is comprised to two main sections: the cluster deposition beamline and the UHV surface analysis chamber. The cluster deposition beamline works by using a 30 Hz, 532 nm Nd:YAG laser, with a laser pulse of about 25-30 mJ, to ablate a metal target, in this case Pd. This forms a mixture of Pd cations, neutrals and anions. Just before the laser pulse strikes the Pd target, a burst of He is leaked into the cluster source chamber in a small clustering volume in front of the Pd target. The He allows for the cooling of the Pd particles as well as enhancement of clustering of the gas phase Pd_n particles. The beam of mixed charge state Pd_n clusters is guided, by a quadrupole ion guide, to a bending lens. At this point the anions and neutrals are selected out of the ion beam and only Pd_n^+ cations are left.

The Pd_n^+ cations are then guided down the beamline with a second ion guide through several stages of differential pumping. The Pd_n^+ cations are then injected into a quadrupole mass selector (QMS) to select which mass Pd cluster will be deposited on the sample. By selecting a specific mass, the QMS is able to select, with atomic resolution, Pd_n^+ clusters where $n \leq 35$. The size selected clusters are then injected into a final ion guide and pass through the exposure mask before being deposited on the sample. The mask has an exit orifice of 2 mm in diameter. Through a retarding potential analysis, the Pd_n^+ cations are deposited with a kinetic energy of 1 eV/atom or less.

As the Pd_n^+ cations hit the surface of the sample, the neutralization current is measured to keep track of the number of clusters hitting the surface. All samples reported in this dissertation, unless otherwise noted, contain the same amount of total Pd

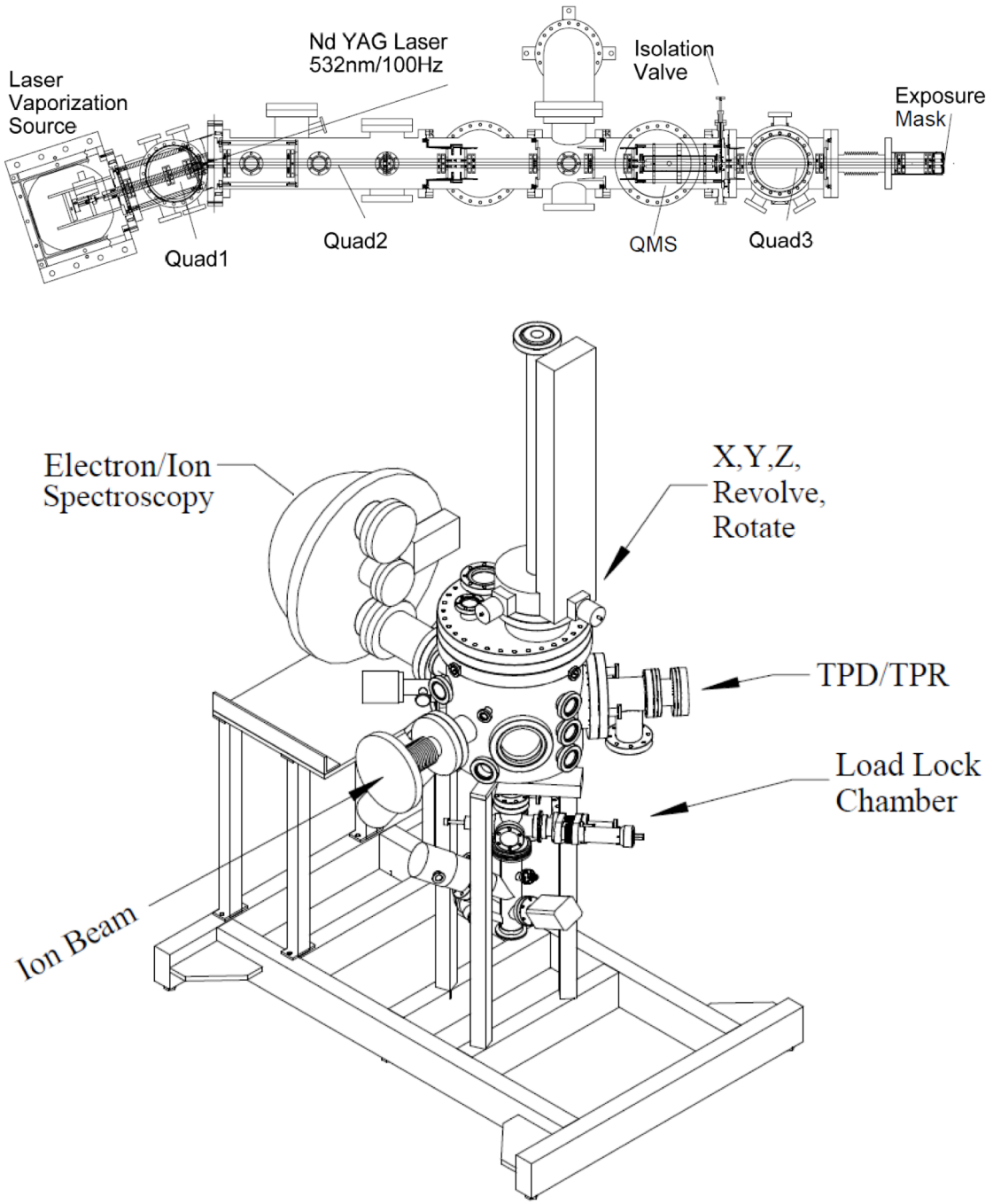

Figure 2.1: The experimental setup with the cluster deposition beamline along the top, and the UHV surface analysis chamber on the bottom. The beamline mates up to the analysis chamber by inserting the exposure mask into the port labeled ion beam.

atoms with a density equal to 0.1 ML of a close packed Pd monolayer, corresponding to $1.53x10^{14}$ Pd atoms/cm^2. This method of Pd deposition resulted in deposition times typically in the range of 3 – 15 minutes, with longer deposition times for Pd_{2-4}.

After Pd was deposited on the sample in the UHV analysis chamber, various *in situ* techniques could be utilized to characterize the catalytic system. The reactivity could be probed via a differentially pumped mass spectrometer with six directional gas dosing tubes. After determining the reactivity of samples with either various Pd_n cluster sizes or changes in the support, it is important to understand what causes said changes in reactivity. This was accomplished via a combination of X-ray photoelectron spectroscopy (XPS), ultraviolet photoelectron spectroscopy (UPS), and ion scattering spectroscopy (ISS) to determine both the electronic and geometric structures of the catalytic system.

A final piece of the instrument is a small antechamber located below the UHV analysis chamber. The sample can be lowered into this chamber through a triple differentially pumped seal to prepare an alumina film onto which the Pd_n^+ cations will be deposited.

2.2 Metal evaporation source

The work in this dissertation all pertains to metal catalysts supported on metal oxide surfaces. Previous experiments for CO oxidation catalyzed via Pd supported on Al_2O_3 grown on a NiAl single crystal resulted in an inactive catalytic system.[2] The reason for this inactivity was due to oxygen spillover onto the alumina support that would subsequently react with Al metal in the NiAl substrate and thicken the alumina film.[3] In

order to get around this problem, a refractory substrate with a good lattice match that forms a stable protective oxide layer was used to grow an epitaxial Al_2O_3 film. Previous recipes from literature were used to create, what was characterized with LEED, to be a highly ordered, stoichiometric alumina film.[4-6]

The process for growing the alumina films consisted of evaporating Al onto the substrate at elevated temperatures (around 960 K) in a background of oxygen. In order to evaporate the Al metal, a metal evaporation source was needed. A diagram of the home built source can be seen in Figure 2.2. The source consists of a small ceramic tube with a ceramic rod friction fit into the back end to form a crucible. The inside is then filled with 5N purity Al wire. The ceramic is wrapped with a Ta heating wire for resistive heating before being inserted into a second ceramic tube. The purpose of the second ceramic is to aid in heat retention and prevent small fluctuations in the heating power supply from causing drastic changes in the Al flux impinging on the sample. A K type thermocouple is cemented on the back of the ceramic crucible setup. This allows for monitoring of the crucible temperature for accurate control of the aluminum evaporation rate. The ceramic setup is then supported between two tantalum posts connected to a 1.33 in. conflat thermocouple/power feedthrough. The feedthrough is attached to a water cooled 1.33 in. to 2.75 in. conflat adaptor.

Mounted on the vacuum side of the adaptor flange is a copper shroud, as shown on the right of Figure 2.2. The copper shroud is screwed down to make good structural and thermal contact with the water cooled flange. The shroud is tapped to allow up to six ceramic screws to center and align the ceramic evaporator to directionally evaporate the aluminum through the exit aperture. Additionally, three degassing vents are located on

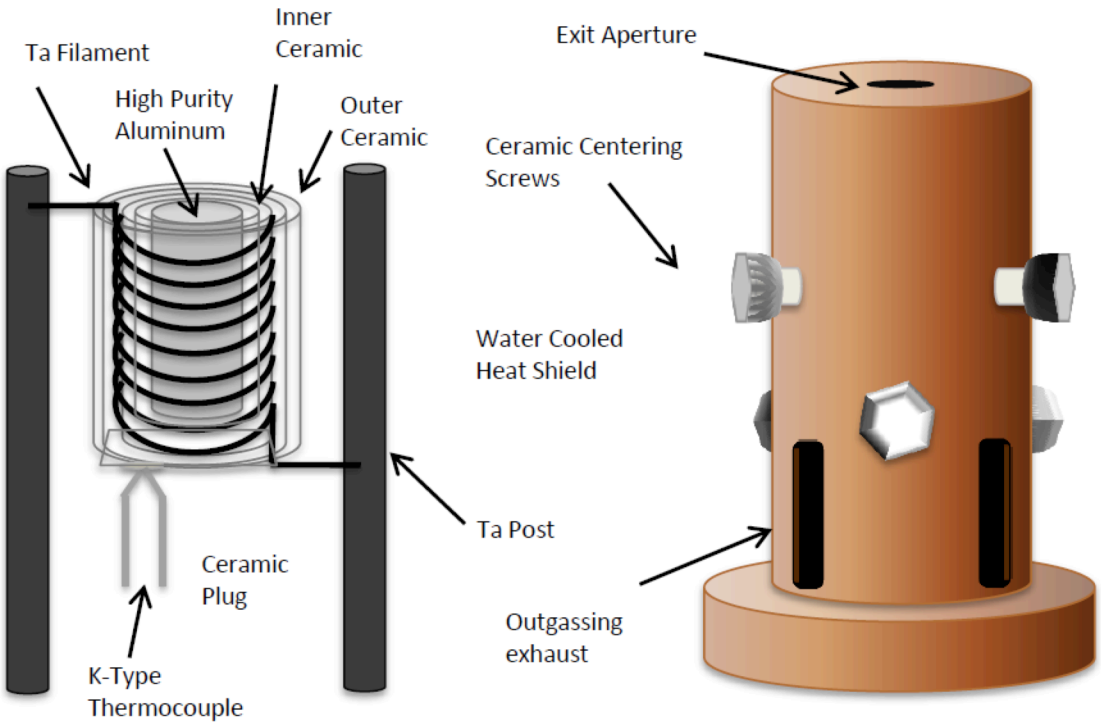

Figure 2.2: Diagram showing the aluminum evaporation source used to grow the alumina films used throughout this dissertation. The aluminum is housed in a thin walled ceramic tube with a ceramic plug in the back end to prevent Al evaporation toward the feedthroughs. The ceramic is then wrapped with a Ta heating filament for resistive heating, and housed in a secondary ceramic tube. This is then placed in the copper shroud which centers and aims the evaporating Al at the substrate.

the sides of the shroud in an effort to minimize the directional dosing of any adsorbates that desorb from the hot evaporator being directed out of the exit aperture toward the sample. The amount of adsorbate contamination is further reduced by the water cooling on the flange in contact with the copper shroud. During a typical film growth without water cooling, the flange is too hot to touch and results in excessive outgassing. However, with water cooling, the flange is around 285 K, which results in a significant pressure drop.

2.3 Monitoring high and low temperatures in UHV

Due to the low temperatures required when conducting catalytic experiments and high temperatures required to clean and anneal refractory substrates, a thermocouple with a temperature range between 73 and 2200 K is needed. Unfortunately, there are no commercially available thermocouples with specifications across that entire range. The deciding factor in selecting a thermocouple is the high temperature limit. Standard K or S type thermocouples, which are accurate at low temperatures ($\leq$ 273 K) melt at the temperatures required for cleaning and annealing both Ta(110) and Re(0001) single crystals. In order to get around this fact, a C type thermocouple was used and implemented utilizing a custom feedthrough, since no commercial options exist.

2.3.1 Problems monitoring a large temperature range in UHV

C type thermocouples are comprised of a pair of 5% and 26% Re/W wires and are highly desirable for applications where high temperature measurements between 273 K and 2593 K are needed. However, due to the tungsten base metal, the thermocouple is

stiff and brittle; this is especially true after exposure to oxygen at high temperatures. The brittleness of the thermocouple can often lead to thermocouple failure when any physical contact is made after high temperature exposures. Another downside to the C type thermocouple is the relative high price of metals as compared to some other thermocouple types such as K type, which consists of alumel and chromel leads. For cost purposes, after the initial thermocouple junction is placed in the desired location, in this case that would be spot welded to a sample in UHV, the remainder of the thermocouple wire is often converted to extension grade thermocouple materials consisting of 405 and 426 alloys.

The extension grade wire has a lower melting point and is considerably cheaper, more flexible, and easier to manipulate to desired shapes without becoming damaged. From a construction standpoint, it is also much easier to braze the 405 and 426 alloys to a ceramic feedthrough that can then be welded to a stainless steel conflat flange for mounting on a vacuum chamber. However, when a C type thermocouple is used below its recommended temperature range, the presence of the 405 and 426 alloys can cause significant instability and incorrect temperature measurements. At low temperatures (below 325 K) the voltage generated at the junction for the W5%Re/W26%Re becomes very small, on the order of fractions of a mV, and eventually become negative at temperatures below 273 K. In fact, in the temperature range from 73 K to 325 K the output voltage is only about 2mV. With the added junctions of W5%Re/405 and W26%Re/426, a few tenths of a millivolt of noise can be imparted on to thermocouple, resulting in large variations in the measured temperature. The voltage change on the thermocouple is largely dependent upon the temperature of the metal/alloy junction.

Therefore, daily changes in the temperature of the room can lead to large changes in the measured temperature.

In order to prevent inconsistencies in the C type thermocouple measurement, ideally the entire length of the thermocouple used should be made out of the W5%Re and W26%Re leads. In practice, this may still be too expensive to connect a thermocouple to a temperature monitor that can be a long distance away. In this case, the extension grade wire should not be used until the extension grade/thermocouple wire lead junction can be made outside of vacuum and in a well-controlled temperature environment. This results in the need for a C type thermocouple feedthrough for use in vacuum chambers. However, such a product is not available in the current market place due to relatively low demand for a thermocouple with a wide measurement range of, at least, 100 K up to 2593 K, as well as difficulty in successfully brazing W/Re alloys to ceramics to make the feedthrough.

Recent manufacturing experiments have shown to be successful in creating a robust, UHV compliant ceramic C type thermocouple feedthrough through the use of preliminary nickel plating of the W/Re metal thermocouple lead. However, due to the strong native surface oxide on the thermocouple leads, a special electrochemical cleaning step is required. If the electrochemical step is not utilized, then the nickel plating can easily be scraped, chipped, or chipped off in a solid sheath-like tube. The following sections describe in detail how to clean and nickel plate a C type thermocouple lead so that it can be silver soldered into a nickel tube already brazed into a ceramic feedthrough (CeramTec North America Corp, part number 9791-06-W). Completion of this C type thermocouple feedthrough setup allowed an accurate temperature reading to be obtained.

This was calibrated with a K type thermocouple in the temperature range of 100 – 1200 K, giving a deviation in the temperature reading within 3 K for all temperatures monitored.

2.3.2 Prepare solutions

2.3.2.1 Cleaning solution

Mix 20% (by weight) NaOH in enough distilled water to clean all parts of thermocouple wire that will be nickel plated.

2.3.2.2 Nickel electroplating solution (Watts-type bath)

Combine the following ingredients to prepare the nickel electroplating solution:

- 85 grams nickel(II) sulfate hexahydrate [$NiSO_4(H_2O)_6$]
- 6.4 grams boric acid [$B(OH)_3$]
- 9.4 grams nickel(II) chloride hexahydrate [$NiCl_2(H_2O)_6$]
- 200 mL distilled water

2.3.3 Prepare thermocouple

Inspect the thermocouple under a microscope to ensure that there is no cracking or splitting. If there is, move to a different section of the thermocouple and be sure to use a Dremel cut off wheel and not wire cutters to prevent further splitting of the thermocouple wire. Brush on a complete coat of Stop-Off Lacquer (Item # 210-1250 from Paul H. Gesswein Co., Inc) wherever nickel plating is not desired. Let dry in air 1 hour or until the Stop-Off Lacquer is no longer tacky to the touch. Note, the Stop-Off

Lacquer is stable in the NaOH cleaning solution and will prevent etching of the metal. If there are small gaps or the lacquer film is not continuous, etching and plating will occur on all exposed metal surfaces. It is a good idea to use a scrap piece of thermocouple to practice with, to ensure you have the process mastered before working on the final piece. To test if the plating was successful on the scrap thermocouple, ordinary solder and flux can be used to tin the thermocouple. The solder will only stick to where the thermocouple has been nickel plated.

2.3.4 Clean the thermocouple

Place the thermocouple wire in the NaOH solution and attach an alligator clip to the end not submerged. Place a counter carbon electrode in the solution and again attach an alligator clip to the top of the carbon electrode. Ensure that the thermocouple and carbon electrodes are not touching, or the circuit will be shorted and not result in cleaning. Apply a voltage of 5-10 volts AC. To make an AC power supply, simply connect a power cord with an inline switch to a 6/12 VAC transformer. When the voltage is applied significant bubbling will occur at the thermocouple. Only clean for a short period of time to reduce excessive thermocouple material loss, as the metal being cleaned is etched away. Cleaning times of approximately 1 minute work well and can cause a C-type thermocouple rod diameter to reduce from 0.039 in. to 0.036 in. Once the AC power is turned off, all bubbling should stop. At this point remove the thermocouple and place into the plating solution. It is of the utmost importance that the transfer from the cleaning solution to the plating solution be as fast as possible to prevent oxidation of the thermocouple surface. Simply pull the thermocouple out and place directly into the

plating solution. DO NOT rinse with water or dry off excess cleaning solution, place directly into the plating solution while it is still dripping wet. The carbon electrode is then also moved into the plating solution; this step can be done more slowly and the excess NaOH can be rinsed off of the carbon electrode with distilled water with no negative effects. Note, do not be alarmed if a film or precipitate forms when putting the electrodes in the plating solution, this is normal and can be prevented/minimized by rinsing the carbon counter electrode in distilled water.

2.3.5 Electroplate the thermocouple

With the thermocouple and carbon electrode now in the plating solution, attach an adjustable DC power supply to the electrodes. Be sure to connect the negative lead of the power supply to the thermocouple (to attract the positive Ni cations) and the positive lead to the carbon electrode. Depending on the scale of the current gauge on the power supply, it may be useful to connect an ammeter in the circuit to monitor the current. Again, ensure that the thermocouple and carbon electrode are not touching. With the power supply turned all the way down, turn on the power supply and increase the voltage until a current of 90-100 mA is achieved (should be around 5-7 volts). There will again be significant bubbling at the thermocouple surface where the nickel is being plated. Electroplating continues for several minutes (10 minutes has been shown to work well). After the plating has finished, turn off the power supply and remove the electrode. There may be some green crystals on the surface of the thermocouple, but these are easily removed with distilled water and a Kimwipe. To remove the Stop-Off Lacquer, clean with acetone and a Kimwipe. It is very difficult/not possible to see the difference in color

of the plated nickel on a freshly cleaned thermocouple, but if there was bubbling in the plating solution, then the Ni did in fact plate on the surface. The thermocouple is now ready to be silver soldered into a feedthrough.

2.4 References

1. M. D. Kane, F. S. Roberts and S. L. Anderson. *International Journal of Mass Spectrometry*, 2014, **370**, 1-15.

2. T. Wu, W. E. Kaden, W. A. Kunkel and S. L. Anderson, *Surface Science*, 2009, **603**, 2764-2770.

3. S. Shaikhutdinov, M. Heemeier, J. Hoffmann, I. Meusel, B. Richter, M. Bäumer, H. Kuhlenbeck, J. Libuda, H.-J. Freund, R. Oldman, S. D. Jackson, C. Konvicka, M. Schmid and P. Varga, *Surf. Sci.*, 2002, **501**, 270-281.

4. P. J. Chen and D. W. Goodman, *Surf. Sci.*, 1994, **312**, L767-L773.

5. Y. Wu, E. Garfunkel and T. E. Madey, *J. Vac. Sci. Technol., A*, 1996, **14**, 2554-2563.

6. Y. Wu, E. Garfunkel and T. E. Madey, *Surface Science*, 1996, **365**, 337-352.

CHAPTER 3

ALUMINA SUPPORT AND Pd_n CLUSTER SIZE EFFECTS ON ACTIVITY OF Pd_n FOR CATALYTIC OXIDATION OF CO

M. D. Kane, F. S. Roberts and S. L. Anderson. Alumina support and Pdn cluster size effects on activity of Pdn for catalytic oxidation of CO. Faraday Discussions, 2013,162, 323-340. The original article can be found online at: http://pubs.rsc.org

3.1 Introduction

Metal-catalysed CO oxidation has been extensively studied, both because it has practical importance, and because it is relatively simple and amenable for study using surface science techniques.[1-12] The rich literature on CO oxidation over oxide-supported Pd catalysts is particularly attractive from the perspective of size-selected cluster measurements, providing mechanistic insight to aid interpretation. Another motivation is that we recently observed non-monotonic cluster size dependence for CO oxidation over $Pd_n/TiO_2(110)$, and found that activity was clearly correlated with variations in Pd_n electronic properties.[9] Here, we report a study under similar conditions, of CO oxidation catalysed by Pd_n deposited on variable thickness alumina films grown on Ta(110).

The literature for CO and O_2 interactions with Pd is enormous, but it is worth mentioning a few relevant results. This reaction has been studied extensively for both Pd single crystals[1, 6, 13-16] and Pd nanoparticles supported on metal oxides.[2, 17-27] It was shown by Ertl and others that CO oxidation on noble metals occurs by a Langmuir-Hinshelwood mechanism, where both reactants must adsorb on the surface before combining to form CO_2, and that kinetics are controlled by competition between CO and oxygen for binding sites.[1, 6, 13, 14] The Freund and Matolin groups studied CO on alumina-supported Pd. They noted an increase in low temperature CO desorption with decreasing Pd particle size, attributed to CO weakly bound atop small Pd particles, as opposed to being bound in high coordination binding sites on larger particles.[3, 24, 28, 29] The Campbell group studied Pd particles grown on both alumina films and single crystal α-Al_2O_3 (0001),[30, 31] examining both Pd sintering behaviour and the nature of O_2 binding. Bowker and co-workers reported studies of TiO_2-supported Pd, probing CO reverse spillover,

oxygen spillover, and strong metal support interaction effects.[32-34] Goodman and co-workers also did important work in this and related systems, exploring pressures bridging the gap between UHV and practical working catalyst conditions.[35-40] They showed that even at elevated pressures, mechanistic insight from UHV studies can be applied.[6, 41, 42] There are also a number of studies of cluster size effects on CO oxidation catalysed by Pd_n, in addition to the Pd_n/TiO_2 study mentioned above. Heiz, Landman, together with many co-workers and collaborators, have studied cluster size effects of Pd_n supported on MgO/Mo(100).[4, 19, 20, 43-48] This work suggests there is an increased activation barrier for O_2 dissociation with decreasing Pd_n cluster size ($n \leq 30$), resulting in higher temperatures required for efficient O_2 activation. It was shown that small amounts of co-adsorbed CO can actually enhance O_2 dissociation. Related work on Au_n/MgO/Mo(100) showed that MgO film thickness could be used to tune the activity of the Au_n clusters for CO oxidation.[49, 50]

We previously attempted a study of CO oxidation over Pd_n/alumina,[8] using the process reported by Shaikhutdinov et al.[3] to grow a 0.5 nm thick alumina film on NiAl(110). At 100 K, O_2 was observed to oxidize all Pd_n studied, with the exception of Pd_4 – an exception that was subsequently explained by theory from the Khanna group[51]. Attempts to study CO oxidation failed, however, because oxygen initially bound to the Pd clusters, readily spills over to the thin alumina support, and reacts with the underlying NiAl, as discussed by Shaikhutdinov et al.[3] In fact, Shaikhutdinov et al. used this effect to thicken the alumina layer beneath their Pd particles, generating an active catalyst. One of the motivations of the present work is to examine both cluster size and alumina film thickness effects in the Pd/alumina system.

3.2 Experimental methodology

3.2.1 Apparatus

The experiments in this paper were conducted in a UHV system with a base pressure ≤ 2 x 10^{-10} Torr as described previously.[52, 53] The vacuum system is made up of three main sections: the cluster deposition beamline, the main deposition/analysis chamber, and the load lock/high-pressure chamber. The differentially-pumped cluster deposition beamline drops the operating pressure from 20 mTorr in the cluster source chamber down to 2 x 10^{-10} Torr in the final chamber leading into the analysis/deposition chamber. A laser vaporization source is used to create Pd_n^+ clusters ($n \leq 25$) that are guided by a series of quadrupole ion guides, mass selected by a quadrupole mass filter, and then guided into the deposition/analysis chamber, where they are deposited on the sample surface at approximately 1 eV/atom. Deposition occurs through a mask with 2 mm orifice, located ~0.1 mm in front of the sample surface. The main deposition/analysis chamber contains facilities for *in situ* characterization using X-ray photoelectron spectroscopy (XPS), ultraviolet photoelectron spectroscopy (UPS), and ion scattering spectroscopy (ISS). In the experiments described here, the XPS was recorded using an Al Kα source, and binding energies were corrected to the Ta $4d_{5/2}$ binding energy of the Ta(110) single crystal used as the substrate for alumina film growth. The main chamber also contains a residual gas analyzer (RGA) to monitor background partial pressures and gas doses, and a differentially pumped section that houses a second mass spectrometer that views the sample through a 2.5 mm diameter skimmer orifice. This mass spectrometer is used to monitor species desorbing from the deposited cluster spot, with minimal sensitivity to species desorbing from outer regions of the sample or from

other surfaces in the vacuum system. When the sample is positioned in front of the skimmer orifice, it can be dosed with gases using a set of seven dosing tubes that are directed toward the sample position, while monitoring gasses in the chamber background and desorbing from the surface, using the two mass spectrometers. The load lock/high-pressure chamber is a small antechamber attached to the bottom of the main chamber, with base pressure $\leq 5 \times 10^{-9}$ Torr. The sample is inserted into the antechamber through a gate valve and triple differential seal, and the antechamber can be pressurized without affecting the main chamber pressure. For the present experiments the antechamber was used for growth of alumina support films under high O_2 pressures.

3.2.2 Model catalyst preparation

Typical samples consist of Pd_n clusters deposited on an alumina film grown on a 5 x 10 x 1 mm Ta(110) single crystal (Surface Preparation Laboratory). The Ta crystal was spot welded to two tantalum heating wires suspended from a pair of tungsten rods attached to a liquid nitrogen-cooled probe, all supported by a manipulator system. The sample temperature was monitored by a K-type thermocouple, spot welded to the back of the Ta(110) single crystal. The sample temperature was controlled between 115 K and 1200 K using resistive heating, or up to 1500 K (limited by the thermocouple) by electron bombardment of the back side of the Ta crystal. Alumina films in the thickness range used here, are conductive enough to allow the Pd_n^+ to neutralize upon deposition. By integrating the sample current during deposition, the number of Pd_n^+ deposited can be determined, allowing production of cluster spots with reproducible Pd coverage. All the samples discussed here had Pd_n deposition densities corresponding to 1.53×10^{14} Pd

atoms/cm^2, i.e., ~0.1 of a close-packed Pd monolayer. Deposition was done at room temperature, with a Pd_n^+ beam energy of 1 eV/atom.

The Ta(110) crystal was cleaned by Ar^+ sputtering while the temperature was held at 900 K, followed by annealing at 1400 K for 1 hour. XPS of the annealed sample was used to verify that no Al or Pd remained from previous experiments. The sample was periodically annealed for longer time periods (up to 48 hours) to help anneal out any build-up of bulk defects over experimental cycles. The alumina film was then grown by evaporation of Al onto the Ta(110) single crystal in the antechamber, while holding the surface at 600 K in a background of 5 x 10^{-6} Torr of ultra-high purity $^{16}O_2$, that was further purified by passing the gas through a frozen ethanol bath (160 K). After growth, the samples were annealed at 700 K for 5 minutes in a background of 5 x 10^{-6} Torr of $^{16}O_2$, to insure that the surface was fully oxidized. This alumina growth procedure was adapted from one described by Goodman and co-workers[54], with the changes being a lower sample temperature during the Al deposition and addition of the postgrowth oxygen annealing. We adopted the lower growth temperature because ISS showed that films grown at higher sample temperatures had small (~1 %) concentrations of Ta atoms in the surface layer, even for films with >6 nm thickness. ISS showed a sharpening of the aluminum and oxygen peaks after the postgrowth annealing, indicating a more homogeneous surface environment in the film. Ratios of the Ta and Al XPS signals were used to determine the thickness of the thin alumina film, using literature values for the photoemission cross sections and β parameters[55] and effective attenuation lengths calculated using the program of Powell et al.[56] The estimated absolute uncertainty in film thickness is ±20%, however, the relative uncertainty in comparing thicknesses of

different films is estimated to be less than 5%.

As discussed below, tests were made of the effects of both alumina film thickness and growth rate on the activity of supported Pd clusters for CO oxidation. Activity was found to be independent of film growth rate for rates below ~0.8 nm/min, but faster rates lead to decreased activity of the supported Pd, presumably due to increased roughness/disorder in the alumina film. Unless stated otherwise, the samples discussed below were prepared with growth rates in the 0.3 - 0.5 nm/min range – well below the range where activity begins to depend on growth rate. As shown below, the alumina film, in absence of deposited Pd, is inert under our conditions.

3.2.3 Characterization and reactivity measurements

After the alumina film was grown and Pd_n was deposited, the sample was characterized by XPS at room temperature in order to measure the core level binding energies of both the Pd_n clusters and the support. The sample was then cooled to 135 K for reactivity studies. After initial cooling, and prior to dosing with reactants, the sample was flashed to 560 K to desorb any adventitious background gases that might have adsorbed during the time required for XPS and sample cooling. The sample was then dosed with 10 L $^{18}O_2$ with the sample held at T_{ox}, followed by a 10 L exposure of ^{13}CO at a sample temperature of 180 K. During dosing, the sample was positioned ~1 cm from the O_2 and CO dosing tubes, and 2 mm from the mass spectrometer skimmer cone. We calibrated the doses by comparing CO adsorption resulting from variable doses delivered through the dose tubes with doses from the chamber background, using TPD from Pd(111) and Ni(100) to calibrate both the amount of adsorbed CO and the mass

spectrometer absolute sensitivity (by measuring saturated monolayer desorption).[57] Every day, we measured the mass spectrometer signal for a fixed background pressure of Ar, allowing us to correct for any day-to-day variations in mass spectrometer sensitivity due to factors such as multiplier gain.

For most experiments, $^{18}O_2$ exposure was done at T_{ox} = 400 K to allow comparison with previous results for $Pd_n/TiO_2(110)$ where strong dependence of CO oxidation activity on Pd_n size was found.[9] The CO dose temperature of 180 K was chosen to be high enough to minimize CO binding to the alumina support, but low enough to result in minimal reaction of the impinging ^{13}CO with oxygen pre-adsorbed during the $^{18}O_2$ dose. To test this latter point, the mass spectral signals for all CO_2 isotopologs were monitored during the ^{13}CO dose. A small pulse of $^{13}C^{16}O^{18}O$ was observed just at the start of the ^{13}CO dose, but the integrated signal in this $^{13}C^{16}O^{18}O$ pulse was only ~2 - 3% of the integrated $^{13}C^{16}O^{18}O$ production observed during the temperature programmed reaction (TPR), confirming that 180 K is, indeed, cold enough to largely suppress reaction.

After dosing, the sample was cooled to the 135 K TPR starting temperature, and moved to a position ~1mm in front of the differentially pumped mass spectrometer orifice. The sample temperature was then ramped at 3 K/sec to 560 K, while the mass spectrometer rapidly cycled between all the masses of interest, to measure species desorbing from the surface. This TPR process (including 400 K $^{18}O_2$ and 180 K ^{13}CO dosing) was repeated two more times to examine how the activity of the samples might change with gas adsorption and heating. Finally, the sample was probed by a ^{13}CO TPD experiment where the $^{18}O_2$ dose was omitted, and only ^{13}CO was dosed (180 K). This

final CO TPD provides a measure of the density of CO binding sites remaining on the surface after the three TPR experiments. In addition to the expected $^{13}C^{16}O^{18}O$ product, the signals for all other CO_2 isotopologs were measured, as were both ^{13}CO and ^{12}CO. We conclude, therefore, that under our conditions, ^{16}O in the alumina film does not participate in the chemistry significantly, and that any adventitious ^{12}CO that might have adsorbed on the samples during deposition, XPS characterization, and cooling, was removed by the combination of the 560 K flash and 400 K O_2 exposure.

Postreaction sample characterization was performed using XPS and ISS. Comparison of pre- and postreaction XPS probes changes in the Pd chemical environment. ISS is sensitive only to the top-most layer of atoms, and because our samples all were prepared with the same total number of Pd atoms deposited, variations in the postreaction Pd ISS intensity provide insight into the fraction of Pd in the surface layer. The Pd ISS signal could be affected both by morphology changes (i.e., single layer vs. multilayer clusters) and by adsorbates remaining on the surface of the Pd clusters after the series of TPR experiments.

3.3 Results and discussion

As reported previously, Pd_n supported on a 0.5 nm alumina film grown on NiAl(110) readily oxidize upon O_2 exposure, but are ineffective for CO oxidation.[8] As discussed by Shaikhutdinov et al.,[3] the problem is that the 0.5 nm film is too thin to serve as an effective barrier to oxygen diffusion, so that oxygen activated on the Pd clusters tends to spill over and react with the underlying NiAl substrate, rather than oxidizing co-adsorbed CO. Therefore, before examining the dependence of Pd_n activity on cluster

size, it is important to understand how alumina film properties vary with thickness, and how thickness influences the activity of Pd_n supported on alumina/Ta(110).

3.3.1 ISS and XPS characterization Pd_{20} on alumina films of varying thickness

Alumina films grown epitaxially on Ta (110), Mo(110) and Re(0001) have been studied by Goodman[54, 58, 59] and shown to have well defined long-range crystal order when prepared with a sample temperature at 900 K. As described above, we used lower annealing temperatures in this experiment, because He^+ ion scattering (ISS) shows that even quite thick films grown or annealed above 900 K have low level Ta contamination in the surface layer, presumably due to Ta diffusion through the alumina thin film. Madey and co-workers used ISS to show that the growth mode of alumina films on Re (0001) and Ru (0001) is dependent on growth conditions. Al deposited on Re (0001) and Ru (0001) grows layer by layer and can then be oxidized to form stoichiometric alumina, however, this method does not lead to good long-range order.[60] Good long-range order was obtained by growing alumina at elevated temperatures (1173 K) in a background of O_2; the growth mode under those conditions was initial formation of 3D alumina islands that coalesced into a continuous film with increasing coverage.[61] In particular, at least 1.5 nm of alumina was required to achieve a continuous film. Figure 3.1 compares ISS data for 0.1 ML Pd_{20} as-deposited on alumina films with 1.4 nm and 4.7 nm thicknesses, grown as discussed above. Note that for the thinner film (1.4 nm ≈ 3 ML), a shoulder is observed on the high E/E_0 side of the Pd peak, indicating that there is Ta in the surface layer. Our relative ISS detection sensitivities for Al, Pd, and Ta, determined by

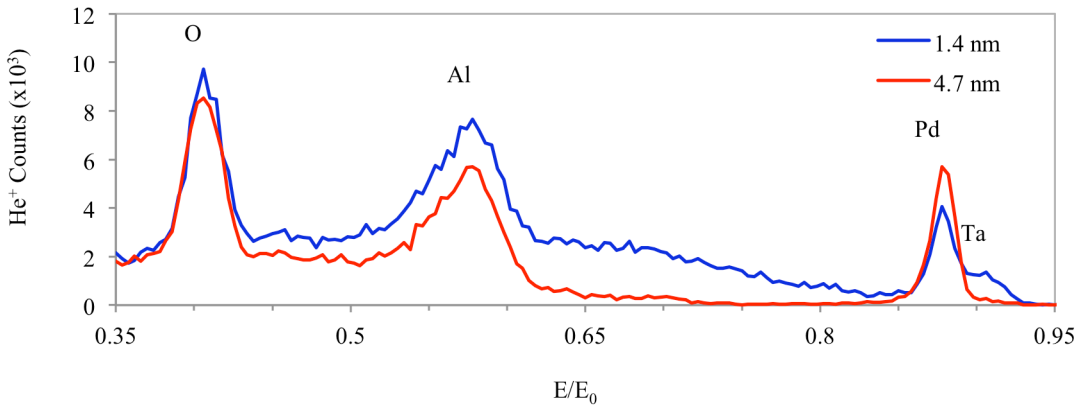

Fig. 3.1: He^+ ISS for as-deposited 0.1 ML Pd_{20} on 1.4 nm (blue) and 4.7 nm (red) alumina films.

measurements on thick alumina films, freshly sputtered/annealed Ta(110), and 0.1 ML Pd on alumina films, are roughly equal for Ta and Pd, but ten times lower for Al. Therefore this Ta shoulder corresponds to ~3.5 % of Ta exposed in the surface layer, indicating the presence of some combination of exposed Ta substrate and/or Ta in the alumina surface layer. For the 4.7 nm film, the Ta shoulder is absent, indicating that a continuous alumina film is present, with no Ta in the surface layer. In addition, note that the background in the 0.5 to 0.8 E/E_0 range is substantially reduced in the thicker alumina film. This continuous background is due to multiple and subsurface scattering, and is sensitive to Ta in the near-surface region, due to the much larger cross section for He^+ scattering from Ta, compared to Al.

The XPS binding energies for Pd on alumina/Ta can vary both due to charging of the alumina film, and possible film thickness-dependent screening/image charge effects on the photoemission final state. To illustrate the magnitude of these effects, Figure 3.2 plots the Al 2s and O 1s binding energies as a function of film thickness, with the binding energy scale shifted so that the Ta $4d_{5/2}$ peak in the Ta(110) substrate is at the literature value of 226.4 eV for metallic Ta.[62] Note that the Al 2s peak was used, rather than the more commonly tabulated Al 2p, because of less interference from Ta photoelectrons. With this approach to setting the binding energy scale, it can be seen that the Al and O binding energies are constant within the experimental uncertainty (~±0.15 eV) for thicknesses up to ~5 nm, but then shift to higher binding energies for thicker films. Nonetheless, they remain within the ranges of binding energies reported in the NIST data base for Al 2s (116.1 - 121.2) O 1s (528.27 – 533.1 eV).[63] It is unclear whether the shift to higher energies for the thicker films simply results from charging, or from formation of

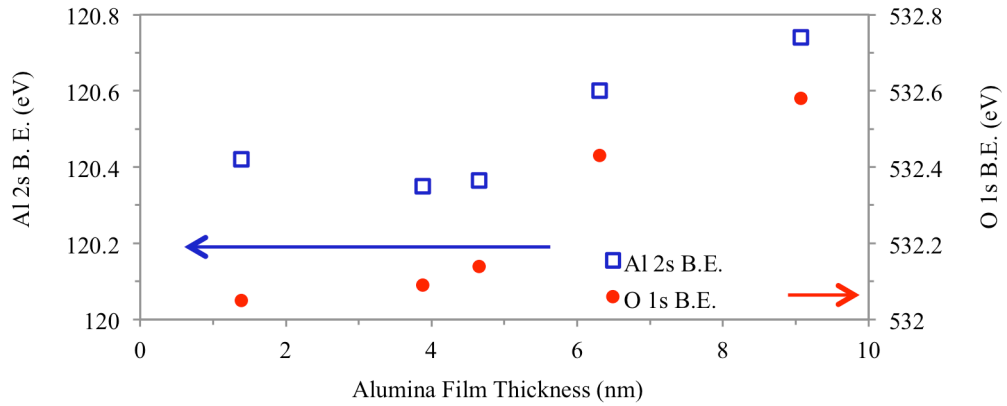

Fig. 3.2: Al 2s binding energy (blue square) and O 1s binding energy (red circle) as a function of alumina film thickness.

a Schottky barrier causing band bending, as suggested by Madey,[61] or some combination of the two. It has previously been reported that thin alumina films (≈ 3 nm or less) grown on a conductive metal substrate do not show significant charging.[64] If the binding energy scale were set using some reference value for either the O 1s or Al 2s peaks, rather than Ta 4d from the conductive support, this might better correct for charging of the film, however, it is not obvious what value should be chosen, or how Schottky barriers might affect this calibration.

From our perspective, the important point is how the Pd 3d binding energies shift both with cluster size and with thickness of the alumina support film. Figure 3.3 shows how the Pd $3d_{5/2}$ binding energy changes for Pd_{20} deposited on alumina films of varying thickness, compared with the analogous changes observed in the Al 2s and O 1s peaks from the films. To allow easy comparison of all three binding energies, they are plotted as shifts relative to the binding energies measured for the thinnest alumina film (1.4 nm). Note that the binding energy scale is inverted to allow better comparison with the CO oxidation activity, also plotted in Figure 3.3, and discussed below.

In contrast to the roughly constant binding energies for Al 2s and O 1s, the Pd 3d binding energy initially shifts to lower binding energy as alumina thickness is increased from 1.4 to ~5 nm. For thicker films, where the Al 2s and O 1s binding energies shift gradually to higher binding energies, the Pd 3d binding energy increases only slightly for 6.3 nm, and then increases dramatically for the thickest film. As already noted, a somewhat different pattern would be obtained if some other method were used to reference the XPS binding energy scale, however, the important point is that the dependence of Pd 3d binding energy on film thickness is qualitatively different from

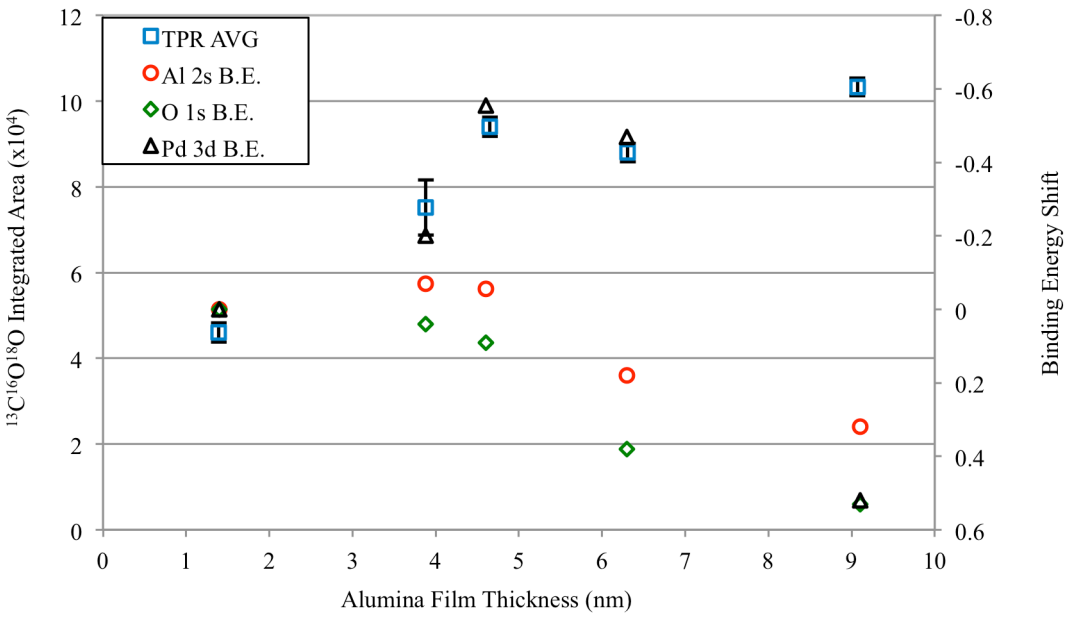

Fig. 3.3: Shift in peak positions from values measured on a 1.4 nm thick film for Al 2s (red circle), O 1s (green diamond) from a freshly grown alumina film and as-deposited Pd 3d binding energies for 0.1 ML Pd_{20}/alumina/Ta(110) as a function of alumina thickness (black triangle). Average $^{13}C^{16}O^{18}O$ production (blue square) in three consecutive TPR runs for the same samples.

those for Al 2s and O 1s, indicating that the chemical environment of the supported Pd changes with film thickness.

It is not clear why the Pd 3d binding energy for the 9.1 nm film is shifted so far to higher binding energy compared to the thinner films. There is some evidence that this thick film charges substantially more than the thinner films, and it may be that the supported Pd clusters charge differently than the underlying support. We note that the Al 2s, O 1s, and Pd 3d peak widths are constant and close to the resolution limit of our (non-monochromatized) XPS system, however, for the 9.1 nm film, the Pd 3d peak width increases by 0.5 eV as compared to that for the thinner films. Interestingly, the peak widths for the Al 2s and O 1s remain unchanged. In the cluster size-dependent reactivity studies, we, therefore kept the alumina support thickness in a narrow range around 5 nm.

3.3.2 The effects of alumina film thickness on the CO oxidation activity of Pd_{20}

Figure 3.4 compares CO_2 signals observed during the first TPR run for a 6.0 nm alumina film grown on Ta(110) (dotted black line), and from Pd_{20} deposited on various thickness alumina films grown on Ta(110). The reaction conditions included O_2 exposure at 400 K, CO exposure at 180 K, and ramping temperature from 135 K to 560 K at 3 K/sec, as described above. The first point to note is that the Pd-free alumina/Ta(110) support generates no significant CO_2, indicating that the CO_2 signal generated from Pd_{20}-containing samples can reasonably be attributed to chemistry associated with the Pd_{20}. For the Pd_{20}-containing samples, it can be seen that for films thinner than ~4.5 nm, the CO oxidation activity increases with increasing alumina thickness.

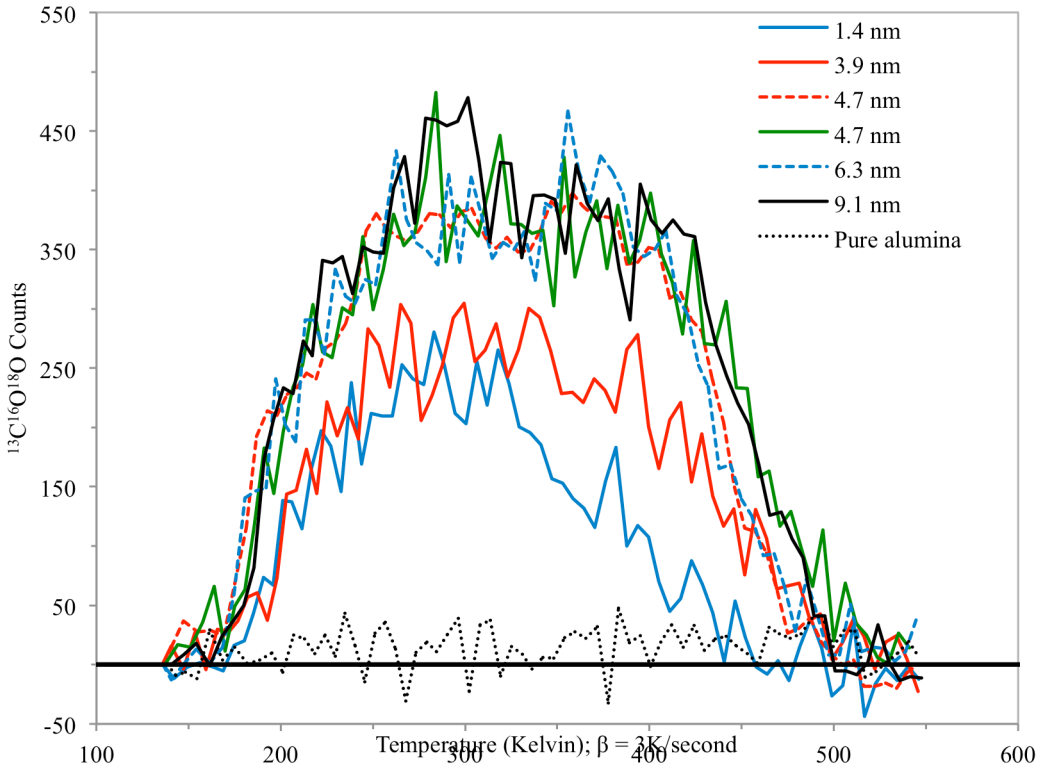

Fig. 3.4: $^{13}C^{16}O^{18}O$ desorption from 0.1 ML Pd_{20}/alumina samples with variable alumina thickness, following 10 L $^{18}O_2$ exposure at 400 K and 10 L ^{13}CO exposure at 180 K. Alumina thickness (nm): 1.4 (solid blue), 3.9 (solid red), 4.7 (dashed red), 4.7 (green), 6.3 (dashed blue), 9.1 (solid black). Dotted black data are for a 6.0 nm pure alumina film with no Pd deposited.

Figure 3.5 shows the integrated CO_2 production observed during three consecutive TPR runs for each Pd_{20}/alumina sample. It can be seen that the integrated CO_2 production is rather consistent from run to run, and this is true as well of the temperature dependence (Figure 3.4). Evidently, the state of the samples does not change significantly from run to run, at least for the rather modest maximum temperature used here. Because the CO_2 production has good run-to-run stability, Figure 3.5 also shows the average and standard error of the integrated CO_2 production for the three runs.

The average CO_2 production is also plotted in Figure 3.3, for comparison with the Pd 3d binding energy. With the exception of the 9.1 nm film, where charging may have been a problem in the XPS, there appears to be a correlation between Pd 3d binding energy and activity. The nature of the correlation – that samples with high Pd 3d binding energies are relatively inactive, and vice versa – is the same as what we observed as a cluster-size-dependent correlation for Pd_n/TiO_2.[9] This similarly suggests that perhaps part of the increase in activity with increasing thickness may be due to changing electronic environment for the supported Pd. As noted, we have no definitive explanation for the large shift to higher binding energy of the Pd binding energy for the 9.1 nm film. As discussed above, there is some evidence that Pd on this thick film is simply charging due to electron emission during XPS, resulting in a spuriously large apparent binding energy. Of course, we cannot rule out other explanations, such as a change in the initial chemical state of the Pd in this sample, although this scenario seems unlikely given that there is virtually no difference in chemical activity of the 9.1 nm film, compared to those in the 4 – 6 nm range.

In addition to the increase in integrated CO_2 production with increasing thickness,

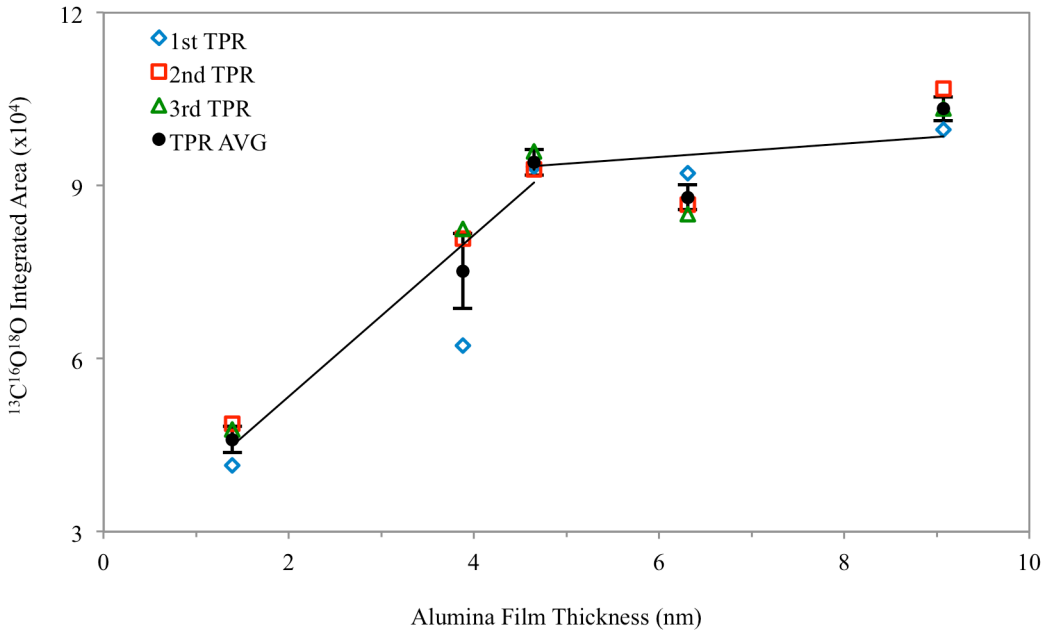

Fig. 3.5: $^{13}C^{16}O^{18}O$ desorption from three consecutive TPR runs on 0.1 ML Pd_{20}/alumina samples, as a function of the alumina film thickness. TPR conditions: 10 L $^{18}O_2$ oxidation at 400 K, 10 L ^{13}CO exposure at 180 K, 3 K/sec heating ramp. The black circles show the average of the three TPR runs (TPR AVG).

the CO_2 desorption temperature dependence is also sensitive to alumina thickness, with relatively less CO_2 desorption at higher temperatures for the thinnest alumina film. Clearly, if sub-4.5 nm alumina films were used for cluster deposition, it would be difficult to separate the effects of cluster size from those from run-to-run variations in alumina thickness. Fortunately, for films thicker than ~4.5 nm, the CO_2 production activity and temperature dependences become nearly independent of alumina thickness. Therefore, the size-dependent experiments described below were all done using films with thicknesses of 5.0 ± 0.3 nm, where sensitivity to thickness is small, but the film is still thin enough that charging is minimal during Pd_n^+ deposition and XPS.

As noted above, for the thinnest alumina film, ISS shows some Ta in the surface layer, which could indicate the presence of exposed areas of the Ta(110) substrate. As a control, we did an experiment where 0.1 ML of Pd_{20} was deposited directly onto a lightly oxidized Ta(110) surface, with no alumina deposited. The deposited Pd_{20} appears in XPS with a Pd 3d binding energy of 336.5 eV (corresponds to a positive 0.34 eV shift in Figure 3.3), which is about what would be expected by extrapolating the binding energy trend in Figure 3.3 to zero alumina thickness. This $Pd_{20}/TaO_x/Ta(110)$ sample showed no CO_2 product under TPR conditions. Unreactive CO was observed to desorb in a feature peaking around 150 K.

In addition to the CO_2 product shown in Figure 3.4, desorption of unreacted ^{13}CO is also observed during TPR. Figure 3.6A shows the ^{13}CO signal recorded during the first TPR run for each sample. Figure 3.6B shows ^{13}CO desorption during a final run, for which the sample was dosed with 10 L ^{13}CO at 180 K as usual, but without the prior $^{18}O_2$ exposure. No CO_2 products are observed during this final TPD run, indicating that no

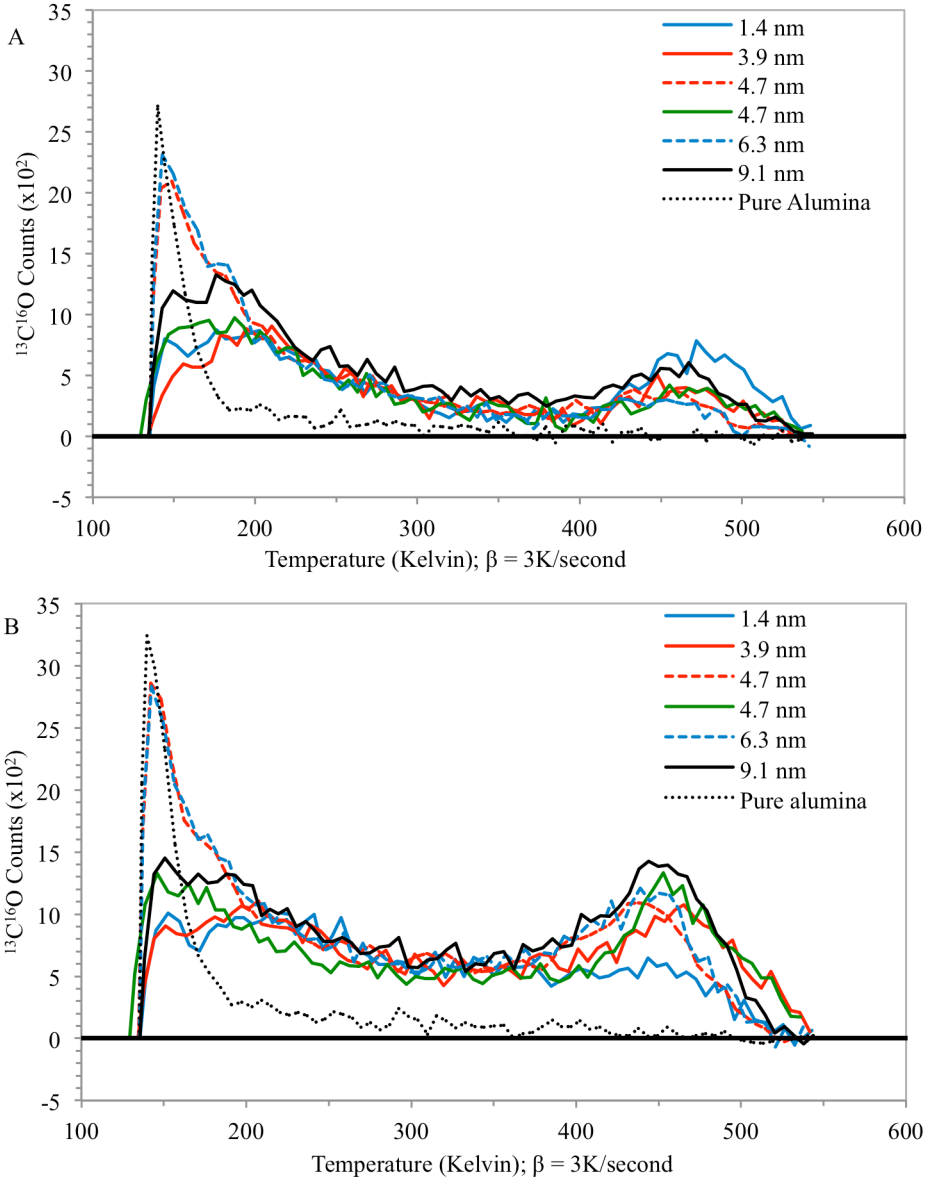

Fig. 3.6: CO_2 and CO desorption from the first TPR run are presented for various samples. (A) Unreacted $^{13}C^{16}O$ desorbing during the first TPR run on samples with 0.1 ML of Pd_{20}/alumina with variable alumina thickness after 10 L $^{18}O_2$ oxidation at 400 K and 10 L ^{13}CO exposure at 180 K. (B) $^{13}C^{16}O$ desorption after 10 L ^{13}CO exposure at 180 K with no O_2 exposure. Alumina film thicknesses (nm): 1.4 (blue), 3.9 (red), 4.7 (dashed red), 4.7 (green), 6.3 (dashed blue), 9.1 (black). Dotted black data are for a 6.0 nm pure alumina film with no Pd deposited.

active oxygen is left on the sample surfaces at the end of the preceding TPR runs.

Ten L ^{13}CO exposure at 180 K should saturate all CO binding sites that are stable at 180 K (mostly associated with Pd), but it should not fill more weakly-bound sites, mostly associated with alumina. As shown in Figure 3.6, however, there was significant ^{13}CO desorption below 180 K, resulting from adsorption of background ^{13}CO remaining after the CO dose, as the sample cooled to the 135 K TPD starting temperature. The magnitude of this sub-180 K ^{13}CO exposure was roughly 0.3 L, however, during the set of experiments shown in Figures 3.4, 3.5, and 3.6, the sample mounting was repaired, which resulted in longer cool-down times, and higher sub-180 K ^{13}CO exposures. The desorption curves shown as solid lines were measured before the sample repair, and those measured afterward are shown as dotted or dashed lines. Comparison of the data sets suggests that the "extra" weakly-bound CO on the postrepair samples has little or no effect on the amount or temperature dependence of the CO oxidation (Figure 3.4), and also does not seem to affect the CO desorption for T >180 K (Figure 3.6). Nonetheless, we note that all the cluster-size-dependent data reported below were taken on the repaired sample, with good run-to-run consistency in the amount of sub-180 K CO adsorbed.

For the 6.0 nm thick alumina film with no Pd (dotted black line), only a sharp desorption feature was observed, beginning as soon as heating started, and with little CO desorbing above ~180 K. For the Pd_{20}/alumina samples there are two new CO desorption features. All the Pd_{20} samples have a low temperature feature that peaks below 200 K, with a tail extending to ~400 K. For the postrepair samples (dashed curves), this Pd-associated desorption feature merges into the sharp feature attributed to desorption from alumina, below ~180 K. In addition to the low temperature feature, the Pd_{20} samples

show a clear desorption peak at around 450 K. These two CO desorption features associated with Pd are qualitatively similar to those observed for CO bound to $Pd_n/TiO_2(110)$ under identical conditions. In that system, it was shown via temperature-dependent ISS experiments, that the low temperature binding site (approximately 200 K for Pd/TiO_2) corresponds to CO bound at the periphery of the Pd clusters, while the high temperature peak (approximately 430 K for Pd/TiO_2) corresponds to CO bound on top of the Pd clusters, such that it prevents He^+ scattering from the underlying Pd.[57]

CO desorption during the final TPD experiments performed after the three sequential TPR runs on each sample are shown in Figure 3.6B (bottom frame). It can be seen that the same three desorption features are observed as in the TPR runs (Figure 3.6A – top frame), however, the intensity is higher, particularly for temperatures above 250 K. This increase is attributed to two factors. In TPR, some fraction of the CO binding sites are presumably blocked by pre-adsorbed ^{18}O, resulting in less ^{13}CO adsorption during the 180 K dose. Furthermore, a significant amount of CO_2 is generated during TPR (compare Figures 3.4 and 3.6A), mostly between 220 K and 450 K, consuming a substantial fraction of the CO adsorbed on the samples. It can be seen that the thinnest of films showed the greatest amount of unreacted CO desorbing at high temperatures (Figure 3.6A), whereas in the final TPD (Figure 3.6B) the amount of high temperature CO desorption increases with alumina film thickness. This trend is consistent with the CO oxidation activity of these samples (Figure 3.4). The thinnest alumina films result in relatively low CO oxidation activity, which leaves a larger fraction of unreacted CO remaining to desorb (compare Figure 3.6A and 3.6B).

One important feature of these model catalysts is that they appear to be quite

stable, at least under the conditions explored. Figure 3.7 shows that both the amount and temperature dependence of CO_2 production for a Pd_{20}/4.7 nm alumina sample were essentially identical in three sequential TPR runs, and also that no significant CO_2 was observed in the final TPD run, where the $^{18}O_2$ exposure was omitted. One could argue that this highly reproducible activity might mean that even before the first TPR run, the Pd_{20} had diffused and sintered into some morphology that is stable under these conditions. As shown below, however, samples prepared with identical Pd coverage, differing only in the size of Pd_n deposited, have significantly different CO oxidation activities, and these cluster size differences are stable in repeated TPR runs. Stable, but size-dependent behaviour is inconsistent with facile diffusion/sintering, thus the results suggest that these samples are, indeed, thermally stable, at least for the rather mild reaction conditions studied. Selected tests were run on samples where up to eight TPR runs were performed, with no significant change from first to last. This high stability is quite different from what we observed under similar conditions for $Pd_n/TiO_2(110)$, where activity dropped rapidly in sequential TPR runs.[65]

ISS was also run on all samples after the series of TPR and TPD experiments. As-deposited ISS was done only for a few, separately prepared samples, to avoid ISS damage effects on the TPR/TPD results. For the few film thicknesses where we have both as-deposited and post-TPR/TPD ISS data, there is no change in Pd ISS intensity, within experimental error (~5%), indicating that the amount of Pd in the surface layer is not significantly affected by TPR/TPD under the conditions used. This observation is consistent with the stability of the TPR results in multiple runs.

Finally, we note that no ^{18}O signal was observed in the post-TPR/TPD ISS data,

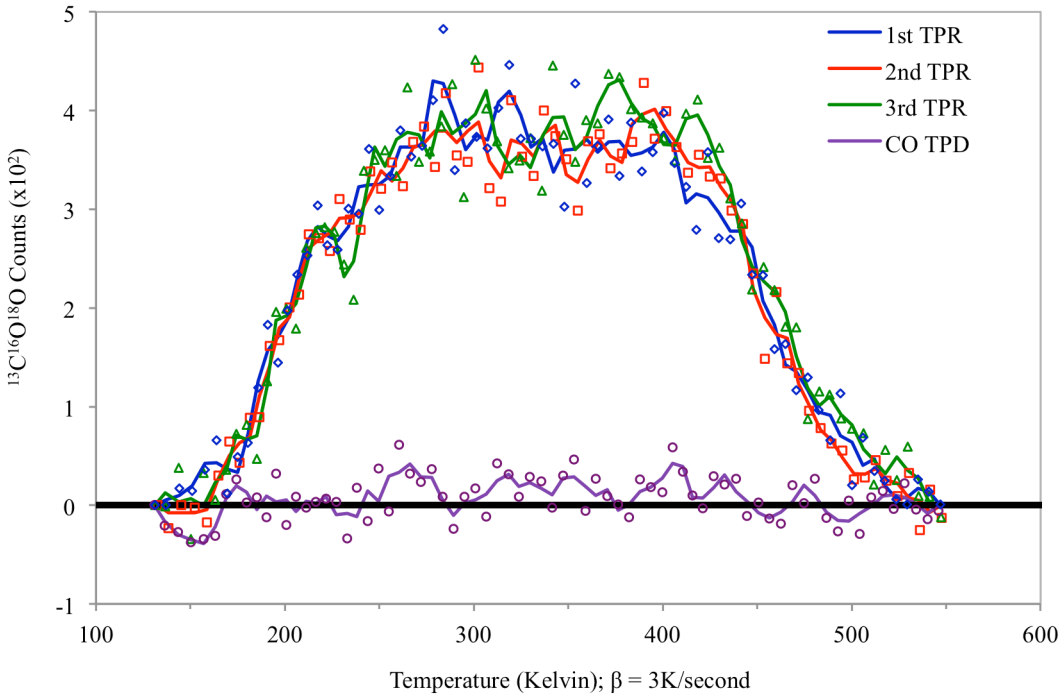

Fig. 3.7: $^{13}C^{16}O^{18}O$ desorption from 0.1 ML Pd_{20} on 4.7 nm thick alumina/Ta(110) in three consecutive TPR runs, each preceded by 10 L 400 K $^{18}O_2$ and 10 L 180 K ^{13}CO exposure. ^{13}CO desorption during a sequent CO TPD run, with 10 L ^{13}CO exposure at 180 K with no O_2 exposure.

indicating that no ^{18}O is left on or in the surface layer, either bound to Pd or to the alumina support. If ^{18}O was left on the surface after TPR, it could be reacted away in the final CO TPD, however, in that case CO_2 should be observed during this final TPD, contrary to observation. Taken together, the ISS and TPD results show that oxygen is the limiting reactant, and is quantitatively reacted away in TPR under our conditions. Furthermore, we can conclude that ^{18}O used in TPR does not spill over to, or exchange with the alumina support, which was grown with normal $^{16}O_2$. After a similar set of TPR and TPD runs for $Pd_n/TiO_2(110)$, 20% - 30% of the surface oxygen is ^{18}O, and it was shown that most of this ^{18}O dissociated on the Pd clusters, and spilled over to the support where it is not active for CO oxidation.[65] The lack of spillover in the Pd/alumina system is presumably one reason why the CO oxidation activity is substantially higher, compared to $Pd/TiO_2(110)$ under identical conditions.

3.3.4 The effects of oxidation condition on activity for CO oxidation by Pd_{20}

In a previous study of CO oxidation over Pd_n/TiO_2 using TPR conditions similar to those here, we found that activity was highly dependent on oxidation temperature. No cluster sizes were active for $T_{ox} \leq 200$ K, select sizes were active for $T_{ox} = 300$K, and all but Pd_1 showed (size-dependent) activity for $T_{ox} = 400$ K.[10] Figure 3.8A shows CO_2 production for a sample prepared by depositing Pd_{20} on a 1.4 nm alumina film, and then probed by sequential TPR runs with 10 L of $^{18}O_2$ at T_{ox}, followed by 10 L ^{13}CO at 180 K. The first three runs had $T_{ox} = 180$ K, 400 K, and 500 K. The final run had $T_{ox} = 400$ K again, but with 50 L $^{18}O_2$ exposure. Figure 3.8B shows desorption of unreacted ^{13}CO

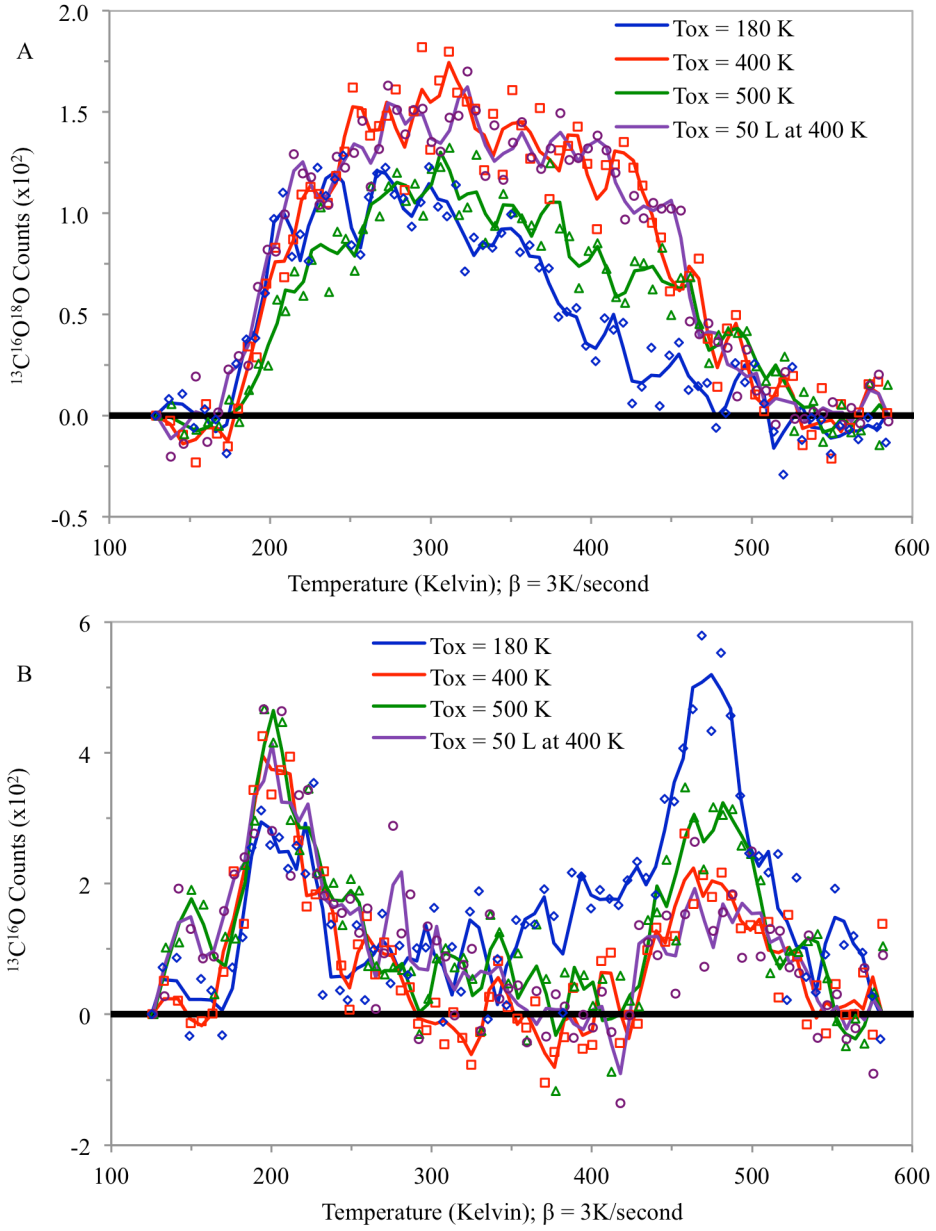

Fig. 3.8: CO_2 and CO desorption from consecutive TPR measurements with viariable oxidation temperatures. (Top) $^{13}C^{16}O^{18}O$ desorption and (bottom) unreacted $^{13}C^{16}O$ desorption from 0.1 ML Pd_{20}/1.4 nm alumina/Ta(110) during consecutive TPR runs with different $^{18}O_2$ exposures: 10 L at 180 K (blue), 10 L at 400 K (red), 10 L at 500 K (green), 50L at 400 K (purple).

measured during the same TPR runs. The maximum CO_2 production was observed in the runs with T_{ox} = 400 K. Oxidizing at 180 K, where $Pd_{20}/TiO_2(110)$ is completely inactive, resulted in almost no change in the low temperature portion of the CO_2 desorption feature, but substantially less CO_2 production above room temperature. Consistent with the decreased overall conversion of CO to CO_2, there was substantially more desorption of unreacted CO in the T_{ox} =180 K run, mostly in the high temperature peak. It is interesting that increasing T_{ox} to 500 K also resulted in significantly lower CO_2 production, but without the large increase in desorption of unreacted CO. Given that CO and oxygen are known to compete for binding sites (see introduction), the decrease in CO_2 production may simply indicate that higher T_{ox} resulted in a greater-than-optimal coverage of the Pd clusters by oxygen. Note, however, that in the second TPR with T_{ox} = 400 K, the $^{18}O_2$ exposure was increased by a factor of 5, which might have been expected to result in similar "over oxidation" of the Pd sites. Instead, the T_{ox} = 400 K TPR 50 L O_2 exposure resulted in essentially identical CO_2 production as seen in the T_{ox} = 400 K TPR.

3.3.5 The effects of Pd_n size (n = 1, 2, 3, 4, 5, 6, 7, 10, 16, 20, and 25) on CO oxidation activity

CO oxidation and CO TPD were studied for a series of Pd_n/alumina/Ta(110) samples, using TPR/TPD conditions identical to those used to generate the data reported in Figures 3.1–7. To avoid confusing the cluster size dependence of interest with effects of alumina film thickness, these samples were all deposited on 5.0 ± 0.3 nm thick films – in the range where activity is insensitive to thickness. For the same reason, the growth

rate was kept in the 0.3 nm/min range, and all experiments reported were done with essentially identical sub-180 K CO exposures. The CO_2 desorption temperature dependence for all cluster sizes was found to be qualitatively similar to those shown for Pd_{20} in Figure 3.7, and desorption of unreactive CO during TPR, and of CO in the final TPD, which also showed bi-modal temperature dependence similar to those shown in Figure 3.6. Also as in Figure 3.7, CO_2 production in successive TPRs was found to be constant within the experimental uncertainty, for all cluster sizes.

The integrated CO_2 production, i.e., the CO oxidation activity, is modestly dependent on cluster size, as shown by the blue squares in Figure 3.9, which show the integrated CO_2 production averaged over the three TPR runs for each sample. The error bars show the standard error in the three runs. The fact that activity is size dependent in a nonmonotonic fashion implies that the samples retain some memory of the size of the deposited clusters, i.e., that diffusion and sintering are not facile enough under the conditions studied to completely average out the effects of deposited size. Furthermore, the fact that activity does not vary significantly in sequential TPR runs, shows whatever the state of the deposited clusters is, it is reasonably stable.

It is interesting to compare the effects of cluster size in this system with those we observed for $Pd_n/TiO_2(110)$, and those observed by Heiz and co-workers for $Pd_n/MgO/Mo(100)$. Under conditions identical to those used for Figure 3.9, CO oxidation over Pd_n/TiO_2 has a stronger size dependence with Pd_1/TiO_2 being essentially inactive, and the other Pd_n/TiO_2 having activities that vary by a factor of ~2.[9] The highest activity in that system was for Pd_{20}/TiO_2, with lower activities observed both for larger and smaller clusters. Even for Pd_{20}/TiO_2, only ~5% of the absorbed CO reacted to form

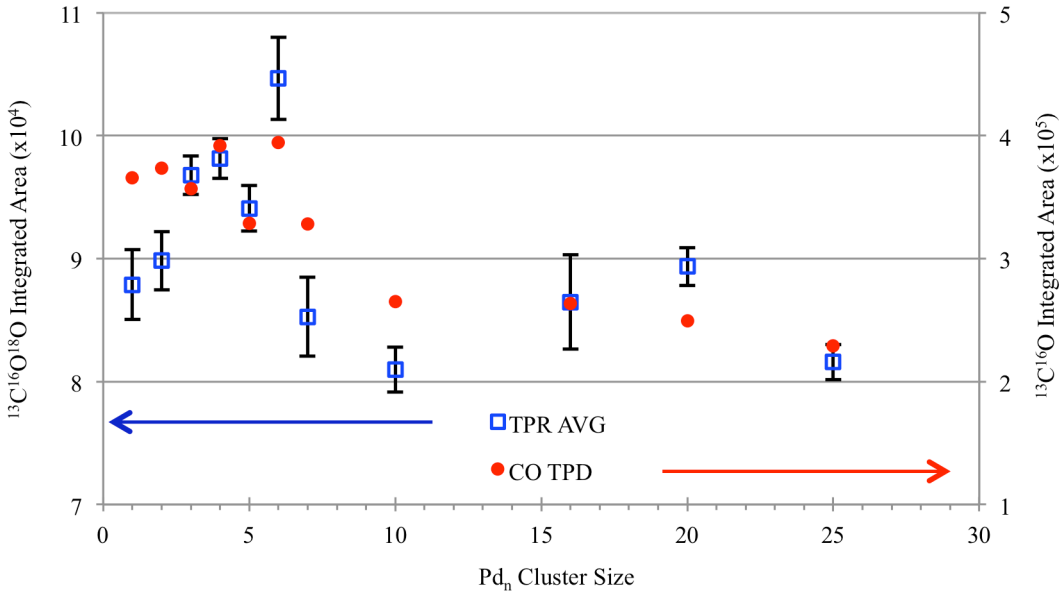

Fig. 3.9: Average $^{13}C^{16}O^{18}O$ production (blue squares) in three TPR runs for samples with 0.1 ML of Pd deposited as different Pd_n, on a 5.0 ± 0.3 nm thick alumina film grown on Ta(110). TPR conditions: 10 L $^{18}O_2$ exposure at 400 K, 10 L ^{13}CO exposure at 180 K. $^{13}C^{16}O$ desorption from a subsequent CO TPD (red dots) with 10 L ^{13}CO exposure at 180 K, but no O_2 exposure.

CO_2, and no activity was observed for T_{ox} below room temperature.[10] In contrast, all Pd_n/alumina/Ta(110) samples are found to be quite active, with ~45% of the adsorbed CO reacting to form CO_2, and substantial activity even for T_{ox} = 180K. As might be expected for a system where reactivity is high for all Pd_n, the dependence on activity is much weaker, amounting to only ~25% variation between least and most reactive. There does appear to be a significant trend of activity increasing from Pd_1 to Pd_6, then dropping abruptly for larger clusters. As shown in Figure 3.10, the increased activity for Pd_n with $n \leq 6$, is correlated with increased CO_2 production at low temperatures, suggesting that the activation energy for the reaction of adsorbed CO and oxygen is smaller for the small clusters.

Also shown in Figure 3.9 is the CO desorption measured in the final CO TPD run, without pre-oxidation of the samples. As noted, no CO_2 is observed in this run, therefore the CO integrated desorption should be a measure of the number of (mostly Pd-associated) CO binding sites on the samples. It can be seen that for Pd_n, $n \leq 6$, the CO intensity is roughly constant, and that it drops by a factor of 30% for $Pd_{10\text{-}25}$. This may indicate that there is a structural transition, such as from single layer to partially two layer structures, with increasing cluster size, and of course this decrease in availability of Pd sites might be expected to be reflected in the CO oxidation activity.

The nonzero activity observed here for deposited Pd_1 might be an indication that atoms deposited on alumina/Ta(110) sinter to form clusters which are reactive. We note, however, that Heiz and co-workers have observed significant activity for model catalysts prepared by deposition of Pd atomic ions on MgO/Mo(100).[4, 44, 46] In particular, they examined CO oxidation over Pd_n/MgO/Mo(100), and found that Pd_1 were active in the

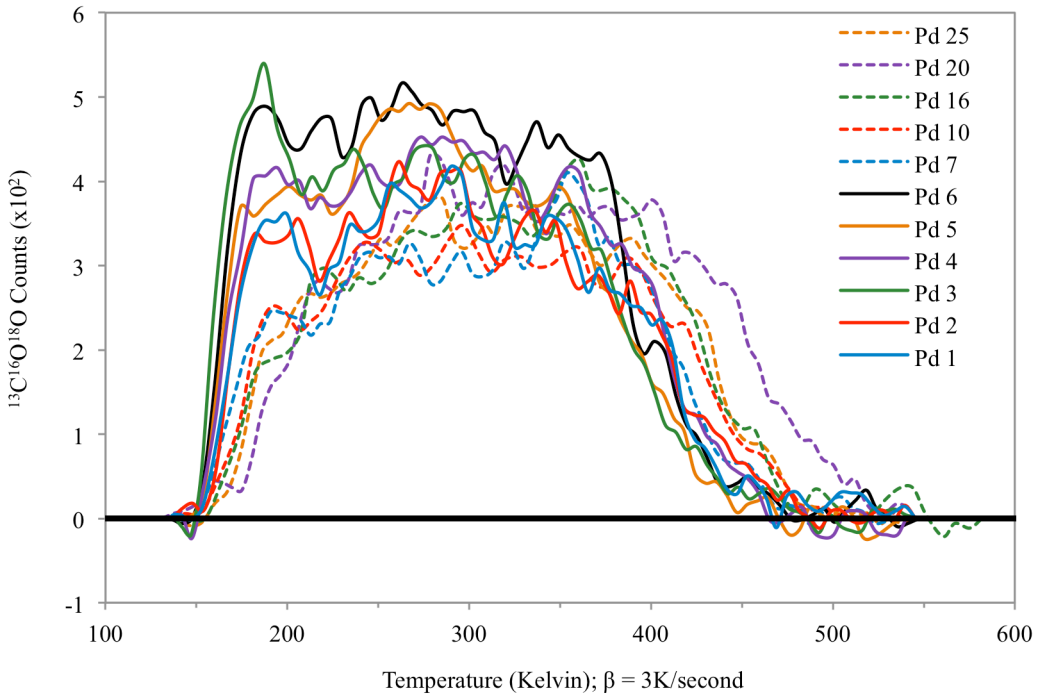

Fig. 3.10: $^{13}C^{16}O^{18}O$ production from the first of three consecutive TPR runs with samples containing 0.1 ML of Pd deposited as different Pd_n, on a 5.0 ± 0.3 nm thick alumina film grown on Ta(110). TPR conditions: 10 L $^{18}O_2$ exposure at 400 K followed by 10 L ^{13}CO exposure at 180 K.

temperature range of 260 – 500 K and the activity is increased when Pd is deposited on electron-rich O-Vacancies in the MgO oxide layer.[66, 67] It was also shown that while there was a strong Pd_n size dependence for deposited clusters, the defect rich film was not shown to enhance the activity for the larger clusters.[20, 48] In future experiments we plan to use ISS on the as-deposited clusters to probe morphology.

The apparent lack of sintering of Pd_n/alumina/Ta(110) observed here is in contrast to studies by other authors of Pd on alumina surfaces. For example, Campbell and co-workers studied Pd particle growth from 0.8 ML equivalents of Pd evaporated onto α-Al_2O_3 (0001), and found particles with average diameter of 5 nm, increasing to ~6 nm after heating to 680 K, and to 8 nm after heating to 1000 K.[30] Similarly, Freund and co-workers have reported a number of studies of Pd particles grown by Pd evaporation and annealing on alumina/NiAl(110) with Pd loadings as low as 0.3ML.[3, 68, 69] One ML of Pd evaporated onto alumina films grown on a Ta support were studied by the Goodman group and showed good thermal stability.[37, 69, 70]

Four factors may increase the thermal stability of our samples. Our alumina films are relatively thick, and grown and annealed at relatively low temperature. Both factors are likely to result in films that are rough and/or defective relative to α-Al_2O_3 (0001) or the crystalline 0.5 nm film grown on NiAl(110), and defects tend to provide anchoring sites for atoms and clusters. Another factor is that preformed clusters deposited on surfaces are expected to diffuse and sinter less than deposited atoms, because more bonds need to be broken, leading to increased diffusion barrier. This effect was demonstrated nicely by Buratto and co-workers for Au_n/TiO_2(110). Au_1 was observed to sinter to large multilayer particles at room temperature, while clusters, even as small as Au_2, were stable

for hours.[71] Furthermore, the Pd loading for our samples is relatively low. This increases intercluster distances, forcing diffusion over longer length scales for sintering to occur. Finally, we were careful in these studies to keep the maximum temperature of the TPR and TPD scans below 575 K, and to minimize the time spent at high temperature.

Figure 3.11 compares the CO oxidation activity with the measured Pd 3d binding energy for as-deposited clusters. It can be seen that the two are generally anticorrelated (note inverted binding energy scale), suggesting that this system is another example where electronic structure of the supported clusters, as probed by the shifting core level, is a controlling factor for activity as an oxidation catalyst. Similar anticorrelations have been seen for CO oxidation over $Pd_n/TiO_2(110)$ [9] and carbon oxidation by water in electrocatalysis by Pt_n on glassy carbon.[72]

3.4 Conclusions

We have used CO_2 production and CO desorption from Pd_{20} deposited on a series of variable thickness alumina films grown on Ta(110) to observe how behaviour of supported Pd changes with support thickness, and to find a thickness range where properties are insensitive to thickness. The alumina film provides a very stable environment for the Pd clusters, such that the size-dependent CO oxidation activity is stable in repeated TPR cycles. There is significant, nonmonotonic variation in activity with size, which is weakly correlated with the density of Pd sites on the surface, but also must depend on properties such as the cluster electronic properties or availability of particular binding sites, which vary with size.

There is more work to be done with this system, including complete

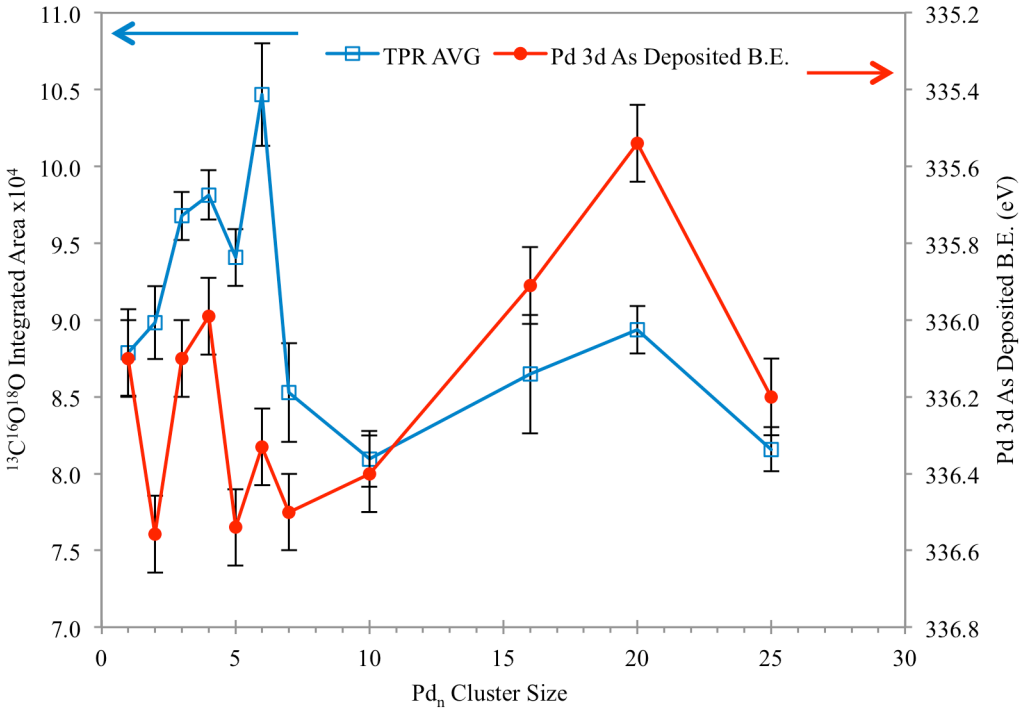

Fig. 3.11: Average $^{13}C^{16}O^{18}O$ production (blue squares) in three TPR runs for samples with 0.1 ML of Pd deposited as different Pd_n, on a 5.0 ± 0.3 nm thick alumina film grown on Ta(110). TPR conditions: 10 L $^{18}O_2$ exposure at 400 K, 10 L ^{13}CO exposure at 180 K. As deposited Pd 3d binding energy (red dots) corresponding to the 0.1 ML of Pd_n deposited on 5.0 ± 0.3 nm thick alumina film used for the size dependent $^{13}C^{16}O$ oxidation studies.

characterization of the as-deposited samples by XPS, UPS, ISS, and CO TPD, temperature-dependent ISS and UPS experiments to probe the nature of oxygen and CO binding, and studies of the effects of Ta incorporation into the alumina surface layer on activity and stability of the catalysts. Nonetheless, it is clear already the Pd_n/alumina/Ta(110) is substantially more active and more thermally stable than Pd_n/TiO_2, and provides an interesting system in which to explore the effects of cluster size on activity and physical properties of model catalysts.

3.5 References

1. H. Conrad, G. Ertl and J. Kueppers, *Surface Science*, 1978, **76**, 323-342.

2. T. Schalow, B. Brandt, D. E. Starr, M. Laurin, S. K. Shaikhutdinov, S. Schauermann, J. Libuda and H.-J. Freund, *Physical Chemistry Chemical Physics*, 2007, **9**, 1347-1361.

3. S. Shaikhutdinov, M. Heemeier, J. Hoffmann, I. Meusel, B. Richter, M. Bäumer, H. Kuhlenbeck, J. Libuda, H.-J. Freund, R. Oldman, S. D. Jackson, C. Konvicka, M. Schmid and P. Varga, *Surf. Sci.*, 2002, **501**, 270-281.

4. S. Kunz, F. F. Schweinberger, V. Habibpour, M. Rottgen, C. Harding, M. Arenz and U. Heiz, *Journal of Physical Chemistry C*, 2010, **114**, 1651-1654.

5. S. Kunz, K. Hartl, M. Nesselberger, F. F. Schweinberger, G. Kwon, M. Hanzlik, K. J. J. Mayrhofer, U. Heiz and M. Arenz, *Phys. Chem. Chem. Phys.*, 2010, **12**, 10288-10291.

6. S. M. McClure and D. W. Goodman, *Chem. Phys. Lett.*, 2009, **469**, 1-13.

7. W. E. Kaden, W. A. Kunkel and S. L. Anderson, *J. Chem. Phys.*, 2009, **131**, 114701.

8. T. Wu, W. E. Kaden, W. A. Kunkel and S. L. Anderson, *Surface Science*, 2009, **603**, 2764-2770.

9. W. E. Kaden, T. Wu, W. A. Kunkel and S. L. Anderson, *Science*, 2009, **326**, 826-829.

10. W. E. Kaden, W. A. Kunkel, M. D. Kane, F. S. Roberts and S. L. Anderson, *J. Am. Chem. Soc.*, 2010, **132**, 13097–13099.

11. M. M. Gadgil, R. Sasikala and S. K. Kulshreshtha, *Journal of Molecular Catalysis*, 1994 **87**, 297-309.

12. M. M. Gadgil and S. K. Kulshreshtha, *Journal of Molecular Catalysis A: Chemical*, 1995 **95**, 211-222.

13. T. Engel and G. Ertl, *Chemical Physics Letters*, 1978, **54**, 95-98.

14. T. Engel and G. Ertl, *Journal of Chemical Physics*, 1978, **69**, 1267-1281.

15. I. Z. Jones, R. A. Bennett and M. Bowker, *Surf. Sci.*, 1999, **439**, 235-248.

16. G. A. Kok, A. Noordermeer and B. E. Nieuwenhuys, *Surface Sci.*, 1983, **135**, 65-80.

17. B. Brandt, T. Schalow, M. Laurin, S. Schauermann, J. Libuda and H.-J. Freund, *Journal of Physical Chemistry C*, 2007, **111**, 938-949.

18. C. J. Harding, S. Kunz, V. Habibpour and U. Heiz, *Phys. Chem. Chem. Phys.*, 2008, **10**, 5875-5881.

19. C. J. Harding, S. Kunz, V. Habibpour and U. Heiz, *Chem. Phys. Lett.*, 2008, **461**, 235-237.

20. C. J. Harding, S. Kunz, V. Habibpour, V. Teslenko, M. Arenz and U. Heiz, *Journal of Catalysis*, 2008, **255**, 234-240.

21. M. Bowker, P. Stone, R. Bennett and N. Perkins, *Surf. Sci*, 2002, **497**, 155-165.

22. V. Matolin, I. Jungwirthova and E. Tomkova, *Prog. Surf. Sci.*, 1990, **35**, 175-178.

23. E. Gillet and V. Matolin, *Z. Phys. D: At., Mol. Clusters*, 1991, **19**, 361-365.

24. I. Stara and V. Matolin, *Surface Science*, 1994, **313**, 99-106.

25. V. Matolin, I. Stara, N. Tsud and V. Johanek, *Prog. Surf. Sci.*, 2001, **67**, 167-181.

26. V. Matolin, V. Johanek, I. Stara, N. Tsud and K. Veltruska, *Surface Science*, 2002, **507-510**, 803-807.

27. J.-H. Fischer-Wolfarth, J. A. Farmer, J. M. Flores-Camacho, A. Genest, I. V. Yudanov, N. Rösch, C. T. Campbell, S. Schauermann and H.-J. Freund, *Phys. Rev. B*, 2010, **81**, 241416 (241414 pages).

28. I. Jungwirthovk, I. Star and V. Matolin, *Surface Science*, 1997, **377-379** 644-649.

29. N. Tsud, V. Joha´nek, I. Stara´, K. Veltruska´ and V. Matolıin, *Surface Science*, 2000, **467**, 169-176.

30. S. L. Tait, Ngo, L.T., Yu, Q., Fain S. C. Jr.. Campbell, C.T., *J. Chem. Phys.*, 2005, **122**, 064712.

31. S. Penner, Bera, P., Pederson S., Ngo, L.T., Harris, J.J.W., Campbell, C. T., *Journal of Physical Chemistry B*, 2006, **110**, 24577-24584.

32. M. Bowker and E. Fourre, *Appl. Surf. Sci.*, 2008, **254**, 4225-4229.

33. R. A. Bennett, C. L. Pang, N. Perkins, R. D. Smith, P. Morrall, R. I. Kvon and M. Bowker, *Journal of Physical Chemistry B*, 2002, **106**, 4688 -4696.

34. M. Bowker, P. Stone, R. Bennett and N. Perkins, *Surf. Sci.*, 2002, **497**, 155-165.

35. M. S. Chen, Y. Cai, Z. Yan, K. K. Gath, S. Axnanda and D. W. Goodman, *Surface Science*, 2007, **601**, 5326-5331.

36. D. C. Meier and D. W. Goodman, *Journal of the American Chemical Society*, 2004, **126**, 1892-1899.

37. E. Ozensoy and D. W. Goodman, *Phys. Chem. Chem. Phys.*, 2004, **6**, 3765-3778.

38. Y. Q. Cai, A. M. Bradshaw, Q. Guo and D. W. Goodman, *Surf. Sci.*, 1998, **399**, L357-L363.

39. D. R. Rainer, M. Koranne, S. M. Vesecky and D. W. Goodman, *Journal of Physical Chemistry B*, 1997, **101**, 10769-10774.

40. D. R. Rainer, M. C. Wu, D. I. Mahon and D. W. Goodman, *J. Vac. Sci. Technol., A*, 1996, **14**, 1184-1188.

41. S. M. McClure, M. Lundwall, F. Yang, Z. Zhou and D. W. Goodman, *Journal of Physics: Condensed Matter*, 2009 **21**, 474223-474230.

42. S. M. McClure, M. Lundwall, Z. Zhou, F. Yang and D. W. Goodman, *Catalysis Letters*, 2009 **133**, 298-306.

43. B. Yoon, U. Landman, V. Habibpour, C. Harding, S. Kunz, U. Heiz, M. Moseler and M. Walter, *J. Phys. Chem. C*, 2012, **116**, 9594-9607.

44. M. Moseler, M. Walter, B. Yoon, U. Landman, V. Habibpour, C. Harding, S. Kunz and U. Heiz, *J. Am. Chem. Soc.*, 2012, **134**, 7690-7699.

45. V. Habibpour, Z. W. Wang, R. E. Palmer and U. Heiz, *Journal of Applied Sciences*, 2011, **11**, 1164-1170.

46. C. J. Harding, S. Kunz, V. Habibpour, V. Teslenko, M. Arenz and U. Heiz, *Journal of Catalysis*, 2008, **255**, 234-240.

47. M. Arenz, S. Gilb and U. Heiz, *Chemical Physics of Solid Surfaces*, 2007, **12**, 1-47.

48. M. A. Roettgen, S. Abbet, K. Judai, J.-M. Antonietti, A. S. Woerz, M. Arenz, C. R. Henry and U. Heiz, *J. Am. Chem. Soc.*, 2007, **129**, 9635-9639.

49. M. E. Vaida, T. M. Bernhardt, C. Barth, F. Esch, U. Heiz and U. Landman, *Physica Status Solidi B: Basic Solid State Physics*, 2010, **247**, 1001-1015.

50. C. Harding, V. Habibpour, S. Kunz, A. N.-S. Farnbacher, U. Heiz, B. Yoon and U. Landman, *J. Am. Chem. Soc.*, 2009, **131**, 538-548.

51. R. Robles and S. N. Khanna, *Phys. Rev. B: Condens. Matter Mater. Phys.*, 2010, **82**, 085428.

52. K. J. Boyd, A. Lapicki, M. Aizawa and S. L. Anderson, *Review of Scientific Instruments*, 1998, **69**, 4106-4115.

53. S. Lee, C. Fan, T. Wu and S. L. Anderson, *J. Chem. Phys.*, 2005, **123**, 124710 124713 pages.

54. P. J. Chen and D. W. Goodman, *Surf. Sci.*, 1994, **312**, L767-L773.

55. J. J. Yeh and I. Lindau, *Atomic Data and Nuclear Data Tables*, 1985, **32**, 1-155.

56. C. J. Powell and A. Jablonski, *NIST Electron Effective-Attenuation-Length Database*, NIST, Gaithersburg, MD, 2011.

57. W. E. Kaden, W. A. Kunkel, F. S. Roberts, M. Kane and S. L. Anderson, *J. Chem. Phys.*, 2012, **136**, 204705.

58. C. Xu and D. W. Goodman, *Chem. Phys. Lett.*, 1996, **263**, 13-18.

59. M.-C. Wu and D. W. Goodman, *J. Phys. Chem.*, 1994, **98**, 9874-9881.

60. Y. Wu, E. Garfunkel and T. E. Madey, *Surf. Sci.*, 1996, **365**, 337-352.

61. Y. Wu, E. Garfunkel and T. E. Madey, *J. Vac. Sci. Technol., A*, 1996, **14**, 2554-2563.

62. C. J. Powell, *Applied Surface Science*, 1995, **89**, 141-149.

63. Nist X-ray Photoelectron Spectroscopy Database, Version 4.1 (National Institute of Standards and Technology, Gaithersburg, 2012); http://srdata.nist.gov/xps/.

64. T. L. Barr, *Thin Solid Films*, 1994, **253**, 277-284.

65. M. D. Kane, F. S. Roberts and S. L. Anderson, *Unpublished results*, 2014.

66. S. Abbet, A. M. Ferrari, L. Giordano, G. Pacchioni, H. Hakkinen, U. Landman and U. Heiz, *Surface Science*, 2002, **514**, 249-255.

67. S. Abbet, U. Heiz, H. Häkkinen and U. Landman, *Phys. Rev. Lett.*, 2001, **86**, 5950-5953.

68. M. Bäumer, J. Libuda, A. Sandell, H. J. Freund, G. Graw, T. Bertrams and H. Neddermeyer, *Ber. Bunsen-Ges.*, 1995, **99**, 1381-1386.

69. M. Heemeier, S. Stempel, S. K. Shaikhutdinov, J. Libuda, M. Bäumer, R. J. Oldman, S. D. Jackson and H.-J. Freund, *Surf. Sci.*, 2003, **523**, 103-110.

70. D. R. Rainer, S. M. Vesecky, M. Koranne, W. S. Oh and D. W. Goodman, *Journal of Catalysis*, 1997, **167**, 234-241.

71. X. Tong, L. Benz, P. Kemper, H. Metiu, M. T. Bowers and S. K. Buratto, *J. Am. Chem. Soc.*, 2005, **127**, 13516-13518.

72. S. Proch, M. Wirth, H.S. White and S. Anderson, *J. Am. Chem. Soc*., 2013, **135**, 3073-3086.

CHAPTER 4

EFFECTS OF ALUMINA FILM THICKNESS ON CO OXIDATION ACTIVITY OVER Pd_{20}/ALUMINA/Re(0001): CORRELATED EFFECTS OF ALUMINA ELECTRONIC PROPERTIES AND Pd_{20} GEOMETRY ON ACTIVITY

4.1. Introduction

Ultrathin oxide films grown on metal single crystals are frequently used as supports for metal-on-metal-oxide model catalysts. They allow the full array of surface analysis tools to be used in mechanistic studies, without complications from surface charging that can limit use of bulk oxide supports.[1-28] One obvious question is how thick the oxide layer must be to realistically represent a bulk oxide, and for model systems with thinner films, what effects on chemistry might result. It has been shown that the thickness of the oxide can have drastic effects on supported metal nanoparticles by affecting the catalytic metal particle geometry.[12, 29] Madey et al. characterized the growth and oxidation of Al films on both Re and Rh single crystals, noting a change in the electronic structure of the alumina films as a function of total film thickness.[30, 31] Other research has suggested that for thin metal oxide films grown on a metal support, tunneling of electrons from the metal support to metal particles supported on the metal oxide films can occur[3, 32]. Work done in the Freund lab has shown the ability to tune the amount of electron transfer from Mo-doped CaO films to supported Au nanoparticles, which affects both the electronic structure and morphology of the nanoparticles.[33] Campbell and co-workers have used calorimetry to explore the effects of CeO_2 film thickness on metal-support binding energies, and found that the energetics change rapidly in the thickness range up to 2 nm, then converge slowly for thicker films.[34] As a final example, the Pacchioni group has described, theoretically, electronic phenomena that occur for thin metal oxide films, such as electron transfer, work function changes, and defect engineering.[12, 32, 35-37]

There has been considerable work on model catalysts grown on thin alumina

films. One commonly used film model is the well characterized, self-limiting alumina film that grows spontaneously on NiAl single crystals heated in O_2. For example, on NiAl(110), a 0.5 nm thick film grows which has excellent order, as shown by both STM and x-ray crystallography.[26, 38-42] The Freund group has used this model system in a number of studies, including CO oxidation over Pd nanoparticles supported on alumina/NiAl(110). It was shown that there is initially considerable spillover of activated oxygen from the Pd to the alumina film, where it diffuses to the NiAl substrate, thickening the film.[43] Eventually, the film surrounding the particles becomes thick enough to act as a diffusion barrier, and the system becomes an excellent model catalyst. We previously studied Pd_n/alumina/NiAl(110), and observed interesting size-dependent Pd oxidation kinetics[44], but were unable to observe oxidation of co-adsorbed CO because of competition from spillover and reaction with the NiAl substrate.[43, 44] Another approach is to grow alumina films epitaxially by evaporation of aluminum onto suitable substrates in an oxygen atmosphere, thereby allowing growth of films with arbitrary thickness. This approach was demonstrated by the groups of Madey[30, 31] and Goodman[45, 46] who showed that alumina films with good long-range order could be grown on Ta(110) and Re(0001) supports. The Goodman group reported a series of experiments utilizing IR spectroscopy to monitor adsorbates on metal clusters on these alumina substrates[15, 47, 48] as well as angle-resolved photoemission to probe the electronic structure of the supported clusters.[49] The Madey group reported on the electronic structure of the alumina films, themselves.[30, 31, 50]

Thin MgO films have also been used in many model catalyst studies.[7, 9, 23, 51-59] The Heiz and Landman groups studied the effects of both composition and thickness of

MgO films on the overall CO oxidation reactivity by Au clusters using both experimental and theoretical methods. Of particular relevance to our research, the combined efforts of Heiz and Landman studied the effects of the MgO(100) substrate on deposited Au_{20}. Despite bulk gold being inactive,[60, 61] Au_{20} deposited on a thin MgO film is active for CO oxidation.[32] Furthermore, the level of activity could be correlated to the interaction of oxygen defect sites providing electron density to the Au_{20} clusters, which could then oxidize CO.[7, 62, 63] Vajda and co-workers reported a study on the thermal stability of Pt clusters deposited on alumina films grown on oxidized silicon substrates. The Pt particle growth occured on incomplete alumina films, but after a complete alumina surface had been formed, the Pt clusters were very stable at elevated temperatures[64]. Similarly, Pd_n clusters deposited on alumina films grown Ta(110) were also shown to be stable in terms of exposed Pd surface area and CO oxidation reactivity for at least eight reaction cycles reaching temperatures of 600 K. However, in the Pd_n/alumina/Ta(110) system, the alumina film thickness (up to 5 nm) showed a controlling effect on the overall CO oxidation activity.[65]

Utilization of thermal evaporation allows for not only a stable film, but also a tunable variable in controlling the metal oxide film thickness. The interest of this paper is focused on the effect of the metal oxide thickness and the identity of the metal support on the reactivity of size-selected Pd_{20} clusters, specifically how the oxide thickness can tune the electronic and geometric properties of the Pd cluster catalysts. CO oxidation was chosen as the test reaction to examine the relationship between film thickness, electronic effects, and activity because there is a wealth of mechanistic information about this reaction catalyzed by both single crystals[66-69] and oxide-supported metal particles.[9,

[67, 70-77] Briefly, it has been shown in literature that CO oxidation, on noble metal catalysts, reacts via the Langmuir Hinshelwood reaction. In this scenario, both the CO and O_2 must first adsorb onto the catalyst before CO oxidation can occur.[68, 69, 78, 79]

Here, we report a study of the effects of varying alumina film thickness on the CO oxidation activity of deposited Pd_{20} clusters. In addition, we have characterized the electronic properties of both the alumina film and the deposited clusters, as well as the morphology of the clusters and the density of different types of binding sites, all as a function of alumina film thickness. Our interest is partly in exploring the possibility that thickness might be used to tune catalytic properties, but the main interest is in using film thickness-dependent correlations of activity with various physical properties to learn about the reaction mechanism, and which factors control activity under our reaction conditions. In typical model catalyst experiments, where the metal clusters grow by nucleation at defects on the support, defect density, cluster size, and metal coverage are interrelated. Given that defect density may be a function of film thickness,[7, 62] it may be difficult to separate the effects of thickness and cluster size. The experiments take advantage of an instrument that allows preparation of model catalysts by deposition of mass-selected clusters on well-defined planar supports to study cluster size effects on both electrochemistry[80] and gas-surface reactions[44, 65, 81-86] including CO oxidation over Pd_n/alumina/Re(0001)[87] – the system of interest here. One of the advantages of this approach is that it is possible to deposit clusters of a particular size (here Pd_{20}), independent of coverage and of the density of defects on the oxide support. The choice of the Pd_n/alumina/Re(0001) system was motivated by observation of unusual, non-monotonic dependence of the CO oxidation activity on the thickness of the alumina

layer.[87] For a system like ultra-thin alumina on Re(0001), properties like the number, type, and density of defects are almost certainly a strong function of the alumina thickness. As a result, samples grown by diffusion and nucleation would tend to have different distributions of cluster/particle sizes as a function of thickness. In order to focus on the inherent alumina thickness effects on electronic structure, catalyst morphology and reactivity, we exploit another capability of size-selected cluster deposition to create samples with clusters of constant size and density, independent of the support properties

4.2. Experimental

4.2.1 Apparatus

Experiments were done in an ultra-high vacuum (UHV) system which has been described previously.[81, 85, 87] Briefly, the vacuum system consists of three main components: a UHV analysis chamber for sample preparation and characterization, a high intensity mass-selected cluster deposition beamline, and a small antechamber attached to the UHV analysis chamber that can be used for thin film preparation, sample exchange/repair, and as a high pressure cell. The cluster deposition beamline allows for cluster formation via laser vaporization into a high pressure pulsed helium flow. Vaporization is driven by a 30 Hz 532 YAG laser operated at 30-60 mJ/pulse. The pressure in this region of the beamline is approximately 45 milliTorr. Cluster ions exiting the source are collected by a quadrupole ion guide, and then the beam is bent 18° in order to eliminate neutrals and anions, and allow coaxial injection of the laser. The ions then pass through additional quadrupole ion guides, a quadrupole mass filter, and a final ion guide, passing through six stages of differential pumping, and dropping the

pressure to ~ 1 x 10^{-9} Torr in the process. The final quadrupole guides the mass-selected clusters up to a lens/deposition mask that is used to control the spot size, and then deposited on the sample, which is positioned just behind the mask. The base pressure in the deposition/analysis chamber is ~1 x 10^{-10}. This beamline generates Pd_n^+ containing up to 35 atoms, with currents up to ~6.5 nA. All experiments reported here were done with Pd_{20} deposited at 1 eV/atom – high enough to minimize space charge effects, but still below the energies expected for Pd-Pd and Pd-aluminum binding.

After sample preparation, analysis was done *in situ* by a combination of X-ray photoelectron spectroscopy (XPS), ultraviolet photoelectron spectroscopy (UPS), and low energy ion scattering spectroscopy (ISS). For all XPS measurements in this paper, Al Kα X-rays were used for irradiation and the measured binding energies were calibrated to the Re $4f_{7/2}$ binding energy of 40.3 eV, using signal from the Re(0001) single crystal used as the base substrate. Note that the raw Re $4f_{7/2}$ binding energy varied by only ~0.03 eV, i.e., charging and other artifacts were small. UPS was done using He I radiation (21.2 eV) generated by a windowless, doubly differentially pumped capillary discharge lamp,[88] operating on ultra-high purity He. For ISS measurements, ultra-high purity helium was leaked into the ion gun, resulting in a chamber pressure of 5 x10^{-7} Torr, He^+ kinetic energy of 1 keV was used. For every measurement, the sample current was measured and used to correct for small day-to-day changes in the He^+ flux. The analysis chamber is also equipped with both a residual gas analyzer (RGA), used to monitor gas doses, and a differentially pumped UTI 100c mass spectrometer used to measure desorption from the surface. This mass spectrometer views the analysis chamber through a 2.5 mm diameter orifice at the tip of a skimmer cone, and the sample is positioned just in front of the

orifice for desorption measurements. When the sample is positioned in front of this mass spectrometer, it is also at the focus of six directional gas dosing lines that can be used in pulsed or continuous modes. The gas fluxes from the dose tubes at the sample position have been calibrated by comparing to doses delivered via the chamber background, and are equivalent to roughly ten times the background pressure.

The antechamber is mounted to the bottom of the analysis chamber, and has a base pressure $\leq 5 \times 10^{-9}$ Torr. As the sample is lowered into this chamber, it passes through a gate valve and a triple differential seal, and when in position, the antechamber pressure can be raised to one atmosphere without affecting the base pressure in the UHV analysis chamber. In the experiments described here, the antechamber was used for growth of the alumina films, minimizing the effects of the required O_2 pressures on the analysis chamber background.

4.2.2 Model catalyst preparation

Samples were prepared by depositing Pd_{20}^{+} clusters on an alumina thin film, grown on a 10 x 5 x 1 mm Re(0001) single crystal (Marketech International Inc). The Re single crystal was spot welded to a pair of tantalum heating wires supported from a pair of tungsten rods attached to a liquid nitrogen cooled cryostat attached to a rotatable XYZ manipulator. The sample temperature was measured using a C-type thermocouple spot welded to the back of the Re single crystal, and could be controlled between 115 K and 1200 K using resistive heating and to well above 2000 K by electron bombardment. Alumina films with thicknesses up to at least 7 nm are conductive enough that the Pd_{20}^{+} neutralized upon deposition, with no signs of charging. By integrating the Pd_{20}^{+}

neutralization current during deposition, it was possible to stop deposition with a precisely defined coverage of Pd, totaling 1.53 x 10^{14} Pd atoms/cm^2, which is equivalent to 0.1 of a close-packed Pd monolayer. It should be noted that the deposition was carried out at room temperature with typical deposition times of about 5 minutes.

Prior to alumina film growth, the Re(0001) crystal was cleaned by annealing at 1775 K for 20 minutes, until no contaminants could be detected via XPS. After cleaning, the sample was lowered into the antechamber and heated to 970 K, while Al was vapor deposited in a background of 5 x 10^{-6} Torr of ultra-high purity $^{16}O_2$ that was further cleaned by passing it through a liquid nitrogen/ethanol bath (~160K). The alumina film growth procedure was adapted from work in the Goodman and Madey groups.[30, 31, 46] In our experiments, the Al/Re XPS intensity ratio is used to estimate the thickness of the alumina film, using literature values for both the photoemission cross sections as well as the β parameters,[89] and effective attenuation lengths calculated from the NIST EAL Database version 1.3.[90] We estimate that the absolute thicknesses are correct to within ~20%, however, the relative uncertainty in comparing thicknesses of different films is estimated to be less than 5%.

In the original development of this alumina/Re growth procedure, it was suggested based on ISS and LEED measurements, that alumina growth proceeds by initial formation of 3D islands that, for thicknesses greater than 1.6 nm, coalesce to form a continuous film, as monitored by ISS, with good long-range order, as monitored by LEED.[15, 46] The ISS measurements showed no evidence of Re signal for thicknesses greater than ~1.5 nm.[30] We find that close examination of the ISS data shows that, even for films that are thick enough to completely block XPS signal from the Re support (>10

nm), there is still significant Re ISS signal, suggesting the presence of Re in the surface layer, presumably due to diffusion into the alumina at the film growth temperature. Quantitation of the Re doping is discussed below. The effect is similar to Ta-doping of alumina films grown on Ta(110).[65] Alumina films free of these metal dopants can be grown at lower temperatures, however, such films have little or no long-range order as determined by LEED.[30]

4.2.3 Characterization and reactivity measurements

After growing a suitable alumina film and depositing 0.1 ML Pd_{20}, samples were characterized by XPS at room temperature to monitor the binding energies of the Re 4f, O 1s, Al 2s, and Pd 3d peaks. As-prepared samples were also examined using UPS and ISS, however, these experiments were done on separately prepared sets of samples to avoid any possibility that ion impact damage (ISS) or adventitious adsorbates (UPS) might interfere with reactivity studies. Immediately after XPS characterization, the sample cryostat was cooled, which took ~30 minutes, at which point the samples were flashed to 560 K to desorb any adventitious adsorbates.

To test the CO oxidation activity of the samples, temperature-programmed reaction (TPR) experiments were conducted. The TPR protocol consisted of first dosing 10 L $^{18}O_2$ at 400 K followed by a 10 L dose of ^{13}CO at 180 K. The CO exposure temperature of 180 K was chosen as being high enough to avoid CO sticking to the alumina support film, and low enough to minimize reaction of impinging CO with the previously dosed $^{18}O_2$. A small amount of $^{13}C^{16}O^{18}O$ product was observed at the beginning of the ^{13}CO dose, however, this amounted to only ~2 - 3% of the total

$^{13}C^{16}O^{18}O$ produced during the TPR experiment, and at least some of that was probably from ^{13}CO reacting with ^{18}O left on the inner surface of the CO dose tube during the $^{18}O_2$ exposure.

After the O_2 and CO exposures, samples were cooled to 135 K, moved to a position 1 mm from the orifice of the mass spectrometer skimmer cone. Next, they were heated at 3 K/sec as both mass spectrometers were rapidly switched between all masses of interest, thereby probing signals for molecules desorbing from the cluster spot, and also signals for molecules desorbing from other surfaces in the analysis chamber. The masses monitored included all the isotopologs of CO and CO_2. For this study, the only masses that showed intensities above baseline were 29 (^{13}CO) and 47 ($^{13}C^{16}O^{18}O$). The absence of other CO or CO_2 isotopologs indicates that ^{16}O from the alumina film was not involved in the chemistry, and that any adventitious ^{12}CO that may have bound to the surface during deposition, XPS analysis, or sample cooling, was desorbed during the 560 K flash, or reacted away during the 400 K oxidation step. After the initial TPR measurement, two additional TPR measurements (with 400 K $^{18}O_2$ and 180 K ^{13}CO exposures) were made in quick succession, in order to examine TPR-induced changes in the model catalyst properties. Finally, the reactivity sequence was ended with a CO temperature-programed desorption (CO-TPD) experiment to probe the density and type of CO binding sites present. For CO-TPD, the sample was exposed only to 10 L ^{13}CO at 180 K, and then cooled to 135 K, and heated at 3 K/sec, monitoring the same masses as in the TPR runs. Note that for all CO-TPD measurements made, no CO_2 production was observed, suggesting that no reactive oxygen was left on the catalysts at the end of the TPR sequence.

The mass spectrometer sensitivity to desorbing CO and CO_2 was calibrated by comparison to signal intensities for known background gas densities of both molecules. Absolute CO and CO_2 desorption amounts derived from this calibration are estimated to be within a factor of 2 of the correct values, as described elsewhere.[87] To account for day-to-day fluctuations in mass spectrometer sensitivity, a daily sensitivity calibration test was performed during the cool-down time, by measuring the Ar^+ signal resulting from a known pressure of argon leaked into the analysis chamber.

After testing the reactivity, postreaction characterization was performed by XPS, UPS and ISS, to determine if any changes had occurred to the sample as a function of the reactivity studies. Changes in the XPS and UPS could infer that there was a change in the chemical environment of the catalyst. ISS, by probing the elemental composition of the top-most layer of the samples, gives insight into changes in sample morphology, such as changes cluster structure, or adsorbates left behind on the surface after reaction. Because ISS damages the samples, and UPS may expose the samples to contaminants coming from the windowless He I lamp; the order of the postreaction characterization is important. In all cases, XPS was done first and in most experiments. UPS was collected after ISS, because we were more interested in changes in morphology. In select experiments, UPS was done before ISS to verify that ISS damage did not cause significant changes in the UPS.

One point to keep in mind is that separately prepared sets of samples were used for the different types of experiments, in order to avoid complications from ISS damage, adventitious adsorbates, etc. As a result, while each type of experiment probed the same range of alumina thicknesses, the particular thicknesses studied are sometimes different.

4.3. Results

4.3.1 ISS characterization of the as-prepared Pd/alumina/Re samples

Figure 4.1a shows raw ISS spectra for various freshly prepared samples. The figure shows results for films up to 4.6 nm thick because the spectra are visually similar for thicker films. ISS results for samples after the sequence of three TPR and one TPD experiments are shown in Figure 4.1b, and will be discussed below. Consider the as-prepared results in Figure 4.1a. The top spectrum is for the freshly cleaned Re(0001) substrate, showing a large peak for He^+ scattering from Re, as well as barely-noticeable signal in the E/E_0 range expected for ^{16}O. This reflects the presence of a small amount of surface oxygen. Because the next step in sample preparation was oxidation with $^{16}O_2$, no attempt was made to eliminate this small ^{16}O impurity. Note that this spectrum has been scaled by a factor of 0.125, because He^+ scattering from Re is quite intense.

The rest of the spectra are for samples with 0.1 ML Pd_{20} deposited. The "Pd/Re" spectrum has Pd_{20} deposited directly on freshly annealed, unoxidized Re(0001), and is scaled by a factor of 0.25. For this spectrum, peaks are observed both for Pd and Re, and the weak signal for ^{16}O is more apparent due to the larger scale factor. It is interesting that in this spectrum, the Re peak intensity is only about half that in the top spectrum (note change in scaling), i.e., deposition of Pd_{20} attenuates signal from the Re substrate more strongly than might be expected from the 0.1 ML equivalent Pd coverage. Pd_{20} is expected to completely attenuate ISS from Re directly underneath the cluster footprint, but apparently there is substantial additional attenuation from some combination of shadowing and reduced He^+ ion survival probability for He^+ scattering off Re immediately surrounding the clusters.

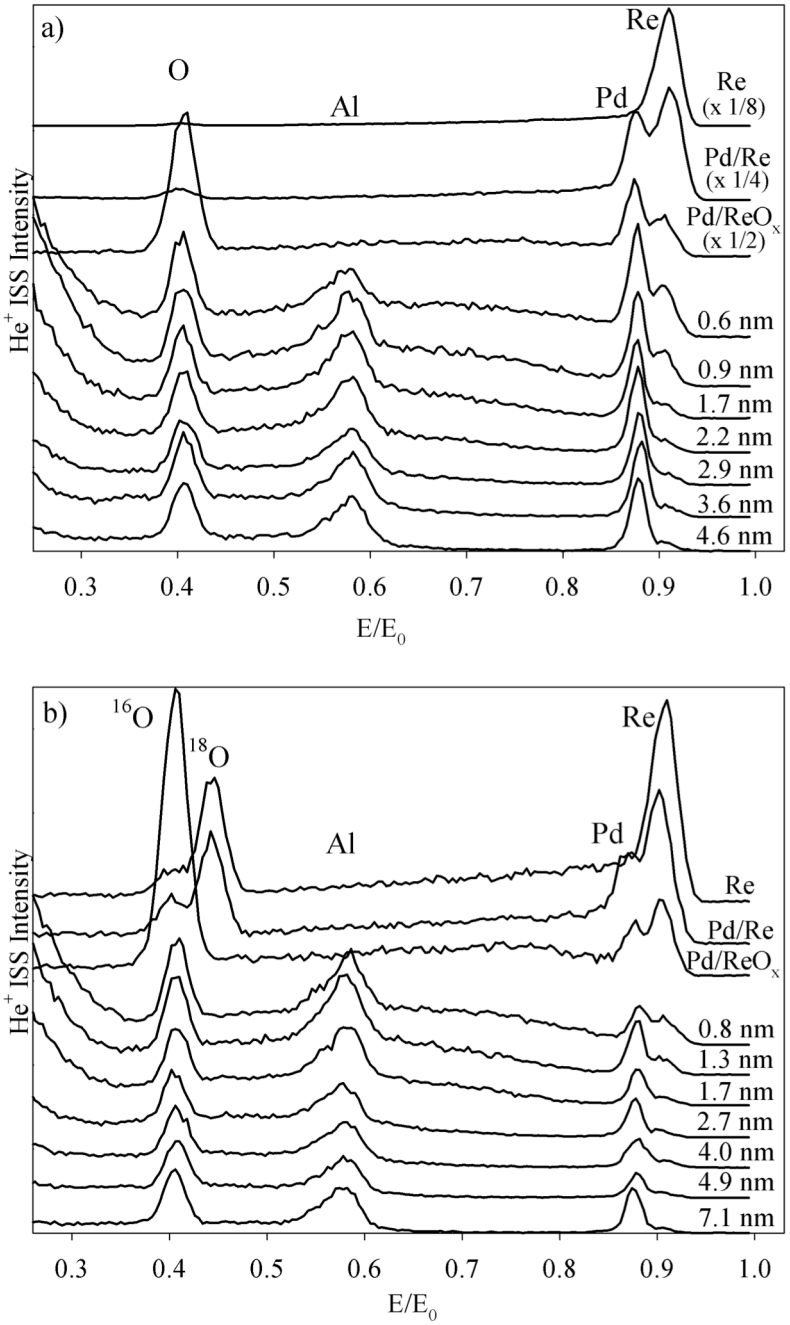

Figure 4.1: He^+ ISS for Re(0001), 0.1 ML Pd_{20} on Re(0001), and 0.1 ML Pd_{20} on alumina films of increasing thicknesses. (a) Freshly deposited samples. (b) Postreaction. Note scale factors for the first three spectra in frame a. Peaks centered at 0.40, 0.44, 0.57, 0.88, and 0.92 correspond to ^{16}O, ^{18}O, Al, Pd and Re.

The more important spectra are for Pd_{20} deposited on oxidized samples with variable thickness alumina films. The "Pd/ReO_x" spectrum is for Pd_{20} deposited on Re that was oxidized under the same conditions used for alumina film growth, but without aluminum evaporation (Note 0.5 scaling). As expected, this spectrum shows a large peak for ^{16}O, a peak for Pd, and a peak for Re which is substantially attenuated by the presence of ^{16}O (and Pd_{20}) in the surface layer. The rest of the spectra are for Pd_{20} deposited on various thickness alumina films grown on oxidized Re(0001). Each has peaks for ^{16}O and Al, and for Pd and Re. As expected for a series of samples containing identical Pd_{20} coverage, the Pd ISS intensity is roughly constant, however, there are subtle variations, discussed below, that indicate thickness-dependent changes in sample morphology.

The Al peak intensity is essentially constant except for the films with thickness ≤ 0.9 nm, where the Al intensity decreases. Given that ISS peak intensities are primarily sensitive to atoms in the surface layer, this pattern suggests that the alumina films are discontinuous for thicknesses ≤ 0.9 nm, but are continuous for films thicker than ~1.7 nm. This conclusion is consistent with reports from the Madey[30] and Goodman[45, 46] groups who found that their films became continuous at about 1.5 nm thickness.

Even for the thickest films, there is still weak ISS signal in the E/E_0 range expected for Re. We previously showed that growth of a 0.5 nm thick alumina film on NiAl(110) was sufficient to completely attenuate Ni ISS signal from the NiAl substrate.[91] Therefore, to explain the weak Re signal remaining well past the thickness where the films are continuous, we propose that Re diffuses into the alumina film at the high growth temperature, resulting in Re surface concentrations that decrease with increasing film thickness. This situation is similar to that recently reported for CaO films grown on Mo

supports.[33] The surface layer Re concentration can be estimated by comparing the Re ISS intensity for each sample with that measured for unoxidized Re(0001), where the surface density is known. As summarized in Appendix A of the supporting information, the Re concentration is estimated to be ~0.5% for 10 nm alumina films, increasing slowly with decreasing film thickness to ~2.2% for the 1.7 nm film. For the 0.9 nm and 0.6 nm films, there is a sharp increase in the Re surface concentration, reaching ~9% for the 0.6 nm film, however, this is in the range where both the literature[30, 31, 46] and our Al ISS intensities suggest that the alumina film is no longer continuous. The sharp increase for the thinnest films is attributed to the appearance of exposed ReO_x patches between alumina islands that make up >90% of the surface.

Given the conclusion that there may be patches of ReO_x exposed for the thinnest alumina films, it is useful to know the level of Re oxidation under different O_2 exposures. The "Pd/ReO_x" spectrum in Figure 4.1a shows that exposure of Re(0001) to alumina growth conditions (~6000 L O_2 at 970 K) results in a large (~3 : 1) O : Re ISS intensity ratio, implying that the surface is heavily oxidized. Since all the alumina/Re samples received the ~6000 L, 970 K O_2 exposure during the alumina growth, any exposed ReO_x should be heavily oxidized. Exposure of unoxidized Re(0001) to the 10 L, 400 K $^{18}O_2$ exposure used in TPR also oxidizes the surface, but not as thoroughly. Figure 4.1b (spectrum "Re") has an (^{16}O+^{18}O) : Re ratio of just 1 : 1.15.

4.3.2 TPR studies of reactivity

The CO oxidation activity of the samples was studied by a sequence of TPR experiments, followed by a final CO TPD experiment. For each TPR run, the sample was

exposed to 10 L $^{18}O_2$ at 400 K, followed by a 10 L ^{13}CO exposure at 180 K, then cooled to ~135 K before starting a 3 K/sec TPR heat ramp. All possible isotopologs of CO, CO_2, water and O_2 were monitored, but under these conditions, the only significant desorption signals were for unreacted ^{13}CO and the expected $^{13}C^{16}O^{18}O$ product. The TPR process (O_2 and CO exposures, 3 K/sec heating) was repeated twice to probe the stability of the samples under heating and adsorbate exposure, and then a final CO TPD run was done (only CO exposure, 3K/sec heating). The $^{13}C^{16}O^{18}O$ desorption in the first of the three consecutive TPR measurements for select samples is shown in Figure 4.2a, and Figure 4.2b summarizes the integrated $^{13}C^{16}O^{18}O$ production in the three TPR runs as a function of alumina film thickness.

The top trace in Figure 4.2a shows results that the alumina films are inert under these conditions. The second spectrum shows another control experiment, demonstrating that there was also no CO oxidation catalyzed by the Re(0001) support. As discussed above, the $^{18}O_2$ exposure used in TPR results in significant oxidation of the Re(0001) surface, but this oxygen is evidently too strongly bound to react with CO, which also adsorbs on this sample (see below).

When Pd_{20} was deposited directly on unoxidized Re(0001), there was substantial $^{13}C^{16}O^{18}O$ production during the first TPR run (Figure 4.2a - "Pd/Re"), amounting to ~0.25 molecules *per* Pd atom on the surface. In subsequent TPR runs on this sample, the $^{13}C^{16}O^{18}O$ signal decreased by ~50% *per* run (solid points in Figure 4.2b for zero film thickness). The postreaction ISS in Figure 4.1b shows that for the "Pd/Re" sample, the Pd intensity was significantly lower after reaction compared to the as-prepared sample, i.e., the fraction of Pd in the surface layer was decreased. Since the TPRs only involved

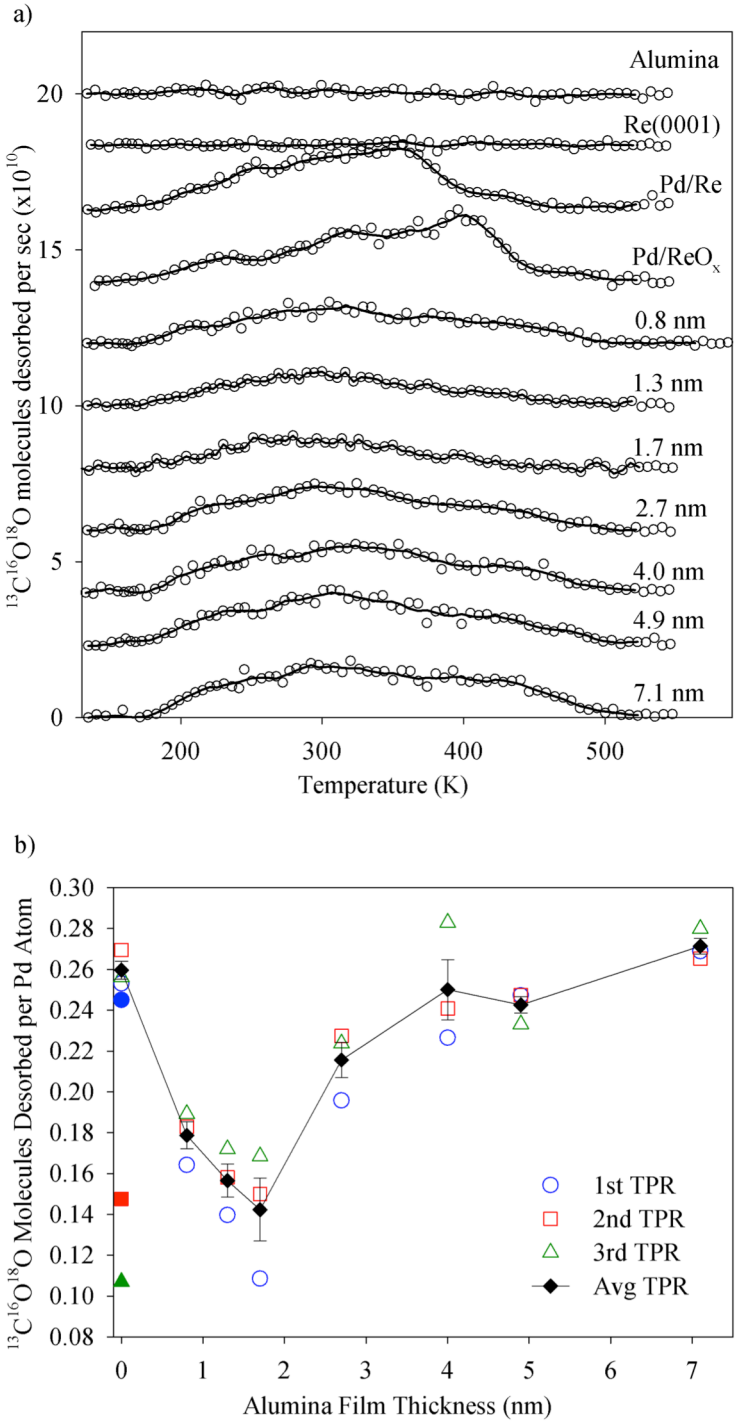

Figure 4.2: Raw and integrated $^{13}C^{16}O^{18}O$ desorption signal from TPR measurements are presented. (a) $^{13}C^{16}O^{18}O$ signal temperature dependence measured in the first TPR cycle on the indicated samples (see text for explanation). (b) Integrated $^{13}C^{16}O^{18}O$ signals measured during three consecutive TPR runs, along with the average from the three runs. The solid points at zero alumina thickness are for Pd_{20} deposited on unoxidized Re(0001), and the open points are for Pd_{20} deposited on oxidized Re(0001).

heating to 550 K, evaporation of the Pd is unlikely, therefore both the loss of CO oxidation activity and of Pd ISS intensity are attributed to changes in Pd morphology, which could include processes such as sintering or Pd dissolution into the Re bulk. We note that when Pd_n was deposited on an unoxidized Ta(110) surface at room temperature, ISS showed no Pd in the surface layer, demonstrating that diffusion into the bulk can be rapid, even for refractory metals at modest temperatures.[65]

As noted above, the thinnest alumina films are thought to be discontinuous, exposing small patches of ReO_x. To probe the chemistry of Pd_{20} on such oxidized Re areas, Figure 4.2a also shows $^{13}C^{16}O^{18}O$ production from Pd_{20} deposited on ReO_x prepared by exposing Re(0001) to ~6000 L O_2 at 970 K. This "Pd/ReO_x" sample has integrated $^{13}C^{16}O^{18}O$ production activity of ~0.26 CO_2/Pd atom, which can be attributed to activity of the supported Pd_{20}, since the oxidized Re is inert. The CO_2 signal from Pd_{20}/ReO_x is quite stable from run to run, as shown by the open points at zero thickness in Figure 4.1b. Evidently, the heavily oxidized ReO_x surface provides a stable support, possibly because the oxide layer is thick enough to block diffusion into the bulk.

The rest of the figure shows data for a selection of samples prepared by depositing 0.1 ML Pd_{20} on various thickness alumina films grown on Re(0001). It can be seen in Figure 4.2a, that the Pd_{20}/alumina samples are all active for $^{13}C^{16}O^{18}O$ production, and that even for the thinnest films, the temperature dependence for $^{13}C^{16}O^{18}O$ desorption is quite different from those for Pd_{20}/Re or Pd_{20}/ReO_x. For all Pd/alumina samples, $^{13}C^{16}O^{18}O$ desorption occurs in a broad, essentially structureless feature, starting at 180 K, peaking near 300 K, and extending to just over 500 K. CO_2 was not observed to stick to Pd_{20}/alumina/Re at 180 K, suggesting that the temperature dependence of the CO_2

signal reflects the kinetics of $^{13}C^{16}O^{18}O$ formation from adsorbed ^{13}CO and ^{18}O (or $^{18}O_2$), rather than the energetics for desorption of the CO_2 product. It is interesting that all the Pd_{20}/alumina/Re samples give such similar temperature dependences, despite the suggestion from ISS that there is significant ReO_x exposed in the 0.8 nm alumina film (Appendix A). No signal is seen for the 400 K $^{13}C^{16}O^{18}O$ desorption peak that dominates the TPR for Pd/ReO_x.

In Figure 4.2b it can be seen that the activity is reasonably stable from run to run, increasing slightly in successive TPR runs for samples with ≤ 4 nm alumina films. One of the interesting features shown in Figure 4.2b is that with increasing alumina thickness, the CO oxidation activity initially decreases sharply, passing through a minimum for films around 2 nm, and then increases to a thickness-independent level for films thicker than ~4 nm. Understanding the mechanistic origins of this modulation of activity in the 1 – 4 nm thickness range, is one of the main goals of this study.

Desorption of CO provides a different probe of the samples' chemical properties. Figure 4.3a shows the desorption of residual, unreacted ^{13}CO during the first TPR run on each sample. Figure 4.3b shows ^{13}CO desorption during the final CO TPD experiment run after the three TPRs. As with the CO_2 desorption data, we show only a selection of the results for the Pd_{20}/alumina/Re samples. For alumina grown on Re(0001), no CO desorption is observed in either the TPR or TPD experiments, indicating that CO simply does not stick on the alumina support. For Re(0001), where there was no CO_2 production in TPR, the adsorbed ^{13}CO is seen to desorb mostly in a strong feature between 180 K and 280 K, presumably corresponding to CO on terrace sites (note x0.05 scaling). There is also a weak feature near 425 K, tentatively attributed to CO bound to steps or defects.

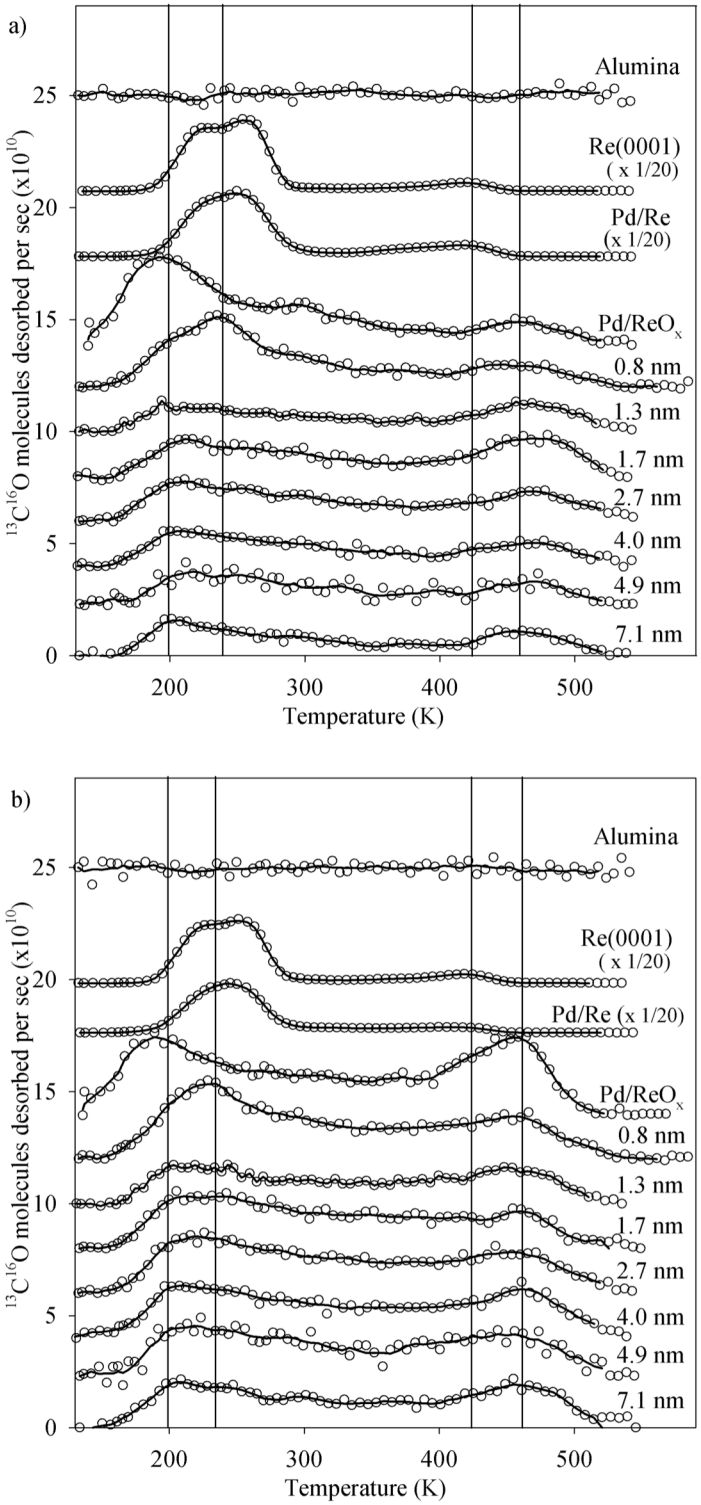

Figure 4.3: CO desorption from various substrates are presented. (a) Desorption temperature dependence for unreacted CO in the first TPR run on each of the indicated samples. (b) Desorption temperature dependence for CO in a final CO TPD run on each sample, made after the set of three TPR runs.

Again, this surface would have been somewhat oxidized during the 10L $^{18}O_2$ exposure used in TPR, but that oxygen is apparently too stable to react with CO, leaving it all to desorb unreacted. Deposition of 0.1 ML of Pd_{20} on the Re surface has little effect on the CO desorption, presumably because the coverage is low and CO sticks efficiently to the Re surface.

For Pd_{20} deposited on heavily oxidized Re ("Pd/ReO_x"), the total amount of CO desorbing is much lower, and peaks just above the 180 K CO dose temperature, with a long tail connecting to weak desorption features peaking near 300 and 460 K. The weak intensity, and the observation that the main peak occurs just above the dose temperature, suggests that that desorption temperature for CO bound to ReO_x terraces is below the 180 K dose temperature, and that we are only observing CO desorbing from Pd_{20} and from defect sites on the ReO_x support. The fact that CO binding to ReO_x is weak, and that CO does not stick at all to alumina/ReO_x is useful from the perspective of allowing CO desorption from Pd_{20} to be observed clearly. For these control samples, the desorption observed in the final CO TPD (Figure 4.3b), after completion of the reaction sequence, is generally quite similar to that observed in the first TPR (Figure 4.3a), with the exception of the Pd/ReO_x sample, where there was a significant increase in the desorption near 460 K.

The Pd_{20}/alumina/Re samples show residual CO desorption during TPR (Figure 4.2a) in two broad components, peaking at ~200K and at ~460K. CO desorption from $Pd_n/TiO_2(110)$ and Pd_n/alumina/Ta(110) is also bimodal, and in those systems we used temperature-dependent ISS to probe the nature of the CO binding sites, with the result that the low temperature binding feature was found to be primarily associated with CO

bound at the periphery of the clusters, while the high temperature feature was primarily associated with CO desorbing from sites on top of the clusters.[85, 87, 92] The integrated amount of unreacted CO desorbing during TPR is weakly dependent on alumina thickness, ranging from ~0.26 CO/Pd atom (5.2 CO/Pd_{20}) for samples in the 1.5 to 3 nm range, decreasing to ~0.22 CO/Pd atom (4.4 CO/Pd_{20}) for the thicker films.

For the sample with alumina thickness of 0.8 nm, the desorption behavior is slightly different, as might be expected since the thinnest films are thought to be discontinuous,[30, 45, 46] exposing some ReO_x. Somewhat surprisingly, however, the temperature dependence is not what might be expected for Pd_{20} on alumina with a small fraction of Pd_{20} on ReO_x, the latter of which might be expected to result in a lowered onset temperature for CO desorption. Instead, the low temperature CO desorption feature appears to have "extra" intensity around 230 K, and as a result, the integrated CO desorption increases to ~0.31 CO/Pd atom, compared to 0.26 to 0.22 CO/Pd for the thicker films. It is not clear where this extra CO is binding, but discontinuous films may provide CO binding sites at alumina-ReO_x boundaries, or on Pt_{20} deposited at such boundaries. In addition, we will show that the electronic properties of both the alumina and the deposited Pd_{20} are strongly dependent on alumina thickness, which may lead to additional CO binding. Whatever the origin, the absence of this 230 K feature for all the samples with thicker films suggests that the alumina films become continuous above ~1.3 nm thickness, in reasonable agreement with both the ISS results and the literature.

If we assume that oxidation and desorption are the only two channels consuming adsorbed CO during TPR, then the sum of the desorption signals for CO_2 and CO provides an estimate for the total amount of CO adsorbed under TPR conditions, i.e., with

pre-adsorbed oxygen. Total CO is found to be roughly constant at ~0.48 CO/Pd atom for samples with alumina films of ≥ 3 nm thickness, corresponding to ~10 CO molecules adsorbed per Pd_{20} cluster. Because the ~50% dip in CO_2 production for alumina films in the 0.8 to 2 nm thickness range (i.e., 10 CO/Pd_{20}) is partially offset by an increase in desorption of residual CO, the total CO adsorption only drops to ~0.4 CO/Pd (8 CO/Pd_{20}). The ratio of integrated intensities for CO_2/(CO+CO_2) is essentially the efficiency with which adsorbed CO is converted to CO_2, and it ranges from ~34% in the 0.8 to 2 nm range, to ~52% for Pd_{20} on thick alumina films. Finally, from the amount of CO_2 produced, we can estimate lower limits on amount of active oxygen bound to the samples after the 400 K 10 L O_2 exposure, which vary from 3 to 5 O atoms per Pd_{20}, depending on film thickness.

In the final TPD measured after the series of TPR runs, the CO desorption observed for the Pd_{20}/alumina/Re samples (Figure 4.3b), is qualitatively similar to that observed in the first TPR, with broadly bimodal desorption and similar peak temperatures. The main difference is that in the final CO TPD, the integrated amount of CO desorbing is ~70% higher, approximately independent of alumina film thickness. An increase is not surprising, and is attributable to two factors. In TPR, 34 to 52% of the initially adsorbed CO is converted to CO_2, but this competing channel is absent in TPD. In addition, we might expect that the O_2 exposure used in TPR might block CO adsorption sites, further reducing the amount of residual CO desorption.

As noted, one of the main goals of this study is to explore the factors that cause the ~50% dip in CO oxidation activity for alumina films with thicknesses between ~0.8 and 3 nm. This behavior suggests that film thickness might be a useful parameter for

tuning catalyst properties, however, our main interest is in using thickness-dependent correlations between activity and other properties of the samples, as a mechanistic probe. One obvious potential correlation is between activity and CO desorption, since both depend on the number and energetics of binding sites on the samples. To separate the low and high temperature desorption components, each TPR and TPD spectrum was fit, as shown in Appendix A. We looked for various correlations, and the two that emerged are shown in Figure 4.4. Activity is found to be inversely correlated with the integrated intensity of the high temperature component of residual (unreacted) CO desorbing during TPR (note inverted scale). Such an anticorrelation is not surprising, because CO oxidation is in competition with desorption of residual CO. The more interesting observation is that there is a strong positive correlation of activity with the high temperature component of CO desorbing in the final TPD. The implications of this correlation will be discussed below.

4.3.3 ISS studies of adsorbate binding and the effects of the reaction sequence

ISS can also be used to probe the nature of adsorbate binding to samples, and is sensitive to both the number and binding geometries. Here, ISS was used to probe oxygen and CO binding, although only a few such experiments were done because each required preparation of several fresh samples to avoid ISS induced damage. Typical ISS data for as-deposited Pd_{20}/alumina/Re (Figure 4.1a) have peaks for O, Al, Pd, and a small shoulder for Re in the alumina film. The 10 L, 400 K O_2 exposure used in TPR was found to cause no change in O, Al, or Re intensities, but oxidation did result in a 15 -

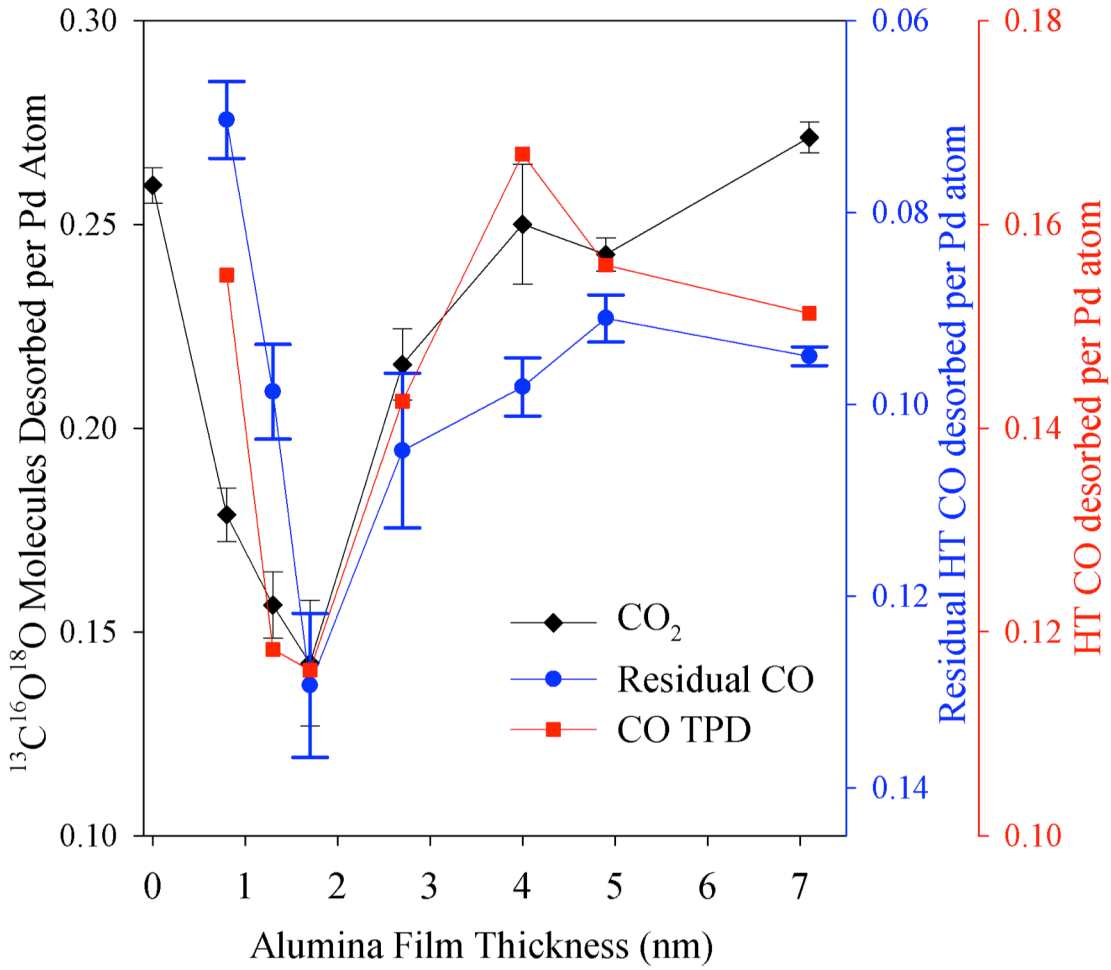

Figure 4.4: CO and CO_2 desorption from Pd_{20} deposited on various thickness alumina films. Black: Integrated CO_2 production averaged over the three TPR measurements on each sample, as a function of alumina film thickness. Blue: Integrated desorption of unreacted CO from the high temperature binding site, averaged over the three TPR runs (note inverted scale). Red: CO desorbing from the high temperature binding site in the final CO TPD run, after the set of TPR runs.

20% attenuation of the Pd intensity. This can be contrasted to a ~70-80% attenuation of Pd signal by the 10 L 180K CO exposure used in TPR. From the CO_2 desorption in TPR (Figure 4.2b), we can estimate that the average number of active O atoms per Pd_{20} ranged from 3 to 5, with the smaller number for samples with alumina thicknesses between 0.8 and 2 nm. From sum of CO_2 and unreacted CO desorption, we can estimate that the total adsorbed CO is roughly thickness-independent at ~10 CO/Pd_{20}.

Adsorbate attenuation of ISS signals results from three effects.[93, 94] Adsorbates bound on top of the surface prevent He^+ scattering from surface layer atoms that lie within shadow cones cast by the adsorbate atoms. In our geometry, these shadow cones are cast at 45° with respect to the surface normal. Another attenuation process is blocking, where He^+ scatters from a Pd atom, but then is prevented from reaching the detector because an adsorbate atom lies in between the scattered He^+ and detector. Since we detect along the surface normal, blocking occurs if adsorbates are bound in atop sites. Finally, when He^+ trajectories pass through the electron cloud of adsorbates, neutralization can occur, reducing the ion survival probability (ISP), and thus ISS signal. All three mechanisms will tend to attenuate Pd ISS signal for adsorbates bound on top of the Pd_{20} clusters, but cause little effect for adsorbates binding to the surrounding alumina support.

The 15 to 20% Pd ISS attenuation observed from adsorption of 3 to 5 O atoms per Pd_{20} implies that each O atom attenuates signal from roughly one Pd atom. This strong attenuation is consistent with oxygen binding on top of the clusters, but does not allow us to distinguish between atop, bridge, or hollow sites. The larger attenuation from CO exposure reflects the fact that CO has two atoms, each casting shadow cones and having

an electron cloud that decreases ISP. In addition, CO sticks efficiently to Pd, essentially saturating the clusters with 10 CO molecules in addition to the 3 to 5 O atoms *per* Pd_{20}. As noted above, if CO exposure is done without pre-adsorbed O, ~70% more CO sticks, and the Pd ISS remains strongly attenuated. In fact, temperature-dependent ISS experiments on $Pd_n/TiO_2(110)$[85] and Pd_n/alumina/Ta(110),[87] which show bimodal CO desorption profiles similar to those in Figure 4.3, suggest that only CO desorbing in the high temperature component is bound on top of the clusters, and the low temperature CO desorption occurs from peripheral sites.

Several interesting features are also observed in the postreaction ISS characterization (Figure 4.1b). Note that for the Re and Pd/Re samples, new peaks are observed corresponding to ^{18}O on the surface, resulting from oxidation of the Re by the 10 L 400 K $^{18}O_2$ exposure. In contrast, no ^{18}O signal is observed for Pd/ReO_x, or for any of the Pd/alumina/Re samples, indicating that both the alumina and ReO_x films are stable with respect to oxygen exchange, and that there is no significant spillover of unreacted ^{18}O from the Pd clusters to the oxide supports. The Pd ISS intensities in the postreaction samples are all somewhat smaller than in the analogous as-prepared samples, showing that the fraction of Pd in the surface layer was reduced. Such decreases can result from reaction-induced sintering of the clusters. However, in this case they simply result from accumulation of adventitious adsorbates on the Pd, because ISS was done after XPS, during which time (20 minutes) the samples were at ~120 K. Supported cluster samples are highly efficient at binding adsorbates via a substrate-mediated process where molecules (e.g., CO) initially bind (weakly) to the alumina support, but diffuse to stable binding sites on the Pd clusters.[83, 85, 87] The presence of such adsorbates can be verified,

and corrected for, by analysis of Pd ISS intensity vs. exposure to the He^+ beam, which preferentially sputters adsorbates.[85, 94] We did this analysis for Pd_n/alumina/Re as part of a study of cluster size effects, and after correction for adsorbates, the Pd signals before and after reaction were found to be identical.[87]

4.3.4 Sample electronic properties as a function of alumina thickness

The electronic structure of the as-prepared alumina films and films with supported Pd_{20} were characterized using a combination of UPS and XPS. The raw UPS for a selection of samples are shown in Figure 4.5a with the binding energy (BE) scale referenced to the Fermi level (E_F) of the Re(0001) support. The spectra are broken into three segments, plotted with different intensity scaling in order to show the important features more clearly. The region near E_F is plotted with 4.5x magnification of the intensity scale, to allow the weak signals to be observed more clearly. The region between 4 eV and 8 eV shows the onset and peak of the alumina valence ("O 2p") band, which dominates the spectra. In this energy range, the energy axis has been expanded slightly to allow the small shifts to be observed more clearly. The region between 8 and 14 eV is omitted because it simply shows a slow decline of the alumina valence band. Finally, the region above 14 eV is plotted on a 100x expanded intensity scale, with the energy scale also expanded to allow shifts in the high BE spectral limits to be observed more clearly. The high BE spectral limits can be used to calculate the sample work functions: $\Phi = h\nu - BE_{limit}$, where Φ is the sample work function, $h\nu$ is the photon energy (21.21 eV), and BE_{limit} is the high BE spectral limit. The work function results are

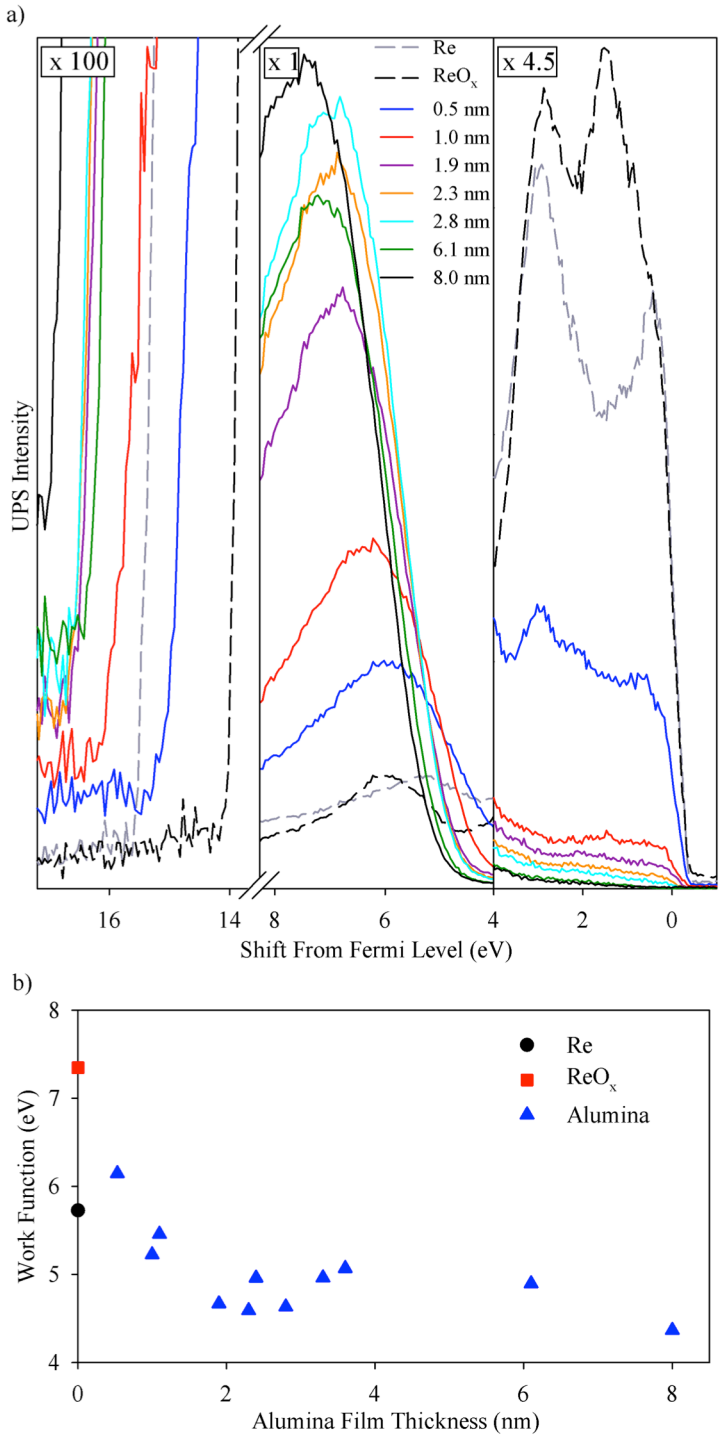

Figure 4.5: A collection of UPS spectra and work functions is presented for samples of varying alumina film thickness. (a) UPS spectra taken for Re(0001) with various thicknesses of alumina films. The spectra have been broken into three energy ranges in order to show features of interest more clearly by applying different scale factors. Spectra are shown for clean Re(0001), Re(0001) after oxidation, and for oxidized Re(0001) with alumina overlayers of the indicated thicknesses. (b) Work functions determined from the high energy cut-off of each spectrum.

summarized in Figure 4.5b.

The spectrum for freshly cleaned Re(0001) has a sharp onset at E_F, little signal in the O 2p region, and $BE_{limit} \approx 15.47$ eV, implying $\Phi \approx 5.72$ eV. This measured Φ is ~0.75 eV higher than literature value reported[95] for Re(0001), and we attribute the difference to the presence of a small amount of surface oxygen on the as-prepared Re(0001) (Figure 4.1a). For the oxidized Re support ("ReO_x"), there is still a sharp onset at E_F, with additional structure both in the near-E_F and O 2p regions, reflecting Re-O binding. BE_{limit} decreases to 13.85 eV, corresponding to an oxidation-induced increase in Φ to ~7.35 eV.

For alumina/Re samples, the spectra change systematically with alumina thickness. In the near-E_F region, the signal from the underlying Re substrate decreases rapidly with increasing film thickness, because Re photoelectrons are attenuated during passage through the alumina film. For the thicker films, there is little intensity remaining in the alumina band-gap region, between E_F and ~4.5 eV. As expected, the alumina valence (O 2p) band intensity increases with thickness, then becomes nearly thickness-independent for films thicker than ~3 nm. There are also slight shifts in the onset and peak energies of this feature. With increasing alumina thickness, BE_{limit} also increases, implying a gradual decrease in the sample work function from ~6 eV for the thinnest films to 4.37 eV for the 8 nm film.

The UPS and XPS results for the alumina valence and core levels of the as-prepared samples are summarized in Figure 4.6a, and results are given for samples with, and without Pd_{20} deposited. Because the alumina valence band is quite broad, what is plotted is actually valence band onset energy, i.e., the BE at the top of the valence band,

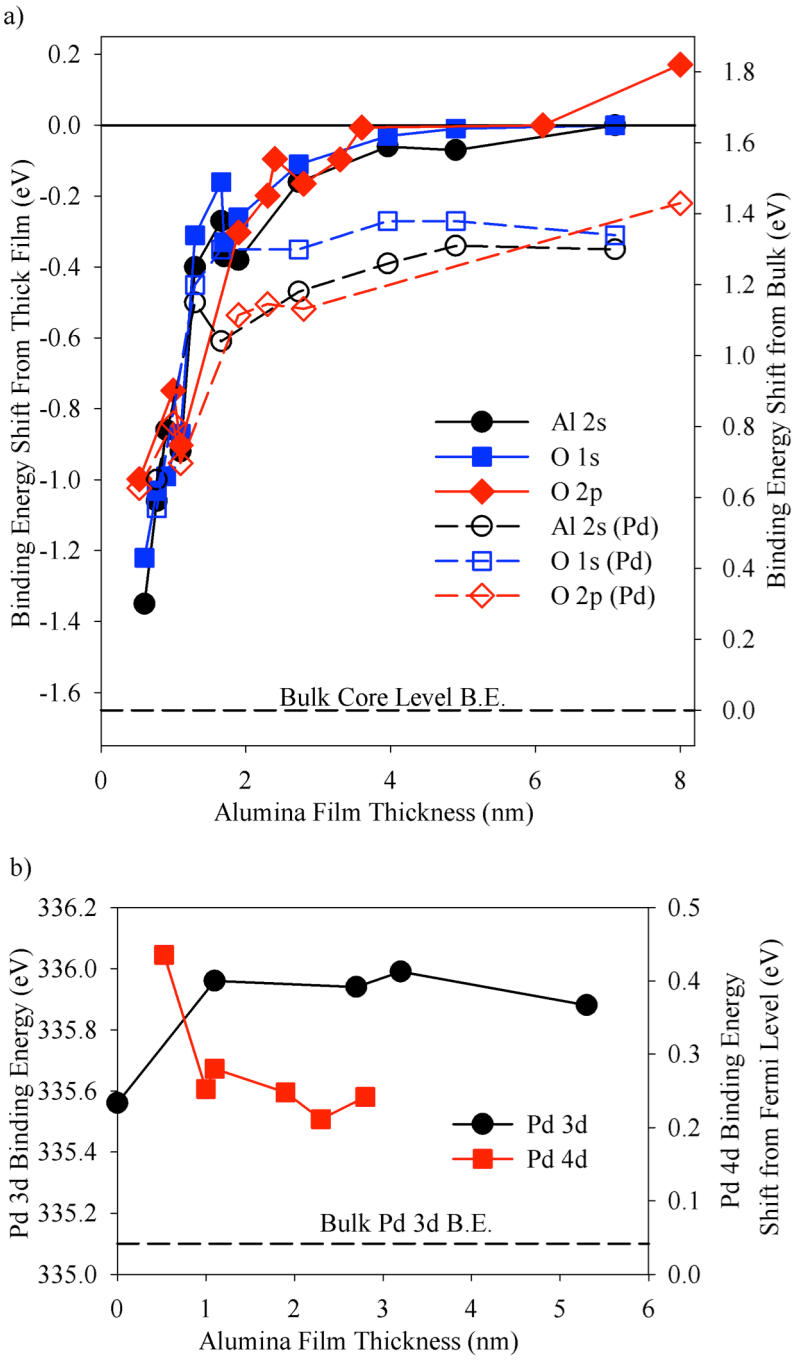

Figure 4.6: Core and valence level binding energies are presented for samples of varying alumina film thickness. (a) Shifts in binding energies for the Al 2s and O 1s core orbitals as well as the O 2p valence level as a function of alumina film thickness. The left scale shows the shift relative to binding energies measured for the thickest film where no charging occurred. The right scale shows shifts relative to bulk alumina. (b) The Pd 3d core level binding energy and the top of the Pd 4d valence band as a function of alumina thickness, relative to the sample Fermi level.

which was estimated using a method suggested by Parkinson and Schlaf.[96, 97] The rising edge of the band was fit to a Gaussian-convoluted step function, and then the slope at the inflection point was extrapolated to baseline to estimate the onset energy. To allow all the results to be plotted together, the figure plots *shifts* in the BEs, and scales are provided for shifts relative to both literature BEs for bulk alumina, and to the limiting BEs measured here for thick alumina films. For both core and valence BEs, the "thick film limit" was taken as the thickest film where there was no evidence of charging during photoemission. Because different sets of samples were used in the XPS and UPS work, this was the 7.1 nm film for XPS data, and a 6.1 nm film for UPS. The increase in BEs for the 8 nm film is a sign that charging is significant for such thick films. Note that the offset between the thick film and bulk limits (1.65 eV) is the average of the measured shifts for the O 1s and Al 2p levels (1.7 eV and 1.6 eV, respectively).

The valence and core levels of the alumina films show remarkably similar shifts with changing alumina thickness. For films thicker than ~3 nm, the BEs are essentially thickness-independent, and shifted by 1.65 eV with respect to bulk alumina. For thinner films, the BEs decrease, but remain well above the bulk alumina limit, even for the thinnest films. Deposition of 0.1 ML of Pd_{20} reduces both the core and valence BEs associated with the thicker alumina films by ~0.4 eV, but has little effect on the alumina BEs for films thinner than ~1.2 nm.

In addition to measuring the electronic properties of the alumina support film, we also used UPS and XPS to characterize both valence and core levels of the deposited Pd_{20} as a function of the alumina thickness. An example of raw UPS for alumina/Re and Pd_{20}/alumina/Re is shown in Appendix A. The alumina discussed in that section was 2.8

nm thick, and only weak and featureless signal was observed in the alumina band gap, between E_F and the top of the alumina valence band at ~4.5 eV. Upon Pd_{20} deposition, weak signal was clearly seen in the band gap region, and the ~0.4 eV deposition-induced shift in the alumina valence band was also noticeable. The Pd signal was analyzed by subtracting out the spectrum measured for the alumina/Re substrate (inset), and then the onset of the Pd band was extracted using the same fitting/extrapolation method used to analyze the alumina valence band.

The Pd 3d core level BEs and onset energies of the Pd valence band are summarized in Figure 4.6b. For Pd_{20} deposited directly on either Re(0001) or on ReO_x, the Pd 3d BE is ~335.5 eV, i.e., essentially identical to that for bulk Pd. For Pd_{20} deposited on alumina/Re, the binding energies are shifted to ~336.0, with no obvious trend with varying film thickness. These measurements have relatively large uncertainty (~±0.2 eV) due to low Pd signal from 0.1 ML coverage, and background from inelastic scattering of 4d photoelectrons from the Re support. The observation that the BEs for Pd_{20}/alumina are greater than that for bulk Pd could be taken as evidence for electron transfer from Pd to alumina, however, as discussed below, we believe that the Pd actually accepts electrons from alumina. Instead, the positive BE shifts reflect reduced final state screening for small clusters supported on an insulating layer.[98-102]

For films thicker than ~1 nm, the onset of the Pd valence band is 0.25 ± 0.04 eV below E_F, i.e., the Pd_{20}/alumina samples still have a band gap, essentially independent of alumina film thickness. The onset energy for the sample with Pd_{20} deposited on a 0.5 nm alumina film, is apparently shifted ~0.2 eV to higher binding energy. However, for such a thin film there is still substantial intensity in the band gap region from the Re substrate

(Figure 4.5a), resulting in high uncertainty for the subtraction/fitting analysis used to extract the Pd valence band onset. Within the uncertainty, therefore, neither the core nor valence levels shift significantly with alumina thickness, even though the alumina levels, themselves, shift by more than 1 eV.

The inset to Figure 4.7 compares the Pd 3d BEs for as-deposited samples, with those measured after a 10 L $^{18}O_2$ exposure identical to that in the first step of the TPR experiments. As expected for an oxidation reaction, the Pd BEs shift to higher energy, but the amount of the shift is dependent on the alumina thickness. As shown in the main frame of Figure 4.7, the thickness dependence of this oxidation-induced core level shift appears to be correlated with the CO oxidation activity. We have only two data points for oxidation-induced shifts in the onset energy of the Pd valence band, but the valence band shifts also appear to correlate with activity.

The observed changes in alumina BEs with thickness (Figure 4.6a) are signatures of thickness-dependent variations in sample electronic properties, and are not simply artifacts of sample charging under the VUV or X-ray beams. If beam-induced charging were significant in this thickness range, then the core and valence BEs of the Pd_{20} deposited on the films should show shifts similar to those of the alumina support, rather than being essentially thickness-independent (Figure 4.6b). Furthermore, the alumina XPS peak widths should tend to increase with thickness due to differential charging, whereas widths actually decrease. Only for films thicker than ~8 nm do we begin to see obvious signs of beam-induced charging (increasing BE shifts and peak broadening).

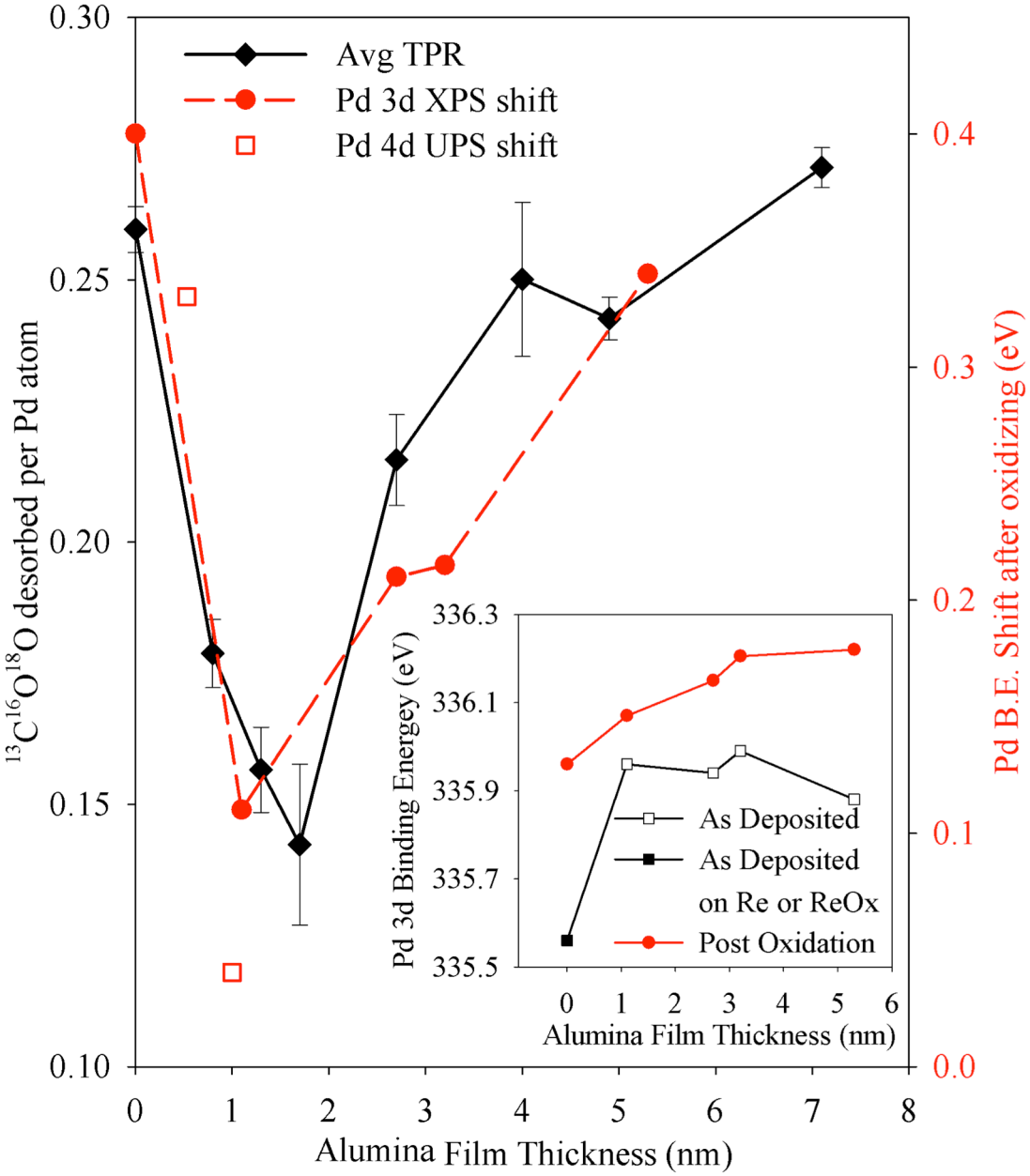

Figure 4.7: Inset: Raw Pd 3d binding energies for as-deposited Pd_{20}, and after exposure to 10 L $^{18}O_2$ at 400 K. Main figure: The shift in Pd 3d and 4d binding energies from O_2 exposure are compared to the CO oxidation activity over a range of alumina thicknesses.

4.3.5. Correlation between Pd ISS intensity and activity

Figure 4.8 shows another correlation of activity with a physical property of the samples. As mentioned above, there is a weak dependence of the as-deposited Pd ISS intensity on the thickness of the alumina film on which Pd_{20} is deposited. As Figure 4.8 shows, the Pd ISS intensity, proportional to the fraction of Pd atoms in the surface layer, has dependence on thickness that correlates well with the thickness-dependent CO oxidation activity. Note that the as-deposited Pd ISS intensities in this figure are not simply the ISS peak intensities from Figure 4.1a, although the thickness dependence there is quite similar. The intensities have been corrected for the effects of any adventitious adsorbates that might have bound to Pd during deposition, using a process discussed elsewhere,[83, 85] in which the Pd intensity is monitored as a function of He^+ flux, and extrapolated back to the limit of zero exposure and zero adsorbate coverage. It is not surprising that a smaller number of Pd surface sites would be correlated with lower activity, however, the ISS intensity only dips by ~14% at the minimum, compared to a ~50% reduction in activity. Clearly the decrease in activity is not simply a Pd surface area effect.

4.4. Discussion

At this point, we have used the ability to vary the alumina thickness to show correlations of activity with Pd ISS intensity, with the density of particular CO binding sites, and with the shift in Pd BEs upon O_2 exposure. Correlation does not imply causation, and in the discussion below we attempt to show how these observations are interrelated and what they tell us about the factors responsible for the thickness-

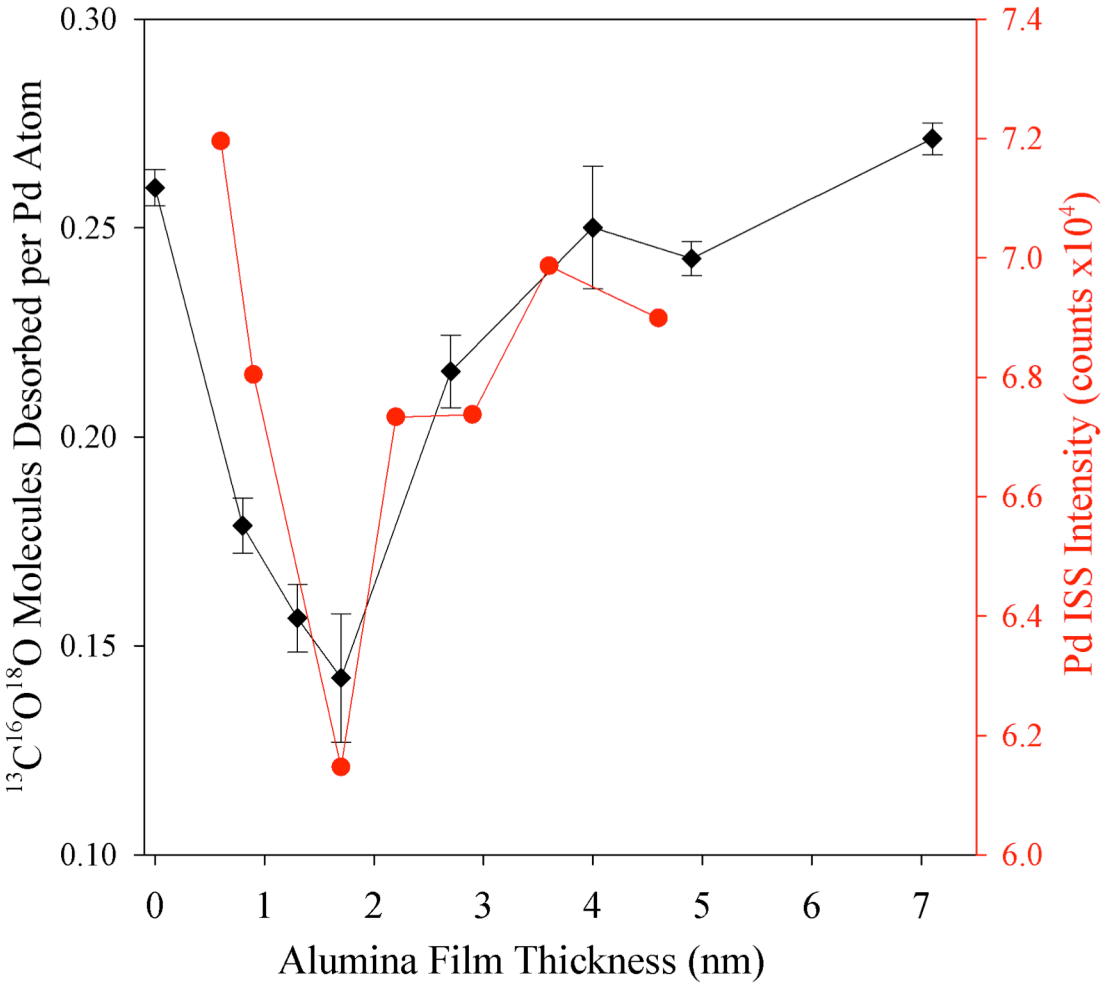

Figure 4.8: Comparison of CO_2 production activity (black – left axis) and Pd ISS intensity (red – right axis) as a function of alumina thickness.

dependent activity.

4.4.1 Rate limiting factors under TPR conditions and thickness correlations.

The interpretation of the activity correlations depends on the reaction mechanism, i.e., the rate-limiting factors under our TPR conditions. Fortunately, CO oxidation over Pd single crystals[66, 68, 69, 78, 103, 104] and various supported Pd nanoparticle samples[105-109] has been well studied, and there is considerable mechanistic information available. The factors limiting activity are strongly dependent on reaction conditions. For example, CO sticks efficiently and binds stably to Pd over a broad temperature range, while O_2 sticking and activation are less efficient, although binding is strong.[9, 84, 110, 111] When CO and O_2 are both present, the two reactants compete for Pd binding sites.[68, 69, 78] Therefore, at low temperatures the Pd sites tend to rapidly become poisoned by CO, and the lack of adsorbed oxygen limits CO_2 production under many conditions. Under steady-state reaction conditions, Pd catalysts are typically not active until the temperature is raised to the point where the CO lifetime on the Pd sites becomes short enough to leave sites available for O_2 adsorption. The TPR protocol used here was done with both O_2 and CO exposures at relatively low temperatures (to minimize thermal effects on the clusters), but the O_2 exposure was done first, precisely to avoid CO poisoning. For sufficiently large O_2 exposures, oxygen coverage can become large enough to block sites needed for CO adsorption, thereby reducing activity[84] and the 10 L exposure used here was chosen to avoid this issue as well. The 10 L CO exposure is sufficient to saturate any Pd sites left unoccupied after the oxygen exposure, and the 180 K CO exposure temperature was

chosen as being low enough to minimize reaction of the pre-adsorbed oxygen with impinging CO, but high enough to avoid CO binding to the alumina support (Figure 4.3). CO_2 production is monitored during the CO dose, and never amounts to more than a few percent of the total CO_2 produced in a TPR cycle.

Several factors indicate that under our TPR conditions, the availability of adsorbed active oxygen is the factor limiting CO_2 production. For the more active catalysts (i.e., Pd_{20} on either ReO_x or on thick alumina films), comparison of the desorption signals for CO_2 and unreacted CO shows that only ~50% of the adsorbed CO reacts, the rest desorbs unreacted. In addition, the fact that no CO_2 production is seen in the final TPD, either during the CO exposure or subsequent heat ramp, indicates that there is no *active* oxygen left on the surface at the end of the preceding TPR run. In fact, the absence of any ^{18}O signal in the postreaction ISS for the Pd/alumina/Re samples shows, at least within the sensitively of the method, that none of the $^{18}O_2$ used in the TPR is left on the surface after the reaction sequence. Taken together, these data show that there is surplus CO on the surface, and that the active adsorbed oxygen is completely consumed in each TPR cycle, i.e., that active oxygen is the activity-limiting reactant.

Figure 4.4 shows that activity is positively correlated with the intensity of CO desorbing in the high temperature feature in CO TPD, and an analogous positive correlation (varying cluster size rather than alumina thickness) was seen for Pt_n/alumina/Re catalysts under similar conditions.[112] For both Pd and Pt, activity appears to be limited primarily by the amount of oxygen activated on the clusters by the O_2 dose. The obvious interpretation of the correlation is that O_2 activation occurs on the same sites that are responsible for the strongest CO binding, so that samples with the largest number

of such sites are the most active, and also have the strongest CO desorption features. Temperature-dependent ISS shows that these sites are predominantly on top of the clusters, in both cases.[85, 87] It is interesting, therefore, that there is an anticorrelation between activity and this high temperature feature measured for residual CO desorbing during TPR. The anticorrelation presumably stems from competition between CO desorption and CO oxidation. Samples which have large numbers of "on top of cluster" sites suitable for O_2 activation (or CO binding in TPD) have more oxygen bound after the O_2 exposure, bind less CO in these sites, and convert more of the CO to CO_2.

In several previous studies[65, 80, 83, 87] we have found cluster size-dependent anti-correlations between core level BEs of the metal clusters and activity as oxidation catalysts under conditions ranging from UHV to aqueous phase electrochemistry. These anticorrelations were rationalized as follows: Activity involves valence electrons, which may also influence core level BEs via screening of the core hole final state. Cluster sizes with particularly stable valence electronic structures should be relatively inactive, but stable valence structure would also tend to reduce core hole screening, thereby increasing the core level BE. Recently, we used UPS to directly probe the cluster valence structure, and have seen a similar anticorrelation between valence band energy and the activity for CO oxidation for Pt_n/alumina.[112]

As shown in Figure 4.7, the situation here is different. The Pd core and valence level BEs for Pd_{20}/alumina/Re samples are essentially independent of the alumina thickness, despite the observation that both core and valence levels of the alumina film are strongly thickness dependent. Instead, CO oxidation activity is correlated with shifts in both the 3d and valence levels resulting from the 10 L O_2 exposure that is first step in

TPR. This correlation provides additional support for the idea that the activity-limiting factor under our conditions is the availability of adsorbed, activated oxygen. The oxidation-induced shifts are attributed to the electron withdrawing effect of forming Pd-O bonds, leaving the Pd centers with partial positive charges that increase the energy required to eject photoelectrons. Therefore, samples with larger shifts have more adsorbed oxygen, and should be more active, if adsorbed oxygen is the limiting reactant.

4.4.2 Thickness effects on sample electronic band structure

We have shown that CO oxidation activity is correlated with physical properties of the samples, such as the fraction of Pd in the surface layer, the density of particular binding sites, and the extent of oxidation during the O_2 exposure. The correlations raise two questions. Why should these properties of the deposited Pd_{20} vary with alumina thickness, and which physical properties are important in controlling chemistry, versus simply being side-effects of the important properties? The fact that all the core and valence levels of the alumina films shift substantially (>1 eV) in the thickness range where the dip in activity is seen (Figure 4.6), suggests that thickness-dependent variations in the electrostatic potential in the film may affect the physical and chemistry properties of deposited Pd_{20}. Therefore, before further addressing the thickness effects, we need to explore how thickness affects the electronic band structure of the films, using measured spectra as inputs.

As shown above, the alumina films have significant surface concentrations of Re, attributed to diffusion of Re from the substrate into the alumina during growth, suggesting that the films also have bulk doping from Re. As shown below, the alumina

films behave like n-doped semiconductors, which is not unreasonable given that Re can adopt a range of oxidation states, most of which are greater than the 3+ state of Al in the alumina lattice. We have estimates for the Re surface concentration as a function of film thickness (Appendix A). To model the band structure of the alumina we need, instead, the Re bulk concentration as a function of depth in the films. The obvious approximation is to equate the dependence of bulk concentration on distance from the Re substrate, with the dependence of the surface concentration on film thickness, i.e., to assume that the thinner films look like slices of a thick film. Because the thinnest films are not continuous, the Re surface concentration in the alumina portion of the films was estimated by extrapolating the trend observed for the thicker, continuous films, giving dopant concentration estimates that range from ~$2x10^{21}/cm^3$ close to the alumina-Re interface, dropping to ~$3x10^{20}/cm^3$ near the surface of a thick film. If we assume, for now, that all Re dopant atoms donate one electron to the alumina conduction band, then we obtain estimates for the free electron density (N_d) as a function of distance from the Re substrate. These estimates for N_d are high compared to those in typical doped semiconductors ($<10^{18}/cm^3$)[113] but still substantially lower than the electron densities in metals (e.g., $8.5x10^{22}$ for copper).

To understand how thickness affects sample properties, it is important to understand electron transfer between the alumina film and the Re support, and the resulting effects on the electronic bands of alumina. The supporting information reviews common band structure models for metal-metal and metal-semiconductor contacts (Appendix A). Here, we just summarize the main points. Figure 4.9 outlines a band structure model for contact between surface-oxidized ReO_x and a thick Re-doped alumina

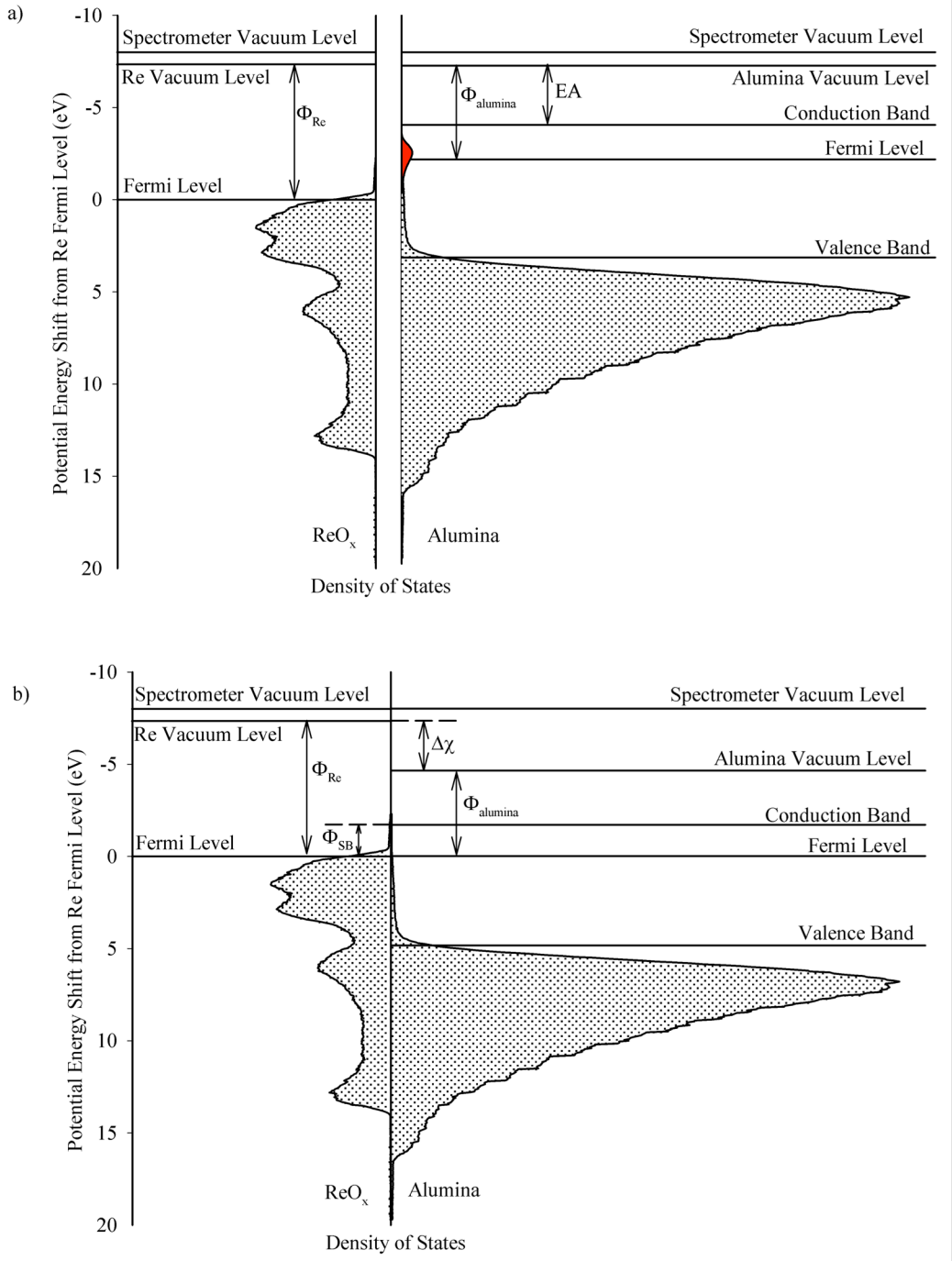

Figure 4.9: Diagram illustrating the density of states for ReO_x and Re-doped alumina based on measured UPS. (a) Situation before ReO_x and alumina are brought into contact. (b). Situation after contact. The red DOS shown for the alumina film in (a) is an exaggerated estimate of the population of states near the conduction band due to Re dopants.

film. Figure 4.9a shows our estimate of the projected occupied density of states (pDOS) for ReO_x (left) and Re-doped alumina (right), before the two are brought into contact. In that case, the vacuum levels (E_{vac}) over each component are identical because each is electrically neutral. The pDOS for ReO_x is simply the measured UPS for the surface-oxidized Re sample, referenced to E_F of the Re(0001) support (E_F^{Re}). As noted above, the UPS sampling depth is ~2 nm, thus the pDOS plotted includes contributions from both bulk-like metallic Re, and the oxidized surface. The measured work function for the ReO_x surface was used for Φ_{Re}, thereby determining E_{vac}.

Obviously, we are not able to measure the UPS for a freestanding alumina film, and the pDOS plotted for alumina is the measured UPS for a 2.8 nm thick alumina/Re sample, modified as follows: We have added a postulated impurity band of Re donor states in the alumina band gap (shaded red). The presence of states near the conduction band minimum would lead to significant density of free (conduction) electrons, and also shift the Fermi level for alumina ($E_F^{alumina}$) close to the bottom of the conduction band. The measured work function for this thick alumina/Re sample was used for $\Phi_{alumina}$, thereby positioning $E_F^{alumina}$ relative to E_{vac}. The figure also indicates the electron affinity of the alumina, EA.

Figure 4.9b shows the situation after contact. Because the Re sample is grounded, the ReO_x energy levels should be unchanged after contact with alumina. The pDOS plotted for alumina is simply the UPS for the 2.8 nm thick alumina/Re sample, and because of the thickness of the alumina layer, the pDOS is dominated by signal from the near-surface region of the alumina. Expected differences in the alumina properties near the Re-alumina interface are discussed below. The states in the alumina film that had

precontact energies above E_F^{Re} have been depopulated by electron transfer to rhenium, thereby dropping $E_F^{alumina}$ into alignment with E_F^{Re}, and positively charging the alumina layer with respect to the grounded Re sample. The positive electrical potential in the film stabilizes the electronic energy levels of the alumina film by $\Delta\chi$, consistent with the observation that the alumina BEs for alumina/Re are substantially higher than those for bulk alumina (Figure 4.6a).

To understand the thickness dependence of the BE shifts, we need to understand the variation in the electronic properties with distance from the Re-alumina interface. The accompanying discussion in Appendix A reviews the standard Schottky-Mott model[114-117] for contact between a metal and an n-doped semiconductor. Specific examples relevant to contact between Re and highly doped alumina films of different thicknesses are shown in Figure 4.10.

Figure 4.10a shows a simplified version of the band diagram for ReO_x in contact with a thick alumina film, where the horizontal position represents distance from the Re-alumina interface, which is indicated by the vertical line. As in Figure 4.9b, free electrons originating from the Re dopant atoms in the alumina film transfer to Re upon contact, aligning the Fermi levels of Re and alumina. Because the metal is conductive, the transferred electrons localize at the Re side of the Re-alumina interface, but the corresponding positive charge is distributed over a thin depletion layer within the alumina, where the free electron density is depleted leaving behind a corresponding density of unscreened Re cations. This charge distribution results in a positive potential building up across the depletion layer, and creation of a Schottky barrier (Φ_{SB}). Within the depletion layer, the potential varies with distance from the interface, causing the

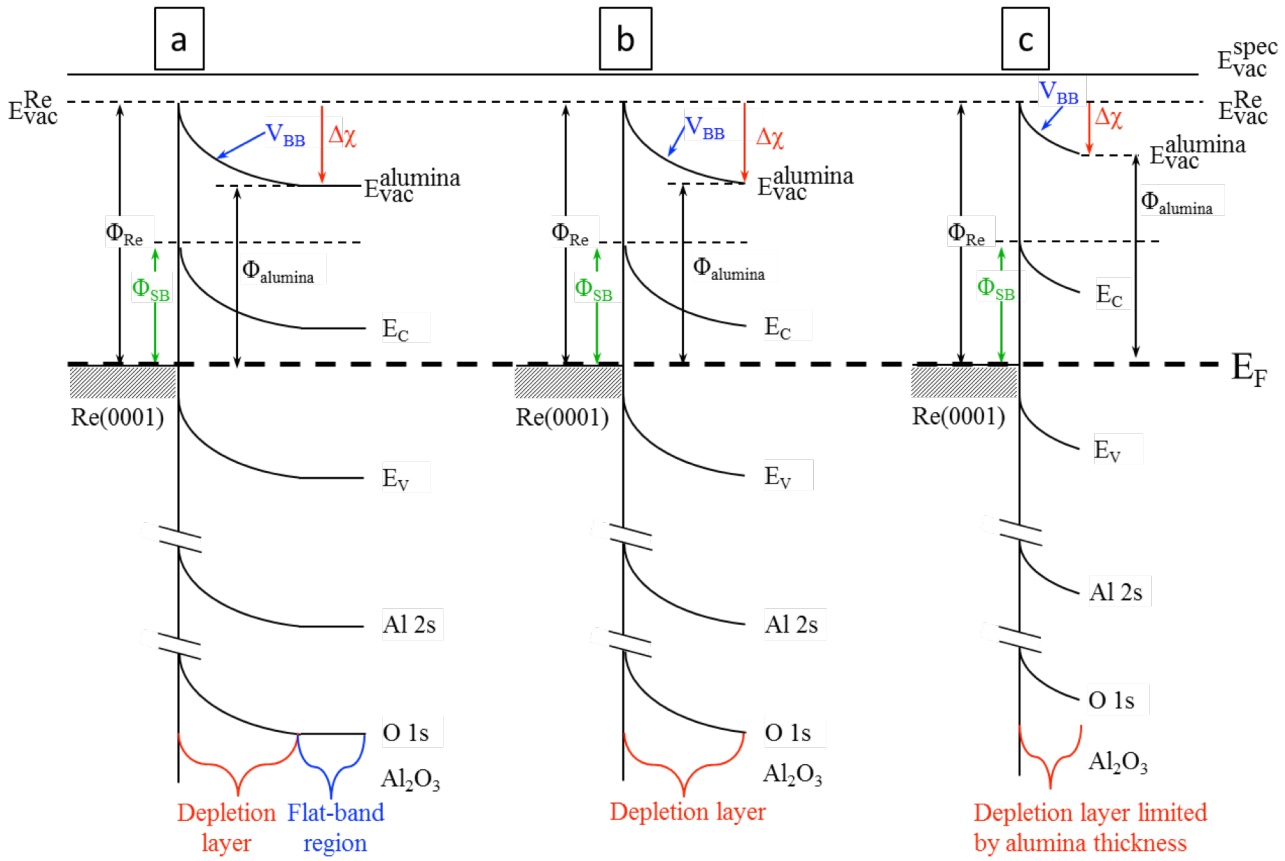

Figure 4.10: Potential energy diagrams illustrating band bending expected for contact of Re with alumina films of thickness (a) much greater than the depletion layer thickness, (b) comparable to the depletion layer thickness, and (c) thinner than the depletion layer.

electronic bands to bend, as shown and discussed in more detail in the supporting information.

In the near-surface region of thick alumina films (outside the depletion layer), the electronic bands are flat, and stabilized by $\Delta\chi$. As a result, the alumina core and valence BEs are shifted to higher energy and independent of alumina thickness, as long as the films are thick enough that XPS and UPS do not "see" the depletion layer. This corresponds to the situation for films thicker than ~4 nm (Figure 4.6a). The shift in the vacuum level implies that the work function for thick films should be low, and thickness-independent, as shown in Figure 4.5b. The pDOS shown in Figure 4.9b, for the near-surface region of a thick film alumina/Re sample, corresponds to this flat-band portion of the band diagram.

The center diagram is for Re in contact with an alumina film with thickness only slightly greater than the depletion layer. The alumina-to-Re electron transfer and the resulting alumina surface potential are still limited by the depletion layer, as in the thicker films, however, the XPS and UPS measurements now sample through the flat-band region, into the depletion layer. The effective attenuation lengths[90] for Al 2s and O1s photoelectrons in alumina are 2.9 and 2.1 nm, respectively (for Al K_α radiation), thus the measured alumina BEs are an exponentially-weighted average over the top ~5 nm of the samples. Similarly, the inelastic mean-free path for electrons with kinetic energy corresponding to the top of the alumina valence band is ~1 nm,[118] therefore the valence band onset energy is also averaged over the top few nm of the samples. Therefore, with decreasing film thickness in this range, we expect the XPS and UPS spectra to become thickness-dependent, as the spectra increasingly sample the potential gradient across the

depletion layer.[113] As shown in Figure 4.6a, the BEs measured by XPS and UPS begin to shift to lower energies for films thinner than ~4 nm. In addition, the full width at half maximum (FWHM) of the XPS peaks (e.g., Al 2s) increases from 2.5 eV for films thicker than ~3 nm, to 3 eV for the thinnest alumina films.

The right hand diagram shows the situation for Re in contact with an alumina film that is thinner than the depletion layer (i.e., thinner than the depletion layer would be in a thick film). In this scenario, the alumina-to-Re electron transfer is limited by the small number of free electrons in the thin alumina film. Therefore, the positive potential built up across the film is smaller than for thicker alumina, resulting in less stabilization of the alumina BEs. As shown in Figure 4.6a, the alumina BEs become strongly thickness-dependent for films thinner than ~1.8 nm, suggesting that the depletion layer is somewhat thinner than that (because the BEs average over the near-surface region). Also, because the vacuum level stabilization is smaller for thinner films, the work function should increase with decreasing alumina thickness, as is seen in Figure 4.5b. Finally, as already noted, the FWHM of the XPS peaks should be large, because of the potential gradient across the alumina film, as is observed.

In addition to the effect of thickness on alumina electronic properties, there are several observations relating to Pd_{20} deposition that also need to be accounted for within this electrostatic/depletion layer model. It is found that depositing 0.1 ML-equivalent of Pd_{20} results in significant (~0.4 eV) shifts of the alumina core and valence levels to lower BE for the thicker alumina/Re samples (Figure 4.6a), however, there is no shift for samples with alumina films thinner than ~1.5 nm. On the other hand, despite the fact that the core and valence BEs of the alumina films shift by more than 1 eV with changing

film thickness, the BEs of the Pd 3d core level for Pd_{20}/alumina/Re are independent of the alumina thickness, within the uncertainty (Figure 4.6b). Finally, it is observed that while the work function of the samples is strongly dependent on alumina thickness (Figure 4.5b), Pd_{20} deposition has negligible (<0.1 eV) effect on the work function.

The electrostatic/depletion layer model can rationalize at least the first two effects. First consider Pd_{20} deposited on thick alumina, where the alumina BEs are shifted ~1.6 eV higher than in bulk alumina, due to charging of the alumina layer by alumina-to-Re electron transfer. If there were no electron transfer between alumina and Pd_{20}, we would expect the Pd 3d BE to be shifted at least 1.6 eV above the bulk Pd BE (335.3 eV).[119] This expected shift is the sum of the ~1.6 eV shift from the positive surface potential of the alumina film, and an additional shift from reduced stabilization of the photoemission final state in small clusters, compared to that in bulk Pd.[98-102, 120, 121] For example, Auger parameter analysis for Pd atoms deposited on SiO_2 indicates that the final state is destabilized by ~0.8 eV compared to bulk Pd.[36] In fact, however, the Pd 3d BEs for our samples are ~336 eV, which is only ~0.7 eV higher than the bulk value.[119] The smaller-than-expected shift suggests, therefore, that there is significant electron transfer from alumina to Pd_{20}, partially cancelling the shifts expected from the alumina surface potential and final state effects. To maintain alignment of $E_F^{alumina}$ with E_F^{Re}, this alumina-to-Pd electron transfer must be compensated by less electron transfer to Re, which would reduce the potential shift between alumina and the grounded Re substrate. This effect accounts for the observation that Pd_{20} deposition causes a ~0.4 eV decrease in the alumina BEs for thick films, as shown in Figure 4.6a.

For alumina films that are thinner than the depletion layer, there are several

effects. Because the surface of such thin films is electron-poor, there would tend to be little alumina-to-Pd electron transfer, which by the argument given above, would explain why Pd_{20} deposition on films thinner than ~1 to 1.5 nm does not cause shifts in the alumina levels (and provide another estimate of the depletion layer thickness). The fact that this transition occurs for alumina with the lack of alumina-to-Pd electron transfer would also tend to shift the Pd 3d BEs to higher energy on the thinnest films, and the low density of free electrons at the surface of these films may cause a further shift to higher BE due to reduced screening of the final state of the supported Pd. On the other hand, the amount of alumina-to-Re electron transfer also decreases for the thinnest films, resulting in less positive alumina surface potentials, which tends to decrease the Pd 3d BEs. Evidently, the three effects largely cancel, such that the Pd BEs are thickness-independent within ~0.2 eV.

The one measurement that appears inconsistent with this alumina-to-Pd electron transfer argument is the observation that the sample work function does not change significantly upon Pd_{20} deposition. If Pd_{20} accepts electrons from alumina, we might expect that the corresponding surface dipole layer should result in a Pd_{20}-induced increase in work function. We have no explanation for this lack of effect, however, we note that a number of groups have reported detailed studies of the effects of anionic adsorbates on work functions, showing that even in cases where a negative surface dipole forms, there is not necessarily an increase in work function.[122-124]

4.4.2 Thickness effects, Pd_{20} binding geometry, and correlations with activity

As shown in Figure 4.8, the Pt ISS intensity varies with alumina thickness in a way that correlates with CO oxidation activity, the density of high temperature CO binding sites (Figure 4.4), and the tendency of the Pd_{20} to oxidize during O_2 exposure (Figure 4.7). The ISS result indicates that the number of Pd atoms in the surface layer goes through a ~14% dip as the alumina thickness varies between 1 and 3 nm. It is, therefore, not surprising that the density of CO binding sites also dips, given the indication from TD-ISS studies[87] the high temperature CO is bound on top of the Pd clusters. Similarly, we might expect a dip in activity as well, because CO oxidation appears to require Pd sites. It is interesting, however, that the dips in high temperature CO binding (~25%) and CO oxidation activity (~50%) are considerably larger than the dip in Pd surface availability.

Before addressing the correlation between these observables, it is useful to discuss what changes in sample morphology might be responsible for the ~14% variation in Pd ISS intensity. One possibility is that Pd_{20} deposited on alumina in the 1 to 3 nm range is prone to sintering at room temperature, producing larger particles with a smaller fraction of Pd in the surface layer, and thus reducing the as-deposited Pd ISS intensity. If sintering were significant for Pd_{20}/alumina at room temperature, it should be greatly accelerated by heating to 560 K during the TPR/TPD runs, and we would expect to see evolution in the CO and CO_2 desorption behavior during the sequence of three TPR experiments. Sintering during TPR and TPD runs would result in postreaction Pd ISS intensity that is substantially lower than the as-deposited intensity. As discussed above,

there is little evolution in the TPR signals, and no evidence of sintering in the post-reaction ISS, implying that sintering at temperatures up to 560 K is not facile. Therefore, we conclude the dip in as-deposited Pd ISS intensity for 1 – 3 nm alumina is not a sign of facile room temperature sintering.

Instead, we attribute the thickness dependence of Pd ISS intensity to changes in as-deposited cluster morphology. A study of cluster size effects on ISS suggests that Pd_{20} on thick film alumina/Re, deposits as flattened islands, with all but a few Pd atoms in the surface layer.[87] The 14% dip in Pd ISS intensity would simply require that the Pd_{20} adopted slightly more compact, multilayer geometries, slightly reducing the fraction of Pd in the surface layer. Given the large changes in alumina surface potential, work function, and band structure that occur in the 1 to 3 nm thickness range, it is not surprising that there might be effects on the Pd-alumina bond strength, leading to thickness-dependent morphology changes.

4.4.3 Mechanistic insights from thickness-dependent correlations

One goal of investigating the effects of alumina thickness on activity is to use thickness-dependent correlations of activity with other properties of the samples (Figures 4, 6-8) to gain insight into the reaction mechanism, and factors that control activity. The situation can be summarized as follows:

1. Under the TPR conditions used here, the CO oxidation activity is limited by the ability of the Pd_{20}/alumina/Re model catalysts to activate oxygen during the 10 L O_2 exposure.

2. Activity is affected by varying the thickness of the alumina support layer, with

relatively high activity for Pd_{20} deposited on thick alumina, or directly on the oxidized ReO_x support, but with a ~50% dip in activity for alumina films in the 1 – 3 nm range. There is no activity for Pd-free alumina or for the oxidized Re substrate under these conditions.

3. Activity is positively correlated with the density of the strongest CO binding sites, and TD-ISS indicates that these sites are on top of the Pd clusters ("on-top" sites). At the thickness corresponding to minimum activity, the density of these sites decreases by 25%.

4. Activity is also positively correlated with the Pd ISS signal, i.e., with the fraction of Pd in the surface layer of the samples. At the thickness corresponding to minimum activity, the Pd ISS intensity dips by 14%.

5. All the core and valence levels associated with the alumina film shift to substantially higher energies as the film thickness is increased from 0.8 to 3 nm, due to rapidly varying alumina surface potential. The dip in activity occurs in the thickness range where the BEs are changing most rapidly, i.e., the range where the film thickness is comparable to the depletion layer thickness.

6. While the Pd 3d BEs are nearly thickness independent, the BE shift induced by O_2 exposure is thickness-dependent, and correlated with CO oxidation activity.

These observations suggest the following explanation for the thickness dependence of the CO oxidation activity. Because only samples with Pd_{20} are active, and activated oxygen is the limiting reactant, it is clear that O_2 binding and activation to Pd_{20} is the critical step under our TPR conditions. O_2 activation typically involves electron transfer from the catalytic center to the antibonding π^* orbital of O_2, weakening the O_2

bond. Therefore, we might expect activity to be enhanced for clusters in electron-rich environments. In addition, the correlation of activity with the density of "on-top" binding sites suggests that oxygen activation also occurs in these sites.

As discussed above, for Pd_{20} deposited on alumina films that are much thicker than the depletion layer, the alumina surface layer has free electrons available, and the XPS/UPS evidence indicates that there is significant electron transfer from alumina to Pd_{20}. At the same time, the ISS results suggest that the Pd_{20} structure exposes a large fraction of the Pd in the surface layer, which is consistent with the observation from TPD, that Pd_{20} on thick alumina exposes a high density of "on-top" binding sites. The combination of electron rich clusters with a high density of the sites required for oxygen activation leads to high CO oxidation activity, which is thickness-independent as long as the film is much thicker than the depletion layer.

For samples with thinner alumina films, the alumina layer is depleted of electrons, which should reduce (or eliminate) electron transfer to Pd_{20}, which, in turn, should reduce the ability of Pd_{20} to activate and bind O_2 by electron transfer into the π^* orbital. Furthermore, the decreases in Pd ISS intensity for these samples suggest that the clusters have more three-dimensional morphology than for thicker alumina, which one might expect as another consequence of electron depletion at the alumina surface. The morphology change is consistent with the lower density of "on-top" binding sites observed by CO TPD. The 50% reduction in activity is, therefore, attributed to combination of lower electron density at the alumina surface, and therefore on the Pd_{20}, and the resulting change in the Pd_{20} morphology.

In this system, activity is also relatively high for Pd_{20} deposited directly on the

oxidized ReO_x surface. The fact that the work function for ReO_x (7.3 eV) is substantially higher than that Re(0001) (Figure 4.5b), suggests that there is a negative surface dipole, consistent with termination by an electron-rich oxygen layer. It is not unreasonable to suppose that Pd_{20} deposited on such an electron-rich surface layer would bind strongly, and undergo significant ReO_x-to-Pd electron transfer, as suggested by the observation that the Pd 3d BE for Pd_{20}/ReO_x is significantly lower than for Pd_{20} on any of the alumina films (Figure 4.6b). Strong Pd-ReO_x binding is consistent with these clusters having flattened structures (high Pd ISS intensity), which in turn, provide a high density of "on-top" binding sites (intense high Temperature CO desorption). The combination of electron-rich clusters with a high density of binding sites for O_2 activation is presumably responsible for the high activity of the Pd_{20}/ReO_x samples. It is interesting that in the Pd/alumina/Ta(110) system, there is also a drop in activity when the alumina film thickness drops below ~4 nm, however, for that system, the activity for clusters deposited directly on the Ta support is negligible.[87] The difference is that in the Pd/Ta(110) experiment, the deposition was done on unoxidized Ta(110), and in that system, ISS showed that the Pd immediately dissolved into the Ta bulk. For Pd_{20} deposited on pre-oxidized ReO_x, the activity was stable over time, and the postreaction ISS showed no evidence of dissolution into the bulk. Even for Pd deposited on unoxidized Re, ISS showed substantial Pd intensity as-deposited (Fig. 4.1a), and the sample had high CO oxidation activity, which, however, decreased rapidly over the three TPR experiments (Figure 4.2b).

4.5. Conclusions

We have exploited the ability to deposit intact, size-selected cluster ions, to prepare a series of samples with identical coverages of Pd_{20} clusters, but with variable thickness alumina films. XPS and UPS shows that electrons transfer from the alumina films to Re, suggesting formation of a depletion layer in the range of 1 to 1.5 nm thick. For the thinner films, the depletion layer is limited by the actual thickness of the alumina film. The CO oxidation activity is low for Pd_{20} deposited alumina films with thicknesses similar to, or thinner than the depletion layer, because such films provide an electron-poor environment, which affects both O_2 activation, and the geometry of the deposited Pd_{20}. For thicker alumina layers, the Pd_{20} becomes electron rich due to electron transfer from the alumina film, enhancing O_2 activation and CO oxidation activity. The alumina-Pd binding is also stronger on the thicker films, resulting in, relatively, flatter cluster structures that provide more binding sites for both O_2 and CO adsorption. The notion of the morphology change and number of reactant binding sites is corroborated through both ISS and TPD/TPR evidence. The combination of electron donation to the Pd clusters from the Re dopants and the increased number of O_2 and CO binding sites, due to cluster geometry, control the overall catalytic activity for a given alumina support film thickness. The manipulation of substrate thickness should prove to be a useful tool for controlling reactivity and morphology in future applications.

4.6. References

1. W. Jin, P.-C. Yeh, N. Zaki, D. Zhang, J. r. T. Sadowski, A. Al-Mahboob, A. M. V. D. Zande, D. A. Chenet, J. I. Dadap, I. P. Herman, et al. Direct Measurement of the Thickness-Dependent Electronic Band Structure of MoS_2 Using Angle

Resolved Photoemission Spectroscopy. *Physical Review Letters*, 2013, **111**, 106801.

2. A. Beniya, N. Isomura, H. Hirata and Y. Watanabe. Lateral Displacement in Soft-landing Process and Electronic Properties of Size-Selected Pt_7 Clusters on the Aluminum Oxide Film on NiAl(110). *Chem. Phys. Lett.*, 2013, **576**, 49-54.

3. J. Zhou, J. Zhou, N. Camillone, III and M. G. White. Electronic Charging of Non-Metallic Clusters. Size-Selected Mo_xS_y Clusters Supported on an Ultrathin Alumina Film on NiAl(110). *Phys. Chem. Chem. Phys.*, 2012, **14**, 8105-8110.

4. R. Robles and S. N. Khanna. Oxidation of Pd_n (n=1-7, 10) Clusters Supported on Alumina/NiAl(110). *Phys. Rev. B: Condens. Matter Mater. Phys.*, 2010, **82**, 085428.

5. V. Maurice, N. Fremy and P. Marcus. Hydroxylation-Induced Modifications of the Al_2O_3/NiAl(001) Surface at Low Water Vapor Pressure. *Surface Science*, 2005, **581**, 88-104.

6. C. Fan, T. Wu, W. E. Kaden and S. L. Anderson. Cluster Size Effects on Hydrazine Decomposition on Ir_n/Al_2O_3/NiAl(110). *Surf. Sci.*, 2006, **600**, 461-467.

7. M. E. Vaida, T. M. Bernhardt, C. Barth, F. Esch, U. Heiz and U. Landman. Ultrathin Magnesia Films as Support for Molecules and Metal Clusters: Tuning Reactivity by Thickness and Composition. *Physica Status Solidi B: Basic Solid State Physics*, 2010, **247**, 1001-1015.

8. H. L. Abbott, A. Aumer, Y. Lei, C. Asokan, R. J. Meyer, M. Sterrer, S. Shaikhutdinov and H.-J. Freund. CO Adsorption on Monometallic and Bimetallic Au−Pd Nanoparticles Supported on Oxide Thin Films. *J. Phys. Chem. C.*, 2010, 17099–17104.

9. B. Yoon, U. Landman, V. Habibpour, C. Harding, S. Kunz, U. Heiz, M. Moseler and M. Walter. Oxidation of Magnesia-Supported Pd_{30} Nanoclusters and Catalyzed CO Combustion: Size-Selected Experiments and First-Principles Theory. *J. Phys. Chem. C*, 2012, **116**, 9594-9607.

10. D. W. Goodman. Chemical and Spectroscopic Studies of Metal Oxide Surfaces. *J. Vac. Sci. Technol., A*, 1996, **14**, 1526-1531.

11. H. J. Freund, M. Baumer and H. Kuhlenbeck. Catalysis and Surface Science: What do we Learn from Studies of Oxide-Supported Cluster Model Systems? *Adv. Catal.*, 2000, **45**, 333-384.

12. H. J. Freund and G. Pacchioni. Oxide Ultra-Thin Films on Metals: New Materials for the Design of Supported Metal Catalysts. *Chemical Society Reviews*, 2008, **37**, 2224-2242.

13. F. Gao and D. W. Goodman. Model Catalysts: Simulating the Complexities of Heterogeneous Catalysts. *Annual Review of Physical Chemistry*, 2012, **63**, 265-286.

14. D. W. Goodman. Model Catalysts: From Extended Single Crystals to Supported Particles. *Surf. Rev. Lett.*, 1995, **2**, 9-24.

15. S. C. Street and D. W. Goodman. Chemical and Spectroscopic Studies of Ultrathin Oxide Films. *Chem. Phys. Solid Surf.*, 1997, **8**, 375-406.

16. C. T. Campbell. Ultrathin Metal Films and Particles on Oxide Surfaces: Structural, Electronic and Chemisorptive Properties. *Surf. Sci. Rep.*, 1997, **27**, 1-112.

17. C. T. Campbell, A. W. Grant, D. E. Starr, S. C. Parker and V. A. Bondzie. Model Oxide-Supported Metal Catalysts: Energetics, Particle Thicknesses, Chemisorption and Catalytic Properties. *Topics in Catalysis*, 2001, **14**, 43-51.

18. K. Judai, S. Abbet, A. S. Woerz, U. Heiz and C. R. Henry. Low-Temperature Cluster Catalysis. *Journal of the American Chemical Society*, 2004, **126**, 2732-2737.

19. J. Libuda, I. Meusel, J. Hoffmann, L. Piccolo, C. R. Henry and H.-J. Freund. The CO Oxidation Kinetics on Supported Pd Model Catalysts: A Molecular Beam/*in situ* Time-Resolved Intrared Reflection Absorption Spetroscopy Study. *J. Chem. Phys.*, 2001, **114**, 4669-4684.

20. M. A. Roettgen, S. Abbet, K. Judai, J.-M. Antonietti, A. S. Woerz, M. Arenz, C. R. Henry and U. Heiz. Cluster Chemistry: Size-Dependent Reactivity Induced by Reverse Spill-Over. *J. Am. Chem. Soc.*, 2007, **129**, 9635-9639.

21. K. B. Lewis, S. T. Oyama and G. A. Somorjai. The Preparation and Reactivity of Thin, Ordered Films of Vanadium Oxide on Au(111). *Surface Science*, 1990, **233**, 75-83.

22. A. Calloni, A. Ferrari, A. Brambilla, F. Ciccacci and L. Duo. Growth of Stoichiometric TiO_2 Thin Films on Au(100) Substrates by Molecular Beam Epitaxy. *Thin Solid Films*, 2012, **520**, 3922-3926.

23. B. Yang, X. Lin, H.-J. Gao, N. Nilius and H.-J. Freund. CO Adsorption on Thin MgO Films and Single Au Adatoms: A Scanning Tunneling Microscopy Study. *The Journal of Physical Chemistry C*, 2010, **114**, 8997-9001.

24. U. Diebold, S. C. Li and M. Schmid. Oxide Surface Science. *Annu Rev Phys Chem*, 2010, **61**, 129-148.

25. N. Nilius. Properties of Oxide Thin Films and Their Adsorption Behavior Studied by Scanning Tunneling Microscopy and Conductance Spectroscopy. *Surface Science Reports*, 2009, **64**, 595-659.

26. G. Kresse, M. Schmid, E. Napetschnig, M. Shishkin, L. Koehler and P. Varga. Structure of the Ultrathin Aluminum Oxide Film on NiAl(110). *Science*, 2005, **308**, 1440-1442.

27. N. D. McCavish and R. A. Bennett. Ultra-Thin Film Growth of Titanium Dioxide on W(100). *Surface Science*, 2003, **546**, 47-56.

28. Y. Murata, K. Nagata, H. Fujimoto, T. Sakurai, M. Okada and Y. Ebe. Electronic Property of Thin Single-Crystal Films of α-Al_2O_3 on Ru(0001). *Journal of the Physical Society of Japan*, 2001, **70**, 793-796.

29. M. Sterrer, T. Risse, M. Heyde, H.-P. Rust and H.-J. Freund. Crossover from Three-Dimensional to Two-Dimensional Geometries of Au Nanostructures on Thin MgO(001) Films: A Confirmation of Theoretical Predictions. *Physical Review Letters*, 2007, **98**, 206103.

30. Y. Wu, E. Garfunkel and T. E. Madey. Growth of Ultrathin Crystalline Al_2O_3 Films on Ru(0001) and Re(0001) Surfaces. *J. Vac. Sci. Technol., A*, 1996, **14**, 2554-2563.

31. Y. Wu, E. Garfunkel and T. E. Madey. Growth and Oxidation of Ultra-Thin Al Films on the Re(0001) Surface. *Surf. Sci.*, 1996, **365**, 337-352.

32. L. Giordano and G. Pacchioni. Oxide Films at the Nanoscale: New Structures, New Functions, and New Materials. *Accounts of Chemical Research*, 2011, **44**, 1244-1252.

33. Y. Cui, K. Huang, N. Nilius and H.-J. Freund. Charge Competition with Oxygen Molecules Determines Growth of Gold Nanoparticles on CaO Films. *Faraday Disc.*, 2013, **162**, 153-163.

34. J. A. Farmer, J. H. Baricuatro and C. T. Campbell. Ag Adsorption on Reduced CeO_2(111) Thin Films. *J. Phys. Chem. C*, 2010, **114**, 17166-17172.

35. G. Pacchioni. Electronic Interactions and Charge Transfers of Metal Atoms and Clusters on Oxide Surfaces. *Physical Chemistry Chemical Physics: PCCP*, 2013, **15**, 1737-1757.

36. W. E. Kaden, C. Büchner, L. Lichtenstein, S. Stuckenholz, F. Ringleb, M. Heyde, M. Sterrer, H.-J. Freund, L. Giordano, G. Pacchioni, et al. Understanding Surface Core Level Shifts Based on the Auger Parameter – a Study of Pd Atoms Adsorbed on SiO_2/Ru(0001) Thin Films. *Physical Review B*, 2014, **89**, 115436.

37. L. Giordano, G. Pacchioni, C. Noguera and J. Goniakowski. Spectroscopic Evidences of Charge Transfer Phenomena and Stabilization of Unusual Phases at Iron Oxide Monolayers Grown on Pt(111). *Topics in Catalysis*, 2013, **56**, 1074-1081.

38. R. M. Jaeger, H. Kuhlenbeck, H.-J. Freund, M. Wuttig, W. Hoffmann, R. Franchy and H. Ibach. Formation of a Well-Ordered Aluminium Oxide Overlayer by Oxidation of NiAl. *Surf. Sci.*, 1991, **259**, 235-252.

39. J. Libuda, F. Winkelmann, M. Bäumer, H.-J. Freund, T. Bertrams, H. Neddermeyer and K. Müller. Structure and Defects of an Ordered Alumina Film on NiAl(110). *Surf. Sci.*, 1994, **318**, 61-73.

40. G. Ceballos, Z. Song, J. I. Pascual, H.-P. Rust, H. Conrad, M. Bäumer and H.-J. Freund. Structure Investigation of the Topmost Layer of a Thin Ordered Alumina Film Grown on NiAl(110) by Low Temperature Scanning Tunneling Microscopy. *Chem. Phys. Lett.*, 2002, **359**, 41-47.

41. T. T. Lay, M. Yoshitake and B. Mebarki. Temperature Effect on Growth of Well-Ordered Thin Al_2O_3 Film on NiAl(110). *J. Vac. Sci. Technol. A*, 2002, **20**, 2027-2031.

42. A. Stierle, F. Renner, R. Streitel, H. Dosch, W. Drube and B. C. Cowie. X-ray Diffraction Study of the Ultrathin Al_2O_3 Layer on NiAl(110). *Science*, 2004, **303**, 1652-1656.

43. S. Shaikhutdinov, M. Heemeier, J. Hoffmann, I. Meusel, B. Richter, M. Bäumer, H. Kuhlenbeck, J. Libuda, H.-J. Freund, R. Oldman, et al. Interaction of Oxygen with Palladium Deposited on a Thin Alumina Film. *Surf. Sci.*, 2002, **501**, 270-281.

44. T. Wu, W. E. Kaden, W. A. Kunkel and S. L. Anderson. Size-Dependent Oxidation of Pd_n ($n \leq 13$) on Alumina/NiAl(110): Correlation with Pd Core Level Binding Energies. *Surface Science*, 2009, **603**, 2764-2770.

45. X. Lai, C. C. Chusuei, K. Luo, Q. Guo and D. W. Goodman. Imaging Ultrathin Al_2O_3 Films with Scanning Tunneling Microscopy. *Chem. Phys. Lett.*, 2000, **330**, 226-230.

46. P. J. Chen and D. W. Goodman. Epitaxial Growth of Ultrathin Al_2O_3 Films on Ta(110). *Surf. Sci.*, 1994, **312**, L767-L773.

47. D. R. Rainer, M. C. Wu, D. I. Mahon and D. W. Goodman. Adsorption of CO on Pd/Al_2O_3/Ta(110) Model Catalysts. *J. Vac. Sci. Technol., A*, 1996, **14**, 1184-1188.

48. M.-C. Wu and D. W. Goodman. Particulate Cu on Ordered Al_2O_3: Reactions with Nitric Oxide and Carbon Monoxide. *J. Phys. Chem.*, 1994, **98**, 9874-9881.

49. Y. Q. Cai, A. M. Bradshaw, Q. Guo and D. W. Goodman. The Size Dependence of the Electronic Structure of Pd Clusters Supported on Al_2O_3/Re(0001). *Surf. Sci.*, 1998, **399**, L357-L363.

50. M. D. Ulrich, R. S. Johnson, J. G. Hong, J. E. Rowe, G. Lucovsky, J. S. Quinton and T. E. Madey. Interface Electronic Structure of Ta_2O_5–Al_2O_3 Alloys for Si-Field-Effect Transistor Gate Dielectric Applications. *Journal of Vacuum Science & Technology B: Microelectronics and Nanometer Structures*, 2002, **20**, 1732-1738.

51. M. Walter, P. Frondelius, K. Honkala and H. Häkkinen. Electronic Structure of MgO-Supported Au Clusters: Quantum Dots Probed by Scanning Tunneling Microscopy. *Physical Review Letters*, 2007, **99**, 096102.

52. M. Sterrer, T. Risse, U. Martinez Pozzoni, L. Giordano, M. Heyde, H.-P. Rust, G. Pacchioni and H.-J. Freund. Control of the Charge State of Metal Atoms on Thin MgO Films. *Physical Review Letters*, 2007, **98**, 096107.

53. Y. D. Kim, J. Stultz, T. Wei and D. W. Goodman. Interaction of Ag with MgO(100). *Journal of Physical Chemistry B*, 2002, **106**, 6827 - 6830.

54. Y. D. Kim, J. Stultz and D. W. Goodman. Identification of Defect Sites on MgO(100) Surfaces. *Langmuir*, 2002, **18**, 3999 - 4004.

55. Y. D. Kim, J. Stultz and D. W. Goodman. Characterization of MgO(100) Thin Film Growth on Mo(100). *Surface Science*, 2002, **506**, 228-234.

56. S. Abbet, A. M. Ferrari, L. Giordano, G. Pacchioni, H. Hakkinen, U. Landman and U. Heiz. Pd_1/MgO(100): A Model System in Nanocatalysis. *Surface Science*, 2002, **514**, 249-255.

57. N. Tanaka, H. Kimata, T. Takashima and T. Kizuka. Ultimate TEM Observation of Tungsten Clusters on MgO(001) Surfaces. *Surf. Rev. Lett.*, 1998, **5**, 723-729.

58. C. Becker and C. R. Henry. A Second CO Adsorption State on Palladium Clusters Supported on MgO(100). *Catalysis Letters*, 1997, **43**, 55-57.

59. J. S. Corneille, J.-W. He and D. W. Goodman. XPS Characterization of Ultra-Thin MgO Films on a Mo(100) Surface. *Surf. Sci.*, 1994, **306**, 269-278.

60. M. Valden, X. Lai and D. W. Goodman. Onset of Catalytic Activity of Gold Clusters on Titania with the Appearance of Nonmetallic Properties. *Science*, 1998, **281**, 1647-1650.

61. M. Haruta. Size- and Support-Dependency in the Catalysis of Gold. *Catalysis Today*, 1997, **36**, 153-166.

62. C. Harding, V. Habibpour, S. Kunz, A. N.-S. Farnbacher, U. Heiz, B. Yoon and U. Landman. Control and Manipulation of Gold Nanocatalysis: Effects of Metal Oxide Support Thickness and Composition. *J. Am. Chem. Soc.*, 2009, **131**, 538-548.

63. R. Pal, L.-M. Wang, Y. Pei, L.-S. Wang and X. C. Zeng. Unraveling the Mechanisms of O_2 Activation by Size-Selected Gold Clusters: Transition from Superoxo to Peroxo Chemisorption. *J. Am. Chem. Soc.*, 2012, **134**, 9438-9445.

64. R. E. Winans, S. Vajda, G. E. Ballentine, J. W. Elam, B. Lee, M. J. Pellin, S. Seifert, G. Y. Tikhonov and N. A. Tomczyk. Reactivity of Supported Platinum Nanoclusters Studied by *in situ* GISAXS: Clusters Stability Under Hydrogen. *Topics in Catalysis*, 2006, **39**, 145-149.

65. M. D. Kane, F. S. Roberts and S. L. Anderson. Alumina Support and Pd_n Cluster Size Effects on Activity of Pd_n for Catalytic Oxidation of CO. *Faraday Disc.*, 2013, **162**, 323 - 340.

66. D. H. Parker and B. E. Koel. Chemisorption of High Coverages of Atomic Oxygen on the Pt(111), Pd(111), and Au(111) Surfaces. *J. Vac. Sci. Technol. A*, 1990, **8**, 2585-2590.

67. A. K. Santra and D. W. Goodman. Catalytic Oxidation of CO by Platinum Group Metals: From Ultrahigh Vacuum to Elevated Pressures. *Electrochimica Acta*, 2002, **47**, 3595-3609.

68. T. Engel and G. Ertl. A Molecular Beam Investigation of the Catalytic Oxidation of Carbon Monoxide on Palladium (111) *Journal of Chemical Physics*, 1978, **69**, 1267-1281.

69. T. Engel and G. Ertl. Surface Residence Times and Reaction Mechanism in the Catalytic Oxidation of Carbon Monoxide on Palladium(111) *Chemical Physics Letters*, 1978, **54**, 95-98.

70. A. Tomita, K.-i. Shimizu, K. Kato, T. Akita and Y. Tai. Mechanism of Low-Temperature CO Oxidation on Pt/Fe-Containing Alumina Catalysts Pretreated with Water. *J. Phys. Chem. C*, 2013, **117**, 1268-1277.

71. M. Moses-DeBusk, M. Yoon, L. F. Allard, D. R. Mullins, Z. Wu, X. Yang, G. Veith, G. M. Stocks and C. K. Narula. CO Oxidation on Supported Single Pt Atoms: Experimental and Ab Initio Density Functional Studies of CO Interaction with Pt Atom on θ-Al_2O_3(010) Surface. *J. Am. Chem. Soc.*, 2013, **135**, 12634-12645.

72. A. Corma, P. Concepcio´n, M. Boronat, M. J. Sabater, J. Navas, M. J. Yacaman, E. Larios, A. Posadas, M. A. Lo´pez-Quintela, D. Buceta, et al. Exceptional Oxidation Activity with Size-Controlled Supported Gold Clusters of Low Atomicity. *Nature Chemistry*, 2013, **5**, 775-781.

73. B. Brandt, T. Schalow, M. Laurin, S. Schauermann, J. Libuda and H.-J. Freund. Oxidation, Reduction, and Reactivity of Supported Pd Nanoparticles: Mechanism and Microkinetics *Journal of Physical Chemistry C*, 2007, **111**, 938-949.

74. X. Tang, J. Schneider, A. Dollinger, Y. Luo, A. S. Woerz, K. Judai, S. Abbet, Y. D. Kim, G. F. Gantefoer, D. H. Fairbrother, et al. Very Small "Window of Opportunity" for Generating CO Oxidation-Active Au_n on TiO_2. *Phys. Chem. Chem. Phys.*, 2014, **16**, 6735-6742.

75. J. Zhang and A. N. Alexandrova. The Golden Crown: A Single Au Atom that Boosts the CO Oxidation Catalyzed by a Palladium Cluster on Titania Surfaces. *Journal of Physical Chemistry Letters*, 2013, **4**, 2250-2255.

76. V. A. Bondzie, S. C. Parker and C. T. Campbell. The Kinetics of CO Oxidation by Adsorbed Oxygen on Well-Defined Gold Particles on TiO_2(110). *Catalysis Letters*, 1999, **63**, 143-151.

77. A. Bourane and D. Bianchi. Oxidation of CO on a Pt/Al_2O_3 Catalyst: From the Surface Elementary Steps to Light-Off Tests IV. Kinetic Study of the Reduction by CO of Strongly Adsorbed Oxygen Species. *Journal of Catalysis*, 2003, **220**, 3-12.

78. H. Conrad, G. Ertl and J. Kueppers. Interactions Between Oxygen and Carbon Monoxide on a Palladium(111) Surface. *Surface Science*, 1978, **76**, 323-342.

79. S. M. McClure and D. W. Goodman. New Insights into Catalytic CO Oxidation on Pt-Group Metals at Elevated Pressures. *Chem. Phys. Lett.*, 2009, **469**, 1-13.

80. S. Proch, M. Wirth, H. S. White and S. L. Anderson. Strong Effects of Cluster Size and Air Exposure on Oxygen Reduction and Carbon Oxidation Electrocatalysis by Size-Selected Pt_n ($n \leq 11$) on Glassy Carbon Electrodes. *J. Am. Chem. Soc.*, 2013, **135**, 3073−3086.

81. M. Aizawa, S. Lee and S. L. Anderson. Sintering, Oxidation, and Chemical Properties of Size-Selected Nickel Clusters on TiO_2 (110). *J. Chem. Phys.*, 2002, **117**, 5001-5011.

82. S. Lee, C. Fan, T. Wu and S. L. Anderson. CO Oxidation on Au_n/TiO_2 Catalysts Produced by Size-Selected Cluster Deposition. *J. Am. Chem. Soc.*, 2004, **126**, 5682-5683.

83. W. E. Kaden, W. A. Kunkel and S. L. Anderson. Cluster Size Effects on Sintering, CO Adsorption, and Implantation in Ir/SiO_2. *J. Chem. Phys.*, 2009, **131**, 114701.

84. W. E. Kaden, W. A. Kunkel, M. D. Kane, F. S. Roberts and S. L. Anderson. Size-Dependent Oxygen Activation Efficiency over Pd_n/TiO_2(110) for the CO Oxidation Reaction. *J. Am. Chem. Soc.*, 2010, **132**, 13097–13099.

85. W. E. Kaden, W. A. Kunkel, F. S. Roberts, M. Kane and S. L. Anderson. CO Adsorption and Desorption on Size-Selected $Pd_n/TiO_2(110)$ Model Catalysts: Size Dependence of Binding Sites and Energies, and Support-Mediated Adsorption. *J. Chem. Phys.*, 2012, **136**, 204705.

86. W. E. Kaden, T. Wu, W. A. Kunkel and S. L. Anderson. Electronic Structure Controls Reactivity of Size-Selected Pd Clusters Adsorbed on TiO_2 Surfaces. *Science*, 2009, **326**, 826-829.

87. M. D. Kane, F. S. Roberts and S. L. Anderson. Mass-Selected Supported Cluster Catalysts: Size Effects on CO Oxidation Activity, Electronic Structure, and Thermal Stability of Pd_n/Alumina ($n \leq 30$) Model Catalysts. *International Journal of Mass Spectrometry*, 2014, **370**, 1-15.

88. F. Sloan Roberts and S. L. Anderson. Note: Hollow Cathode Lamp with Integral, High Optical Efficiency Isolation Valve: A Modular Vacuum Ultraviolet Source. *Review of Scientific Instruments*, 2013, **84**, 126101.

89. J. J. Yeh and I. Lindau. Atomic Subshell Photoionization Cross Sections and Asymmetry Parameters: $1< Z < 103$. *Atomic Data and Nuclear Data Tables*, 1985, **32**, 1-155.

90. C. J. Powell and A. Jablonski. *NIST Electron Effective-Attenuation-Length Database*, NIST, Gaithersburg, MD, 2011.

91. S. Lee, C. Fan, T. Wu and S. L. Anderson. Hydrazine Decomposition over Ir_n/Al_2O_3 Model Catalysts Prepared by Size-Selected Cluster Deposition. *J. Phys. Chem.*, 2005, **109**, 381-388.

92. W. E. Kaden, W. A. Kunkel, F. S. Roberts, M. Kane and S. L. Anderson. Thermal and Adsorbate Effects on the Activity and Morphology of Size-Selected Pd_n/TiO_2 Model Catalysts. *Surface Science*, 2014, **621**, 40-50.

93. J. W. Rabalais, *Principles and Applications of Ion Scattering Spectrometry: Surface Chemical and Structural Analysis*, Wiley, New York, 2003.

94. M. Aizawa, S. Lee and S. L. Anderson. Deposition Dynamics and Chemical Properties of Size-Selected Ir Clusters on TiO_2. *Surf. Sci.*, 2003, **542**, 253-275.

95. A. Englemann. Über die Bestimmung der Lichtelektrischen Grenzwellenlänge am Rhenium. *Ann. d. Physik*, 1933, **409**, 185-208.

96. R. Schlaf, P. G. Schroeder, M. W. Nelson, B. A. Parkinson, C. D. Merritt, L. A. Crisafulli, H. Murata and Z. H. Kafafi. Determination of Interface Dipole and Band Bending at the Ag/tris(8-hydroxyquinolinato) Gallium Organic Schottky Contact by Ultraviolet Photoemission Spectroscopy. *Surf. Sci.*, 2000, **450**, 142-152.

97. R. Levy and M. Boudart. Platinum-like Behavior of Tungsten Carbide in Surface Catalysis. *Science*, 1973, **181**, 547-549.

98. Y. Kitsudo, A. Iwamoto, H. Matsumoto, K. Mitsuhara, T. Nishimura, M. Takizawa, T. Akita, Y. Maeda and Y. Kido. Final State Effect for Au 4f Line from Gold-Nano-Particles Grown on Oxides and HOPG Supports. *Surf. Sci.*, 2009, **603**, 2108-2114.

99. J. G. Tao, J. S. Pan, C. H. A. Huan, Z. Zhang, J. W. Chai and S. J. Wang. Origin of XPS binding Energy Shifts in Ni Clusters and Atoms on Rutile TiO_2 Surfaces. *Surf. Sci.*, 2008, **602**, 2769-2773.

100. B. Bellamy, S. Mechken and A. Masson. Metallic Clusters Surface Interaction: The Case of Palladium/Silicon Oxide (SiO_x)/n-silicon (100). *Z. Phys. D: At., Mol. Clusters*, 1993, **26**, 61-63.

101. G. K. Wertheim. Electronic Structure of Metal Clusters. *Z. Phys. D*, 1989, **12**, 319-326.

102. M. G. Mason. Electronic Structure of Supported Small Metal Clusters. *Phys. Rev. B*, 1983, **27**, 748-762.

103. I. Langmuir. The Mechanism of the Catalytic Action of Platinum in the Reactions $2CO + O_2 \rightarrow 2CO_2$ and $2H_2 + O_2 \rightarrow 2H_2O$. *Transactions of the Faraday Society*, 1921.

104. I. Langmuir. Chemical Reactions on Surfaces. *Transactions of the Faraday Society*, 1921.

105. J. Libuda, I. Meusel, J. Hoffmann, J. Hartmann and H.-J. Freund. Reaction Kinetics on Supported Model Catalysts: Molecular Beam/*in situ* Time-Resolved Infrared Reflection Absorption Spectroscopy Study of the CO Oxidation on Alumina Supported Pd Particles. *J. Vac. Sci. Technol. A*, 2001, **19**, 1516-1523.

106. I. Meusel, J. Hoffmann, J. Hartmann, M. Heemeier, M. Bäumer, J. Libuda and H.-J. Freund. The Interaction of Oxygen with Alumina-Supported Palladium Particles. *Catalysis Letters*, 2001, **71**, 5-13.

107. I. Meusel, J. Hoffmann, J. Hartmann, J. Libuda and H.-J. Freund. Size Dependent Reaction Kinetics on Supported Model Catalysts: A Molecular Beam/IRAS Study of the CO Oxidation on Alumina-Supported Pd Particles. *Journal of Physical Chemistry B*, 2001, **105**, 3567 -3576.

108. I. Stara and V. Matolin. The Influence of Particle Size on CO Adsorption on Pd/Alumina Model Catalysts. *Surface Science*, 1994, **313**, 99-106.

109. E. Gillet and M. H. El-Yakhloufi. Supported Palladium (Pd_n) (n=1-20) Cluster Reactivity: Carbon Monoxide Chemisorption. *Z. Phys. D: At., Mol. Clusters*, 1993, **26**, 64 -66.

110. M. S. Chen, Y. Cai, Z. Yan, K. K. Gath, S. Axnanda and D. W. Goodman. Highly Active Surfaces for CO Oxidation on Rh, Pd, and Pt. *Surface Science*, 2007, **601**, 5326-5331.

111. I. Z. Jones, R. A. Bennett and M. Bowker. CO Oxidation on Pd(110): A High-Resolution XPS and Molecular Beam Study. *Surf. Sci.*, 1999, **439**, 235-248.

112. F. S. Roberts, M. D. Kane, E. T. Baxter and S. L. Anderson. Oxygen Activation and CO Oxidation Over Size-Selected Pt_n/alumina/Re(0001) Model Catalysts: Correlations With Valence Electronic Structure, Physical Structure, and Binding Sites. *Physical Chemistry Chemical Physics*, 2014, DOI: 10.1039/c1034cp02083a.

113. Z. Zhang and J. T. Yates, Jr. Band Bending in Semiconductors: Chemical and Physical Consequences at Surfaces and Interfaces. *Chem Rev*, 2012, **112**, 5520-5551.

114. W. Schottky. The Semiconductor Theory of the Blocking Layer and Point Rectifier. *Zeitschrift fuer Physik*, 1939, **113**, 367-414.

115. W. Schottky. Semiconductor Theory of the Barrier Film. *Naturwissenschaften*, 1938, **26**, 843.

116. N. F. Mott. The Contact Between a Metal and an Insulator or Semiconductor. *Proceedings of the Cambridge Philosophical Society*, 1938, **34**, 568-572.

117. N. F. Mott. The Mean Free Path of Electrons in Polar Crystals. *Proceedings of the Royal Society of London, Series A: Mathematical, Physical and Engineering Sciences*, 1939, **171**, 496-504.

118. G. A. Somorjai. *Chemistry in Two Dimensions: Surfaces*, Cornell University Press, Ithaca, 1981.

119. J. F. Moulder, W. F. Stickle, P. E. Sobol, K. D. Bomben and J. J. Chastain & R. C. King, eds. *Handbook of X-ray Photoelectron Spectroscopy*, Physical Electronics, Eden Prarie, MN, 1995.

120. S. Peters, S. Peredkov, M. Neeb, W. Eberhardt and M. Al-Hada. Size-Dependent XPS Spectra of Small Supported Au-Clusters. *Surf. Sci.*, 2013, **608**, 129-134.

121. B.-H. Mao, R. Chang, S. Lee, S. Axnanda, E. Crumlin, M. E. Grass, S.-D. Wang, S. Vajda and Z. Liu. Oxidation and Reduction of Size-Selected Subnanometer Pd Clusters on Al_2O_3 Surface. *J. Chem. Phys.*, 2013, **138**, 214304.

122. A. Michaelides, P. Hu, M. H. Lee, A. Alavi and D. King. Resolution of an Ancient Surface Science Anomaly: Work Function Change Induced by N Adsorption on W(100). *Physical Review Letters*, 2003, **90**.

123. P. Bagus, D. Käfer, G. Witte and C. Wöll. Work Function Changes Induced by Charged Adsorbates: Origin of the Polarity Asymmetry. *Physical Review Letters*, 2008, **100**, 125501.

124. T. Leung, C. Kao, W. Su, Y. Feng and C. Chan. Relationship Between Surface Dipole, Work Function and Charge Transfer: Some Exceptions to an Established Rule. *Physical Review B*, 2003, **68**, 195408.

CHAPTER 5

MASS-SELECTED SUPPORTED CLUSTER CATALYSTS: SIZE EFFECTS ON CO OXIDATION ACTIVITY, ELECTRONIC STRUCTURE, AND THERMAL STABILITY OF Pd_n/ALUMINA ($n \leq 30$) MODEL CATALYSTS

Reprinted from M. D. Kane, F. S. Roberts and S. L. Anderson. International Journal of Mass Spectrometry, 2014, 370, 1-15, with permission from Elsevier. The original article can be found online at: http://www.sciencedirect.com

5.1. Introduction

Catalysts are important in 35% of the world GDP[1], thus it is not surprising that there is extensive fundamental and applied research aimed at improving catalytic activity and selectively.[2-18] Typical supported catalysts are quite complex and difficult to characterize in detail, and an important research thrust uses model catalysts to simplify the problem and allow important properties to be varied and measured in detail, to extract mechanistic insight. Among other approaches to tuning catalyst properties, using bi- or tri-metallic combinations,[7, 19-22] or varying the size of the catalytic metal particles are common.[2, 23-28] Understanding the effects of particle size is complicated by the fact that there is typically a broad distribution of sizes present, and it is generally not possible to vary size independently, without also changing other properties such as metal loading or support structure. Consider gold nanocatalysts, which have received tremendous attention over the past decade, using a wide variety of approaches.[17, 29-33] Much of the original work focused on the properties of Au nanoparticles in the 2 – 5 nm size range, because these were the obvious species detectable in conventional electron microscopy.[34-37] Planar model catalyst work suggested that smaller gold structures were reactive,[38-45] and size-selected cluster deposition experiments similar to those discussed here, showed significant activity for gold clusters as small as seven or eight atoms.[15, 17, 30, 46-50] Development of aberration-corrected scanning transmission electron microscopes allows features on the atomic scale to be detected in supported catalysts, and allowed studies showing that clusters in the ~10 atom size range are highly active under realistic conditions.[51, 52]

Preparation of catalysts by deposition of mass-selected cluster ions on well

characterized supports, provides a powerful mechanistic tool, allowing studies where cluster size, composition, density, and impact energy can be varied independently. Cluster deposition has applications in catalysis, magnetic and electronic materials, as well as being useful in studying the fundamental properties of nanostructures. Our group has focused on exploring size-dependent correlations between catalytic activity and physical properties such as cluster electronic structure and morphology, using CO oxidation to probe systems such as Au/TiO_2,[49] $Pd/TiO_2(110)$,[6, 24, 53, 54] Pd/Al_2O_3,[55, 56] and Pt/Al_2O_3.[57] We also recently observed a very strong size-dependent correlation between Pt electronic structure and electrocatalytic activity for Pt/glassy carbon, where some sizes showed the expected Pt redox and oxygen reduction activity, but other sizes efficiently catalyzed electro-oxidation of carbon by water. [2] The Heiz group has reported numerous studies of catalysis with recent work including CO oxidation kinetics over Pd clusters deposited on MgO,[13, 14, 58-61] optical spectroscopy of deposited clusters and adsorbates,[62, 63] studies of oxide support thickness effects on cluster activity,[15, 64] Pt_n deposition on CdS nanorod films for photocatalysis studies,[65] and STM studies of cluster mobility on graphene/Ru(0001) Moiré supports.[66] In collaboration with Arenz, this group has also reported studies of electrocatalytic activity of supported Pt clusters.[67-71] Harbich and co-workers have carried out STM and reactivity studies of deposited clusters, and recently reported studies focusing on the fundamentals of CO oxidation over Pt_n/TiO_2[72, 73] and of electrocatalysis, using an approach where Pt clusters are deposited directly on a solid electrolyte, allowing electrochemistry to be studied *in vacuo*.[7, 74] The Vajda group has an active program where size-selected catalysts are studied in a variety of reactors, recently focusing on *in operando* studies using tools such as x-ray scattering, to probe chemistry

under realistic reaction conditions.[75 76-78 79 10, 80 81 9 4, 82, 83] Buratto and co-workers have used cluster deposition in conjunction with STM and theory to examine stability and reactivity of several types of clusters on TiO_2(110), with recent work focusing on vanadia clusters on titania.[84] Ganteför and co-workers developed another instrument combining cluster deposition with STM and used this for a number of studies of Au_n deposited on several supports.[85-88] This work has proceeded in collaboration with Kim and coworkers, recently focusing on gold chemistry under ambient conditions.[32, 89-91] Watanabe and coworkers have an instrument that allows STM, XPS, and high pressure reactivity studies of size-selected model catalysts[92] and have reported studies of CO oxidation over Pt_n/TiO_2(110)[11, 93] and correlations with core level binding energies. White and co-workers studied properties and reactivity of Mo_4S_6 deposited on Au(111)[94], and used two photon photoemission to probe charging of several different size and stoichiometry Mo_xS_y clusters on alumina supports.[95] Chorkendorff, Nielsen, and co-workers have developed a program using mass-selected cluster deposition to study chemistry and morphology changes under both UHV and high pressure reaction conditions.[96-98] Recently, Bowen, Fairbrother, Ganteför and co-workers have reported work on deposited clusters including stability of size-selected Mo nanoparticles on highly ordered pyrolytic graphite (HOPG),[99] and gold clusters supported on TiO_2 showing single atom sensitivity to reactivity for CO oxidation.[100]

For the system studied here, CO oxidation over Pd/alumina, there has been a tremendous amount of relevant work that provides valuable mechanistic insight. Briefly, using Pd single crystals and other bulk surfaces, it had been shown that CO and O_2 combine to form CO_2 via a Langmuir-Hinshelwood mechanism that entails adsorbed CO

reacting with adsorbed O atoms.[101-105] It was also shown that oxygen and CO compete for the same binding sites such that a 60% saturation dose of CO prevents dissociative binding of O_2 on Pd(110). The kinetics of the CO oxidation reaction over Pd single crystals[103-106] and Pd/alumina nanoparticle catalysts[107-111] have been discussed in detail. Furthermore, it was determined for room temperature experiments, that CO and O_2 have reasonably high sticking coefficients of 0.5 and 0.4, respectively.[112] For Pd(111) it was shown that for greater than ~0.15 ML coverage of oxygen, dissociative adsorption of further oxygen became an activated process.[113] In the temperature-programmed reaction (TPR) experiments discussed below, the samples were exposed to O_2 prior to CO, to avoid CO poisoning. There has also been considerable previous work on Pd clusters/nanoparticles on alumina films. For example, Goodman and coworkers investigated the Pd cluster size needed to transition from nonmetallic to metallic characteristics, [114] as well as the adsorption and further oxidation of Pd clusters in the size range of 25 – 70 nm on powdered alumina surfaces. [115, 116] The Freund group did similar studies for Pd nanoclusters in the 0.5-14 nm range deposited on alumina films grown on NiAl(110), examining particle growth[117] and CO binding via infrared spectroscopy, to probe charge transfer between the particle and the alumina support.[118] The self-limiting, 0.5 nm thick alumina film that grows on NiAl(110) when heated in O_2 has been used in numerous model catalyst studies. We previously attempted to study CO oxidation over size-selected Pd_n deposited on alumina/NiAl(110), but no reaction was observed.[56] Experiments by Shaikhutdinov et al. on CO oxidation over Pd nanoparticles grown on the same support showed that the problem was that the alumina film was too thin to act as an efficient diffusion barrier, allowing oxygen activated on the Pd clusters to react with the

NiAl substrate, in preference to CO.[114] In the experiments below, thicker alumina films are grown by aluminum evaporation in an O_2 atmosphere, following methods developed to produce alumina films on Ta, Re, or Ru single crystals.[119-121] Epitaxial growth of alumina on Ta and Re crystals provides a chemically inert, thermally stable support which is ideal for the size-dependent mechanistic studies discussed below.[55, 57] The alumina support isolates the Pd clusters from the underlying metal support, but the oxide also influences the chemistry. For example, as discussed below, both the overall reactivity and its size dependence is substantially different for Pd_n supported on alumina films vs. TiO_2(110), under identical conditions.

5.2. Experimental

5.2.1 The Apparatus

The experiments were done in the vacuum system shown in Figure 5.1, which has been briefly described previously,[49, 50, 55, 122] however, a number of changes have been made to improve operation. The system consists of two main sections: a cluster deposition source/beamline (top) and an ultra-high vacuum (UHV) surface preparation/analysis system (bottom). The coaxial laser vaporization cluster ion source is shown in detail in Appendix B. The beam from a frequency-doubled Nd:YAG laser (30 Hz, 30 – 60 mJ/pulse) is focused on the Pd target through the cluster exit nozzle, creating a Pd-containing plasma. Approximately 300-500 microseconds before the laser pulse, helium is pulsed into the elliptical source volume using a piezoelectric pulsed valve (4500 Torr through a 1 mm orifice for 1 msec) to help confine and cool the plasma, leading to supersaturation and cluster formation. The cluster size distribution can be

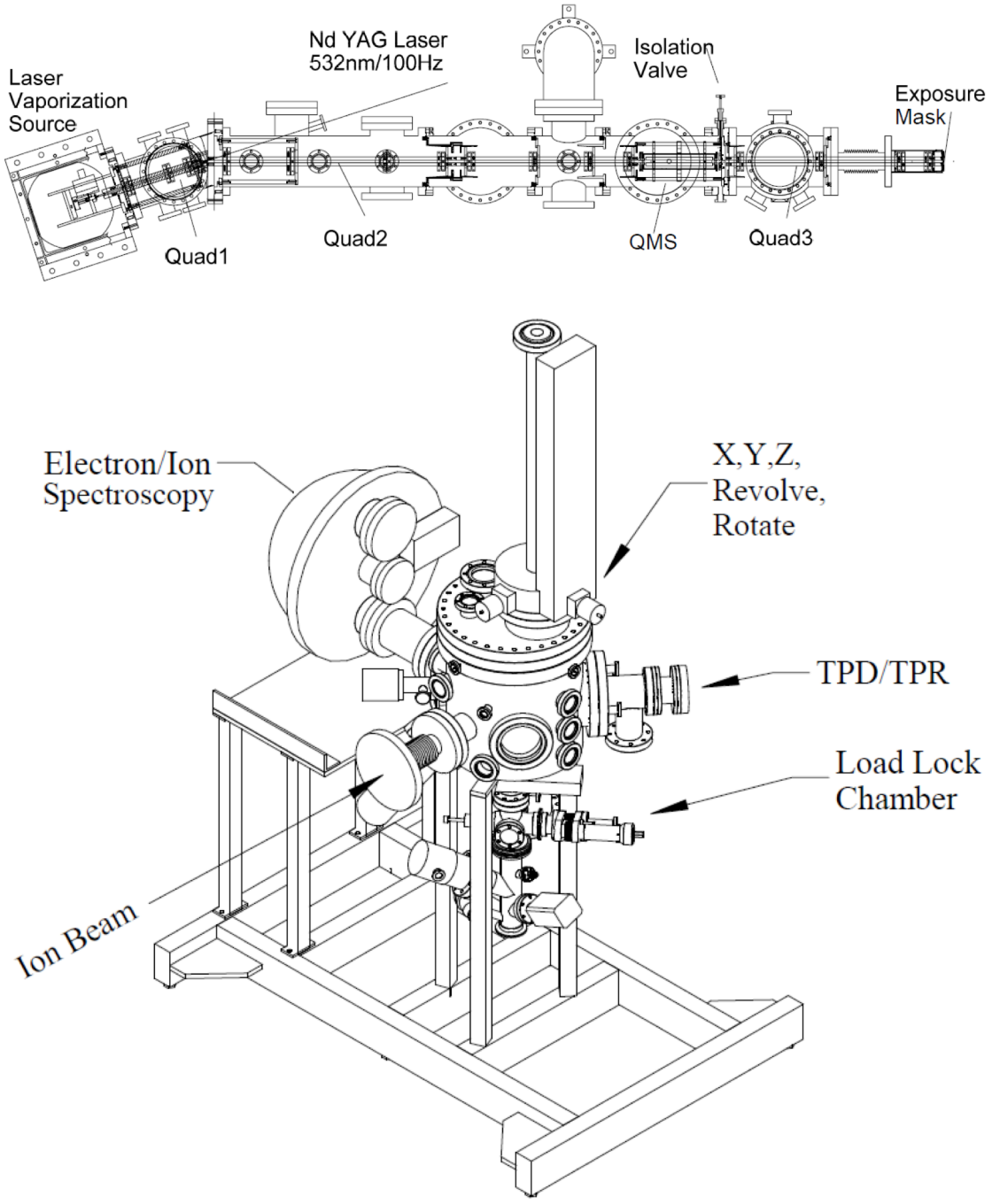

Figure 5.1: Cluster deposition beamline (top), and UHV surface preparation and analysis system (bottom). The beamline is connected to the UHV system at the flange labeled "Ion Beam"

controlled to some extent by changing the source residence time, via interchangeable exit tubes of various lengths.

The Pd target is glued to a spring-loaded aluminum block, which is mounted to an X-Y translation stage, allowing the target to be rastered, so that vaporization occurs uniformly over the target area (~1 cm x 2 cm). A target can be used for about 100 deposition experiments before becoming rough enough to seriously degrade source stability. The target is then simply sanded flat and reused until the laser begins to penetrate through to the glue layer. Two targets, each good for > 300 depositions, can be fabricated from a single 99.9% Pd one ounce bullion bar, making the target cost negligible. A good seal and low sliding friction between the target and source body is critical, and for this purpose, a 0.1 mm thick Teflon gasket is bonded around the edge of the target. Motion of the X-Y stage is driven by stepping motors, allowing easy control over the raster pattern. The motors and source body are water-cooled to prevent overheating and enhance clustering.

The cluster-containing helium expands out of the exit nozzle, directly into the first of a series of quadrupole ion guides, which collects the ionized clusters and allows helium to pump away. Pressure in the source chamber is ~45 mTorr during deposition, dropping to ~5 mTorr in the first quadrupole chamber. All potentials on the beamline are referenced to an adjustable common potential, which is varied to set the deposition energy. The source is typically biased at -5 V with respect to this common potential, and the first quadrupole ion guide is biased at 0 V, decelerating the clusters, which exit the source with considerable kinetic energy due to the helium expansion. This ion guide is operated with radio-frequency (RF) amplitude of 200-500 V, at a frequency of 1.8 MHz.

The first quadrupole guides the clusters to a split electrode, built into the differential wall between the "Quad1" and "Quad2" vacuum chambers. At this point, the positive ions are deflected by 18°, and enter the second quadrupole guide. The bend eliminates negative ions and neutrals from the beam and allows coaxial injection of the laser into the source. The second quadrupole guides the clusters ions through three additional differential pumping walls, and operates with an RF voltage of 300-550 V at 1.8 MHz, with a DC bias potential of approximately 3 V, depending on cluster size. The pressure at the exit of this second quadrupole (in the "QMS" chamber) is ~2 x 10^{-6} Torr during operation, with base pressure of 2 x 10^{-8} Torr.

The ions are focused from the second quadrupole guide into a mass selecting quadrupole (QMS) operated at 880 KHz, able to mass-select Pd_n^+ to at least n = 30. The QMS is homemade, with 9.5 mm diameter rods and short RF-only pre- and postfilter sections that can be adjusted to optimize transmission, and is driven by commercial electronics (Extrel). The cluster mass spectrum shows no evidence of multiply charged species such as Pd_n^{m+} (n odd), indicating that our operating conditions generate predominantly singly charged cluster ions. The QMS is operated at sufficient resolution to baseline resolve the spectrum of Pd_n^+ produced in the source, thus the clusters deposited on the substrate are exactly size-selected. The more difficult question is whether the clusters remain intact, or whether they agglomerate or shatter upon impact. The instrument does not have scanning tunneling or other imaging capabilities, thus we rely on indirect evidence on this issue. In particular, we observe that both chemical activity and spectral properties of samples vary significantly with deposited cluster size, thus implying that the model catalysts retain "memory" of the deposited size. At the exit

of the QMS, the mass-selected cluster beam passes through a set of four lenses, which also function as a differential pumping wall. A 1 mm thick, pneumatically actuated slide valve is built into one of the lenses, allowing the beamline to be isolated from the UHV section of the instrument except during cluster deposition. This capability is critical, allowing the source and other beamline components to be serviced without venting the UHV section of the instrument, which must be baked for several days after exposure to atmosphere. After passing through the valve/lens, the clusters enter a final quadrupole ion guide (Quad3), operated with RF voltage of 150-600 V at 2.0 MHz, with DC bias potential of roughly -20 V. The pressure in the Quad3 chamber during deposition is 10^{-8} Torr, and the base pressure is in the mid-10^{-10} Torr range.

At the exit of the final quadrupole guide, the ions pass through a thin, 2 mm diameter electrode that functions as a lens, exposure mask, and differential pumping aperture. For deposition, the sample substrate is positioned 1 mm behind the exposure mask and grounded via an electrometer, to allow continuous measurement of the current of Pd_n^+ on the sample. For the experiments described below, the cluster deposition energy was set at 1 eV/atom, as determined by retarding potential analysis on the deposition substrate. One eV/atom is smaller than typical metal-metal bond energies, as well as typical bond energies of metal atoms to oxide supports, and thus corresponds to soft landing condition, while still allowing high beam intensities to be delivered to the sample. Intensity is critical, even in UHV, to minimize adventitious contamination of the highly dispersed clusters.[54, 123, 124] The total Pd coverage deposited on each sample was held constant at 1.53×10^{14} Pd atoms/cm^2, equivalent to 10% of a close-packed Pd monolayer (0.1 ML equivalent). The samples differ, therefore, only in the size of the

Pd_n^+ with which the Pd coverage is delivered. Typical deposition currents for various cluster sizes are listed, along with the corresponding deposition times are located in Appendix B. The fact that deposition times are longest for small clusters (~ 30 minute deposition times) reflects the fact that the source was optimized for large clusters (~5 minute deposition times), by using a long exit nozzle to increase the residence time.

The analysis chamber is equipped with tools for surface preparation and analysis, allowing chemical and physical properties of the samples to be probed without air exposure. Tools available include X-ray photoelectron spectroscopy (XPS), ultraviolet photoelectron spectroscopy (UPS) and low energy He^+ ion scattering spectroscopy (ISS) for electronic structure and morphology characterization. In addition, the chamber is equipped with two mass spectrometers for reaction studies. One is a residual gas analyzer (SRS Inc. RGA-100) used to monitor gas doses to the sample. To monitor reactants and products desorbing from the catalyst samples, we use the arrangement shown in Appendix B. A UTI 100c quadrupole, driven by 2.1 MHz Extrel electronics, is housed in a separately pumped UHV chamber that views the analysis chamber through a 2.5 mm diameter aperture at the tip of a skimmer cone, which is surrounded by six directional gas dosing lines. The dosing lines are fed by three variable leak valves and three pulsed valves, allowing both pulsed and continuous gas exposures. During dosing, the sample is positioned 2 mm from the skimmer orifice, and is typically moved 1 mm from the orifice for desorption studies. The directional dosing tubes provide a ten-fold increase in exposure at the sample surface, relative to the exposure at the chamber walls, thereby minimizing degradation of the chamber vacuum during reactivity studies. The exposure rate from the tubes was calibrated by comparing exposures through the tubes

and by backfilling the chamber.[53]

The clusters are deposited on an alumina support film, which is grown on a 10 x 5 x 1 mm Re(0001) single crystal (Marketech International), spot welded to a pair of Ta heating wires, which are spot welded to a pair of 1 mm thick Ta support rods that hang from a liquid nitrogen-filled cryostat. The cryostat is mounted on a XYZ/rotation manipulator, which is, in turn, mounted on a 38 cm diameter homemade rotary platform, with triple, differentially pumped seals. The combination allows the sample to be positioned for deposition, spectroscopy, mass spectral probing, or surface preparation. The sample can be cooled to ~125 K and resistively heated to 1200 K. For the higher temperatures required during sample cleaning/annealing, electron bombardment from the back side heats the sample to 2200 K. Temperature is measured by a type C thermocouple spot welded to the back of the Re(0001) single crystal. Commercial type C vacuum feedthroughs use pins made from 405/426 extension alloy, rather than actual type C material (W5%Re and W26%Re), and in our experience, the performance was inadequate at cryogenic sample temperatures, where the type C sensitivity (mV/K) is low. Feedthroughs were, therefore, fabricated using 1 mm pins of type C material, nickel plated and soldered into tubular commercial feedthroughs. The resulting thermocouple system was calibrated against a K type thermocouple attached to the sample, with excellent agreement over the temperature range from 125 – 1600 K (i.e., $< T_{melt}$ for K type wire).

A small UHV "load lock" chamber is attached to a port under the analysis chamber, as shown in Figure 5.1. When the sample is lowered into this small chamber, it is isolated by another triple differentially pumped seal, allowing the lower chamber to be

pressurized up to 1 atm without affecting the analysis chamber pressure. For the experiments here, the lower chamber was used to grow the alumina support film, to avoid exposing the analysis chamber to high $^{16}O_2$ pressure, which tends to result in elevated water background, presumably due to reaction with hydrogen on the chamber walls. The lower chamber can also be opened for repair of the aluminum vaporization source or sample, as needed.

5.2.2 Model catalyst preparation

Typical samples consisted of 0.1 ML-equivalent of Pd_n deposited on an alumina support film grown on a Re(0001) single crystal, following procedures developed by Wu et al.[120] and Chen et al.[121] To clean and prepare the Re crystal for an experiment, the sample was simply heated in vacuum to 1770 K for 25 minutes. The sample was then probed by XPS to ensure that all of the alumina and Pd from the previous experiments was desorbed, and to check for carbon or other contaminants. Occasionally, particularly if the previous experiment involved an unusually thick alumina film, it was necessary to repeat the cleaning process. According to the literature, heating in this temperature range is also sufficient to anneal the Re crystal, resulting in a sharp LEED pattern.[125] After cleaning, the only contaminant observed was oxygen, present in sub-monolayer concentrations, which is not a problem because the next step in the sample preparation involves heating the Re in oxygen, prior to starting alumina deposition. The alumina film was grown in the lower chamber resistively heating the Re(0001) crystal to 970 K in a background of $5x10^{-6}$ Torr of ultrahigh purity $^{16}O_2$, which was further purified by passing the O_2 gas line through an ethanol/liquid nitrogen bath just before leaking into the lower

chamber. Aluminum was evaporated onto the Re support in the O_2 atmosphere, using a home-made evaporator consisting of a shrouded, resistively heated alumina crucible filled with 99.999% aluminum. The film growth rate was set to 0.2 ± 0.01 nm/min, as determined from Al and Re XPS peak intensities as a function of deposition time.

Similar alumina films grown using this procedure have been characterized by LEED and ISS.[119-121, 126] It was reported that the films grow by coalescence of islands, forming complete, continuous films at ~0.6 nm thickness for alumina grown on Ta(110), and at ~1.5 nm for alumina grown on Re(0001). Our ISS results show a small, but significant Re signal in ISS, even for films up to 10 nm thick, suggesting that there is diffusion of Re into the alumina, doping the surface layer with ~1% Re.[127] Such doping of oxide overlayers by diffusion of atoms from the support crystal has been seen in other systems,[6, 55, 128, 129] and the dopant atoms may act as anchoring sites for deposited metal clusters.[128] We carried out a detailed study of the thickness dependence of both the physical and chemical properties of the alumina/Re(0001)[127] and alumina/Ta(110) films,[55] and as expected, the properties become thickness-independent for films thicker than ~2.7 nm and 4.5 nm, respectively. Because of Re doping, the alumina films are reasonably conductive, and signs of charging (e.g., shifts in UPS or XPS peak energies) are observed only for films thicker than ~7 nm.[127] To avoid this issue in the present study, all experiments were done on films in the 3-6 nm thick range. The thickness was estimated from the intensity ratios of the Al 2s and Re 4f peaks measured by XPS, using photoemission cross sections and β parameters from the literature,[130] and effective attenuation lengths calculated using the NIST Electron Effective-Attenuation-Length Database.[131] The estimation ignores Re mixing into the alumina film, and therefore the

thicknesses are slightly underestimated. The estimated absolute uncertainty in film thickness is ±20%, however, the relative uncertainty in comparing thicknesses of different films is estimated to be less than 5%.

5.2.3 Characterization and reactivity measurements

After preparation and characterization of the alumina film, Pd_n was deposited at 300 K with a Pd density of 0.1 ML equivalent in a ~2 mm diameter spot. A combination of XPS and UPS was used to probe the sample electronic structure, both as deposited, and after changes due to a sequence of surface reactions. XPS was done using Al Kα X-rays from a dual anode source, and UPS was done using He I radiation (21.1eV) from a differentially pumped discharge lamp.[132] After XPS characterization of the freshly deposited Pd_n/alumina samples, the samples were cooled to ~130 K in approximately 25 minutes, for temperature-programmed reaction (TPR) studies of activity.

The sequence used in the TPR studies is as follows. The samples were first flashed to 560 K to remove any adventitious adsorbates, then cooled quickly to 400 K (~2 min), at which point they were exposed to 10 L of $^{18}O_2$, corresponding to roughly two O_2 molecules impinging per surface atom, on average. The oxygen is 99 at.% ^{18}O, and was passed through an ethanol/liquid nitrogen bath (~160 K) to remove any condensable contaminants. After oxidation, the sample was cooled to 180 K where it was exposed to 10 L of $^{13}C^{16}O$. This CO dose temperature was chosen for comparison to previous studies of CO oxidation over Pd_n/TiO_2. The sample was then cooled to 135 K and centered 1 mm in front of the differentially pumped mass spectrometer, then heated to 560 K at 3 K/sec, while the mass spectrometer rapidly cycled between monitoring mass

18 (H_2O or ^{18}O), 20 ($H_2{}^{18}O$), 36 ($^{18}O_2$), and all isotopologs of CO and CO_2.

To allow observation of changes in sample chemical properties induced by TPR, each sample was probed by three sequential TPR runs, including oxidation at 400 K and CO exposure at 180 K. After completion of the three TPR runs, the sample was probed by CO temperature-programmed desorption (TPD), using a protocol identical to that used for TPR, with the exception that there was no $^{18}O_2$ exposure. Because (see below) CO binds to Pd_n, but not to the alumina film, the CO TPD results provide a measure of the Pd binding site density remaining after TPR. Furthermore, measuring CO_2 desorption during this final CO TPD run probes the extent to which any reactive ^{18}O is left on the surface at the conclusion of the TPR runs. It is useful, mechanistically, to convert the ion signals recorded during TPR/TPD to the corresponding number of CO or CO_2 molecules desorbing from the samples. The sensitivity calibration procedure is discussed in the supplementary information, and the molecular fluxes given below are estimated to be accurate to within a factor of 2. For reasons described in Appendix B, it appears that the estimates may be on the low end of the uncertainty range.

Finally, to probe Pd_n morphology and adsorbate binding, scattering of 1 kV He^+ (i.e., ISS) was used, with either low (0.15μA) or high (1.15 μA) He^+ flux. Raw ISS data consist of kinetic energy (E) spectra for He^+ scattered from the surface, plotted as a fraction of the incident energy (E_0). Only a small fraction of the incident beam survives to scatter from the surface as He^+, mostly in events where He^+ scatters from a single atom in the surface layer.[54, 122, 133] Such events lead to well defined peaks, with E/E_0 indicating the mass of the surface atom. A broad background results from subsurface and/or multiple scattering events, and this signal is weak because the He^+ ion survival

probability is low in such trajectories. ISS, therefore, is a probe of the distribution of different elements in the top-most layer of the sample. As such, it is sensitive to cluster morphology, and binding of adsorbates on the cluster surface. Because ISS damages the surface, these experiments were either done at the end of an experimental sequence to generate "postreaction" results, or using separately prepared samples to generate "as-deposited" results.

5.3. Results and discussion

5.3.1 Pd_n size dependent reactivity

Figure 5.2 shows typical TPR results, in this case for a Pd_{25}/alumina/Re(0001) sample exposed to 10 L of $^{18}O_2$ at 400 K, and 10 L of ^{13}CO at 180 K. As shown below, results for other cluster sizes are similar. The sample was then cooled to 130 K, and heated at 3K/second while monitoring all CO, O_2, and CO_2 isotopomers. No desorption signal was observed for $^{18}O_2$, and the only significant signals for CO and CO_2 were residual, unreacted $^{13}C^{16}O$ and the $^{13}C^{16}O^{18}O$ product. It can be concluded, therefore, that ^{18}O bound on the surface does not desorb as $^{18}O_2$ in this temperature range, and that ^{16}O present in the alumina film is not significantly involved in CO oxidation under these conditions. Data are shown for the three sequential TPR runs, and for the subsequent CO TPD run, where the 400 K $^{18}O_2$ exposure was omitted. Control experiments on alumina/Re(0001) without deposited Pd show no evidence for CO_2 production, indicating that the active sites are associated with Pd.

One obvious point is that both the CO_2 production and residual CO desorption are

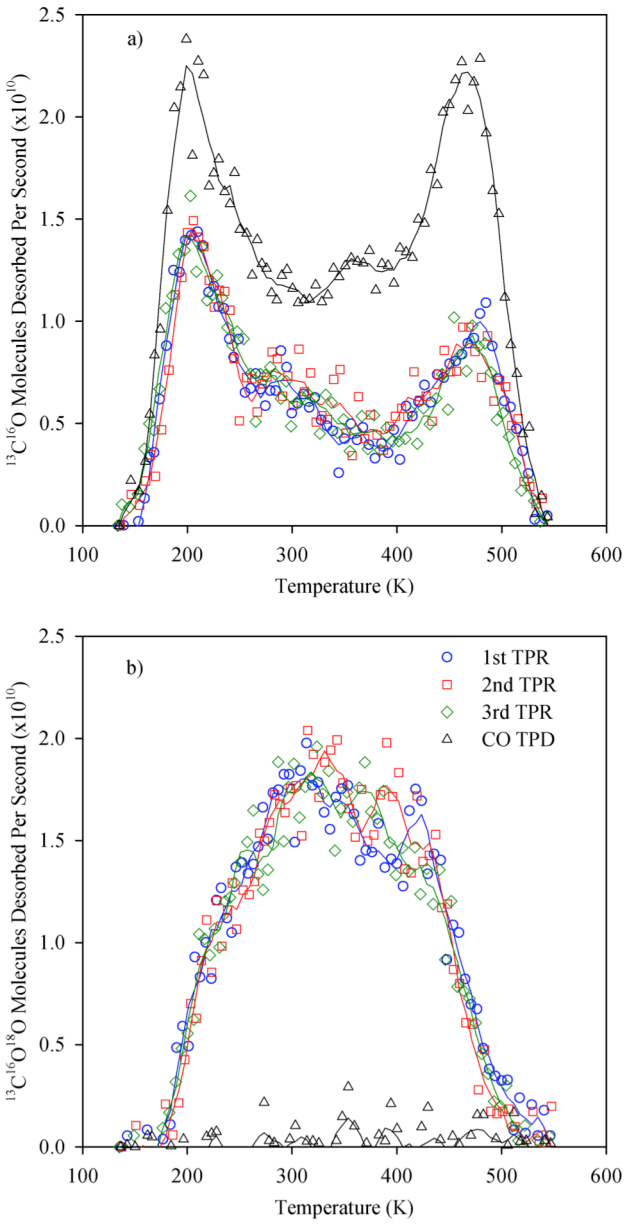

Figure 5.2: Consecutive CO and CO_2 desorption from a sample of 0.1 ML Pd_{25}/alumina/Re(0001). (a) Residual CO desorption during three consecutive TPR measurements on Pd_{25}/alumina/Re(0001), followed by a CO TPD measurement. (b) CO_2 production during each of the three TPR measurements, and the CO TPD measurement. For both of these figures the first, second, and third TPR measurements are plotted in blue (circles), red (squares), and green (diamonds), respectively. The final CO TPD measurement is plotted in black (triangles). For all TPR measurements, the sample was exposed to 10 L $18O_2$ at 400 K and 10 L ^{13}CO at 180 K. The final CO TPD measurement were exposed to the same 10 L ^{13}CO at 180 K, with no $^{18}O_2$ exposure.

consistent from run to run, i.e., the model catalyst, as prepared, is quite stable under these conditions. Further probes of catalyst stability are discussed below. CO_2 is produced in a broad feature that starts at 180 K, and terminates at ~500 K. The observation that the CO_2 feature starts at 180 K simply reflects the fact that the CO exposure was done at 180 K, reacting away any adsorbed oxygen capable of reacting at lower temperatures. The CO_2 produced during the CO dose was also measured, and amounts to only 2-3% percent of the total CO_2 production. Furthermore, the lack of ^{12}CO or $^{12}C^{16}O^{18}O$ desorption during TPR suggests that any adventitious ^{12}CO that might have adsorbed on the sample during deposition, XPS characterization, and cooling, was removed by the combination of the 560 K flash and 400 K O_2 exposure.

Desorption of unreacted CO is bimodal, and the sharp decline in CO_2 production at high temperatures is coincident with growth of the higher temperature CO desorption peak. The most obvious interpretation is that oxygen activated on the clusters is the limiting reactant, and that it is all reacted away by about 500K, leaving the balance of the CO to desorb unreacted. There may be some oxygen remaining on the clusters, but so stably bound that it is unreactive in the temperature range where CO remains on the surface. If so, this stably bound oxygen cannot have any effect on O_2 activation, CO binding, or CO_2 production in the second and third TPR experiments, which seems unlikely. Testing for the presence of active oxygen was part of the purpose for the final CO TPD experiment, carried out after the three TPR runs. Production of CO_2 and CO isotopomers was monitored, both during the 180 K ^{13}CO exposure, and during the subsequent heat ramp. No CO_2 was observed, indicating that there is no *active* oxygen left on the surface at the end of the TPR.

The amount of CO desorbing in this final CO TPD is roughly twice the amount of residual CO desorbing during TPR. There are two contributing factors. A significant fraction of the CO adsorbed on the pre-oxidized samples is reacted away during TPR. Additionally, CO and oxygen are expected to compete for binding sites, thus adsorption of oxygen probably blocks sites for subsequent CO adsorption. This competition between CO and oxygen for binding sites is also observed for bulk Pd surfaces or larger Pd nanoparticles.[103-105, 134]

One question is whether the broad CO_2 desorption temperature dependence is controlled by the energetics for the reaction of $CO_{ads} + O_{ads}$ on the surface, or by the desorption energy of the CO_2 product. Typically, CO_2 binds weakly to metal surfaces,[135-138] and to see if that is also true here, we ran TPD experiments where Pd_n/alumina/Re(0001) samples were exposed to CO_2 at various temperatures. It is not obvious whether sticking of molecular CO_2 should be an activated process or not, therefore we tried this experiment using CO_2 exposure temperatures ranging from 180 K to 400 K. In no case was there any evidence of CO_2 sticking to the surface. It is conceivable that CO_2 formed on the surface by reaction might have different desorption properties, but we tentatively conclude that the CO_2 temperature dependence during TPR, reflects the energetics of the CO oxidation reaction, rather than CO_2 desorption. In that case, there is clearly a considerable range of activation energies, presumably reflecting the variety of O and CO binding sites possible on these samples.

Figure 5.3 shows how the integrated CO_2 production varies with cluster size. Results from each of the three TPR runs are shown as open symbols, and the average of the three runs is shown as a solid symbol. Roughly 0.2 CO_2 molecules are produced *per*

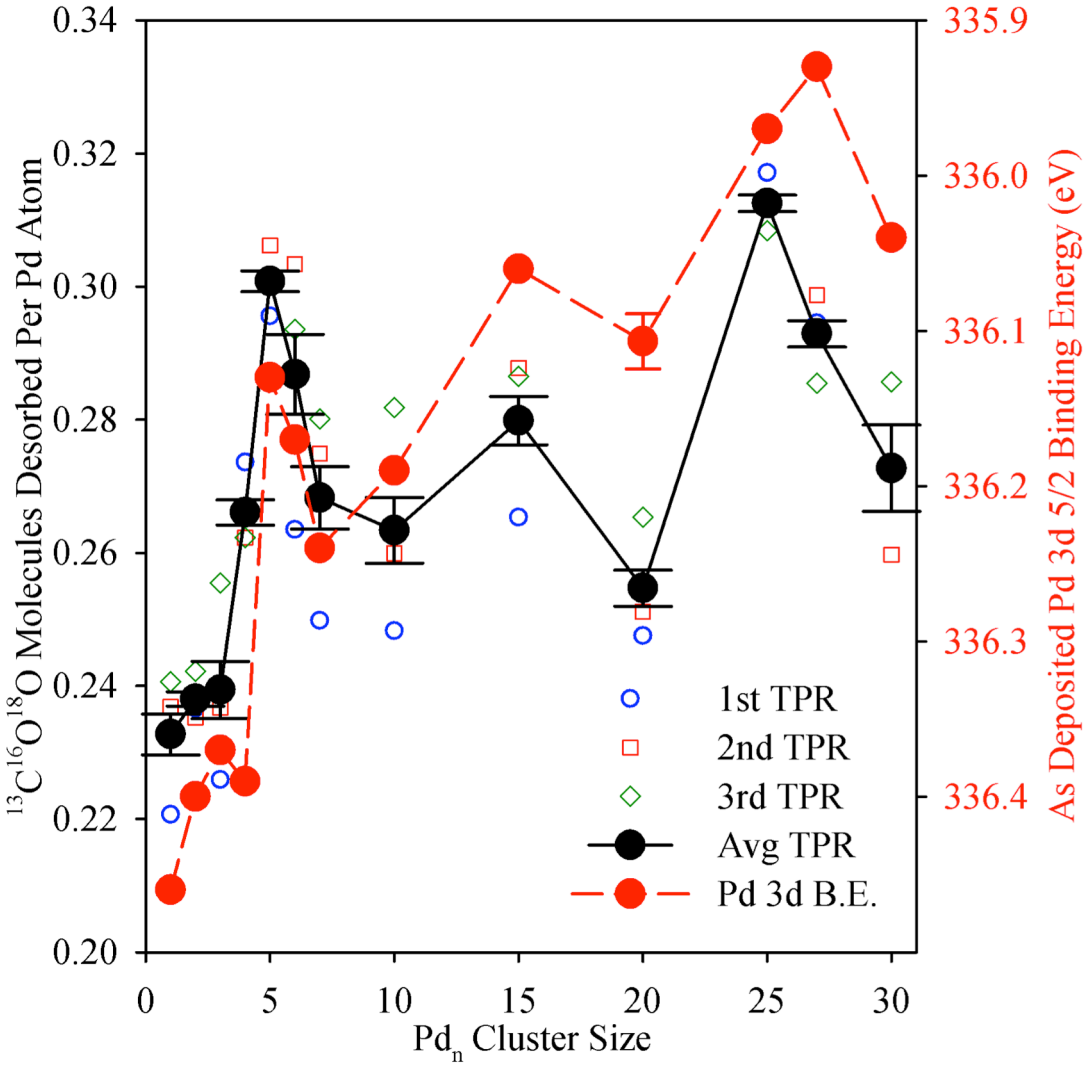

Figure 5.3: The integrated amount of CO_2 produced from the first, second, and third TPR measurements are plotted against the left axis, as a function of Pd_n cluster size, along with the average of the three TPR measurements, with error bars representing the standard error. The as-deposited Pd 3d 5/2 binding energy is plotted against the right axis (note inverted scale). The error bar on the point for Pd_{20} is the standard error from a series of measurements on different samples.

deposited Pd atom, thus the number of CO_2 produced *per cluster* increases from ~0.8 for Pd_4 to ~6 for Pd_{30}, although, as discussed, these numbers are probably low, by up to a factor of 2. As indicated, the results are quite stable from run to run, so that the random error is only ~1%. It can be seen that activity is weakly dependent on cluster size, varying by only ~40%. The most reactive samples had Pd_5 and Pd_{25} deposited.

Appendix B shows the variation in integrated CO desorption with cluster size, showing both total CO, and CO associated only with the high temperature (HT) desorption component, in both TPR and TPD experiments. The separation of the HT component was based on simulations of the data, discussed below. The results are shown as CO/Pd atom, and again, could be low by up to a factor of 2. For the TPD measurements, where there is no competition with adsorbed oxygen for binding sites, the coverage of CO is roughly constant at ~0.45 CO/Pd atom, with ~0.2 CO/Pd desorbing in the HT desorption feature. The observation of weak dependence of CO coverage on cluster size is not surprising, and is consistent with the ISS results discussed below. During TPR, the amount of unreacted CO desorbing is reduced by roughly a factor of 2, for both the total and HT CO desorption, due to some combination of CO oxidation to CO_2 and competition between oxygen and CO for binding sites. Comparison of Figures 5.3 and Appendix B shows that roughly equal integrated amounts of CO and CO_2 desorb during TPR, i.e., about half the CO adsorbed during TPR is converted to CO_2 under these conditions. Furthermore, the combined CO and CO_2 desorption during TPR is similar to the CO desorption during the TPD run, suggesting that binding site competition between pre-adsorbed oxygen and CO does not substantially reduce the amount of CO that adsorbs. By comparing the temperature dependence for CO_2 production for different size

clusters, shown in Appendix B, it can be seen that Pd_5 and Pd_{25} have increased reactivity at temperatures above 400K. This suggests that these two active clusters are able to activate more oxygen, which results in CO_2 production at higher temperatures before the oxygen is depleted.

To further probe the kinetics of O_2 activation on the Pd clusters, and to test the hypothesis that activated oxygen is the limiting reagent under these conditions, additional experiments were performed. If oxygen is limiting, then one might expect that using a larger O_2 exposure might lead to additional adsorption of oxygen, and therefore higher CO oxidation activity. This hypothesis was tested for Pd_5 using a TPR protocol identical to that used above, but increasing the $^{18}O_2$ exposure from 10 L to 50 L (at 400 K). This resulted in no change in either the CO_2 production, or the amount of residual CO desorbing. Evidently, 10 L O_2 exposure at 400 K is sufficient to saturate all sites capable of binding active oxygen, so that additional O_2 exposure has no significant effect. The result is reminiscent of the observation that O_2 dissociative adsorption on Pd(110) becomes an activated process when the coverage exceeds 0.15 ML,[113] i.e., O_2 dissociative adsorption is self-limiting. We also examined the possibility that oxygen binding might have an activation barrier by running another series of TPR measurements where the protocol was as above, except that the 10 L $^{18}O_2$ exposures were carried out at 180 K, rather than 400 K. Again, there was no significant change in the CO_2 production, indicating that the kinetics of oxygen binding are still efficient enough at 180 K to saturate the limited number of active oxygen binding sites. The lack of activation energy is consistent with experiments performed on Pd_n/alumina/NiAl, where temperatures as low as 100 K were shown to oxidize Pd, as shown by a shift in the Pd 3d core level.[50]

It is interesting to compare CO oxidation over Pd_n/alumina/Re(0001) with results under identical conditions for CO oxidation over Pd_n on different oxide supports. For Pd_n/alumina/Ta(110)[55] the dependence of activity on size is also relatively weak, varying by 30% from the most active (Pd_6) to least active (Pd_{10} and Pd_{25}) clusters. In contrast, variations by more than a factor of 5 are seen for Pd_n/TiO_2(110) under similar conditions.[24] To some extent, the weak size dependence for Pd_n/alumina is not surprising, because the activity in both Pd_n/alumina systems is quite high under these conditions, with ~45% of the CO converted to CO_2, while the Pd_n/TiO_2 conversion is at most ~5%. In the case of the Pd_n/alumina systems CO_2 production appears to be limited by availability of active oxygen. In that case, one might suppose that for the much less active Pd_n/TiO_2(110) system, which is also shown to be oxygen-limited,[53] increasing the O_2 exposure would increase CO_2 production, however, there is another factor at play. On the TiO_2(110) support, prepared by vacuum annealing, ~8% of the surface unit cells have a vacancy in the bridging oxygen position,[50] and at the temperatures reached in the TPR/TPD experiments, interstitial Ti^{3+} is known to diffuse to the surface.[129, 139, 140] Both provide binding sites for O atoms, and as a result, ^{18}O initially bound to the Pd clusters can, instead of oxidizing CO, spill over and bind on the TiO_2 support. This issue is discussed further in the next section.

5.3.2 ISS investigation of cluster morphology and CO binding sites

When using ISS to determine cluster morphology, stability or adsorbate binding locations, it is important to be able to be able to disentangle the effects of adventitious

background gases. A detailed explanation of the processed used in this study to negate the effects of elemental sensitivity, postreaction adsorbates and the inherent destructive nature of ISS measurements has been proved in Appendix B.

Figure 5.4 summarizes the as-deposited and postreaction Pd ISS results as a function of cluster size. Because the as-deposited and postreaction experiments each require a fresh sample, it was not practical to repeat the experiments for every cluster size, and as-deposited ISS was only done for a subset of the clusters. To assess reproducibility, we ran three as-deposited and three postreaction experiments on six separate Pd_{20}/alumina samples, and the standard errors are shown as error bars on those points. It can be seen that the reproducibility of the as-deposited ISS is quite high, and this has been our experience with previous systems as well. As expected, the reproducibility for the postreaction analysis is lower, due to the extrapolation required to account for the adsorbates present.

For the as-deposited clusters, the Pd ISS signal decreases by ~30% as the cluster size is increased from Pd_2 to Pd_{25}, indicating that the fraction of Pd atoms in the surface layer of the sample also decreases slowly with increasing size. If we assume that in Pd_2/alumina, the clusters lie flat on the surface, then the trend suggests that Pd_5 also deposits as a single layer island, but that with increasing size, a small fraction of the Pd atoms begin to form a second layer, thereby attenuating scattering from underlying Pd. The transition to multilayer cluster structures is similar to what was observed for $Pd_n/TiO_2(110)$,[24] but unlike that for $Au_n/TIO_2(110)$,[141] $Ir_n/TiO_2(110)$[142] and $Ni_n/TiO_2(110)$,[143] where the decrease with size is more rapid, indicating formation of more three-dimensional structures.

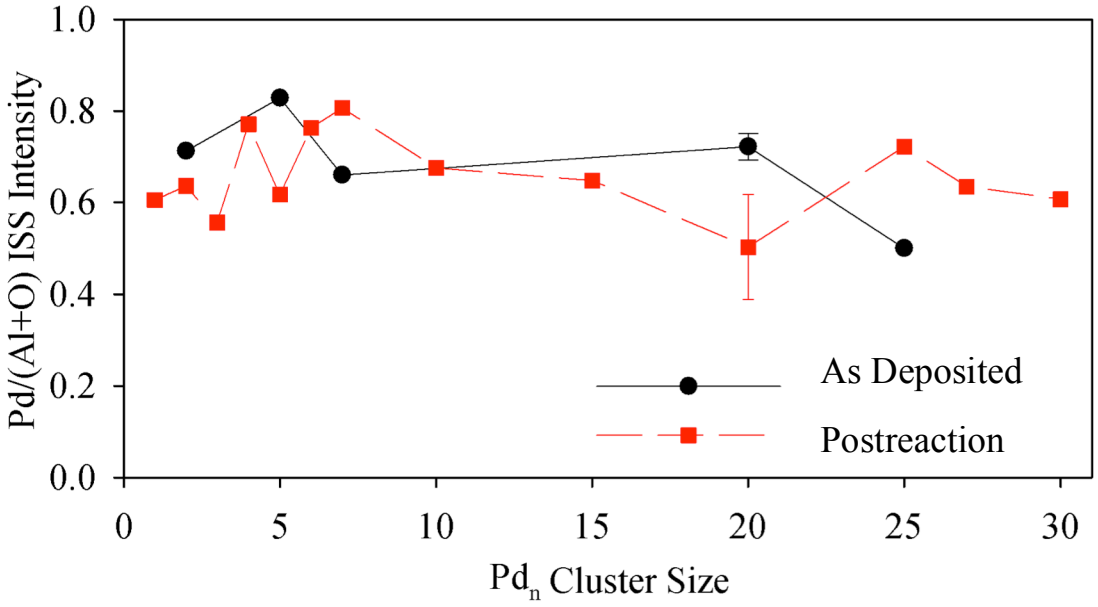

Figure 5.4: The Pd/(Al+O) ratio determined in ISS is plotted as a function of Pd_n cluster size both as deposited (circles) and after reaction studies consisting of three TPR measurements and a CO TPD (squares).

More surprisingly, once the attenuation from adsorbates is corrected for, there is little if any difference between the as-deposited and postreaction Pd ISS intensity. The implication is that while reaction may leave some adsorbates on the surface, the structure of the underlying Pd is not significantly changed. Presumably this is one factor accounting for the high stability of these samples in sequential TPR experiments.

ISS can also be used to probe changes in samples at different stages of the sample preparation and TPR process. When 0.1 ML equivalent of Pd_n is deposited on an alumina film, both O and Al peaks are attenuated, as expected, but the Al attenuation is slightly larger, suggesting a tendency for clusters to deposit such that they cover more aluminum than oxygen sites. The Pd, Al, and O signals are unchanged by the 560 K flash, suggesting that that the Pd clusters are stable up to 560 K. After exposure to 10 L $^{18}O_2$ at 400 K, however, there is a ~20% drop in Pd signal, with no change in Al or O signals, including no significant shoulder for ^{18}O on the ^{16}O peak. This result implies that there is no significant adsorption of ^{18}O on the alumina film, but there is ^{18}O bound to Pd in geometries that attenuate He^+ scattering. The relationship between oxygen coverage and Pd ISS attenuation depends on the type of oxygen binding site. If O were bound directly atop Pd atoms, then every O atom would block scattering from one Pd atom, thus the O coverage would be ~20% of the Pd coverage (≈2% of the surface layer). If, on the other hand, O atoms bind in other sites not directly atop Pd atoms, then the coverage would probably need to be higher in order to attenuate Pd ISS by 20%. In either case, however, the total ^{18}O coverage would be too small to produce a distinguishable peak at E/E_0 = 0.44 given the relatively high multiple scattering background. In contrast to the small effect of O_2 exposure, 10L exposure to CO results in almost complete attenuation of the

Pd signal, with little change in the Al and O signals. This result implies that the Pd clusters are essentially saturated with CO, at least some of which is bound on top of the clusters. As discussed above, after the series of three TPR and one TPD experiments, followed by XPS analysis, the Pd ISS intensity initially attenuated by adsorbates, recovering with increasing He^+ flux; however, there is no significant change in O and Al signals, indicating that the adsorbates remaining on the surface are bound mainly to Pd.

The absence of a postreaction signal for ^{18}O, is in contrast to what was observed for $Pd_n/TiO_2(110)$ under identical conditions, where an ^{18}O feature corresponding to >20% of the total surface layer oxygen was observed.[6] This large ^{18}O feature implied that ^{18}O, initially activated and bound on the Pd clusters, spilled over to the TiO_2 support to bind at vacancies or to Ti^{3+} interstitials that diffuse to the surface at high temperatures.[129, 139, 140] This spillover process is in competition with CO oxidation, and presumably was responsible for the relatively low (<10%) CO oxidation efficiency in the Pd/TiO_2 system. Similarly, oxygen spillover was proposed as an explanation for the negligible CO oxidation activity observed for Pd_n/alumina/NiAl(110), where the alumina film is only 0.5 nm thick.[56, 144] Evidently, oxygen spillover is not significant for Pd/alumina/Re(0001), presumably because the film is fully oxidized and thick enough to act as a diffusion barrier. Instead, the adsorbed oxygen remains on the Pd clusters, reacting with high efficiency.

5.3.3 Correlations with Pd electronic properties

XPS was used immediately after Pd_n deposition to characterize the as-deposited Pd. Because the alumina films are thin enough to allow observation of the Re 4f peaks

from the Re(0001) support, the XPS energy scale was set to align the Re $4f_{7/2}$ peak to the literature value (40.3 eV) for bulk Re. The shift required was only ~0.2 eV, and quite reproducible from day to day. This approach does not compensate for charging of the alumina film, however, no evidence for charging is seen for the alumina film thicknesses used in this study. The Pd 3d peak also has $3d_{5/2}$ and $3d_{3/2}$ spin orbit components, and in fitting the spectra, the peak splitting was constrained to the literature value of 5.26 eV.[145] The Pd 3d binding energies discussed below are for the larger $3d_{5/2}$ peak, and are plotted in red against the secondary axis in Figure 5.3. Note that the Pd 3d binding energy scale is inverted to make it easier to compare the binding energies and CO_2 production activities as a function of cluster size. As expected, the Pd $3d_{5/2}$ binding energies are substantially greater than the value for bulk Pd (335.1 eV),[145] due to factors such as the more limited relaxation and core hole screening possible in small clusters, compared to that in bulk metal.[146-149] For the same reason, it is expected that the binding energy should generally decrease with increasing cluster size, converging to the bulk value for nanoparticles that are large enough to have bulk-like electronic structure.[147, 150]

In addition to this overall trend, there is a fluctuation, where Pd_5 and Pd_6 show binding energies that are significantly lower than expected from the overall trend. There are other apparent fluctuations, however, only this one is statistically significant. It appears that there is an anticorrelation between Pd 3d binding energy and activity, i.e., samples with high Pd 3d binding energy are relatively unreactive, and vice versa. Clearer anticorrelations of this sort have been observed for CO oxidation over Pd_n/TiO_2[24] and Pt_n/alumina,[57] where the size-dependent fluctuations in both reactivity and XPS binding energies were substantially larger. A strong anticorrelation was also found

between activity for carbon oxidation and Pt 4f binding energy in an electrocatalytic study of Pt_n/glassy carbon.[2] Such anticorrelations between binding energy and activity for oxidation catalysis can be rationalized in terms of either initial or final state effects on the binding energies. In an initial state picture, the variation in Pd binding energy with size would be attributed to varying electron density on the Pd clusters, due to electron transfer between the Pd clusters and support. Clusters in an electron rich environment (i.e., with a partial negative charge) tend to have low binding energies, and an electron rich environment might also aid in activating adsorbed oxygen, by electron transfer to the O_2 π^* orbitals. Conversely, if the clusters have lost electron density to the support, that would tend to increase the Pd 3d binding energy, and decrease the ability to activate O_2. It has been previously shown that Pd deposited on alumina surfaces, can cause a dipole to form due to electron charge transfer from the alumina support to the Pd clusters.[151, 152] From a final state perspective, clusters that have particularly polarizable valence electronic structure would tend relax and screen the core-hole final state more than clusters with more tightly bound valence electrons, and one would also expect that loosely (tightly) bound valence electrons would be more (less) efficient for O_2 activation. In reality, both initial and final state effects probably contribute to the variations in Pd 3d binding energy.

We also examined the cluster size dependence of the onset of the Pd valence band, as shown in Figure 5.5. The zero of the electron binding energy (i.e., the sample Fermi level, E_F) was obtained from the spectrum of silver foil attached to the sample holder. Examples of the near-E_F region of the raw UPS for alumina/Re(0001) and Pd_{10}/alumina/Re(0001) are shown in frame (a) of the figure. The spectra are dominated

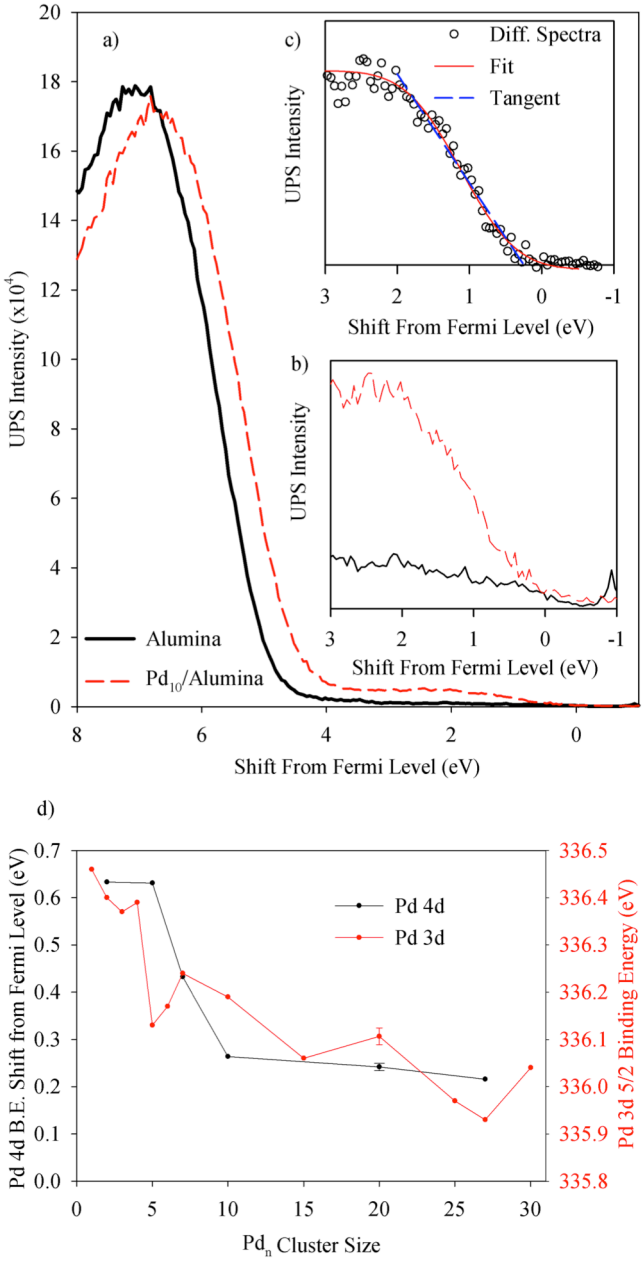

Figure 5.5: Determination of Pd 4d onset position and comparison to Pd 3d core level elections are presented. (a) UPS spectra for a clean alumina film before (solid black) and after Pd_{10} deposition (dashed red), with energy referenced to the Fermi level of the sample, EF. Inset (b) shows the near-EF region on a reduced scale. Inset (c) shows the subtracted spectrum (black circles), and the fit to the spectrum used to determine the onset energy of the Pd valence band(solid red). The intersection of the line tangent to the inflection point of the fit is plotted (dashed blue) to indicate the Pd valence band onset energy. Frame (d) shows the Pd valence band onset energy as a function of Pd_n cluster size (black – left axis), and Pd 3d 5/2 core level binding energy (red – right axis).

by the O 2p band from the alumina film, which has an onset at ~4.5 eV below E_F. Figure 5.5b shows the near-E_F region on a magnified scale, demonstrating that the signal from Pd_{10} is easily observed, due to its location in the alumina band gap. The UPS for the clean alumina film shows a weak, featureless background in the 0 to 4 eV binding energy range. This background results from a combination of midgap states in the alumina, primarily due to ~1% Re doping in the film, and emission from the Re substrate, strongly attenuated by passage through the alumina. Signal due to deposited Pd_{10} is much larger than the background, and the background-subtracted spectrum is shown in Figure 5.5c. It can also be seen that the addition of Pd to the alumina film shifts the O 2p band closer to E_F, and there is also a shift in the high energy spectral cutoff (not shown) that implies an increase in surface work function. Neither of these shifts has significant dependence on deposited cluster size. The Pd valence band onset energies vs. cluster size were extracted by first subtracting the alumina background from the spectra for each as-deposited sample. The residual Pd signal was then fit by a Gaussian-convoluted step function, and the onset energy was taken as the horizontal intercept of the line tangent to the inflection point, as depicted in Figure 5.5c. This procedure, suggested by Gutmann,[153] approximately corrects for instrumental broadening.[154]

Figure 5.5d shows the shift in the Pd valence band onset energy as a function of cluster size, and compares this indicator of valence structure to the Pd 3d core level binding energy. There is an overall decrease in binding energy with increasing cluster size, expected due to better screening and delocalization of the final state charge, but it is clear that the valence onset energy for Pd_5 is anomalously high relative to E_F, i.e., Pd_5 is less bulk-like than might be expected from the overall trend. It is interesting that the

trends of electronic stability with cluster size appear to be opposite for core and valence electrons. Pd_5 has an anomalously low 3d binding energy, and anomalously high valence band onset energy. It is not clear why this might be true, or how this connects with activity as measured in TPR.

5.3.4 The nature of CO binding

To better understand the reaction mechanism, it is instructive to examine the CO desorption behavior in more detail. Figure 5.6a shows the results of a CO TPD experiment, taken after three TPR measurements and exposure to 10 L CO at 180 K, then heated, without any O_2 exposure. The open black circles are experimental data while the solid red and blue lines show a fit to the temperature dependence (bottom axis) of the CO intensity. The dashed black curve shows the sum of the two components, which have been adjusted to give a fit to the experimental signal. The temperature dependence was simulated using the Polanyi-Wigner rate expression, as discussed by Redhead,[155] assuming first order desorption, as expected for a molecular adsorbate like CO. The desorption signal I(t) can be written:

$$I(t) \propto \frac{-d\theta}{dt} = (\theta \cdot \nu) \cdot e^{\frac{-E_{desorption}}{k_b T}} \qquad (1)$$

where θ is the coverage, ν is a prefactor, $E_{desorption}$ is the desorption energy, and T is the temperature at time t. Ideally, the prefactor should be determined from a series of experiments, however, given the difficulties and significant time inherent to preparing these samples, this approach is impractical. We have assumed ν to be 10^{14} s^{-1}, in the

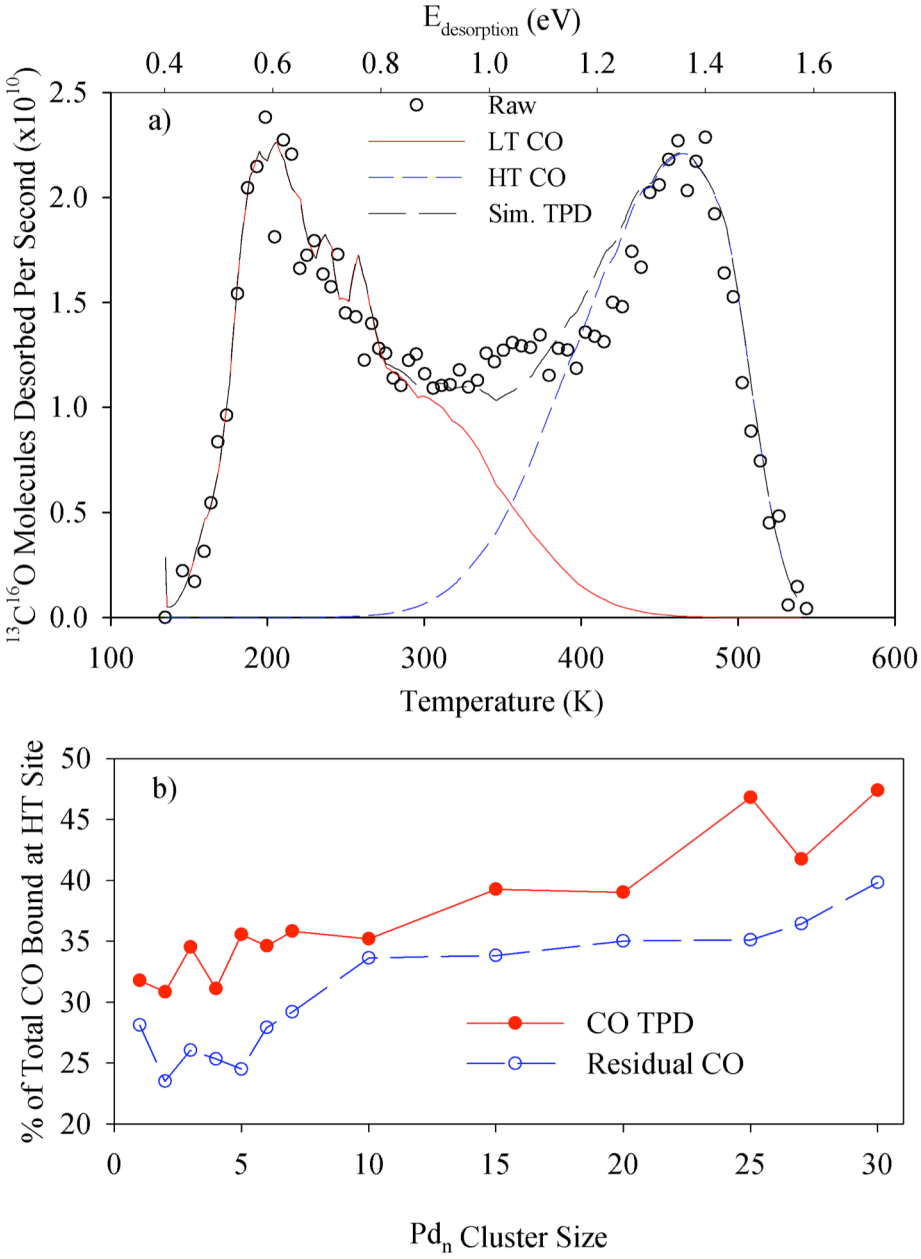

Figure 5.6: Determination of low and high temperature CO desorption peak areas are compared for several Pd_n cluster sizes. (a) CO desorption during CO TPD from Pd_{25}. The open black circles are the raw CO desorption while the solid red and dashed blue lines are fits to the low and high temperature components, based on a simulation of the desorption kinetics. The dashed black line is the simulated TPD, i.e., the sum of the two features. By referring the simulated TPD curve to the $E_{desorption}$ axis plotted across the top of the figure, the distribution of desorption energies can be seen. (b) The intensities of the high temperature desorption feature, as a percent of total CO desorption, for CO TPD (solid red) and residual CO in TPR (open blue).

middle of the range typically seen for CO desorption,[54] and have tested the sensitivity of the extracted desorption energy distributions to the value of ν. The extracted $E_{desorption}$ distribution shifts by ~7% for an order of magnitude change in ν, providing an estimate for the systematic uncertainty in the $E_{desorption}$ and relative intensities.[54] The figure also shows the $E_{desorption}$ distribution, plotted against the top axis, which has been constructed so that the temperature and $E_{desorption}$ distributions are roughly superimposed. It can be seen that the low temperature desorption feature corresponds to $E_{desorption}$ peaking near 0.6 eV, while the high temperature desorption feature corresponds to $E_{desorption}$ peaking near 1.4 eV.

Figure 5.6b shows the intensity of the high temperature CO desorption peak, as a percent of the total CO desorption intensity, determined from the integrated intensities of the TPD simulation components. It can be seen that for both the residual CO desorbing during TPR, and the CO desorbing during the final CO TPD experiment, the fraction of the CO in the high temperature desorption feature increases with increasing cluster size, and accordingly, the fraction desorbing in the low temperature feature decreases. Since CO is not observed to bind to the alumina film in this temperature range, both CO desorption features are clearly associated in some way with the Pd clusters, and the obvious question is how the CO is bound. We might, for example, expect CO to bind on top of the Pd clusters, but there might also be sites where CO is bound to the alumina at the cluster periphery, or at the cluster-support interface.

The nature of the CO binding sites associated with the two desorption features was probed by temperature-dependent ISS (TD-ISS), as shown in Figure 5.7. These data are for Pd_{20} (a representative large cluster) deposited on a alumina film grown on

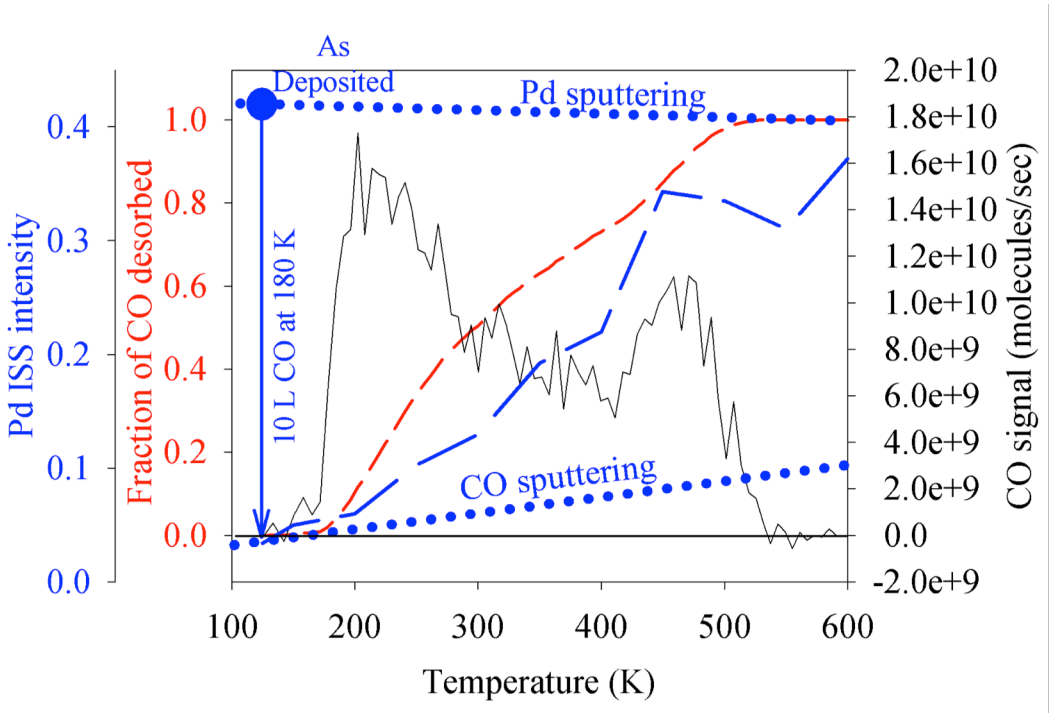

Figure 5.7: CO TD-ISS for Pd20/alumina/Ta(110). See text for explanation.

Ta(110), and similar results were obtained for Pd_2/alumina (a representative small cluster). Furthermore, the behavior for Pd_n/alumina is quite similar to that observed for CO binding to $Pd_n/TiO_2(110)$.[6] The figure shows a CO TPD spectrum, taken using the protocol described above, showing the two CO desorption features. A curve is also shown that gives the fraction of the total CO desorption that has occurred at each temperature. The results of two different ISS experiments are also shown, done on two freshly prepared samples. One simply measured the as-deposited ISS intensities, using the same procedure that will be discussed in Appendix B. The result is the data point at 0.42 on the left hand axis, which is the Pd ISS intensity normalized to the sum of the Al and O intensities. All other points in the TD-ISS data set were taken using low flux scans on a separately prepared sample, in order to minimize the effects of He^+ sputtering. The point at ~0.03, directly below the as-deposited point, shows the Pd intensity measured after exposure to 10 L CO at 180 K, followed by cooling to 130 K. The subsequent points in the TD-ISS curve were obtained by heating the sample to the indicated temperatures, then taking a low flux ISS scan as the sample cooled. We did not measure ISS while the sample was being heated because we wanted to monitor the He^+ flux, which required the heating connections to be broken temporarily.

As noted, intensity in ISS peaks mostly results from single scattering events, primarily involving atoms in the top-most sample layer. The >90% drop in Pd signal resulting from the 10 L CO exposure indicates that CO is binding to the Pd clusters in such a way as to almost completely attenuate He^+ scattering from Pd. In our ISS geometry (45° angle of incidence, detection along the surface normal), CO binding on top of the clusters is expected to strongly attenuate scattering from Pd, while CO binding

around the cluster periphery would attenuate scattering from Pd only if the CO extended high enough off the surface to cast a scattering shadow cone[133] intersecting Pd atoms in the cluster. The near-total attenuation observed is additional support for the idea that the absolute coverage estimated above (Figure 5.3 and Appendix B) is probably on the low side of our factor of 2 uncertainty window.

Note that as the sample is heated, the Pd ISS signal gradually increases. Two effects contribute. As CO is thermally desorbed, underlying Pd is exposed to the He^+ scattering, however, it is also important to take into account the increase in Pd ISS signal that occurs due to CO loss by He^+ sputtering.[54] The line labeled "CO sputter rate" was measured by preparing an identical CO-saturated sample, then running a series of low flux ISS measurements while keeping the sample at 130 K, so that sputtering is the only CO loss mechanism. Of course, He^+ sputtering also removes Pd, and the "Pd sputter rate" line was measured by preparing yet another sample, and then simply probing it repeatedly with low flux ISS. It can be seen that the Pd intensity loss rate from sputtering is much lower than the rate of Pd ISS recovery from sputtering of overlying CO.

From the TPD results, it can be seen that heating to 300 K results in desorption of 50% of the total CO coverage, but the Pd ISS signal only recovers to a small extent. By 420 K, 75% of the CO has desorbed, with ~50% recovery of the Pd ISS signal. In the temperature above 420 K, the rate of Pd ISS recovery increases sharply, leading to about half the total Pd ISS recovery, despite the fact that only 25% of the total CO desorbs above 420 K. As expected, the Pd ISS plateaus as the CO desorption goes to completion. The implication of these results is that the most strongly bound CO is in sites on top of the clusters, where its desorption leads to a strong recovery of He^+ scattering from the

underlying Pd. The less efficient attenuation from the more weakly bound sites indicates that this component of the CO is bound in geometries that do not efficiently shadow or block He^+ scattering from Pd, such as sites around the cluster periphery. Similar behavior was seen for Pd_2 on this same support as well as for $Pd_n/TiO_2(110)$,[54] which also shows bimodal CO desorption; for that system, Liu[156] showed via DFT that the strongest CO binding sites are bridging sites on the cluster surface, but that there are also sites, with only about half the binding energy, where CO is bound around the cluster periphery in geometries that would not lead to significant attenuation of He^+ scattering from Pd.

The notion that the stronger binding sites are on the cluster surface, while the weaker sites are around the cluster periphery suggests that the relative population of CO in the stronger binding sites should increase with increasing cluster size. For example, if the Pd_n clusters deposited as circular, single layer thick islands, then the surface area *per* cluster would vary like n, while the perimeter length would vary like $n^{1/2}$. Since the number of clusters deposited varies like n^{-1}, the total number of "on-top" sites on the samples would be n-independent, while the total number of perimeter sites would decrease like $n^{-1/2}$. For noncircular structures, the details would be different, but as long as the morphology is not strongly size-dependent, as suggested by Figure 5.4, then we would expect the ratio of "on-top" to peripheral sites to increase with cluster size. Just such an increase in the fraction of high temperature CO desorption is observed, as shown in Figure 5.6b.

One final aspect of the TD-ISS results merits comment. The Pd ISS intensity at the end of the experiment is ~12% lower than what would be expected from the as-deposited intensity, taking the Pd sputter rate into account. As shown in Appendix B,

there is an even attenuation after the TPR/TPD sequence, which, however, is largely reversed by light He^+ sputtering. The explanation proposed herein was partial coverage by adsorbates on the clusters, however, it is also possible that TPR and TPD lead to restructuring of the clusters to more compact geometries, where a smaller fraction of Pd atoms is in the surface layer. Such restructuring could involve sintering to form larger clusters, or simply isomerization to more multilayer cluster structures. The difficultly with the restructuring scenario is that it would be difficult to explain the restoration of the Pd ISS intensity, essentially to the as-deposited values (Figure 5.4) by light He^+ sputtering. On this evidence, molecular adsorbates appear to be the more likely explanation for the postreaction drop in Pd ISS. The nature of the adsorbates is unclear. The chamber background pressure does increase during TPR and TPD due to the gas doses and desorbing molecules, and there may be some readsorption during the 20 minutes when the sample was probed by XPS, prior to the ISS measurements. There may also be some CO or O left on the surface at the end of the TPR/TPD experiments, although we did not observe any additional CO desorption in test experiments carried out to 610 K, nor is there any *active* oxygen left on the samples at the conclusion of TPR, as shown by absence of CO_2 production in subsequent CO exposure and heating (Figure 5.2b).

5.3.5 Steady state reactivity

TPR is a probe of activity under unrealistic conditions, where O_2 is allowed to interact with the samples prior to CO exposure. For selected sizes we also examined CO oxidation activity under constant flows of both reactants, as the temperature was stepped

from 340 K to 600 K. The sizes studied were Pd_5, Pd_{20}, and Pd_{25}, representing the two most reactive (5, 25), and one of the least reactive (20) samples under TPR conditions. These experiments were done by exposing the samples to CO and O_2 flows from the dosing tubes (Appendix B) that resulted in increases in chamber pressure of $5x10^{-9}$ Torr and $1x10^{-7}$ Torr, respectively, for ^{13}CO and $^{18}O_2$. The fluxes at the sample position were equivalent to local pressures roughly an order of magnitude higher, and still in a 1:20 ratio.

The experiments began with growth of the alumina film, deposition of 0.1 ML equivalent of Pd_n, and characterization by XPS, just as in the TPR experiments. The sample was then exposed to 50 L of $^{18}O_2$ at 340 K to generate an initial concentration of adsorbed oxygen. The sample was next exposed to a constant flow of CO, generating a spike of CO_2 product, which decayed to baseline within 50 seconds, as the CO removed the initial oxygen coverage. At that point, the $^{18}O_2$ flow was resumed (leaving the CO flowing as well), resulting in a small steady-state flux of CO_2 product. The CO flow was started first in order to get its flow rate stabilized before starting the much larger O_2 flow. The initial CO_2 steady state production rate is quite small, because, as well established,[20, 61, 103, 157] CO binds efficiently to sites on the Pd, poisoning them for O_2 activation until the sample temperature becomes large enough to result in significant CO desorption rate. In our protocol, where the O_2 flow was 20 times larger than the CO flow, a small but significant CO_2 production rate was observed even at 340 K.

Once steady flows of CO and O_2 were established, the sample temperature was increased in 20 degree steps, with each temperature held constant until the CO_2 production rate became constant, signaling that a steady-state coverage of reactants had

developed. In Figure 5.8a, each black vertical line with a temperature above it indicates the time when the sample temperature controller was set to that temperature. The sample then took roughly 40 seconds to ramp to the set temperature, and then further time was allowed for the CO oxidation kinetics to reach steady state. For example, at 525 seconds the set point was changed to 400 K, the sample reached 400 K at 565 seconds, and then the kinetics took another ~10-15 seconds to reach the new steady state, at which point the set point was raised to 420 K. The 20 K temperature steps continued up to 600 K. After ~200 seconds at 600K, the heat was shut off, allowing the temperature to drop slowly back to 340 K, and it can be seen that the CO_2 production during cooling qualitatively retraced the behavior during heating, as might be expected from the high stability that these samples showed during repeated TPR measurements over the same temperature range. The fact that the temperature and intensity of the peak CO_2 production were slightly different in the heating and cool-down phases of the experiment, probably just reflects the faster cooling rate, which did not allow time for steady state to be achieved. At 2000 seconds (340 K sample temperature), the CO flow was turned off, resulting in no significant change in CO_2 production. 100 seconds later, the O_2 flow was turned off, resulting in an essentially immediate cessation of CO_2 production. Clearly, at this temperature, activated, adsorbed oxygen is the limiting reagent.

Several points should be noted. It can be seen that the time width of the temperature steps initially decreased as the temperature was stepped to ~500 K, and then got wider again as the temperature increased to 600 K. Over the same temperature range, the CO_2 production rate increased, peaking at ~460 K, then decreased by 60% by the time the temperature reached 600 K. The time widths of the temperature steps were

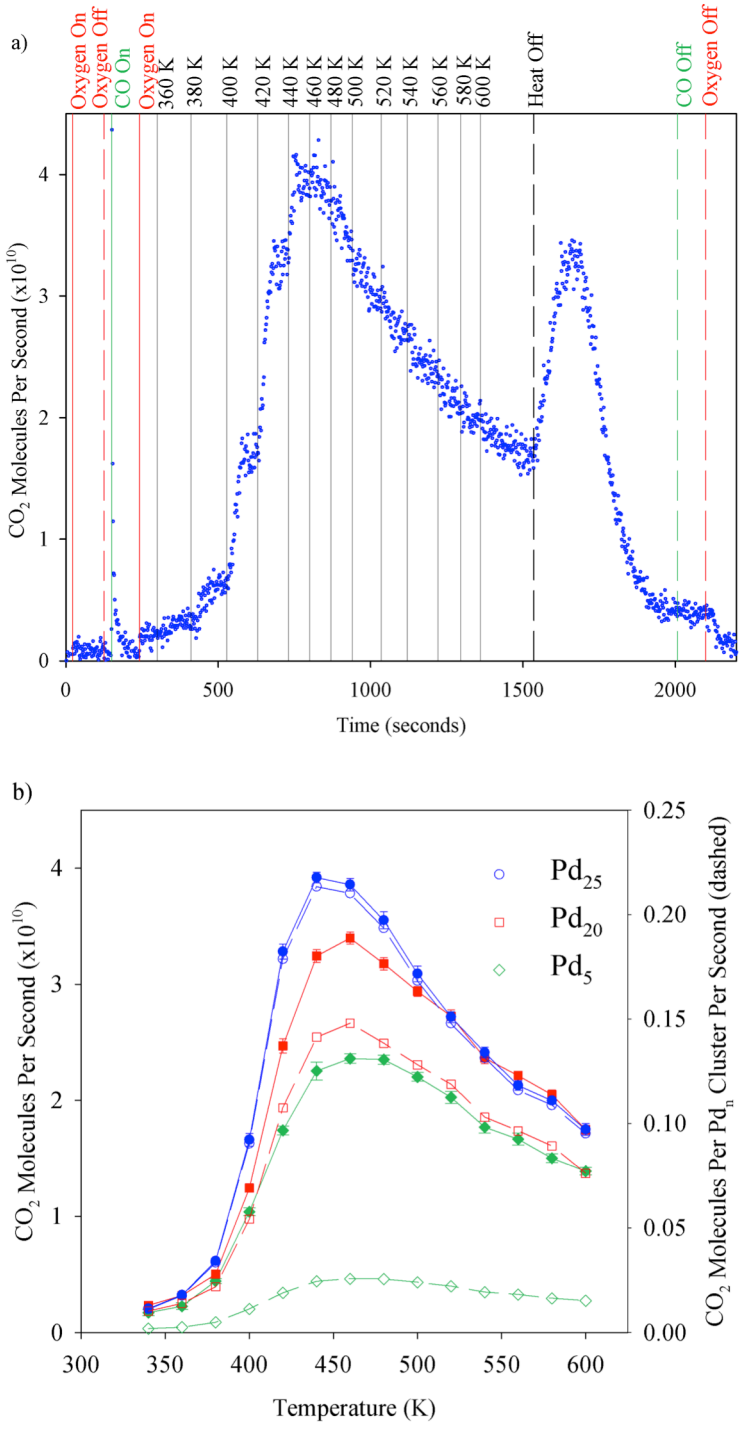

Figure 5.8: Steady state CO oxidation over Pd_n is presented. (a) Raw CO_2 production from Pd_{25}/alumina/Re(0001) under steady state flow conditions, as described in the text. (b) Comparison of steady state CO oxidation activity for Pd_{25} (blue circles), Pd_{20} (red squares), and Pd_5 (green diamonds) showing both total CO_2 per second (solid lines, left axis) and CO2 produced per Pd_n cluster per second (dashed lines, right axis).

determined by the combination of the time needed to reach the new set temperature, and the time it took the CO_2 signal to stabilize. Changes in the time widths, therefore, reflect changes in the time it took to for the kinetics to reach steady state.

In the temperature range of these experiments, the kinetically important processes are adsorption of oxygen, adsorption of CO, desorption of CO, and reaction of adsorbed CO and oxygen to form CO_2, which is assumed to desorb as it forms. O_2 desorption is not expected in this temperature range, nor was any observed in our TPR experiments. At low temperatures, stable CO binding tends to poison the surface, so that CO_2 production is limited by the availability of binding sites for oxygen adsorption and activation. As the temperature is raised through the range where the CO begins to desorb, (see TPD spectrum in Figure 5.6), additional sites for oxygen activation become available, increasing the reaction rate on the surface, which both increases the CO_2 production and shortens the time to reach steady state coverage of the reactants. At temperatures above 500 K, the CO lifetime on the surface becomes so short that the CO_2 production rate is limited by the low surface concentration of CO (the CO pressure is 20 times lower than the O_2 pressure). One interesting point is that TPD shows that our samples clearly have two types of CO binding sites. At the temperatures probed in these experiments, the sites responsible for the low temperature CO desorption component, which TD-ISS suggests are largely around the cluster periphery, would be largely empty, even at the 340 K starting temperature. The fact that the samples are still CO-poisoned at 340 K suggests that oxygen activation is not efficient in peripheral sites. On the other hand, the fact that the CO_2 production rate peaks in the temperature range where the high temperature CO TPD feature also peaks, suggests that it is these sites, identified as being

on-top of the Pd clusters, that are responsible for the oxygen activation and CO_2 production.

Figure 5.8b compares the CO_2 production temperature dependence measured for Pd_5, Pd_{20} and Pd_{25}, where each data point is the steady state CO_2 signal at the indicated temperatures. The CO_2 ion signal has been converted to CO_2 molecules *per* second, and given the total of 4.59×10^{12} Pd atoms deposited in the form of different clusters in the 2 mm cluster spot, we also give the signal in terms of CO_2 molecules *per* cluster *per* second. The corresponding peak turnover frequencies on a *per* Pd atom basis are $\sim 5.1 \times 10^{-3}$ CO_2 *per* Pd atom *per* second for Pd_5, $\sim 7.4 \times 10^{-3}$ for Pd_{20}, and $\sim 8.5 \times 10^{-3}$ for Pd_{25}. Note also that the order of activity on a *per* atom basis is different under steady state conditions ($Pd_{25} > Pd_{20} > Pd_5$), compared to TPR ($Pd_5 \gtrsim Pd_{25} > Pd_{20}$), presumably reflecting subtle cluster size effects on the energetics and kinetics for CO desorption and oxygen activation. Under TPR conditions, where the samples were oxidized prior to CO exposure, but with a relatively small O_2 exposure, the activity appears to be primarily correlated with the ability of the clusters to binding and activate oxygen. In the steady state measurements, activity is more obviously related to CO desorption kinetics, i.e., by the need to free up suitable sites for O_2 adsorption and activation.

5.4. Conclusions

It has been shown that size selected Pd_n clusters can be efficiently deposited on thin, conductive alumina films for both chemical and physical investigation as model catalysts. Through a combination of CO TD-ISS coupled with CO TPD, it is found that Pd_n/Al_2O_3 has two types of CO binding sites, with more weakly bound CO in sites around

the cluster periphery, and the more strongly bound CO in sites on top of the clusters. Steady state CO oxidation experiments suggest that the high temperature CO binding site is important for both oxygen activation and binding of reactive CO, leading to CO_2 production. Under TPR experimental conditions used here, the CO_2 production appears to be limited by the amount of activated oxygen, which varies as a function of cluster size. For the steady state reaction conditions, competition between CO and O_2 for binding sites determines the reactivity, particularly at low temperatures. Interestingly, the total amount of CO_2 produced during TPR only varies by only about 40% between the most and least active clusters, while in the steady state study the CO_2 turnover frequency varies by nearly a factor of 2 for Pd_5 and Pd_{25}, even though these are the two most active cluster sizes under TPR conditions. Presumably the difference is related to the size- and temperature-dependent affinities for different size clusters for CO and O_2.

5.5. References

1. Z. Ma and F. Zaera, *Heterogeneous Catalysis by Metals, Encyclopedia of Inorganic Chemistry*, John Wiley & Sons, Ltd., 2006.

2. S. Proch, M. Wirth, H. S. White and S. L. Anderson, *J. Am. Chem. Soc.*, 2013, **135**, 3073−3086.

3. H. Yoshida, Y. Kuwauchi, J. R. Jinschek, K. Sun, S. Tanaka, M. Kohyama, S. Shimada, M. Haruta and S. Takeda, *Science*, 2012, **335**, 317-319.

4. G. Kwon, G. A. Ferguson, C. J. Heard, E. C. Tyo, C. Yin, J. DeBartolo, S. Seifert, R. E. Winans, A. J. Kropf, J. Greeley, R. L. Johnston, L. A. Curtiss, M. J. Pellin and S. Vajda, *ACS Nano*, 2013, **7**, 5808-5817.

5. M. Moses-DeBusk, M. Yoon, L. F. Allard, D. R. Mullins, Z. Wu, X. Yang, G. Veith, G. M. Stocks and C. K. Narula, *J. Am. Chem. Soc.*, 2013, **135**, 12634-12645.

6. W. E. Kaden, W. A. Kunkel, F. S. Roberts, M. Kane and S. L. Anderson, *Surface Science*, 2014, **621**, 40-50.

7. C. Xia, C. Falgairette, Y. Li, G. Foti, C. Comninellis and W. Harbich, *Applied Catalysis, B: Environmental*, 2012, **113-114**, 250-254.

8. S. V. Ong and S. N. Khanna, *Surf. Sci.*, 2012, **606**, 965-970.

9. F. R. Negreiros, L. Sementa, G. Barcaro, S. Vajda, E. Apra and A. Fortunelli, *ACS Catalysis*, 2012, **2**, 1860-1864.

10. L. M. Molina, S. Lee, K. Sell, G. Barcaro, A. Fortunelli, B. Lee, S. Seifert, R. E. Winans, J. W. Elam, M. J. Pellin, I. Barke, V. von Oeynhausen, Y. Lei, R. J. Meyer, J. A. Alonso, A. Fraile Rodriguez, A. Kleibert, S. Giorgio, C. R. Henry, K.-H. Meiwes-Broer and S. Vajda, *Catalysis Today*, 2011, **160**, 116-130.

11. Y. Watanabe, X. Wu, H. Hirata and N. Isomura, *Catalysis Science & Technology*, 2011, **1**, 1490-1495.

12. C. T. Campbell, A. W. Grant, D. E. Starr, S. C. Parker and V. A. Bondzie, *Topics in Catalysis*, 2001, **14**, 43-51.

13. B. Yoon, U. Landman, V. Habibpour, C. Harding, S. Kunz, U. Heiz, M. Moseler and M. Walter, *J. Phys. Chem. C*, 2012, **116**, 9594-9607.

14. M. Moseler, M. Walter, B. Yoon, U. Landman, V. Habibpour, C. Harding, S. Kunz and U. Heiz, *J. Am. Chem. Soc.*, 2012, **134**, 7690-7699.

15. C. Harding, V. Habibpour, S. Kunz, A. N.-S. Farnbacher, U. Heiz, B. Yoon and U. Landman, *J. Am. Chem. Soc.*, 2009, **131**, 538-548.

16. H. Hakkinen, S. Abbet, A. Sanchez, U. Heiz and U. Landman, *Angewandte Chemie, International Edition*, 2003, **42**, 1297-1300.

17. U. Landman, B. Yoon, C. Zhang, U. Heiz and M. Arenz, *Topics in Catalysis*, 2007, **44**, 145-158.

18. J.-H. Fischer-Wolfarth, J. A. Farmer, J. M. Flores-Camacho, A. Genest, I. V. Yudanov, N. Rösch, C. T. Campbell, S. Schauermann and H.-J. Freund, *Phys. Rev. B*, 2010, **81**, 241416.

19. S. Ali, N. A. Mohd Zabidi and D. Subbarao, *Chemistry Central Journal*, 2011, **5**, 68.

20. J. Zhang and A. N. Alexandrova, *Journal of Physical Chemistry Letters*, 2013, **4**, 2250-2255.

21. H. L. Abbott, A. Aumer, Y. Lei, C. Asokan, R. J. Meyer, M. Sterrer, S. Shaikhutdinov and H.-J. Freund, *J. Phys. Chem. C.*, 2010, **114**, 17099-17104.

22. G. Schmid, S. Emde, V. Maihack, W. Meyer-Zaika and S. Peschel, *J. Mol. Catal. A: Chem.*, 1996, **107**, 95 -104.

23. I. V. Yudanov, A. Genest, S. Schauermann, H.-J. Freund and N. Rösch, *Nano Lett*, 2012, **12**, 2134-2139.

24. W. E. Kaden, T. Wu, W. A. Kunkel and S. L. Anderson, *Science*, 2009, **326**, 826-829.

25. C. Becker and C. R. Henry, *Catalysis Letters*, 1997, **43**, 55-57.

26. R. C. Baetzold, *J. Phys. Chem.*, 1978, **82**, 738 -744.

27. S. Abbet, A. Sanchez, U. Heiz, W. D. Schneider, A. M. Ferrari, G. Pacchioni and N. Rosch, *Surface Science*, 2000, **454-456**, 984-989.

28. A. V. Beletskaya, D. A. Pichugina and N. E. Kuz'menko, *Nanotechnol Russia*, 2011, **6**, 717-722.

29. S. K. Buratto, M. T. Bowers, H. Metiu, M. Manard, X. Tong, L. Benz, P. Kemper and S. Chretien, *Chem. Phys. Solid Surf.*, 2007, **12**, 151-199.

30. T. M. Bernhardt, L. D. Socaciu, J. Hagen, D. Popolan, J. Le Roux, U. Heiz and L. Woeste, *Clusters and Nano-Assemblies: Physical and Biological Systems, [International Symposium],* Richmond, VA, United States, Nov. 10-13, 2004, 2005, 1-9.

31. V. Habibpour, Z. W. Wang, R. E. Palmer and U. Heiz, *Journal of Applied Sciences*, 2011, **11**, 1164-1170.

32. D.-C. Lim, C.-C. Hwang, G. Gantefoer and Y. D. Kim, *Phys. Chem. Chem. Phys.*, 2010, **12**, 15172-15180.

33. F. Krumeich, E. Muller and R. A. Wepf, *Micron*, 2013, **49**, 1-14.

34. X. Lai and D. W. Goodman, *J. Mol. Catal. A: Chem.*, 2000, **162**, 33-50.

35. M. Haruta, S. Tsubota, T. Kobayashi, H. Kageyama, M. J. Genet and B. Delmon, *Journal of Catalysis*, 1993, **144**, 175-192.

36. M. Valden, X. Lai and D. W. Goodman, *Science*, 1998, **281**, 1647-1650.

37. M. Valden, S. Pak, X. Lai and D. W. Goodman, *Catalysis Letters*, 1998, **56**, 7-10.

38. C. C. Chusuei, X. Lai, K. A. Davis, E. K. Bowers, J. P. Fackler and D. W. Goodman, *Langmuir*, 2001, **17**, 4113-4117.

39. D. C. Meier, X. Lai and D. W. Goodman, in *Surface Chemistry and Catalysis*, eds. A. F. Carley, P. R. Vavies, G. J. Hutchings and M. S. Spencer, Kluwer/Plenum, New York, 2002, pp. 147-189.

40. M. S. Chen and D. W. Goodman, *Science*, 2004, **306**, 252-255.

41. V. A. Bondzie, S. C. Parker and C. T. Campbell, *Catalysis Letters*, 1999, **63**, 143-151.

42. V. A. Bondzie, S. C. Parker and C. T. Campbell, *J. Vac. Sci. Technol. A*, 1999, **17**, 1717-1720.

43. S. C. Parker, A. W. Grant, V. A. Bondzie and C. T. Campbell, *Surf. Sci.*, 1999, **441**, 10-20.

44. C. C. Chusuei, X. Lai, K. Luo and D. W. Goodman, *Topics in Catalysis*, 2001, **14**, 71-83.

45. H. M. Ajo, V. A. Bondzie and C. T. Campbell, *Catalysis Letters*, 2002, **78**, 359-368.

46. U. Heiz, A. Sanchez, S. Abbet and W.-D. Schneider, *European Physical Journal D: Atomic, Molecular, Optical and Plasma Physics*, 1999, **9**, 35-39.

47. J. Hagen, L. D. Socaciu, U. Heiz, T. M. Bernhardt and L. Woeste, *European Physical Journal D: Atomic, Molecular and Optical Physics*, 2003, **24**, 327-330.

48. L. D. Socaciu, J. Hagen, T. M. Bernhardt, L. Woeste, U. Heiz, H. Haekkinen and U. Landman, *Journal of the American Chemical Society*, 2003, **125**, 10437-10445.

49. S. Lee, C. Fan, T. Wu and S. L. Anderson, *J. Am. Chem. Soc.*, 2004, **126**, 5682-5683.

50. T. Wu, W. E. Kaden and S. L. Anderson, *J. Phys. Chem. C*, 2008, **112**, 9006-9015.

51. A. Corma, P. Concepcio´n, M. Boronat, M. J. Sabater, J. Navas, M. J. Yacaman, E. Larios, A. Posadas, M. A. Lo´pez-Quintela, D. Buceta, E. Mendoza, G. Guilera and A. Mayoral, *Nature Chemistry*, 2013, **5**, 775-781.

52. A. A. Herzing, C. J. Kiely, A. F. Carley, P. Landon and G. J. Hutchings, *Science*, 2008, **321**, 1331-1335.

53. W. E. Kaden, W. A. Kunkel, M. D. Kane, F. S. Roberts and S. L. Anderson, *J. Am. Chem. Soc.*, 2010, **132**, 13097–13099.

54. W. E. Kaden, W. A. Kunkel, F. S. Roberts, M. Kane and S. L. Anderson, *J. Chem. Phys.*, 2012, **136**, 204705.

55. M. D. Kane, F. S. Roberts and S. L. Anderson, *Faraday Discussions*, 2013, **162**, 323.

56. T. Wu, W. E. Kaden, W. A. Kunkel and S. L. Anderson, *Surface Science*, 2009, **603**, 2764-2770.

57. F. S. Roberts, M. D. Kane, E. T. Baxter and S. L. Anderson, *Physical Chemistry Chemical Physics*, 2014, DOI: 10.1039/c1034cp02083a.

58. C. J. Harding, S. Kunz, V. Habibpour and U. Heiz, *Phys. Chem. Chem. Phys.*, 2008, **10**, 5875-5881.

59. C. J. Harding, S. Kunz, V. Habibpour and U. Heiz, *Chem. Phys. Lett.*, 2008, **461**, 235-237.

60. C. J. Harding, S. Kunz, V. Habibpour, V. Teslenko, M. Arenz and U. Heiz, *Journal of Catalysis*, 2008, **255**, 234-240.

61. S. Kunz, F. F. Schweinberger, V. Habibpour, M. Rottgen, C. Harding, M. Arenz and U. Heiz, *Journal of Physical Chemistry C*, 2010, **114**, 1651-1654.

62. A. Kartouzian, M. Thaemer, T. Soini, J. Peter, P. Pitschi, S. Gilb and U. Heiz, *J. Appl. Phys.*, 2008, **104**, 124313.

63. M. Thaemer, A. Kartouzian, P. Heister, S. Gerlach, M. Tschurl, U. Boesl and U. Heiz, *J. Phys. Chem. C*, 2012, **116**, 8642-8648.

64. M. E. Vaida, T. M. Bernhardt, C. Barth, F. Esch, U. Heiz and U. Landman, *Physica Status Solidi B: Basic Solid State Physics*, 2010, **247**, 1001-1015.

65. M. J. Berr, F. F. Schweinberger, M. Doeblinger, K. E. Sanwald, C. Wolff, J. Breimeier, A. S. Crampton, C. J. Ridge, M. Tschurl, U. Heiz, F. Jaeckel and J. Feldmann, *Nano Letters*, 2012, **12**, 5903-5906.

66. B. Wang, B. Yoon, M. Koenig, Y. Fukamori, F. Esch, U. Heiz and U. Landman, *Nano Letters*, 2012, **12**, 5907-5912.

67. M. Nesselberger, M. Roefzaad, R. Faycal Hamou, P. Ulrich Biedermann, F. F. Schweinberger, S. Kunz, K. Schloegl, G. K. H. Wiberg, S. Ashton, U. Heiz, K. J. J. Mayrhofer and M. Arenz, *Nature Materials*, 2013, **12**, 919-924.

68. S. Kunz, K. Hartl, M. Nesselberger, F. F. Schweinberger, G. Kwon, M. Hanzlik, K. J. J. Mayrhofer, U. Heiz and M. Arenz, *Phys. Chem. Chem. Phys.*, 2010, **12**, 10288-10291.

69. K. Hartl, M. Nesselberger, K. J. J. Mayrhofer, S. Kunz, F. F. Schweinberger, G. H. Kwon, M. Hanzlik, U. Heiz and M. Arenz, *Electrochimica Acta*, 2010, **56**, 810-816.

70. M. Nesselberger, S. Ashton, J. C. Meier, I. Katsounaros, K. J. J. Mayrhofer and M. Arenz, *Journal of the American Chemical Society*, 2011, **133**, 17428-17433.

71. S. J. Ashton, A. Novo, K. J. J. Mayrhofer and M. Arenz, *ECS Transactions*, 2009, **25**, 455-462.

72. S. Bonanni, K. Ait-Mansour, H. Brune and W. Harbich, *ACS Catalysis*, 2011, **1**, 385-389.

73. S. Bonanni, K. Ait-Mansour, W. Harbich and H. Brune, *J. Am. Chem. Soc.*, 2012, **134**, 3445-3450.

74. C. Xia, M. Hugentobler, Y. Li, G. Foti, C. Comninellis and W. Harbich, *Electrochemistry Communications*, 2011, **13**, 99-101.

75. G. A. Ferguson, C. Yin, G. Kwon, E. C. Tyo, S. Lee, J. P. Greeley, P. Zapol, B. Lee, S. Seifert, R. E. Winans, S. Vajda and L. A. Curtiss, *J. Phys. Chem. C*, 2012, **116**, 24027-24034.

76. E. C. Tyo, C. Yin, M. Di Vece, Q. Qian, G. Kwon, S. Lee, B. Lee, J. E. DeBartolo, S. Seifert, R. E. Winans, R. Si, B. Ricks, S. Goergen, M. Rutter, B. Zugic, M. Flytzani-Stephanopoulos, Z. W. Wang, R. E. Palmer, M. Neurock and S. Vajda, *ACS Catalysis*, 2012, **2**, 2409-2423.

77. S. Lee, M. D. Vece, B. Lee, S. Seifert, R. E. Winans and S. Vajda, *Phys. Chem. Chem. Phys.*, 2012, **14**, 9336-9342.

78. S. Lee, M. Di Vece, B. Lee, S. Seifert, R. E. Winans and S. Vajda, *ChemCatChem*, 2012, **4**, 1632-1637.

79. W. Deng, S. Lee, J. A. Libera, J. W. Elam, S. Vajda and C. L. Marshall, *Applied Catalysis, A: General*, 2011, **393**, 29-35.

80. S. Vajda, S. Lee, K. Sell, I. Barke, A. Kleibert, V. von Oeynhausen, K.-H. Meiwes-Broer, A. F. Rodriguez, J. W. Elam, M. M. Pellin, B. Lee, S. Seifert and R. E. Winans, *J. Chem. Phys.*, 2009, **131**, 121104.

81. S. Lee, M. Molina Luis, J. Lopez Maria, A. Alonso Julio, B. Hammer, B. Lee, S. Seifert, E. Winans Randall, W. Elam Jeffrey, J. Pellin Michael and S. Vajda, *Angewandte Chemie (International ed. in English)*, 2009, **48**, 1467-1471.

82. S. Vajda, M. J. Pellin, J. P. Greeley, C. L. Marshall, L. A. Curtiss, G. A. Ballentine, J. W. Elam, S. Catillon-Mucherie, P. C. Redfern, F. Mehmood and P. Zapol, *Nat. Mater.*, 2009, **8**, 213-216.

83. B.-H. Mao, R. Chang, S. Lee, S. Axnanda, E. Crumlin, M. E. Grass, S.-D. Wang, S. Vajda and Z. Liu, *J. Chem. Phys.*, 2013, **138**, 214304.

84. S. P. Price, X. Tong, C. Ridge, V. Shapovalov, Z. Hu, P. Kemper, H. Metiu, M. T. Bowers and S. K. Buratto, *Surf. Sci.*, 2011, **605**, 972-976.

85. B. Klipp, M. Grass, J. Muller, D. Stolcic, U. Lutz, G. Gantefor, T. Schlenker, J. Boneberg and P. Leiderer, *Applied Physics A: Materials Science & Processing*, 2001, **73**, 547-554.

86. D. C. Lim, R. Dietsche, M. Bubek, G. Gantefoer and Y. D. Kim, *ChemPhysChem*, 2006, **7**, 1909-1911.

87. D. C. Lim, R. Dietsche, M. Bubek, T. Ketterer, G. Gantefoer and Y. D. Kim, *Chem. Phys. Lett.*, 2007, **439**, 364-368.

88. R. Dietsche, D. C. Lim, M. Bubek, I. Lopez-Salido, G. Gantefoer and Y. D. Kim, *Appl. Phys. A: Mater. Sci. Process.*, 2008, **90**, 395-398.

89. D. C. Lim, R. Dietsche, G. Gantefoer and Y. D. Kim, *Chem. Phys. Lett.*, 2008, **457**, 391-395.

90. D. C. Lim, R. Dietsche, G. Gantefoer and Y. D. Kim, *Chem. Phys.*, 2009, **359**, 161-165.

91. D. C. Lim, R. Dietsche, G. Gantefoer and Y. D. Kim, *Appl. Surf. Sci.*, 2009, **256**, 1148-1151.

92. Y. Watanabe and N. Isomura, *J. Vac. Sci. Technol., A*, 2009, **27**, 1153-1158.

93. N. Isomura, X. Wu, H. Hirata and Y. Watanabe, *J. Vac. Sci. Technol., A*, 2010, **28**, 1141-1144.

94. J. M. Lightstone, M. J. Patterson, P. Liu, J. C. Lofaro, Jr. and M. G. White, *J. Phys. Chem. C*, 2008, **112**, 11495-11506.

95. J. Zhou, J. Zhou, N. Camillone, III and M. G. White, *Phys. Chem. Chem. Phys.*, 2012, **14**, 8105-8110.

96. S. Murphy, C. Strebel, S. B. Vendelbo, C. Conradsen, Y. Tison, K. Nielsen, L. Bech, R. M. Nielsen, M. Johansson, I. Chorkendorff and J. H. Nielsen, *Phys. Chem. Chem. Phys.*, 2011, **13**, 10333-10341.

97. D. N. McCarthy, C. E. Strebel, T. P. Johansson, A. den Dunnen, A. Nierhoff, J. H. Nielsen and I. Chorkendorff, *J. Phys. Chem. C*, 2012, **116**, 15353-15360.

98. C. Strebel, S. Murphy, R. M. Nielsen, J. H. Nielsen and I. Chorkendorff, *Phys. Chem. Chem. Phys.*, 2012, **14**, 8005-8012.

99. X. Li, K. Wepasnick, X. Tang, D. H. Fairbrother, K. H. Bowen, A. Dollinger, C. H. Strobel, J. Huber, T. Mangler, Y. Luo, S. Proch and G. Gantefoer, *J. Appl. Phys.*, 2014, **115**, 104304.

100. X. Tang, J. Schneider, A. Dollinger, Y. Luo, A. S. Woerz, K. Judai, S. Abbet, Y. D. Kim, G. F. Gantefoer, D. H. Fairbrother, U. Heiz, K. H. Bowen and S. Proch, *Phys. Chem. Chem. Phys.*, 2014, **16**, 6735-6742.

101. I. Langmuir, *Transactions of the Faraday Society*, 1922, **17**, 621-654.

102. I. Langmuir, *Transactions of the Faraday Society*, 1922, **17**, 607-620.

103. H. Conrad, G. Ertl and J. Kueppers, *Surface Science*, 1978, **76**, 323-342.

104. T. Engel and G. Ertl, *Chemical Physics Letters*, 1978, **54**, 95-98.

105. T. Engel and G. Ertl, *Journal of Chemical Physics*, 1978, **69**, 1267-1281.

106. D. H. Parker and B. E. Koel, *J. Vac. Sci. Technol. A*, 1990, **8**, 2585-2590.

107. I. Stara and V. Matolin, *Surface Science*, 1994, **313**, 99-106.

108. E. Gillet and M. H. El-Yakhloufi, *Z. Phys. D: At., Mol. Clusters*, 1993, **26**, 64 -66.

109. I. Meusel, J. Hoffmann, J. Hartmann, M. Heemeier, M. Bäumer, J. Libuda and H.-J. Freund, *Catalysis Letters*, 2001, **71**, 5-13.

110. I. Meusel, J. Hoffmann, J. Hartmann, J. Libuda and H.-J. Freund, *Journal of Physical Chemistry B*, 2001, **105**, 3567 -3576.

111. J. Libuda, I. Meusel, J. Hoffmann, J. Hartmann and H.-J. Freund, *J. Vac. Sci. Technol. A*, 2001, **19**, 1516-1523.

112. I. Z. Jones, R. A. Bennett and M. Bowker, *Surf. Sci.*, 1999, **439**, 235-248.

113. L. Hanley, Guo, Xingcai and J. T. Yates, Jr., *Journal of Chemical Physics*, 1989, **91**, 7220-7227.

114. Y. Q. Cai, A. M. Bradshaw, Q. Guo and D. W. Goodman, *Surf. Sci.*, 1998, **399**, L357-L363.

115. D. R. Rainer, S. M. Vesecky, M. Koranne, W. S. Oh and D. W. Goodman, *Journal of Catalysis*, 1997, **167**, 234-241.

116. D. R. Rainer, M. C. Wu, D. I. Mahon and D. W. Goodman, *J. Vac. Sci. Technol., A*, 1996, **14**, 1184-1188.

117. M. Bäumer, J. Libuda, A. Sandell, H. J. Freund, G. Graw, T. Bertrams and H. Neddermeyer, *Ber. Bunsen-Ges.*, 1995, **99**, 1381-1386.

118. M. Frank, M. Bäumer, R. Kuehnemuth and H.-J. Freund, *Journal of Physical Chemistry B*, 2001, **105**, 8569-8576.

119. Y. Wu, E. Garfunkel and T. E. Madey, *Surface Science*, 1996, **365**, 337-352.

120. Y. Wu, E. Garfunkel and T. E. Madey, *J. Vac. Sci. Technol., A*, 1996, **14**, 2554-2563.

121. P. J. Chen and D. W. Goodman, *Surf. Sci.*, 1994, **312**, L767-L773.

122. W. E. Kaden, W. A. Kunkel and S. L. Anderson, *J. Chem. Phys.*, 2009, **131**, 114701.

123. C. R. Henry, *Surf. Sci. Rep.*, 1998, **31**, 235-325.

124. H.-J. Freund, *Angew. Chem., Int. Ed. Engl.*, 1997, **36**, 453-475.

125. W. Braun, G. Meyer-Ehmsen, M. Neumann and E. Schwarz, *Surface Science*, 1979, **89**, 354-360.

126. X. Lai, C. C. Chusuei, K. Luo, Q. Guo and D. W. Goodman, *Chemical Physics Letters*, 2000, **330**, 226-230.

127. M. D. Kane, F. S. Roberts and S. L. Anderson, *In Preparation*, 2014.

128. Y. Cui, K. Huang, N. Nilius and H.-J. Freund, *Faraday Disc.*, 2013, **162**, 153-163.

129. M. Bowker, P. Stone, R. Bennett and N. Perkins, *Surface Science.*, 2002, **497**, 155-165.

130. J. J. Yeh and I. Lindau, *Atomic Data and Nuclear Data Tables*, 1985, **32**, 1-155.

131. C. J. Powell and A. Jablonski, *NIST Electron Effective-Attenuation-Length Database*, NIST, Gaithersburg, MD, 2011.

132. F. Sloan Roberts and S. L. Anderson, *Rev. Sci. Instrum.*, 2013, **84**, -.

133. J. W. Rabalais, *Principles and Applications of Ion Scattering Spectrometry: Surface Chemical and Structural Analysis*, Wiley, New York, 2003.

134. M. S. Chen, Y. Cai, Z. Yan, K. K. Gath, S. Axnanda and D. W. Goodman, *Surface Science*, 2007, **601**, 5326-5331.

135. J.-D. Grunwaldt and A. Baiker, *Journal of Physical Chemistry B*, 1999, **103**, 1002-1012.

136. P. Liu, Y. Yang and M. G. White, *Surf. Sci. Rep.*, 2013, **68**, 233-272.

137. T. L. Thompson, O. Diwald and J. John T. Yates, *Journal of Physical Chemistry B*, 2003, **107**, 11700 -11704.

138. M. Maciejewski, P. Fabrizioli, J.-D. Grunwaldt, O. S. Becker and A. Baiker, *Phys. Chem. Chem. Phys.*, 2001, **3**, 3846-3855.

139. M. Bowker, P. Stone, R. Bennett and N. Perkins, *Surf. Sci.*, 2002, **511**, 435-448.

140. R. A. Bennett, P. Stone and M. Bowker, *Catalysis Letters*, 1999, **59**, 99-105.

141. S. Lee, C. Fan, T. Wu and S. L. Anderson, *Surface Science*, 2005, **578**, 5-19.

142. M. Aizawa, S. Lee and S. L. Anderson, *Surf. Sci.*, 2003, **542**, 253-275.

143. M. Aizawa, S. Lee and S. L. Anderson, *J. Chem. Phys.*, 2002, **117**, 5001-5011.

144. S. Shaikhutdinov, M. Heemeier, J. Hoffmann, I. Meusel, B. Richter, M. Bäumer, H. Kuhlenbeck, J. Libuda, H.-J. Freund, R. Oldman, S. D. Jackson, C. Konvicka, M. Schmid and P. Varga, *Surf. Sci.*, 2002, **501**, 270-281.

145. J. F. Moulder, W. F. Stickle, P. E. Sobol, K. D. Bomben and J. J. Chastain & R. C. King, eds., *Handbook of X-ray Photoelectron Spectroscopy*, Physical Electronics, Eden Prarie, MN, 1995.

146. S. Peters, S. Peredkov, M. Neeb, W. Eberhardt and M. Al-Hada, *Surf. Sci.*, 2013, **608**, 129-134.

147. V. Senz, T. Fischer, P. Oelssner, J. Tiggesbaumker, J. Stanzel, C. Bostedt, H. Thomas, M. Schoeffler, L. Foucar, M. Martins, J. Neville, M. Neeb, T. Moeller, W. Wurth, E. Ruehl, R. Doerner, H. Schmidt-Boecking, W. Eberhardt, G. Gantefoer, R. Treusch, P. Radcliffe and K. H. Meiwes-Broer, *Phys. Rev. Lett.*, 2009, **102**, 138303/138301-138303/138304.

148. C. Binns, *Surf. Sci. Rep.*, 2001, **44**, 1-49.

149. G. K. Wertheim, *Z. Phys. D*, 1989, **12**, 319-326.

150. S. B. DiCenzo, S. D. Berry and J. E. H. Hartford, *Phys. Rev. B*, 1988, **38**, 8465–8468.

151. S. Ogawa and S. Ichikawa, *Physical Review B*, 1995, **51**, 17231-17234.

152. N. Tsud, V. Joha´nek, I. Stara´, K. Veltruska´ and V. Matolı´n, *Surf. Sci.*, 2000, **467**, 169-176.

153. S. Gutmann, M. A. Wolak, M. Conrad, M. M. Beerbom and R. Schlaf, *Journal of Applied Physics*, 2010, **107**, 103705.

154. R. Schlaf, P. G. Schroeder, M. W. Nelson, B. A. Parkinson, C. D. Merritt, L. A. Crisafulli, H. Murata and Z. H. Kafafi, *Surf. Sci.*, 2000, **450**, 142-152.

155. P. A. Redhead, *Vacuum*, 1962, **12**, 203-211.

156. P. Liu, *J. Phys. Chem. C* 2012, **116**, 25337−25343.

157. S. Lee, B. Lee, F. Mehmood, S. Seifert, J. A. Libera, J. W. Elam, J. Greeley, P. Zapol, L. A. Curtiss, M. J. Pellin, P. C. Stair, R. E. Winans and S. Vajda, *J. Phys. Chem. C*, 2010, **114**, 10342-10348.

CHAPTER 6

CONCLUSION

6.1 Conclusions

The work presented in this dissertation focuses on the effects of both the metal oxide support thickness as well as Pd_n cluster size on the catalytic oxidation of CO. In order to conduct these experiments, first a reliable aluminum evaporation source and C type thermocouple needed to be designed and constructed. Despite following well characterized recipes for growing a highly ordered crystalline alumina film, these experiments could not achieve the same described surfaces. On the Ta substrate, lower sample temperatures were used to eliminate Ta doping in the film, while for the Re substrate, the amount of Re dopant varied as a function of film thickness.

It is interesting that the film thickness dependence is different for an alumina film grown on Ta(110) vs Re(0001). Pd_n/Ta(110) was shown to be unstable and unreactive at room temperature, while being very active on Re(0001), though still unstable throughout the course of several TPR measurements. The dependence on film thickness likely is dependent upon the amount of charge transfer between the alumina film and both the substrate and Pd_n clusters. As the amount of electron density is increased for the Pd 4d valence band, there is a respective increase in CO activity. Based on both systems, it appears likely that the increase in activity is related to an increase in the amount of oxygen that can be bound in a reactive state. Changes in the Pd 3d binding energy as a result of oxidation correlate well with activity as a function of film thickness, suggesting that the binding of oxygen is the limiting reagent under the conditions studied. This is further corroborated via changes in the oxygen dose temperature or total exposure changing the overall CO_2 production.

The cluster size effect for these systems does not show a strong dependence for

total CO oxidized per mass Pd deposited, but does show a significant variation in the TOF for CO oxidation based on cluster size. This, in combination with the effect of the film thickness, provides several variables with which to tune the overall reactivity.

APPENDIX A

SUPPORTING INFORMATION INCLUDED FOR

CHAPTER 4

A.1. ISS determination of Re surface concentration

One of the key factors in the properties of the alumina/Re(0001) support is the presence of Re dopant atoms in the alumina film. The Re concentration was estimated from ISS as follows: The percent coverage of Re at the surface of the alumina films was estimated by simply comparing the Re ISS peak intensity measured for the alumina films, to the Re ISS peak intensity for clean, unoxidized Re(0001), where the surface density is known (~1.5 x 10^{15}/cm^2). The alumina/Re samples were prepared by first cleaning the Re by high temperature annealing, followed by growth of the alumina film. The film was then examined with XPS to determine the film thickness (< 5 min), and then immediately probed by ISS. Because the experiment time was so short, we neglect the effects on the Re intensities of any adventitious adsorbates. Figure A.1 shows the estimated Re surface concentration, expressed as percentages of the Re concentration in Re(0001). It can be seen that for thick films, the surface concentration is ~0.5%, increasing to ~2% for 2 nm films. The sharp increase in apparent Re surface concentration for thinner films is taken as evidence that these films (~2 ML nominal thickness) are, in fact, discontinuous, exposing an area of oxidized Re. The observed change in CO TPD temperature dependence for the thinnest films also is consistent with a change in film morphology, and the conclusion that the films are discontinuous is consistent with literature.[1-4]

To estimate the Re concentration in the surface of the alumina portions of the discontinuous films, we simply extrapolated from the curve for the thicker films. This estimate of Re surface concentrations is based on the assumption that the only contribution to the ISS peaks is scattering from single atoms in the surface layer. This assumption, common in ISS analysis, is based on the observation that even though a large

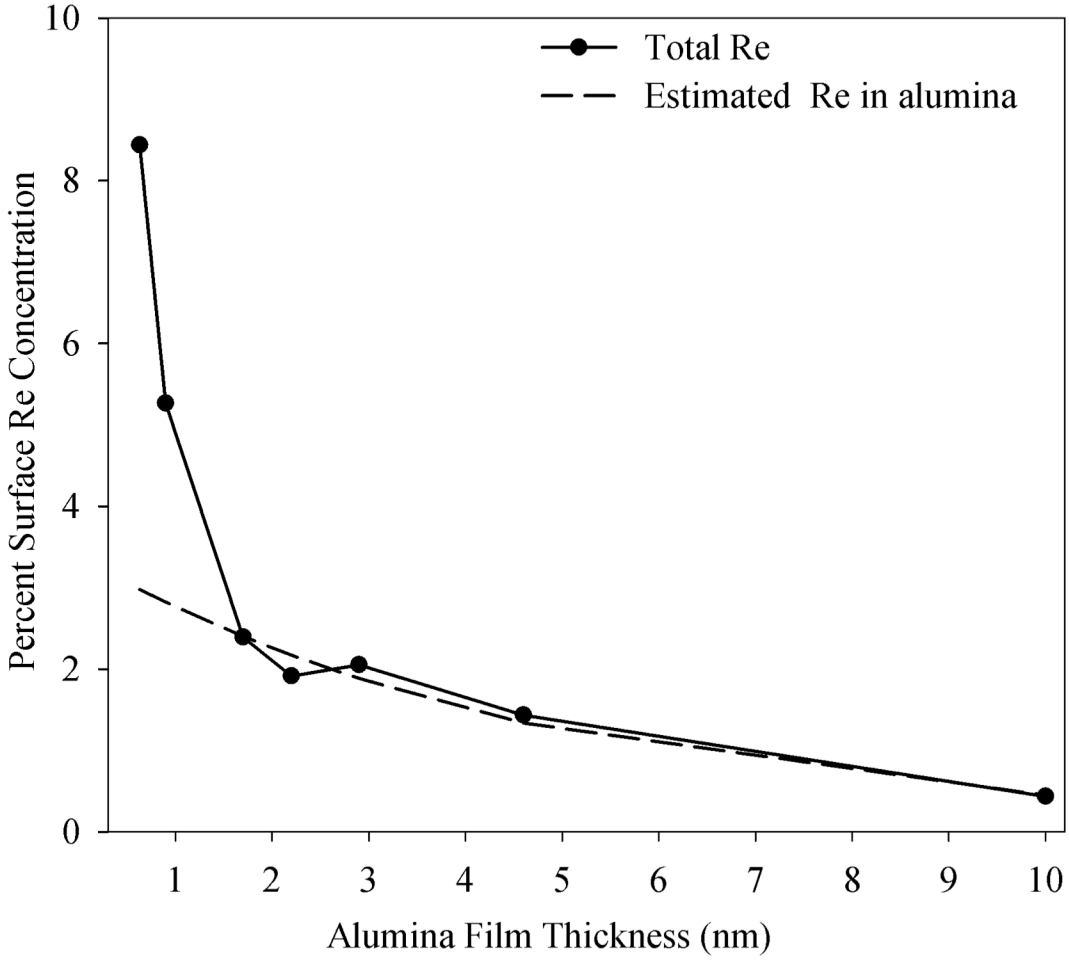

Figure A.1: Experimental Re surface concentration is plotted as the solid line. The dashed line is an estimate for the Re concentration in the alumina.

fraction of the incident He^+ penetrates well below the surface, only a tiny fraction of this "penetrating" escapes toward the detector as He^+, and most of that has undergone multiple scattering processes, and contributes to the broad background at low E/E_0, rather than to the ISS peaks (Chapter 4). For typical samples it is, therefore, reasonable to neglect subsurface contributions to ISS peak intensities. Here, however, we have a thin film composed of low atomic number (Z) elements (= low scattering cross sections), with a large concentration of a high Z scatterers (Re) only a few nanometers below the surface. Therefore, particularly for the thinner films, there may be a small contribution to the Re ISS peaks from subsurface scattering, thus the inferred Re "surface" concentrations in Figure A.1 should be taken as upper limits on the true surface concentrations.

If we assume that the surface concentration for a film of thickness z is identical to the bulk concentration for a thicker film at distance z from the Re support, then we can estimate how the Re concentration varies with z. The figure shows this "estimated Re in alumina curve," fitted to the surface concentration in the thickness range where the films are continuous.

A.2. Fitting the CO desorption temperature dependence

As discussed in Chapter 4, CO desorption during both TPR and CO TPD measurement is bimodal, and to approximately separate the two components, the spectra have been fit. An example of CO desorption spectrum for a CO TPD from a typical Pd20/alumina/Re(0001) sample is shown in Figure A.2. To fit the data, we first corrected for background by subtracting a linear baseline that was determined by averaging the raw signal just below and above the temperature range where CO desorption is observed. As

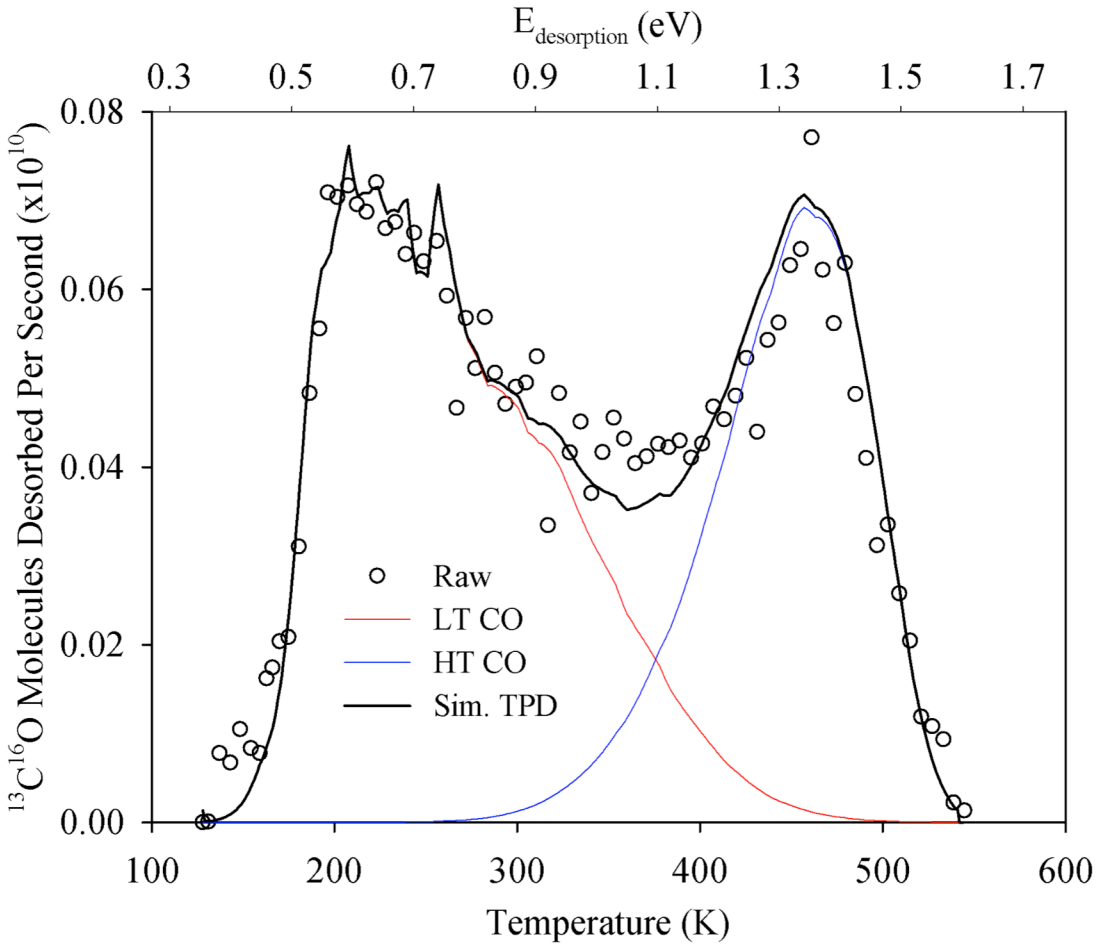

Figure A.2: Experimental CO desorption signal from the final CO TPD on a sample containing Pd_{20} deposited on a 4.0 nm alumina film is plotted as points. The red and blue curves are simulations of the LT and HT desorption components, and the black curve is the simulated total desorption.

described previously,[5-7] the subtracted spectra were fit using a simulation based on the Polanyi-Wigner rate expression[8] as shown in equation 1. We can see that the signal intensity (I) as a function of time, is related to the surface coverage (θ), a prefactor (ν), the molecular desorption energy (Edesorption), the Boltzmann constant (kb), and the Temperature (T).

$$I(t) \propto \frac{-d\theta}{dt} = (\theta \cdot \nu) \cdot e^{\frac{-E_{desorption}}{k_b T}} \qquad (1)$$

In this case, we are not trying to extract desorption energetics from the fits, thus we simply assumed $\nu = 10^{14}$ – roughly in the middle of the range of prefactors in the literature for CO desorption from Pt. The input to the simulation is a distribution of CO population vs. desorption energy, $P(E_{desorption})$. $P(E_{desorption})$ is combined with the rate expression to calculate a simulated CO desorption temperature dependence, which is compared to the experimental result. The input $P(E_{desorption})$ distribution is adjusted until the simulation fits the experiment. The solid black line passing through the experimental data points is the simulated spectrum, and the red and blue curves show the breakdown of the spectrum into low temperature (LT) and high temperature (HT) components. Note: the "noise" in the simulated spectrum reflects small fluctuations in the heating rate, which are measured and included in the simulation.

A.3. Determination of the Pd valence band onset

As shown in Chapter 4, the amount of signal in the alumina band gap region in the UP spectra varies with alumina thickness. Most of this signal is attributed to electrons emitted from the Re support, passing through the alumina film. To extract the intensity due to the Pd_{20} in the Pd_{20}/alumina/Re(0001) samples, it is necessary to subtract this background, and then fit the remaining signal.

The process is illustrated in Figure A.3. Figure A.3a shows the UPS for both a clean alumina film of 2.8 nm thickness and for the same film after deposition of 0.1 ML Pd_{20}. Note the significant shift in the alumina band, reflecting electron transfer between alumina and Pd, as discussed in the main paper. There is also an increase in the signal located in the band gap region, between E_F and ~4.5 eV, due to Pd_{20}. Figure A.3b shows a zoomed in view of this region of interest, clearly showing both the background and the increased signal due to Pd_{20}. Figure A.3c shows the difference between the UPS taken after and before Pd_{20} deposition, i.e., the net signal due to Pd_{20}. This subtracted spectrum was then fit using a procedure suggested by Parkinson and Schlaf.[9, 10] The spectrum is fit with a Gaussian-convoluted step function, and then a line tangent to the inflection point of the fit curve is extrapolated to the baseline, providing an estimate for the onset energy of the Pd valence band. This same procedure was also used to determine the onset energy of the alumina valence band (Chapter 4), and the high binding energy spectral limit, used to calculated the work functions plotted in Chapter 4.

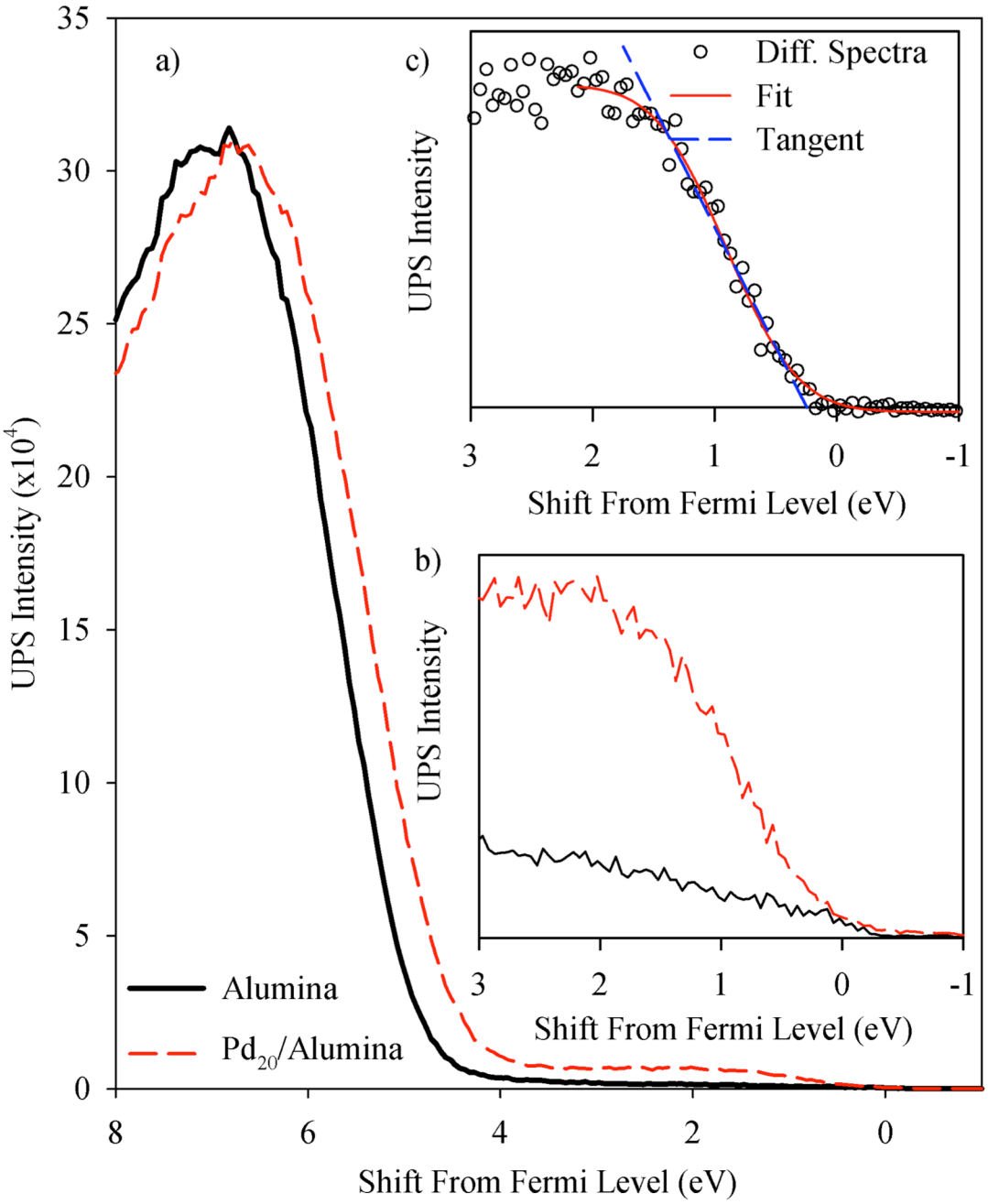

Figure A.3: The fitting process to determine the Pd valence level onset energy is presented. a.) UPS spectra for a clean alumina film 2.8 nm thick, before (solid black) and after (dashed red) deposition of 0.1 ML of Pd_{20} deposition (dashed red). b.) A zoomed view of the between E_F and 3 eV. c.) The subtracted spectrum with fit and extrapolation to baseline.

A.4. Review of common band structure models at metal-semiconductor contacts

Before discussing the model developed to account for the observed shifts in XPS and UPS with alumina thickness, we first review basic models for contacts between dissimilar materials, to define terminology. The discussion here is primarily based on the review by Zhang and Yates,[11] as well as additional literature sources.[3, 12-17] In our experiments, the Re support is grounded, and therefore in the following discussion we assume that potentials and energy levels of the Re are fixed.

A.4.1. Metal-metal contact

First consider contact between two dissimilar metals (Re and Pd), as depicted in Figure A.4. Figure A.4a shows a schematic of the filled electron bands for the two metals before they are brought into contact. Since both metals are electrically neutral, the potentials just outside each metal (the vacuum levels, E_{vac}) are identical. Because the two metals have different work functions, their Fermi levels are initially different. We also show the vacuum level of the spectrometer (E_{vac}^{spec}), which is determined by the work function difference between Re and the material used to coat the interior surfaces of the spectrometer (Au). E_{vac}^{spec} is important because it affects the measured photoelectron kinetic energies, and must be taken into account in calculating the binding energies, however, it is constant during the experiments.

Figure A.4b shows the situation after the two metals are placed in contact and allowed to reach thermal equilibrium. Because E_F^{Pd} was initially higher than E_F^{Re}, upon contact, electrons flow from Pd to Re until the Fermi levels are brought into alignment,

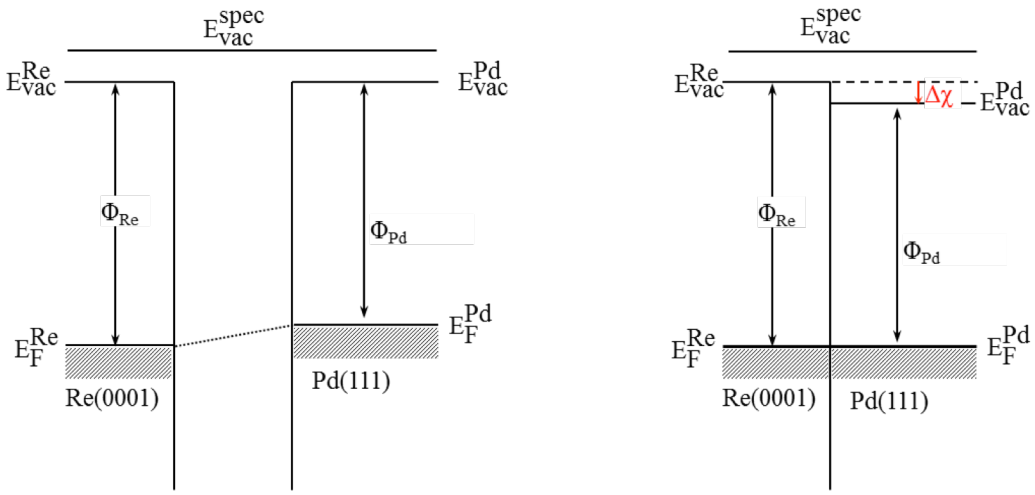

Figure A.4: Model of band structure for dissimilar metals before (a) and after (b) they are brought into contact.

thereby creating a contact potential $\Delta\chi$. This shifts the vacuum level over the Pd, i.e., the Pd develops a positive potential relative to the grounded Re, and this potential stabilizes the Pd electronic energy levels.

A.4.2. Metal-semiconductor contact

Because the alumina films in this experiment are n-doped, we discuss only the case of a metal contact with an n-doped semiconductor. We first consider contact between n-doped alumina and Re, but for low doping levels more typical of levels found in semiconductor devices (Figure A.5). The precontact situation is shown on the left. In this case, the alumina Fermi level is shifted above the band gap center due to the dopant-induced donor states ($< 10^{18}/cm^3$) near the top of the band gap. In the precontact situation, both Re and alumina are electrically neutral, thus their vacuum levels are aligned. The diagram has been drawn with the alumina having a smaller work function and higher Fermi level ($E_F^{alumina}$), because this matches the experimental results. The figure also shows the electron affinity of the alumina (EA), which is the difference between the conduction band minimum and the vacuum level. For a metal, the electron affinity and work function are equal.

Figure A.5b shows the same system in contact and thermal equilibrium. Electrons have flowed from the alumina to Re until the Fermi levels are brought into alignment, however, because the density of free electrons in the alumina (determined by doping level) is low, the situation is different than in a metal-metal junction. The electron transfer depletes the free electrons in a "depletion layer" on the alumina side of the interface, leaving unscreened dopant cations behind, and building up a positive potential.

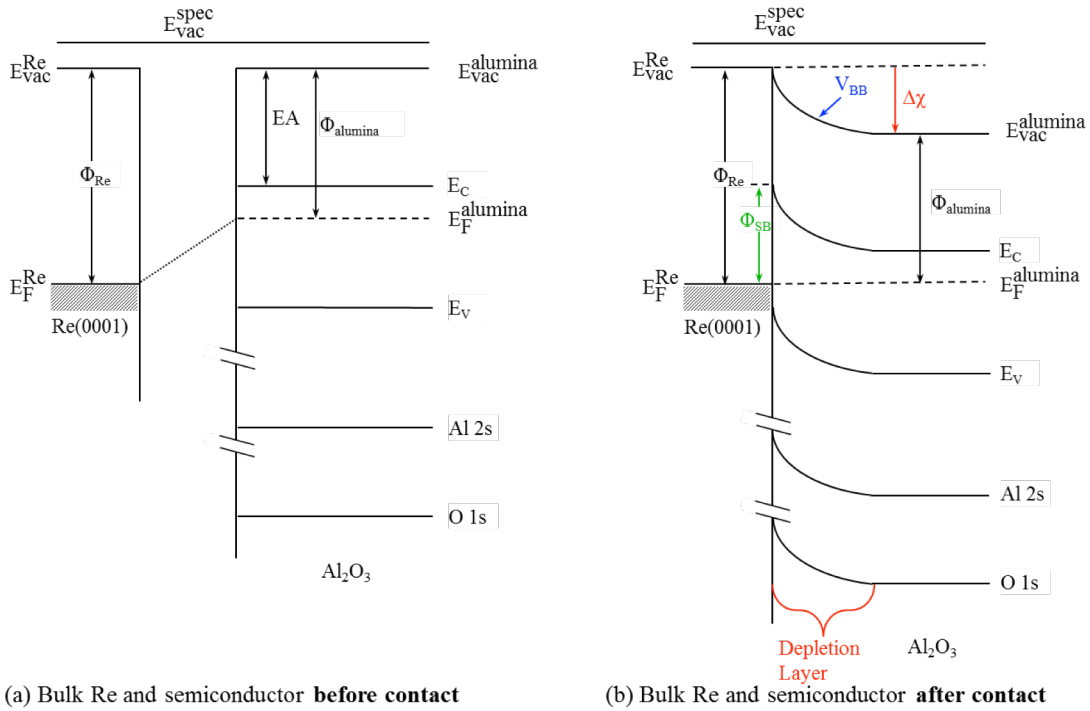

(a) Bulk Re and semiconductor **before contact** (b) Bulk Re and semiconductor **after contact**

Figure A5: A typical metal-semiconductor potential energy diagram is presented. a.) Band structure for Re and lightly n-doped alumina before contact. b.) Situation after contact.

The electrons transferred to the Re conduction band localize along the Re side of the interface, creating a Schottky barrier, Φ_{SB}, that blocks additional electron transfer. The build-up of positive potential across the depletion layer generates a band-bending potential, V_{BB}, that increases across the depletion layer. As a result, the potential energy of electrons ($-e \cdot V_{BB}$) drops across the depletion layer, asymptotically approaching bulk values shifted by $\Delta\chi$ at long distances from the interface.

This Schottky-Mott model idealizes the interface, neglecting the effects of bond formation, interfacial mixing, and other interfacial chemistry. In real Schottky contacts, such effects result in a reduction of the actual barrier height, compared to Φ_{SB} calculated from the difference between E_F^{Re} and $EA^{alumina}$. Note that the thickness of the depletion layer is inversely proportional to the square root of the carrier density. For lighly doped semiconductors, the depletion layer can be in the few hundred nanometer range,[11] i.e., much thicker than the films of interest here. In this case, band bending over the thickness of the film would be negligible. In principle, the same process occurs at metal-metal contacts, however, because the electron density is orders of magnitude higher in metals, the depletion layer thickness is on the order of the atomic spacing, i.e., outside the validity of this kind of continuum model.

The final example is the one most relevant to the experiments here, i.e., Re in contact with a highly doped alumina film. Figure A.6a shows the situation before contact. The only obvious difference, compared to the previous example, is that the higher doping level leads to $E_F^{alumina}$ being located closer to the conduction band minimum than in Figure A.5. Figure A.6b shows the situation after contact and establishment of thermal equilibrium. Qualitatively, the behavior is idential to that in the

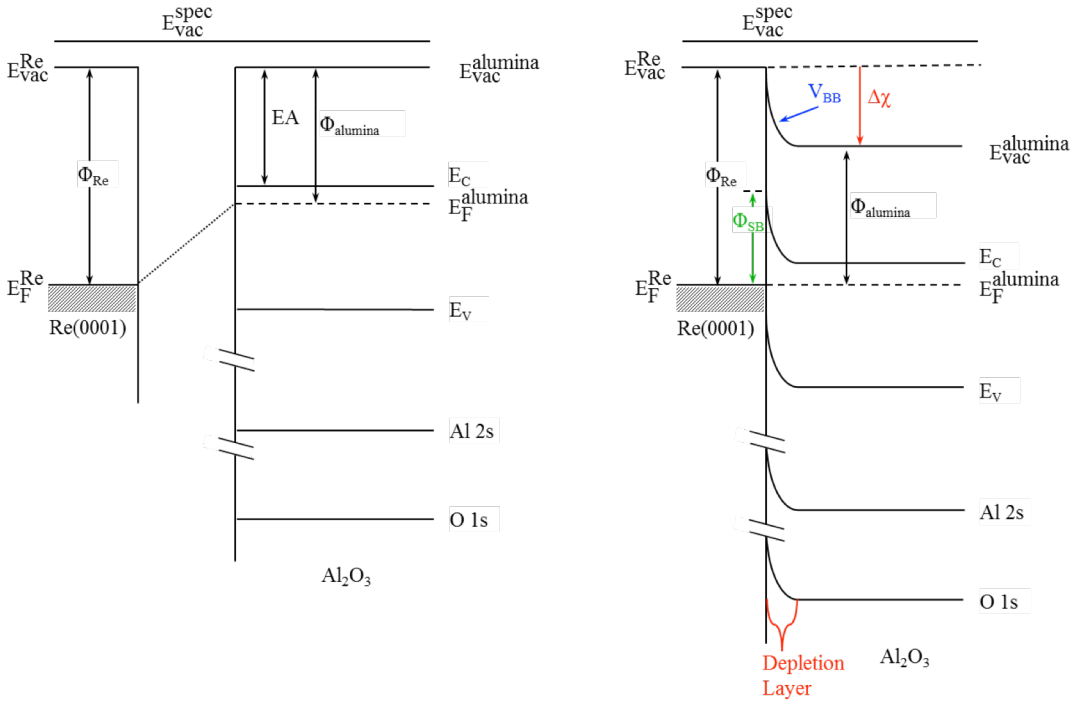

(a) Bulk Re and highly doped semiconductor **before contact**

(b) Bulk Re and highly doped semiconductor **after contact**

Figure A.6: A typical ohmic contact potential energy diagram is depicted. a.) Band structure for Re and lightly n-doped alumina before contact. b.) Situation after

previous example, but the high density of free electrons in the alumina means that only a thin layer need be depleted in order to create the potential shift that brings the Fermi levels into alignment. From the perspective of this idealized model, the conductivity of such a junction is high because tunneling through the thin barrier is efficient. Furthermore, in real junctions, chemical bonding and mixing at the interface lower the barrier height. The result is that current through the contact is approximately linear with applied voltage, hence such contacts are called "ohmic" contacts.

For our alumina films, the doping level is high enough to make the depletion layer thin, however, the films themselves are also thin. In essence, the situation is similar to that in Figure A.6b, but with the sample truncated within or just beyond the depletion layer. As a result, on the length scale of the films, band bending may be significant, and the free electron density and electrostatic potential at the sample surface will vary with thickness, depending on whether the film is thicker or thinner than the depletion layer.

A.5. Modeling the band structure

Based on the support in our experiment being metallic Re (with an oxidized surface layer), in contact with Re-doped alumina, it is possible to develop a simple model that qualitatively accounts for the observed thickness-dependent shifts in alumina core and valence level binding energies. The model, illustrated in Figure A.7, is based on the standard Schottky-Mott model for contact between a metal and an n-doped semiconductor. We will first describe the standard model, and then the changes made for the system here. Figure A.7a shows the excess charge density distribution (i.e., the deviation from charge neutrality) on both sides of the interface. As discussed above,

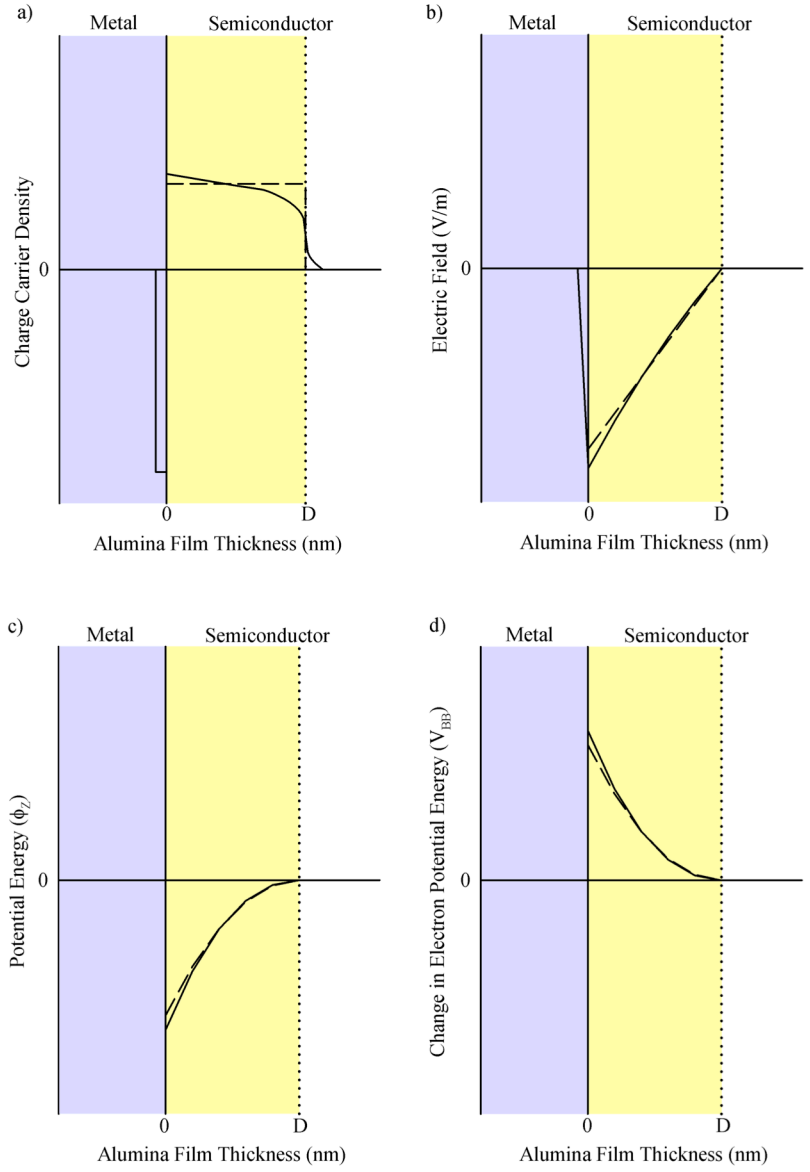

Figure A.7: Theoretical and calculated electronic properties across the depletion layer of a metal-semiconductor contact. (a) Estimated charge carrier density, (b) electric field, and (c) potential across the depletion layer as a function of distance from the metal support, for an alumina film deposited on Re. In each case, the dashed line is the result of a simplified model where the carrier density (N_d) is assumed to be independent of distance from the support. The solid curves qualitatively include the effects of the variation of Re dopant density with distance from the support. (d) The electron potential energy change due to band bending (V_{BB}) shows how these factors generate V_{BB} in the potential energy diagrams depicted in Figures A.5 and A.6.

there is electron buildup in the metal side of the interface, and because electrons are depleted for some distance into the semiconductor, there is an excess of dopant cations. In the standard model, the dopant concentration is assumed to be uniform, and a sharp transition is assumed between the depletion layer and the bulk of the semiconductor. In reality, the dopant density varies with distance from the Re support, and some blurring of the boundary is also expected, as shown by the dashed curve.

As shown in Figure A.7b, this charge distribution results in an electric field across the depletion layer, which is linear in the standard model. In essence, the field is strong at the interface, and dies across the depletion layer due to screening by the excess cation density. The potential as a function of distance from the interface, $\phi(z)$, is obtained by integrating the electric field, and the result is shown in Figure A.7c. Finally, the potential energy of an electron in this electric field, i.e., the band-bending potential, $V_{BB}(z)$, is simply $-e \cdot \phi(z)$. All the electron bands are modified by V_{BB}, resulting in the band bending behavior shown in Figures A.5, A.6, and A.7d.

One critical parameter in the model is the thickness of the depletion layer, which determines the thickness at which the binding energies become thickness-independent (Chapter 4). Factors that affect the depletion layer thickness include the dopant density, the probability that each dopant atom donates an electron to the conduction band, the initial noncontact difference between the Fermi level of the alumina ($E_F^{alumina}$) and the Fermi Level of the Re (E_F^{Re}), and the actual film thickness, which obviously sets an upper limit on the thickness of the depletion layer. From the experimental perspective, it is also important to note, as discussed in the main text, that the XPS and UPS results average over the near-surface region of the samples.

For an idealized (sharp-edged) depletion layer with cation density N_d and thickness D, the functional form of the band bending potential can be written:[11]

$$D = \sqrt{\frac{2\,\epsilon_{alumina}\epsilon_0(\Phi_{Re}-\Phi_{alumina})}{e\,N_d}} \quad . \qquad (2)$$

where $\epsilon_{alumina}$ is the relative dielectric constant of alumina, and ϵ_0 is the vacuum permittivity constant. With the constraint that the total potential energy change across the depletion region is equal to Φ_{Re}-$\Phi_{alumina}$, we can relate D to the properties of the contact:

For 1% Re doping (roughly the average for our alumina films), and assuming that each Re atom donates one electron to conduction band, $N_d = 6.8x10^{20}/cm^3$. Using the measured values for Φ_{Re} (7.3 eV) and $\Phi_{alumina}$ (4.9eV), we obtain a value for D equal to 1.9 nm. This can be compared to the 1 to 1.5 nm depletion layer thickness estimated from the spectra. Considering the many approximations in the idealized model, the agreement is reasonable. As discussed in the main paper, the shifts in the alumina BEs with film thickness suggests that the alumina-to-Re electron transfer is determined by the depletion layer thickness for thick films, but limited by the alumina thickness for films thinner than the depletion layer.

A.6. References

1. X. Lai, C. C. Chusuei, K. Luo, Q. Guo and D. W. Goodman. Imaging Ultrathin Al_2O_3 Films with Scanning Tunneling Microscopy. *Chem. Phys. Lett.*, 2000, **330**, 226-230.

2. P. J. Chen and D. W. Goodman. Epitaxial Growth of Ultrathin Al_2O_3 Films on Ta(110). *Surf. Sci.*, 1994, **312**, L767-L773.

3. Y. Wu, E. Garfunkel and T. E. Madey. Growth and Oxidation of Ultra-Thin Al Films on the Re(0001) Surface. *Surf. Sci.*, 1996, **365**, 337-352.

4. Y. Wu, E. Garfunkel and T. E. Madey. Growth of Ultrathin Crystalline Al_2O_3 Films on Ru(0001) and Re(0001) Surfaces. *J. Vac. Sci. Technol., A*, 1996, **14**, 2554-2563.

5. F. S. Roberts, M. D. Kane, E. T. Baxter and S. L. Anderson. Oxygen Activation and CO Oxidation Over Size-Selected Pt_n/alumina/Re(0001) Model Catalysts: Correlations With Valence Electronic Structure, Physical Structure, and Binding Sites. *Physical Chemistry Chemical Physics*, 2014, DOI: 10.1039/c1034cp02083a.

6. M. D. Kane, F. S. Roberts and S. L. Anderson. Mass-Selected Supported Cluster Catalysts: Size Effects on CO Oxidation Activity, Electronic Structure, and Thermal Stability of Pd_n/Alumina ($n \leq 30$) Model Catalysts. *International Journal of Mass Spectrometry*, 2014, **370**, 1-15.

7. W. E. Kaden, W. A. Kunkel, F. S. Roberts, M. Kane and S. L. Anderson. Thermal and Adsorbate Effects on the Activity and Morphology of Size-Selected Pd_n/TiO_2 Model Catalysts. *Surface Science*, 2014, **621**, 40-50.

8. P. A. Redhead. Thermal Desorption of Gases. *Vacuum*, 1962, **12**, 203-211.

9. R. Schlaf, P. G. Schroeder, M. W. Nelson, B. A. Parkinson, C. D. Merritt, L. A. Crisafulli, H. Murata and Z. H. Kafafi. Determination of Interface Dipole and Band Bending at the Ag/tris(8-hydroxyquinolinato) Gallium Organic Schottky Contact by Ultraviolet Photoemission Spectroscopy. *Surf. Sci.*, 2000, **450**, 142-152.

10. R. Levy and M. Boudart. Platinum-like Behavior of Tungsten Carbide in Surface Catalysis. *Science*, 1973, **181**, 547-549.

11. Z. Zhang and J. T. Yates, Jr. Band Bending in Semiconductors: Chemical and Physical Consequences at Surfaces and Interfaces. *Chem Rev*, 2012, **112**, 5520-5551.

12. N. Nilius. Properties of Oxide Thin Films and their Adsorption Behavior Studied by Scanning Tunneling Microscopy and Conductance Spectroscopy. *Surface Science Reports*, 2009, **64**, 595-659.

13. J. Robertson. Band Offsets, Schottky Barrier Heights, and their Effects on Electronic Devices. *Journal of Vacuum Science & Technology A: Vacuum, Surfaces, and Films*, 2013, **31**, 050821.

14. K. M. Tracy, P. J. Hartlieb, S. Einfeldt, R. F. Davis, E. H. Hurt and R. J. Nemanich. Electrical and Chemical Characterization of the Schottky Barrier Formed Between Clean n-GaN(0001) Surfaces and Pt, Au, and Ag. *Journal of Applied Physics*, 2003, **94**, 3939-3948.

15. W. Schottky. The Semiconductor Theory of the Blocking Layer and Point Rectifier. *Zeitschrift fuer Physik*, 1939, **113**, 367-414.

16. W. Schottky. Semiconductor Theory of the Barrier Film. *Naturwissenschaften*, 1938, **26**, 843.

17. L. Q. Zhu, N. Barrett, P. Jégou, F. Martin, C. Leroux, E. Martinez, H. Grampeix, O. Renault and A. Chabli. X-ray Photoelectron Spectroscopy and Ultraviolet Photoelectron Spectroscopy Investigation of Al-Related Dipole at the HfO_2/Si Interface. *Journal of Applied Physics*, 2009, **105**, 024102.

APPENDIX B

SUPPORTING INFORMATION INCLUDED FOR

CHAPTER 5

B.1. Experimental

B.1.1 The apparatus (supplemental figures and tables)

Table B.1 details the typical deposition time and measured sample current due to neutralization of the 0.1 ML deposited Pd_n^+ clusters on the surface when deposited at 1 eV/atom. The high currents for Pd_1 suggests that it is easy to create an environment in which no two Pd atoms combine. The dip in deposition current for Pd_{2-4} suggests that, in the current set up, the system is optimized to form clusters > 4 atoms in size.

Figure B.1 shows a detailed view of the laser vaporization source within the cluster deposition/source beamline pictured in Figure 5.1. It can be seen that the Pd vaporization target is mounted on an XY stage to allow for target rastering. A small burst of ultrahigh purity helium is injected into the clustering volume via a piezoelectric pulsed valve. During this helium pulse, the frequency doubled Nd:YAG laser is directed onto the vaporization target in order to form a Pd containing plasma. The plasma is further cooled by the helium pulse and promotes cluster formation. The formed clusters are then ejected out of the cluster exit nozzle and into the first quadrupole ion guide.

B.1.2 Mass spectrometer calibration

In order to gain a better understanding of the system and a relative amount of CO/CO_2 associated with each Pd atom/cluster under reaction conditions, an effort was made to calibrate the signal originating from the differentially pumped mass spectrometer shown in Figure B.2. We have previously[1] done this conversion using factors determined by measuring desorption from saturated CO layers of known coverage. Here, we used a different approach, with quite similar conversion factors resulting. With the sample

Table B.1: Typical Pd_n^+ deposition times and neutralization currents measured at the sample with a retarding potential to deposit the clusters at 1 eV/atom.

Pd_n^+ Cluster size	**Deposition Time (min)**	**Deposition Current at 1 eV/atom (pA)**
1	4	3000
2	28	214
3	29	138
4	27	111
5	8	300
6	5	400
7	4	429
10	3	400
15	2	400
20	3	200
25	4	120
27	6	74
30	10	40

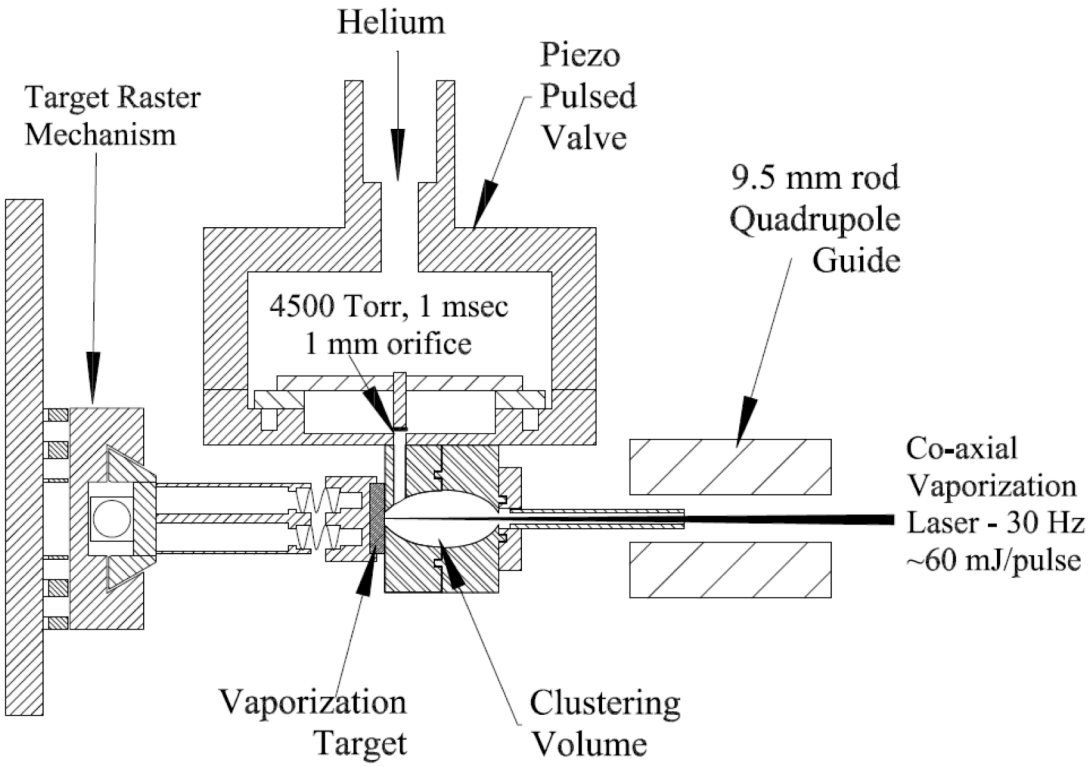

Figure B.1: Cross sectional view of the co-axial laser vaporization source.

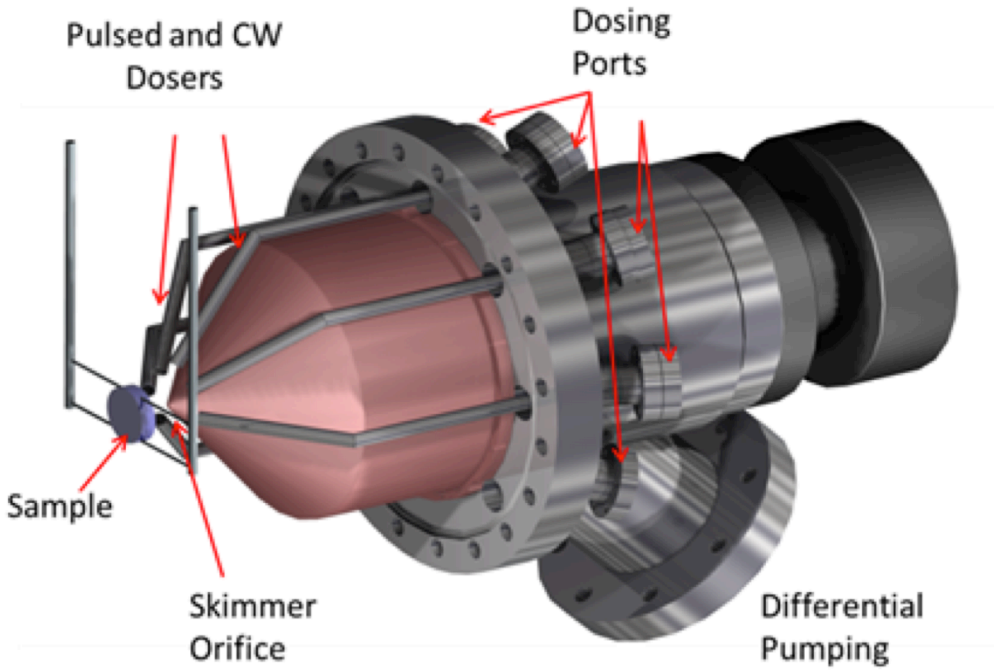

Figure B.2: Schematic of the differentially pumped mass spectrometer used in reactivity studies, showing skimmer cone and directional gas dosing lines. Note: colors are for contrast – all parts are constructed from stainless steel.

positioned away from the skimmer orifice, CO or CO_2 were leaked into the main UHV chamber at several different pressures, as measured by a nude ion gauge and corrected for ion gauge sensitivity using manufacturer's data. The CO^+ or CO_2^+ signal on the TPR/TPD mass spectrometer was then measured under ionizer and mass filter settings identical to those used in the TPR/TPD experiments. It is straightforward to calculate the flux of molecules passing through the 2.5 mm diameter orifice in the skimmer cone, and thus derive factors for converting CO or CO_2 flux into the mass spectrometer to CO^+ or CO_2^+ signal. To check for possible day-to-day variations in sensitivity due to electron multiplier gain drift, for example, a similar comparison of pressure vs. ion signal was made every day.

There are a number of factors that complicate the problem, adding systematic uncertainty. The skimmer orifice is not thin walled, but has a thickness of ~ 1mm, and the cluster spot (~2 mm) is somewhat smaller than the orifice (2.5mm). While desorption from a flat surface typically has the same cosine angular distribution as molecules effusing through an orifice, it is not clear whether this assumption is reasonable for molecules desorbing from clusters on a surface. Finally, it is not obvious, *a priori* how the detection sensitivity might vary with the angle that the molecules enter the skimmer cone. To assess the sensitivity to angle, we examined the variation in signal levels for CO desorption with respect to sample-orifice distance. If detection were strongly biased toward molecules entering along the mass spectrometer axis, then intensity would vary slowly with sample-orifice distance. Instead, we find a factor of ~2 variation as the sample is moved 1 mm closer to the orifice. This result indicates that due to collisions with surfaces inside the mass spectrometer housing, the signal is essentially averaged

over a wide range of angles. Finally, it is not clear what effect sample temperature (hence the velocities of desorbing molecules) might have on detection efficiency. Generally, faster molecules spend less time in the ionization volume, and therefore are detected with lower sensitivity, however, if most molecules collide with surfaces in the mass spectrometer (as suggested by the strong variation with sample-orifice distance), then the effect of sample temperature would largely be erased. Because we have no way of measuring the variation in detection efficiency with desorption angle, distance from the spot center, and sample temperature, we simply assume that the efficiencies are identical for molecules desorbing from the sample and molecules entering the mass spectrometer in the gas-phase calibration experiments, and that efficiency is independent of distance from the centerline and sample temperature.

Taking all this into consideration, we convert the measured ion signals to molecular desorption fluxes, with estimated systematic uncertainty of roughly a factor of 2. Examination of the results suggests that the reported fluxes are probably near the low end of this uncertainty range. For example, the integrated amount of CO desorbing from Pd_n/alumina after a saturation exposure at 180 K amounts to ~0.5 CO molecules per Pd atom, which is lower than might be expected for saturation CO coverage on a small cluster. It is also lower than the coverage suggested by electrochemical CO stripping measurements which found ~9 CO adsorbed per Pt_9 cluster supported on glassy carbon.[2] In the following, we give desorption fluxes based on the experimentally determined conversion factors, however, the true fluxes are probably higher, possibly by up to a factor of 2.

B.2 Results

B.2.1 CO desorption trends

Figure B.3 depicts the cluster size dependent CO desorption from samples during a both a CO TPD and as residual, unreacted CO from a TPR measurement. The figure depicts the CO as both the total amount desorbing from the surface, and the CO desorbing only from the high temperature desorption peak as determined in Figure 5.6a.

B.2.2 CO_2 production temperature dependence

Figure B.4 shows CO_2 desorption during the first TPR for selected Pd_n/alumina/Re(0001) samples. Note: enhanced CO_2 desorption around 425K for Pd_5 and Pd_{25}.

B.2.3 Disentanglement of adsorbates and elemental sensitivity in ISS

The protocol used to determine the "as-deposited" Pd ISS intensity for the samples is illustrated in Figure B.5, for Pd_{20}/alumina/Re(0001). Samples were first probed by a series of three low flux ISS measurements followed by 10 high flux ISS measurements (approximately 21 seconds per measurement). In the raw spectra shown in the inset, it can be seen that there are peaks due to O, Al, Pd, and a small feature tentatively attributed to Re. The relationship between peak intensities and surface layer concentrations is not straightforward, because ISS intensities also depend on the cross sections and He^+ ion survival probability (ISP) for scattering from different elements, and on the geometry of the surface layer. For example, the three main peaks have similar

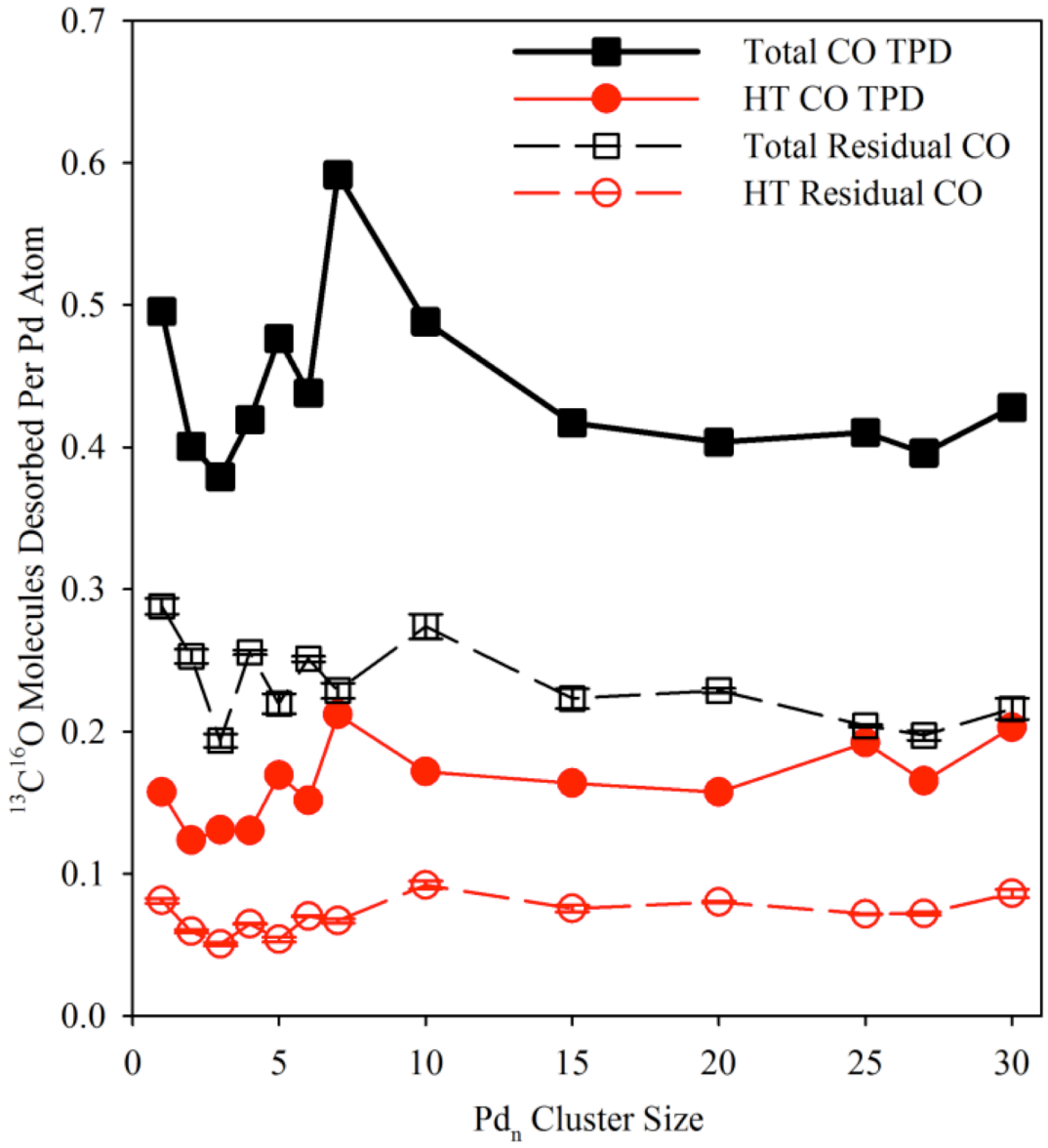

Figure B.3: Integrated total desorption of CO per Pd atom ("Total CO TPD") and desorption in the high temperature feature (HT CO TPD) measured in TPD are plotted as solid lines. Integrated desorption of total unreacted CO during TPR ("Residual CO") and of just the high temperature residual CO are plotted as dashed lines. Error bars on the residual CO measurements show the variation in the three consecutive TPR measurements.

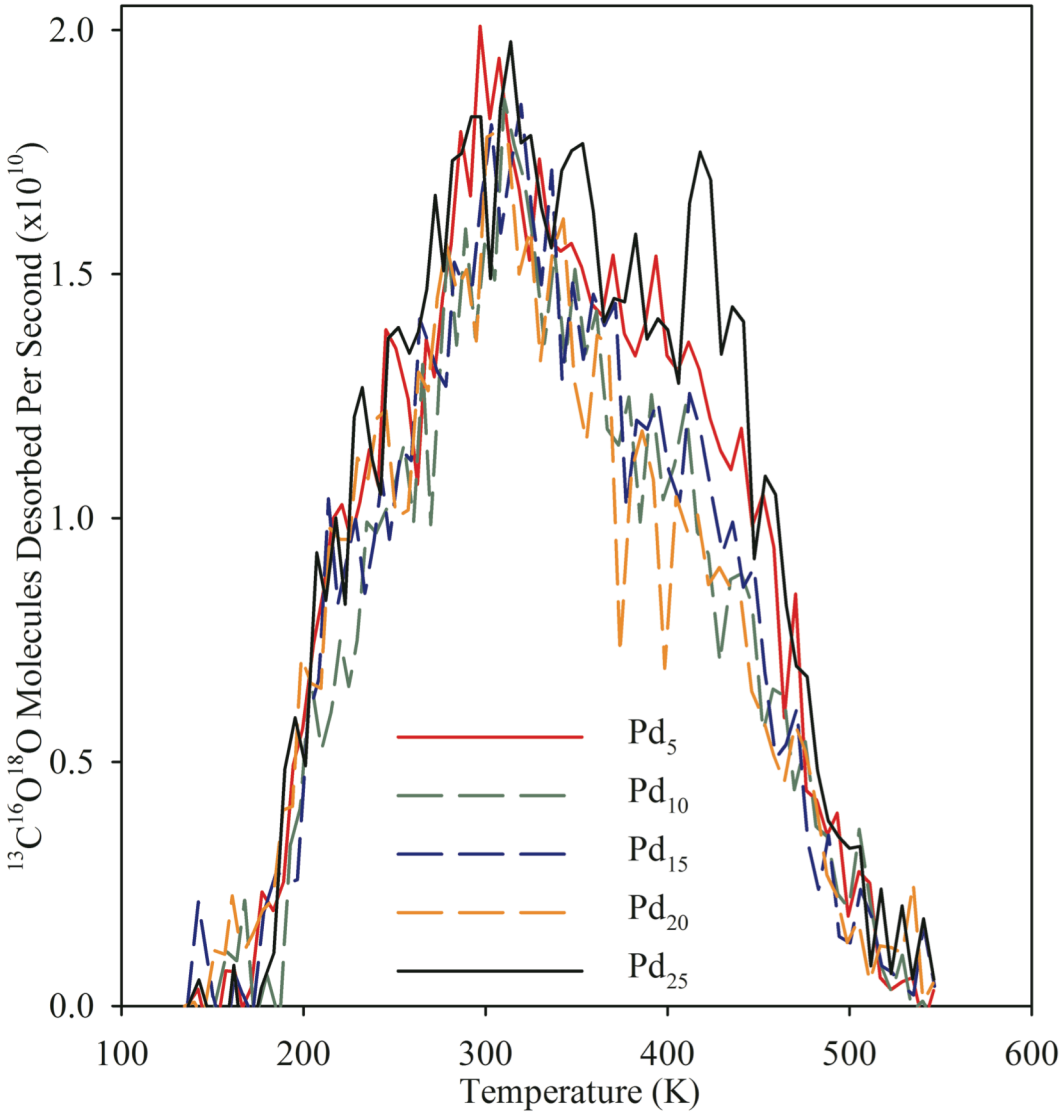

Figure B.4 shows the temperature dependence of CO_2 production for samples with selected cluster sizes. In general, the results are quite similar, as might be expected from the fact that the activity is weakly dependent on cluster size under these conditions. It can be seen that for the two most active sizes (Pd_5 and Pd_{25}), there is more CO_2 production at all temperatures, but particularly at temperatures above 400 K, compared to the less active samples. This observation suggests that more oxygen was adsorbed and activated by Pd_5 and Pd_{25}.

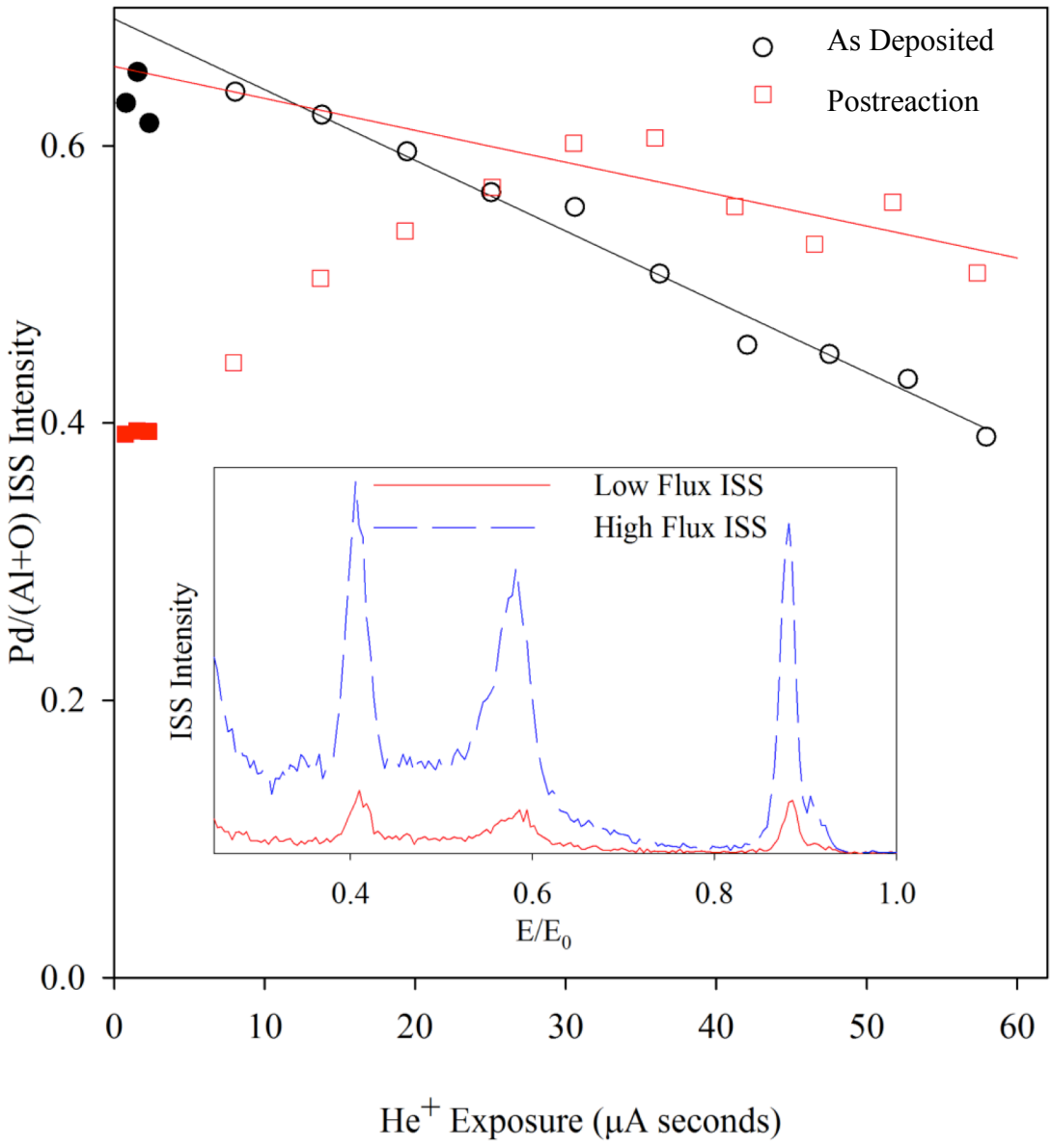

Figure B.5: Inset: Raw ISS spectra for as-deposited Pd_{20} measured with high He^+ flux (blue) and low He^+ flux (red). The peaks at 0.41, 0.58, 0.88, and 0.91 correspond to single scattering from O, Al, Pd, and Re atoms, respectively. The background between peaks results from multiple scattering. Main figure: Normalized Pd ISS intensity for Pd_{20}, as a function of He^+ exposure during a sequence of three low flux measurements (filled symbols) followed by 10 high flux measurements (empty symbols). Data are shown for a Pd_{20} sample both as-deposited (circles) and after reaction (squares).

intensities, despite the Pd coverage being only 0.1 ML-equivalent, and the alumina surface being oxygen terminated. On the other hand, changes in ISS intensities for different cluster sizes, or at different stages in reaction studies, provide valuable insight into changes in morphology, and binding of adsorbates.

The main frame of Figure B.5 plots the Pd ISS signal as a function of He^+ exposure, for Pd_{20}/alumina, both as-deposited, and after the sequence of three TPR and one TPD experiments. The Pd ISS intensity is determined as the integrated, background-subtracted peak area, and is normalized to the sum of the Al and O intensities in order to correct for any day-to-day variation in the He^+ beam intensity. For as-deposited Pd_{20}, it can be seen that there may be a slight increase in Pd ISS intensity during the initial measurements, which could be the sign of a very small coverage of some adventitious adsorbate. Adsorbates attenuate He^+ scattering from the underlying Pd atoms by a combination of shadowing, blocking, and reduced ion survival probability.[1, 3-5] For our ISS geometry (45° incident angle, detection along the surface normal) the attenuation should only affect Pd atoms directly under or immediately surrounding the adsorbate binding site. Such an increase occurs because adsorbates are sputtered faster than Pd due to their relatively weak binding to the surface,[1, 3, 4] thereby exposing underlying Pd. In the subsequent high flux measurements, a slow decrease in Pd signal due to Pd sputtering is observed. The Al and O intensities are essentially constant, presumably because sputtering of Al or O from the surface layer simply exposes more Al or O in underlying layers. To determine the "as-deposited" Pd ISS intensity, the high flux measurements are extrapolated back to the limit of zero He^+ exposure and zero adsorbate coverage, as indicated by the trend line.

An example of postreaction ISS analysis is also plotted in Figure B.5. In this case, the initial Pd intensity is attenuated by ~40%, compared to the as-deposited result, and the Pd signal increases substantially during the first ~25 μA-sec of He^+ exposure, before beginning to decrease due to Pd sputtering. The signal recovery indicates that a substantial fraction of the initial attenuation is attributable to the presence of adsorbates blocking He^+ scattering from the Pd clusters. Some of the adsorbates may have been left on the surface after the TPR/TPD series, however, there was undoubtedly also some adventitious adsorption during the 20 minutes when the sample was probed by XPS, prior to postreaction ISS. Regardless of the source, the attenuation due to the adsorbates can be approximately corrected for using the same extrapolation procedure used for the as-deposited samples. For this particular sample, the extrapolated postreaction Pd ISS intensity was essentially identical to that for the as-deposited sample, although there obviously is considerable uncertainty in the long extrapolation that results from the large initial adsorbate load.

B.3. References

1. W. E. Kaden, W. A. Kunkel, F. S. Roberts, M. Kane and S. L. Anderson, *J. Chem. Phys.*, 2012, **136**, 204705.

2. M. Nesselberger, M. Roefzaad, R. Faycal Hamou, P. Ulrich Biedermann, F. F. Schweinberger, S. Kunz, K. Schloegl, G. K. H. Wiberg, S. Ashton, U. Heiz, K. J. J. Mayrhofer and M. Arenz, *Nat. Mater.*, 2013, **12**, 919-924.

3. M. Aizawa, S. Lee and S. L. Anderson, *Surf. Sci.*, 2003, **542**, 253-275.

4. W. E. Kaden, W. A. Kunkel and S. L. Anderson, *J. Chem. Phys.*, 2009, **131**, 114701.

5. J. W. Rabalais, *Principles and Applications of Ion Scattering Spectrometry: Surface Chemical and Structural Analysis*, Wiley, New York, 2003.